NOTE TO USERS

INVESTIGATION OF PARTICLE INHALABILITY

Theresa Renée Anthony

A dissertation submitted to the faculty of the University of North Carolina at Chapel Hill in partial fulfillment of the requirements for the degree of Doctor of Philosophy in the Department of Environmental Sciences and Engineering, School of Public Health.

Chapel Hill
2005

Approved by

Advisor: Professor Michael Flynn

Reader: Professor Douglas Crawford-Brown

Reader: Dr. Alfred Eisner

Reader: Professor David Leith

Reader: Professor Leena Nylander-French

Reader: Professor Michael Symon

ABSTRACT

THERESA RENÉE ANTHONY: Investigation of Particle Inhalability

(Under the direction of Dr. Michael Flynn)

This research investigated particle inhalability in low velocities typical of occupational settings. Because of difficulties suspending uniform particle concentrations in low velocity wind tunnels, the goal was to develop a computational fluid dynamic (CFD) model suitable to study inhalability. The first step in this study was to determine the appropriate simplifications to the human form. An experimental study compared the velocity field and particle aspiration for a 2/3-scale human mannequin and a stacked elliptical cylinder: velocity field differences were limited to a region within 20 mm upstream of the mouth orifice and, more importantly, the fraction of aspirated particles was significantly larger for the simpler geometric surrogate than for the fully-featured mannequin. Knowing that detailed facial features were critical to large particle aspiration, a small-scale humanoid CFD model was developed and its predictions were compared to the experimental results. The standard *k*-epsilon model provided reasonable estimates of the velocity field in the forward-facing orientation, even though rigorous studies have reported poor performance of this model in the wake of a surrogate human. Particle aspiration simulations using this model confirmed that the moderate under-estimations of vertical velocity field affected particle transport from a source, but that the model is still useful for the exploration of particle inhalability using the assumption of a uniform particle concentration and laminar particle transport. The final step in this study examined a human-scale version of this CFD model, where three velocity conditions were simulated to investigate particle inhalability. One condition was matched to data in the literature, and agreement was found for particles < 68 μm. Simulations of aspiration efficiency for larger particles under-estimated those reported by others. However, the other authors' experimental biases may have over-estimated aspiration efficiency by under-sampling the reference concentration. Although this research does not consider

other orientations needed to fully define aspiration efficiency, the facing-the-wind orientation studied here is associated with the maximum aspiration efficiency. These results provide evidence that the omni-directional aspiration efficiency curve for low velocity environments decreases below the 50% asymptote given by the American Conference of Governmental Industrial Hygienists' inhalable particulate mass collection efficiency curve guideline.

ACKNOWLEDGEMENTS

I extend my sincerest thanks to all in Baity Lab who made this journey worth taking, especially for the patience, determination, and unfailingly high expectations of Maryanne Boundy, a mom and friend to all. To David Leith and Mike Flynn, I give a special thanks for the years of nagging to convince me to return to Carolina: your continued support and mentoring are invaluable. To the rest of my committee, your insights and generosity of time are also greatly appreciated. And to the friends that I have made along the way, the laughter and tears (and jubilation at the Dean Dome) will be treasured always.

Support of equipment and funding are greatly appreciated. The U.S. EPA at RTP provided me with access to and assistance with the low velocity wind tunnel and aerosol generating equipment. The Department of Education provided me with GAANN funding for the start of my studies. Both NIOSH and NIEHS provided me with funding to support the bulk of this research. The 3M Corporation also awarded me with an industrial hygiene scholarship. I am grateful to all these institutions for their commitment to higher education and investment in research.

Were it not for the desire for both knowledge and excellence instilled by my parents, I would not have completed this work. My last conversation with my father in 1989 discussed returning to school to learn about a field that I have since come to love: I know he would be proud of this work. Mom, a simple thanks is insufficient to express my gratitude for your help these past four years, let alone all the years preceding them. Without you, I would not be the person I am today. Finally, a thanks to my brothers, Mike and Robert Craig, for no longer asking me "so, when are you going to get done?"

TABLE OF CONTENTS

LIST OF TABLES

LIST OF FIGURES

CHAPTER 1: INTRODUCTION

1.1 Statement of Problem

Particle size is a primary factor to predict inhaled particle deposition in the human respiratory system. Large (>10 μm) particles deposit primarily by impaction in the upper respiratory region and have been associated with deleterious health effects. Nasal lesions and cancers are associated with the deposition of wood dust, nickel, chromium, and formaldehyde-contaminated particles. Large insoluble materials, including oil mists and copper-chromated arsenate on wood dust, deposit in the upper airways and can be transported to the gastrointestinal tract via clearance mechanisms where adverse effects may manifest. In addition, soluble particles that react quickly with tissue, such as allergens and radioactive materials, are of concern regardless of where they deposit in the respiratory system. Historically, methods to measure exposures to aerosols have excluded large particles that would deposit in the upper airways.

However, in 1985, criterion was proposed to address large particle sampling to estimate exposures to materials that cause health effects regardless of where they deposit once inhaled. This performance criterion required samplers to collect particles with the same efficiency as that of a breathing human. "Particle inhalability" became the term used to describe the aspiration efficiency of a breathing human's mouth and nose. It is defined as the ratio of the inhaled particle concentration to the upstream uniform particle concentration. Since the initial work of Ogden and Wood in 1975, many experimental and numerical investigations have studied aspiration for particle sizes up to 100 μm. The inhalable particulate mass (IPM) collection efficiency curve proposed by the American Conference of Governmental Industrial Hygienists (ACGIH) in 1985 remains unchanged today, given as:

$$IPM = 0.5\,(1 + e^{-0.06d}),\ d \leq 100\ \mu m \tag{1.1}$$

where d is the aerodynamic particle diameter.

However, the experimental studies used to develop this curve were conducted in wind tunnels with freestream velocities considerably larger than the mean occupational air velocity of 0.3 m s^{-1} (Baldwin and Maynard, 1998). These and traditional thin-walled sampler studies had previously demonstrated that particle aspiration depends on the freestream velocity, as well as the breathing rate and orientation to the wind. Recent attempts to investigate aspiration at low velocities have illustrated the difficulty maintaining uniform particle concentrations in low velocity environments. Aitken *et al.* (1999) and Hsu and Swift (1999) attempted "calm air" inhalability studies, but their findings conflicted. Although both agreed that aspiration efficiency decreased with increased particle size, these researchers presented different relationships between aspiration efficiency and particle size. Hsu and Swift reported that particles larger than ~150 μm were not inhalable, while Aitken *et al.* found that particles as big as 150 μm were aspirated with 50% efficiency. Kennedy and Hinds (2002) conducted more traditional mannequin studies at 0.4 m s^{-1} freestream velocity but reported particle suspension problems, particularly for the larger particles.

Numerical studies have provided an alternative method to investigate particle inhalability that avoids the uniform particle suspension problems. Most of these simulations have represented the human form with simple geometric shapes and round mouth openings. Furthermore, these numerical investigations were also performed at velocities greater than the 0.3 m s^{-1} typical of occupational environments. Dunnet and Ingham's study (1988) was the only one to investigate the results of numerical simulations to mannequin experiments. They reported that facial features may become important to particle transport in low suction – high freestream velocities.

No computational fluid dynamic (CFD) study has used a realistic human form to investigate particle inhalability. Air flow around a human surrogate and, in some cases, contaminant transport near this form have been simulated using CFD, but results have been presented without rigorous verification. Roache (1998) indicates that CFD practitioners have focused on qualitative simulations of complex problems rather than achieving quantitatively accurate solutions to simpler representations of the same problem. For instance, Murakami *et al.* (1999) simulated air motion around a heated

human form and Brohus (1997a) and Hayashi *et al.* (2002) simulated contaminant transport near heated human forms, but neither examined the mesh densities or verified convergence.

Exposure-related CFD studies that have addressed verification include studies of particle transport in the wake of cylinders, which were used as much simpler surrogates for the human form. Although iterative and mesh convergence was addressed, these studies identified problems using a steady-state *k*-epsilon model to estimate exposures in the near wake where time-dependent eddy shedding is important (Flynn *et al.*, 2005).

A CFD model based on realistic human anthropometry has not been developed to examine particle aspiration, particularly in low velocities representative of the occupational environment. This research develops such a model and provides a quantitative assessment of the model's performance. Steady-state simulations with the human form facing the wind avoid the time-dependent phenomenon in the near wake, and this orientation is reported to be associated with the maximum aspiration efficiency to uniform particle concentration (Tsai *et al.*, 1995). The results from the forward-facing aspiration studies provide an upper limit to the particle inhalability curve and provide guidance to the inhalable particulate mass concentration criterion for samplers used in occupational environments.

1.2 Research Objectives

The objective of this research was to determine particle inhalability in low velocities that are typical of occupational settings. The focus of this work was to develop a CFD model to investigate particle inhalation using a 3-dimensional human form. This research consisted of three phases, with the following specific objectives:

1. Determine the adequacy of a simplified geometric form to study particle inhalability. This goal was accomplished by comparing velocity measurements and inhaled particle concentrations between two small-scale mannequins.
2. Develop and evaluate a CFD model at the experimental scale; specifically evaluate the performance of the standard *k*-epsilon model. The experimental

conditions from objective 1 were modeled; verification of simulations and validation with experimental data were assessed.

3. Develop a human-scale model and evaluate particle aspiration efficiency. The geometry and system of equations from objective 2 were scaled to human-scale; verification was assessed; particle simulations were conducted to determine aspiration efficiency for three different velocity conditions representative of occupational settings.

1.3 Summary of Findings

1.3.1 Experimental Evaluation of Mannequin Shape

Velocity fields and particle aspiration fractions were compared between a stacked elliptical cylinder and a realistic human mannequin. Both forms had the same mouth opening shape and size, but the human mannequin had realistic facial features, specifically lips, nose and chin. Because of the size limitations of the wind tunnels used, scaled models were required for this part of the study. All experiments were conducted with the mannequin facing the wind. Because this orientation is associated with maximum aspiration efficiency for large particles (Tsai *et al.,* 1995), it was optimal for the velocity measurements and desirous for the later computational studies.

Significant velocity differences were identified only within 20 mm of the mannequin mouth, indicating that the facial features affected flow only near the mannequin face. These velocity differences were associated with key facial landmarks. Due to the restriction of air imposed by the lips, a larger streamwise velocity was identified upstream of the anatomical mannequin's mouth, but larger vertical velocities were identified just above and below the cylinder's mouth. As anticipated, streamwise velocities under the chin were larger for the anatomical mannequin, while velocities at and above the nose were smaller for the anatomical mannequin.

The median aspirated particle size was 60 μm for both mannequins. However, the mass concentrations were significantly larger for the elliptical mannequin over the range of velocities studied: on average, the elliptical form aspirated 88% more mass than the anatomical form. Because the particles reaching the mouth were influenced by gravity,

particle impaction on the lips and nose of the anatomical mannequin resulted in these decreased inhaled mass concentrations.

The differences in velocity field and mass aspiration between these two forms were significant. This phase concluded that aspiration efficiency modeling should include a realistic representation of the human face.

1.3.2. Development of CFD Model

Because phase 1 of this research indicated that a realistic human head was required to study particle aspiration, a three-dimensional representation of a human form was generated. The complexity of the facial features was included, but a simple elliptical cylinder represented the torso. The size of the computational domain matched the study wind tunnels. To minimize computational costs, the human form was truncated at the hips and lateral symmetry was assumed, modeling only the right half of the human form and wind tunnel.

Convergence of the CFD model was achieved near the head of the mannequin, but farther upstream, the mesh was still too coarse. The average element size was 0.4 mm near the mouth but 5.81 mm at the wind tunnel entrance.

The velocity estimations agreed reasonably well with experimental data, although the vertical velocity component was under-estimated in nearly all locations. The truncation of the mannequin at the hip could have contributed to these differences. Low particle seeding in experimental work resulted in insufficient data to validate the turbulence kinetic energy model.

Particle simulations identified a maximum aspiration fraction for 57.5 μm particles, whereas the maximum experimental aspiration fraction occurred at 66.5 μm. This 9-μm difference is consistent with the under-estimation of vertical velocity identified in the velocity validation and an under-representation of the particle momentum out of the nozzle. The simulated aspiration fractions were orders of magnitude greater than the experimental values. This finding is probably due to a poor representation of the turbulent wake behind the nozzle, which increased particle dispersion in experimental tests.

1.3.3 CFD Investigation of Particle Inhalability

The geometry and mesh density from phase 2 of this study were scaled by a factor of 1.5 to represent the human-scale system. Three velocity conditions were investigated. The 0.2 m s^{-1} freestream and 1.81 m s^{-1} inhalation velocities matched the Reynolds numbers of the small-scale system of phase 2 (Re = 1910). The 0.4 m s^{-1} freestream and 4.33 m s^{-1} inhalation velocities matched experimental data provided by Kennedy and Hinds (2002). The 0.2 m s^{-1} freestream and 4.33 m s^{-1} inhalation velocities were evaluated to examine the interaction between freestream and breathing velocities. The human-scale systems had similar iterative and mesh convergence characteristics to the small-scale system: convergence was demonstrated near the mannequin head, but additional refinement upstream of the mannequin was still needed.

For the 0.4 m s^{-1} freestream velocity simulations, the aspiration efficiencies for particles $\leq$ 68 μm agreed with data from Kennedy and Hinds (2002). Larger particles had smaller simulated aspiration efficiencies compared to the experimental data. For these large particles, gravitational settling dominated particle motion: the horizontal orientation of reference sampling probes in the experimental studies may have contributed to under-sampling of these particles, resulting in the reporting of larger experimental aspiration efficiencies.

For particles $\leq$ 52 μm, aspiration efficiency did not vary significantly over the velocities studied (coefficient of variation < 0.06). However, as the particle size increased, aspiration efficiency was more affected by flow conditions (coefficient of variation ranged from 0.14 to 1.65).

Because bounce may have contributed to secondary aspiration in the experimental data, particle bounce was estimated by locating upstream areas where particles moved toward the mouth but terminated on the outer lip surfaces. Particle bounce with 100% secondary aspiration was inferred from these simulations. Resulting aspiration efficiencies over-estimated aspiration data from Kennedy and Hinds. Hence, not all particles that hit the lips while moving towards the mouth are expected to result in secondary aspiration.

1.4 Implications of Findings

The steady-state *k*-epsilon model provided a reasonable representation of time-dependent breathing. The results from these aspiration efficiency studies provide guidance useful to the re-evaluation of the ACGIH IPM curve as well as to the practice of assessing personal exposures to particles in occupational settings. The work also provides guidance to the development and use of CFD modeling to examine occupational exposures.

1.4.1 IPM Criterion

This work identified the importance of facial features to the study of particle inhalability. The dimensions of the nose and lips were not varied, but their presence resulted in deposition of particles traveling toward the mouth. Because a larger nose or lips could increase particle deposition on these features, additional examination is warranted. Nose breathing was not examined in this work, but it is anticipated to be less efficient than the mouth as particles would have to turn upwards into the nose. Hence, simulations with the small nose, mouth breathing, and forward-facing orientation reflect the highest aspiration efficiency condition for the range of velocities studied.

The current ACGIH criterion is independent of velocity and recommends that particles larger than 50 μm should be sampled with 50% efficiency. Compared to the aspiration efficiencies reported in this work, the ACGIH IPM criterion recommends over-sampling of large particles in low velocity environments. Hence, an investigation of inhalable sampler performance in low velocities is recommended to determine whether aspiration efficiencies of existing inhalable samplers are comparable to the inhalable curves presented here. Furthermore, the inhalable criterion should specify both particle size and workplace velocities to ensure that sampler aspiration efficiencies truly match human aspiration efficiencies.

1.4.2 Exposure Assessments

These aspiration studies also provide information useful to estimate exposures to aerosol point sources. Simulations identified that small particles generated upstream at

the mouth height of the worker would be inhaled. However, large particles generated at this same height would not be inhaled because particle motion is dominated by gravity.

The particle aspiration studies also highlight concerns regarding sampler positioning on workers. Sampler positioning may not be a significant concern when the spatial distribution of particles is uniform throughout a workplace. However, if a worker is exposed to an aerosol from a point source, the placement of an inhalable sampler is critical. For example, depending on the distance between an aerosol source and the worker, larger particles generated at mouth height would settle through the "breathing zone" but could be aspirated into a sampler positioned at the worker's lapel, hence *over-estimating* worker exposure. The sampling biases associated with the location of an inhalable sampler require serious investigation.

The simulations for these studies also provide information on dermal deposition. The investigation of particle "bounce" examined the critical area associated with particles terminating on the lips. While particle bounce is an important consideration in mannequin studies, most particles landing the lips of a real person would stick to this moist skin, where subsequent ingestion is likely. For larger particles, the proportion of particles depositing on the lips was larger than that inhaled. The CFD model developed to investigate inhalability is well suited to model dermal deposition on the face.

1.4.3 CFD Modeling

This research provides the first verified and validated CFD model of an inhaling human with realistic facial features. A significant portion of this work focused on evaluating the performance of the CFD simulations. *Any* CFD simulation can provide estimates of fluid flow. However, an examination of the *quality* of the estimated flow field is necessary to determine whether the finite discretization sufficiently represents the continuum under investigation.

This work assessed the model's performance using two methods: traditional CFD verification and grid convergence testing detailed by Roache (1999) as well as a more heuristic approach introduced by Flynn and Eisner (2004). With the grid convergence method, two- and three-mesh error norms were examined and orders of accuracy were determined to assess monotonic convergence of solutions. With the second approach,

solutions from sequentially refined meshes were compared using least-squares regressions. Where slopes were 1, intercepts were 0, and coefficients of determination approached 1, increasing mesh densities would yield negligible changes in the solutions. This second method provided a more qualitative yet intuitive approach to assess convergence, whereas the first method was necessary to assign uncertainties to the estimates provided by the model.

Validation of the solutions to the CFD model was assessed for each of the three velocity components. The simulated velocity was validated at specific locations where the range of uncertainty for a measured velocity overlapped the range of uncertainty for the estimated velocity. In this work, the measured lateral velocities had larger variability than other velocities because data were reflected from the left to the right of the mannequin despite some asymmetry in the mannequin. Because of this large measurement uncertainty, a larger proportion of simulated vertical velocities were validated. This validation highlights the conundrum associated with validating CFD models: the more uncertain the simulated or experimental data, the more likely the model will be validated; yet good research attempts to minimize uncertainty. Small confidence intervals surrounding data could prevent validation of a reasonably well performing model, and large confidence intervals could result in validation of a poor model. In this event, examination of the simulated data using traditional statistical regressions, discussed above, is useful to show and examine agreement in data trends.

In CFD simulations, the finer the mesh, the more the finite discretization represents a continuum. The models developed and presented in this work had denser meshes than have been reported by others investigating flow past humanoid forms. For the human-scale system in this study, the average element size was 1.7 cm, significantly smaller than other studies: 4.4 cm for Hyun and Kleinstreuer (2001), 4.4 cm for Murakami *et al.* (1999), and 8.1 cm for Brohus (1997a). In addition, the element size on the mouth of this study (0.4 mm) was more refined than other researchers investigating contaminant transport (2 mm used by Hyun and Kleinstreuer, 2001). No mesh convergence studies were presented for these coarser mesh simulations. Although some of these researchers used different turbulence models that might perform sufficiently with their coarser meshes, convergence had not been assessed. Based on the mesh convergence

investigations of this study and the relative mesh coarseness of previous CFD simulations, earlier work may have larger uncertainty than the model presented in this study. This work sets the standard to evaluate quantitatively the performance of CFD simulations, specifically to the field of occupational hygiene.

1.5 Future Research

The gaps left by this research include the resolution of kinetic energy, the examination of other orientations relative to the freestream, and the investigation of particle bounce. If the model is to be useful to investigate both particle aspiration from a source or to investigate turbulent particle behavior, the resolution of kinetic energy is still required. A low Reynolds number model, such as the *k*-omega, or the k-epsilon realized model may better equipped to handle the low turbulence. However, the mesh density and boundary layer near the human head will require adjustments to accommodate the wall assumptions for this system of equations.

However, the model was sufficient to examine particle aspiration using laminar particle motion. Re-orientation of the human form within the computational domain would be reasonably easy, although the assumption of lateral symmetry would no longer apply. For orientations other than facing-the-wind and back-to-wind, the human form geometry would require investigation with a full human form, essentially doubling the mesh size. The computational requirements of Fidap were maximized for the study presented here, and either the reduction in the domain size or the use of alternative CFD software capable of handling computations requiring more than 2GB RAM would be necessary. Furthermore, as the mannequin is rotated to the backward-facing direction, modeling difficulties are anticipated, as aspiration would occur in the wake where the standard *k*-epsilon model has performed poorly with non-inhaling surrogate human forms.

Finally, a complete investigation of particle bounce near the lips would require additional simulations and post-processing using particle ricochet. A study is first needed to determine the occurrence and conditions of bounce from particles that hit a human lip. The selection of an appropriate angle of reflection for particle bounce introduces a source of uncertainty, and its influence should also be assessed.

CHAPTER 2:
EVALUATION OF FACIAL FEATURES ON PARTICLE INHALATION

2.0 Abstract

Computational fluid dynamics (CFD) and numerical investigations of particle inhalability and contaminant exposure have used simple geometrical surrogates for a breathing human form, but the effect of eliminating facial features has not been investigated. In this work, the velocity field and particle aspiration associated with two differently shaped mannequins were investigated to determine if an elliptical form was sufficient to represent the complexity of fluid flow associated with an inhaling human. Laser Doppler anemometry was used to measure velocity, and both optical sizing and gravimetric analysis were used to measure particle aspiration from an aerosol source. All tests were performed with continuous inhalation through the mouth, with the mannequin facing the 0.3 m s^{-1} freestream. Although limitations in the laser Doppler optics prevented velocity measurements at distances closer than 11 mm in front of the mannequin mouth opening, significant velocity differences were identified up through 20 mm in front of the mouth opening. This indicated that facial features affected the flow field only near the face. Because of these differences, particle aspiration was compared between mannequins for three different velocity ratio conditions using an aerosol source. Even with relatively large variability in aspirated concentration in this study, the aspirated mass concentration was significantly less for the anatomical mannequin relative to the elliptical form. Thus, the simplified elliptical cylinder does not sufficiently

---

Reproduced with permission from Anthony, T. Renée, Michael R. Flynn and Alfred Eisner, Evaluation of Facial Features on Particle Inhalation, *Ann. occup. Hyg.* 49(2): 179-193 (2005)

characterize the fluid dynamics near the mouth of an inhaling human form at these limited test conditions. Future computational fluid dynamics and numerical simulations to investigate human aspiration of particles should incorporate the complex features of the human face to adequately investigate particle aspiration in low velocity environments.

2.1 Background

The investigation of human health effects associated with inhaling airborne contaminants requires the determination of dose received by the exposed individual. Because dose is often estimated by measuring contaminant concentration near the breathing zone of a potentially exposed person, samplers must be designed to collect particles with efficiencies similar to that of the breathing human. Inhalable particles must be sampled with a device whose size-selective efficiency matches the American Conference of Governmental Industrial Hygienists (ACGIH) inhalable particulate mass (IPM) curve (ACGIH, 2004):

$$\text{IPM}\ (d_{ae}) = 0.5\ [1+\exp(-0.06 d_{ae})] \qquad (2.1)$$

where:

d_{ae} = aerodynamic diameter of the particle, μm

This equation specifies that aspiration efficiency for a small particle is nearly 100% but approaches 50% for particles ≥ 50 μm.

This equation was developed from wind tunnel experiments where a breathing mannequin, rotated through 360°, was exposed to uniform concentrations of monodisperse particles (Vincent and Armbruster, 1981; Armbruster and Breuer, 1982; Ogden and Birkett, 1977 and 1978). The aspiration efficiency of these mannequins defined the inhalable curve for particles 1 to 100 μm in diameter.

However, to maintain adequate uniform concentrations of large aerosols (Vincent and Mark, 1982; Vincent *et al.,* 1990), mannequin tests to generate this curve were conducted with velocities greater than typical indoor workplace values of 0.1 to 0.3 m s^{-1} (Baldwin and Maynard, 1998). Kennedy and Hinds (2002) investigated inhalability with a mean

velocity field of 0.4 m s^{-1}, but they reported difficulties maintaining uniform concentrations of large particles at this low velocity. Aitken *et al.* (1999) and Hsu and Swift (1999) attempted calm air inhalation studies, but reported different trends in the shape of the aspiration efficiency curves: Hsu and Swift reported an exponential decay beginning with greater than 100% efficiency for 13 μm particles and decreasing efficiencies to nearly 0% for 135 μm particles, whereas Aitken *et al.* indicated a linear trend that extrapolates to 0% efficiency for 263 μm particles at a 20 Lpm breathing rate.

Because of the difficulties associated with wind tunnel studies, particle aspiration has been investigated numerically using two- and three-dimensional computational fluid dynamics. Dunnett and Ingham (1986) and Ingham and Hildyard (1991) reported the aspiration efficiency of two-dimensional representations of a human form as an infinitely long cylinder. Similar two-dimensional work by Chung and Dunn-Rankin (1992) was validated with experimental work (Chung *et al.*, 1994, Chung and Dunn-Rankin, 1997). Fully three-dimensional studies have been limited to spherical bluff bodies, equivalent to a head without a neck and torso (Dunnett, 1997 and 1999, and Dunnett and Vincent, 2000). Erdal and Esmen (1995) presented a theoretical model of an approximation to a human form using a hemispherical top on a circular cylinder with a round opening for the mouth. Their results from inhalation in a 0.5 m s^{-1} freestream indicated that aspiration efficiency appeared to approach zero for particles of 200 μm.

These geometric simplifications to the complex human form provide insight into particle aspiration, but the appropriateness of using a simple shape to represent particle inhalation for a human has not been investigated. Due to the complicated geometry, no computational fluid dynamic study has investigated particle inhalability with an anatomical representation of a human face. A spherical representation of the human head without a neck and torso ignores the streamwise velocity reduction and lateral and vertical velocity flows induced by the mannequin bluff body, identified as significant in early high velocity mannequin studies of inhalability (Ogden and Birkett, 1977; Vincent and Mark, 1982). In addition, the importance of anatomical facial features on the velocity field has not been fully investigated. Ogden and Birkett (1977) investigated the impact of anatomical features by smoothing facial features and found the features had little effect on aspiration efficiency. However, their smoothing retained the protrusions

of the nose and lips and the recession below the chin, which are not included when modeling a simple sphere as a substitute for the human shape.

Numerical simulations by Dunnett and Ingham (1988) used a sphere to represent the mannequin head studied by Ogden and Birkett. The authors indicated that deviation between the experimental mannequin study and the numerical simulation was significant for the low suction rate conditions ($U_s = 1.07$ m s^{-1}), where the facial structure likely had more influence on the overall velocity field since suction no longer dominated ($R = U_o/U_s = 2.57$). Differences between the spherical form and the mannequin were insignificant as the velocity ratio neared unity ($R = 1$). However, the low freestream velocity ($R < 1$) present in many occupational environments has not been explored. In this case, inhalation dominates the velocity field, and differences in the shape of the lips and other facial features that affect the streamlines into the mouth might also be critical to the aspiration efficiency of a breathing human.

CFD modeling to investigate particle aspiration avoids the fundamental problem associated with wind tunnel experiments, namely obtaining a uniform suspension of large particles in a low velocity environment. However, the appropriate representation of the human form in these modeling efforts has yet to be addressed. Therefore, the primary aim of this study was to compare a simple geometric form with a complex anatomical mannequin to determine whether the simple form is sufficient to study particle inhalability in computational fluid dynamics studies. Wind tunnel velocity fields were compared between similarly dimensioned inhaling mannequins to determine where and how facial features contributed to significantly different flow fields into the inhaling mouths. Second, particle aspiration was studied using the same mannequins to determine differences in inhaled mass concentrations associated with these velocity field differences. From these tests, the appropriateness of using simple geometric forms to model particle inhalability was evaluated. Results from this study provide guidance to future computational fluid dynamic investigations of particle inhalation.

2.2 Methods

All experiments were conducted with the mannequins facing the wind. The baseline condition studied in both the velocity and particle phases of this study was a freestream

velocity of 0.3 m s^{-1} and continuous inhalation at 10 Lpm. For particle aspiration experiments, the additional conditions of 0.9 m s^{-1} freestream velocity and 20 Lpm inhalation rate were also investigated.

2.2.1 Mannequins

Two test mannequins were used to compare velocity fields and particle aspiration. Because of the size limitations posed by the wind tunnels used in this study, scaled forms were used. The dimensions of a commercially available complex anatomical mannequin were used to create a stacked elliptical form for this comparison study. Figure 2.1 illustrates the shapes of the (a) anatomical mannequin and (b) elliptical form used in this study.

Anatomical Mannequin. A commercially available doll, My Size Barbie™ (Mattel Inc., El Segundo, CA), was used as the basis for the anatomical mannequin. Modifications were necessary to ensure that the mannequin dimensions represented a 50th percentile human female-US (Tilley, 1993). The final dimensions of the form, and the relationship to the 50th percentile anatomical female, are summarized in Table 2.1. The neck height was decreased on the original mannequin by 1.9 cm during the fitting of a filter mechanism through which to draw air to simulate breathing. The torso was padded, and the anatomical mannequin was dressed with loose clothing to effectively increase its torso width. The hair was removed, and a rounded-rectangular opening was made in the mouth (0.396 cm tall by 1.645 cm wide). Nearly 18% of the overall height, 16.6 cm, was removed from the legs to accommodate the optical requirements of the wind tunnel. On a full-scale human, this removal was equivalent to truncation at the knees. Although the shortened model was less than ideal, this reduction in bluff body size was anticipated to have been minimal to the velocity field near the face of the inhaling mannequin. The mannequin was coated with a static dissipative coating (Clear Water-Borne Polyurethane Static Dissipative Coating, Specialty Coatings Company, Inc., Elk Grove, IL) to minimize electrostatic effects.

Elliptical Form. The elliptical form was made by stacking a smaller elliptical cylinder onto an elliptical cylindrical torso, at the shoulder height. The stacked cylinder aligned the head's major axis with the torso's minor axis, to mimic the human form. The top cylinder matched the anatomical mannequin's head width (9.6 cm) and depth (10.8 cm), and the bottom cylinder matched the anatomical mannequin's torso width (15.5 cm) and depth (11.5 cm). The size and position of the mouth opening was matched to that of the anatomical mannequin.

The key differences between these two mannequins included the elimination of torso features, including arms and legs, as well as the facial features, including nose, cheeks, forehead, chin, and neck. Another important difference between the forms was the location of the mouth opening relative to the surrounding bluff-body of the face: the elliptical form's mouth was centered on the surface of the cylinder, yet, the mouth opening on the anatomical mannequin was recessed behind the surface of the lips and the nose. As is shown in Figure 2.2, the lower lip projected approximately 5.8 mm, the upper lip 8 mm, and the nose approximately 10.2 mm in front of the mouth opening.

Scaling. Focusing on the key parameters that were anticipated to affect the velocity field near the inhaling mouth, the average ratio for the scaled mannequin dimensions and a 50^{th} percentile female was 0.65. For the frontal head diameter (D_{head}) and mouth dimension ratios, this scaling factor was 0.66.

Experimental conditions were established to ensure that the results of this velocity field study were pertinent to full-scale conditions based on physical dimension ratios and Reynolds numbers. These critical parameters and the test conditions are provided in Table 2.2. The mouth dimension ratio (D_1/D_2) for the mannequins and human form was set at 4.15. The Reynolds number was set at 1590 based on inhalation velocity and an equivalent mouth diameter, defined as the diameter of circular opening of equal area to the rounded rectangular mouth orifice (D_{eq}). The test condition of 10 Lpm inhalation associated with the inhaling mannequin was equivalent to 15.11 Lpm inhalation of a full-scale human. Continuous inhalation of 15.11 Lpm is equivalent to the peak inhalation rate associated with a sinusoidal breathing pattern of 7.55 Lpm, which is in the range of at-rest breathing for a full scale human (U.S. EPA, 1997). The Reynolds number based on the head diameter (9.6 cm) and the freestream velocity (0.3 m s^{-1}) was set at 1910.

This value is equivalent to a human-scale velocity of 0.2 m s^{-1} and is within the range of typical indoor air velocities reported by Baldwyn and Maynard (1998).

Breathing Simulation. Continuous inhalation was simulated with a high volume pump. Tubing connected the pump to the tapered back section of an electrically conductive 25 mm cassette, which was grounded during experiments. These filter holders were connected to a cylindrical fitting permanently mounted inside the mannequin mouth. For velocity measurements, a cellulose backup pad was placed inside the filter holders. For particle concentration experiments, a treated polycarbonate filter was placed in front of the backup pad to collect particles.

2.2.2 Test System – Velocity Measurements

Wind Tunnel. Velocity experiments were conducted at the U.S. EPA wind tunnel at the Research Triangle Park, NC (Heist *et al.*, 2003b). The closed-circuit wind tunnel measured 1.2 m in height by 1.5 m wide, with a 7 m test section. The blockage ratio of a mannequin in this wind tunnel was less than 6%, indicating that the walls of the wind tunnel had negligible affect on the velocity field near the mannequin. Glass windows formed the sides and top of the wind tunnel to allow use of a laser Doppler anemometer. A theatrical smoke generator (Martin Magnum Pro 2000, Martin Professional, Denmark) with Euro Fog Machine Liquid (American DJ Supply, Inc., Los Angeles, CA) was used to generate 2 to 3 μm seed particles for velocity measurements.

As illustrated in Figure 2.1, the major axis of the wind tunnel was defined as the X-axis, positive in the main direction of flow, with the lateral direction defined as +Y to the mannequin's right and vertically upward as +Z. The origin of the axis system was at the center of the mannequin's mouth.

Laser Doppler Anemometry. Velocity measurements were obtained using a laser Doppler anemometer (LDA) (Dantec 41N10 Traversing Amplifier, 58N10 PDA Signal Processor, and Sizeware 2.0 software, Dantec Dynamics A/S, Denmark) with a Coherent INNOVA 306 laser (Laser Innovations, Moorpark, CA). This method allowed for non-invasive and simultaneous measurements of the three velocity components. An argon-ion laser beam was split into three wavelength components, two beams for each wavelength (U_x = 488

nm, U_y = 514.4 nm and U_z = 476.5 nm). These beams were conveyed via fiber optic cables to fixed transmitting optics on a moveable traverse system. For these experiments, the U_x and U_z velocity components relied on near-forward scattering, whereas the U_y relied on backward scattering. To ensure that the three velocity measurements obtained by the LDA corresponded to an individual particle passing through the laser Doppler measurement volume, the processor's validation level was investigated, and sufficient noise filtering was identified at a –1 decibel validation setting. Bandwidths, which determine the velocity over which velocity measurements could be measured, were generally set to cover the velocity ranges of -0.1 to 0.4 m s^{-1}, although when close to the mouth, a larger bandwidth (-0.4 to 1.3 m s^{-1}) for U_x was required to measure velocities greater than 0.4 m s^{-1}. The smaller bandwidth allowed faster data acquisition where the velocity field was sufficiently below the upper bandwidth velocity.

At each measurement location, a time-series of 500 validated velocity measurements resulted in sufficiently stable mean velocity and turbulence intensity. An average of 56 seconds (s.d.= 40 seconds) was required to obtain the 500 velocity measures at each location. The variability in sample duration was due to operational issues such as changes in seed particle concentration, deposition of particles on the wind tunnel windows, and subtle changes in alignment of optics due to minor ambient temperature changes.

Measurement Region. Velocity measurements were made within a three-dimensional volume that extended 100 mm upstream and +/-30 mm laterally and vertically from the center of the mannequin's mouth. Measurements were made at 5 mm increments in the lateral and vertical directions and 10 mm increments in the upstream direction, with additional measurements closer to the mouth where velocity direction and magnitude were likely to change over smaller distances.

Operating Condition Verification. At the beginning and end of every test day, velocity measurements were made in an empty wind tunnel to ensure the freestream remained at 0.3 m s^{-1}. Twenty-four measurements were made in the plane of the mannequin mouth (X = 0) as well as 150 mm upstream of the mouth to provide freestream velocity data. The inhalation rate through the mannequins was monitored with a Bios Dry Cal DC-Lite

calibrator (model DCL-M Rev. 1.8, Bios International Corp., Butler, NJ). Breathing rates were 10.07 Lpm (s.d.= 0.017) for the anatomical mannequin and 10.06 Lpm (s.d.= 0.021) for the elliptical mannequin, sufficiently similar for the comparative analysis to follow (2-tailed t-test: $p = 0.156$).

2.2.3 Test System – Particle Concentration Measurements

Wind Tunnel. Inhaled aerosol concentration experiments were conducted in a second wind tunnel located in Baity Air Lab (UNC, Chapel Hill). The tunnel was 1.2 m high by 1.5 m wide and 2.4 m in length. To minimize turbulence intensity within the wind tunnel, a 6.3 cm thick fiberglass paint arrestor pad (Hess Industries, Astoria, NY) was placed on the opening of the wind tunnel, behind which was a thin-walled grid, with openings 15.24 cm by 15.24 cm and 15.24 cm deep. Mannequins were positioned facing the wind, with the center of the mouth opening 152.3 cm downstream of the wind tunnel opening, centered laterally, and 64.9 cm above the wind tunnel floor

Aerosol Generation. This study did not attempt to generate a uniform aerosol concentration in the wind tunnel but rather generated aerosols at fixed locations relative to the inhaling mouths of the mannequins. As such, particle aspiration efficiency was not investigated, but a comparison of the performance of the two forms was allowed. A polydisperse liquid aerosol was generated with a Lechler ultrasonic spray system [US 1 nozzle (710.070.16.50) with US 1 generator (071.091.01.11), Lechler, Inc., Metzengin, Germany]. Inland Oil 99 (density = 0.86 g cc^{-1}, Inland Vacuum Industries, Churchville, NY) was pumped from a reservoir to the nozzle at 0.45 mL min^{-1} (s.d.= 0.016 mL min^{-1}) using a MasterFlex pump (Cole-Palmer Instrument Co., Niles, IL). To optimize aerosol delivery, compressed air was applied to the nozzle at 2 Lpm. In all tests, the nozzle was oriented horizontally towards the back of the wind tunnel with the outlet 32 cm downstream of the wind tunnel opening and centered laterally within the freestream.

Three velocity ratios were investigated: $R = U_o/U_s = 0.33$ (0.9 m s^{-1} freestream and 10 Lpm inhalation), $R = 0.11$ (0.3 m s^{-1} freestream and 10 Lpm inhalation), and $R = 0.056$ (0.3 m s^{-1} freestream and 20 Lpm inhalation).

Because particle aspiration and not aspiration efficiency (with a uniform aerosol field) was investigated, the aerosol source was positioned to optimize the particle

concentration inhaled by the mannequins. For the low freestream velocity (0.3 m s^{-1}), the nozzle was 101.65 cm above the wind tunnel floor. This allowed for sufficient particle settling in the region upstream of the mannequin to allow particle aspiration. For the highest freestream velocity investigated (0.9 m s^{-1}), aerosol released at the previous height was insufficient to allow the large particles to reach the mannequin mouth, as the majority of the aerosol passed over the mannequin head. For 0.9 m s^{-1} freestream velocity, the nozzle was lowered to 80.1 cm above the floor to obtain adequate seeding into the mouth.

Particle Sizing. For the baseline condition (R = 0.11), the size distribution of particles collected inside the mouth was investigated. Samples were collected inside the mannequin mouth on 25 mm diameter polycarbonate filters (2 μm pore size, Nuclopore Track-Etch Membrane, Whatman Inc., Clifton, NJ) treated with Nyebar Q (2.0%, lot 0212200, Nye Lubricants, Fairhaven, MA) to cause the liquid aerosol to bead on the filter surface (Carlton and Flynn, 1997). The spread factor, defined as the ratio of the flattened droplet diameter on the filter to the round airborne droplet diameter for this oil / Nyebar Q / polycarbonate combination was 1.31 (s.d.= 0.028) (Prabhu, 2003). Particles were optically sized using a Nikon Microphot FXA microscope (Nikon, Garden City, NY) operating in bright field at 40x magnification. This microscope was fitted with a camera (Optronics DEI 750 3-chip CCD, Goleta, CA) to digitally photograph images of the collected aerosol droplets. For each filter, images of sixty fields equally spaced in a radial scheme (Leith and First, 1976) were analyzed to determine particle size distribution for each filter. The particle size distributions were compared between forms to determine differences in aspirated particle sizes and count concentration.

Mass Concentration. Particle mass concentrations were compared between mannequins for all three velocity ratios using the differences between post- and pre-inhalation weights of the treated polycarbonate filters. For a given set of velocity conditions, six paired replicate samples were collected over a two-day period, alternating test mannequins to obtain paired samples. Blanks were collected by sampling through the mannequin mouths without aerosol generation; these blanks were collected prior to each aspiration test and confirmed that filter weight changes were due solely to the challenge aerosol.

2.2.4 Data Analysis

Velocity Measurements. To compare velocity fields, velocity data were paired, by measurement location, for the two mannequins. At locations where replicate data existed for a mannequin, the mean of each velocity component was used. Velocity differences between the forms were calculated using:

$$\Delta U_{i,j} = U_{i,j}^{A} - U_{i,j}^{E} \tag{2.2}$$

where

$\Delta U_{i,j}$ = difference between velocity component i at location j

$U_{i,j}^{A}$ = velocity component i associated with anatomical mannequin, at location j

$U_{i,j}^{E}$ = velocity component i associated with elliptical form, at location j

Data were analyzed individually and then grouped and analyzed regionally, based on anatomical feature locations. To indicate significantly different velocity fields between the forms, two criteria were required: (1) the velocity differences must have exceeded the measurement uncertainty of +/- 0.020 m s^{-1} and (2) velocities must differ by at least 10%.

The maximum replicate velocity difference of 0.020 m s^{-1} was used as the first test of significance. This uncertainty was determined by analyzing replicate velocity measurements taken at the same location for a given mannequin. Over all replicate measurements, the maximum difference in any velocity component at any one location was the streamwise velocity (U_x) of 0.020 m s^{-1}, approximately 6% of the freestream horizontal velocity. Maximum lateral (U_y) and vertical (U_z) component measurement differences were on the same order of magnitude, at 0.016 m s^{-1} for U_y and 0.018 m s^{-1} for U_z.

The 10% velocity difference limit was established to ensure that velocity differences were significantly greater than the turbulence intensity over the measurement volume. The mean turbulence intensity was 3.1% (s.d.= 2.1%) over all velocity measurements with both inhaling mannequins. Hence, 99% of the time, the turbulence intensity at any

one location was less than 9.4%. An absolute relative velocity ratio, $|\Delta U_{i,j} / U_{i,j}^{A}|$, greater than 9.4% would indicate that the velocity difference between the forms was significantly greater than the turbulence intensity over the measurement volume.

In addition to velocity magnitude differences, the locations where velocity changed direction were investigated. The Cartesian coordinate system was less than ideal for describing this, as a lateral flow that was positive in some locations represented air that was directed into the mouth, whereas in other locations the positive sign indicated flow away from the mouth. Thus, the cylindrical coordinate system was adopted by transforming lateral and vertical data into radial vectors and using the streamwise direction (X) as the system axis, maintaining the origin at the mouth center. Using this scheme, zero radial velocity contours for a given distance upstream of the mouth (X) were used to identify locations where the fluid changed from going towards the X-axis (negative, into the mouth) to going away from the X-axis (positive, away from the mouth). The area contained within the zero radial velocity contours defined the inhalation streamtube. Zero-velocity contours were generated using cubic spline interpolation. Between-form differences in areas bounded by these zero velocity contours were evaluated to examine whether the size of the approaching inhalation streamtube was significantly different. These flow field differences could result in differences in particle motion in the region of the inhaling mouth and could result in different aspiration efficiencies for the two mannequins.

Particle Concentration Measurements. Because of the short sample time associated with particle sizing tests, at R = 0.11, data were grouped by form to generate a fractional size distribution and determine the median aspirated particle diameter. Additional aspirated mass concentration data were paired by form for each of the three test conditions (R = 0.056, 0.11, 0.33), and paired t-tests were used to examine statistical differences.

2.3 Results

2.3.1 Velocity Comparison

Velocity data were obtained at 1171 paired locations. The closest measurement occurred 11 mm upstream of the mouth opening (X = -11 mm), although a portion of the

measurement locations in this plane were unobtainable due to blockage of the laser beam by the facial features. Figure 2.3 provides example velocity vectors in the midsagittal plane (Y = 0) as an illustration of the measurement area and flow orientation. In this figure, the velocity data is superimposed over a scaled image of the anatomical mannequin, shown with a streamtube created by incense smoke to visualize the velocity field in the wind tunnel.

Freestream Verification. The daily freestream velocities averaged 0.300 m s^{-1} (s.d.= 0.003 m s^{-1}) in the streamwise direction (U_x) during the entire test period. No difference in mean streamwise (U_x) velocity between forms was identified during the study ($p = 0.86$). The lateral velocity (U_y) was slightly positive, or to the mannequin's right, at +0.004 m s^{-1} (s.d.= 0.005). Tests for the elliptical mannequin had slightly less positive (0.002 m s^{-1}) lateral freestream velocity than the freestream on days that the anatomical mannequin was tested (0.006 m s^{-1}), but the differences were not statistically significant ($p = 0.24$). The vertical freestream velocity (U_z) was slightly downward, at an average of -0.006 m s^{-1} (s.d.= 0.008). A significant difference ($p = 0.018$) in vertical velocity was identified between days when the elliptical mannequin was tested (U_z = -0.001 m s^{-1}) compared to days when the anatomical mannequin velocity field was tested (U_z = -0.011 m s^{-1}), indicating that vertical velocity differences in mannequin tests may be partially attributed to differences in freestream conditions. These differences, however, were less than the measurement uncertainty (0.020 m s^{-1}) used to compare velocity fields between mannequins. For all freestream velocity component measurements ($n = 2448$), the mean turbulence intensity was 2.3%, with a standard deviation of 3.6%. Turbulence intensity did not vary significantly between velocity components.

Radial Velocity Contours. Significant differences between the radial velocity contours for the two inhaling mannequins were assessed at distances of 11 and 15 mm from the mannequins' mouths. Zero radial velocity contours are provided in Figure 2.4 for (a) X = -11 mm and (b) X = -15 mm. The contour data is superimposed over a scaled image of the anatomical mannequin to illustrate the locations of facial features. With the elliptical cylinder, radially inward velocities at locations above the center of the mouth ($Z > 0$) were identified only as close as X = -11 mm ($Z < 21$ mm at $Y = 0$). With the anatomical

mannequin, however, inward radial velocity above the mouth center existed further upstream, at X = -11 (Z < 17 mm), -15 (Z < 12 mm), and at -20 mm (Z < 2 mm). Hence the facial structure created downward airflow into the inhaling mouth at greater distances anterior to the mouth as compared to the featureless elliptical form. Below the mouth, the radial velocity was towards the mouth center due to the upward velocity component (U_z) caused primarily by flow around the bluff body.

Statistical significance between the widths and heights of these zero radial velocity contours was evaluated using paired t-tests. At X = -11 mm, the differences in widths of the zero velocity contours were statistically significant ($p = 0.025$), but the height was not ($p = 0.36$). At X = -15 mm, both the widths ($p = 0.0002$) and heights ($p = 0.0007$) were statistically significantly different. Wilcoxon signed-rank tests yielded similar conclusions. Hence, the size of the streamtube that approached the inhaling anatomical mannequin was significantly larger than that of the elliptical mannequin at 11 and 15 mm in front of the mouth opening.

Velocity Differences. A summary of the velocity difference analysis is provided in Table 2.3. Coordinates of locations where velocity differences exceeded the maximum measurement uncertainty are provided, grouped by anatomical region. The average velocity for those coordinates is provided for both mannequins, and the average velocity ratio is given for the data group.

The locations of significant differences in streamwise velocity (U_x) are identified in Figure 2.5. In the mouth region, the average velocity for the elliptical form was only 80% of the anatomical mannequin velocity. Under the chin, the average streamwise velocity was again significantly greater for the anatomical mannequin compared to the elliptical form ($U_{xE}/U_{xA} = 81\%$). Above the mouth to just under the tip of the nose, conditions reversed, as the streamwise velocity associated with the elliptical form was greater than that of the anatomical form ($U_{xE}/U_{xA} = 132\%$). At (X, Y, Z) = (-11, 0, 20), the velocity ratio U_{xE}/U_{xA} was 570%, as the measurement location for the anatomical form was just in front of the tip of the nose ($U_{xA} = 0.018$ m s^{-1}). Additional regions were identified as significantly different between the two mannequins, below the mouth to the mannequin left ($U_{xE}/U_{xA} = 87\%$), above the mouth to the mannequin right (U_{xE}/U_{xA} =

117%), and to the left above the nose (U_{xE}/U_{xA} = 81%). Because of the lateral asymmetry of these significant regions, mannequin misalignment or facial asymmetry may contribute to these differences in velocity field.

The locations of significant vertical velocity (U_z) differences are illustrated in Figure 2.6. Just under the mouth, the average velocity ratio (U_{zE}/U_{zA}) was 74%, indicating a greater upward velocity towards the mouth with the anatomical mannequin. In the region at and above the mouth center, the vertical velocity at each location was significantly more downward with the anatomical mannequin compared to the elliptical form (U_{zE}/U_{zA} = -90%). Additionally, under the chin and near the midsagittal plane, the average velocity ratio (U_{zE}/U_{zA}) was 164%, indicating that the anatomical chin/neck resulted in not only greater streamwise velocity (U_x), as seen earlier, but also reduced upward velocity due to the recessed neck. Finally, above the tip of the nose ($Z \geq 20$ mm), across all lateral distances measured, and up through X = -20 mm, the vertical velocity associated with the anatomical mannequin was significantly greater than that of the elliptical form (U_{zE}/U_{zA} = 47%).

Regions of significant lateral velocity (U_y) differences are illustrated in Figure 2.7. Although lateral velocity components were incorporated into the previous radial velocity contour analysis, the lateral velocity field differences are presented independently, due to the identified asymmetry. Lateral velocities, directed away from the face centerline, were greater for the elliptical form on the left (-Y) side at chin height (U_{yE}/U_{yA} = 142%) and the entire right (+Y) side of the face (U_{yE}/U_{yA} = 224%). On the right side of the face at chin height ($Z \leq -20$ mm), the lateral velocity magnitudes were also significantly greater with the elliptical form through X = -20 mm (U_{yE}/U_{yA} = 191%, $p < 0.0001$), matching the volume on the left side. There were only two locations where the lateral velocity was significantly more away from the mannequin centerline for the anatomical mannequin: in the region of the nose (U_{yE}/U_{yA} = 23%) and medially under the chin. Under the chin near the mannequin center, the velocity ratios ranged from +18% to -1200% but in each of these 12 locations, the lateral velocities associated with the anatomical form were at least 0.020 m s^{-1} more towards the left than its paired elliptical velocity. Close examination of the mannequin face revealed that the right (+Y) side was 2 mm wider than the left (-Y) side, centering on the nose tip. Because the mouth opening was centered on this nose tip,

this discrepancy may account for the significant lateral velocity differences on the right but not on the left of the mannequin.

2.3.2 Particle Aspiration Comparison

Particle size distributions for aspirated particles were similar for both forms. For the same baseline condition used in the velocity comparison study (R = 0.11), the size distributions for aspirated particles were similar for both forms. Sample times were limited to 1 minute or less for these tests to ensure sufficient particle spacing on the filter for sizing, but these short sample durations resulted in large variation between particle counts for a given mannequin. Thus, data were combined for the six tests for each mannequin to obtain an average particle distribution, shown in Figure 2.8. The median count diameter for both forms was 60 μm, equivalent to a Stokes number of 0.03, using:

$$St = (\rho_p d^2/18\mu(U_o/D_{eq}) \quad (2.3)$$

where St is Stokes number, ρ_p is particle density (0.86 g cc^{-1}), d is the particle diameter, μ is air viscosity, U_o is freestream velocity, D_{eq} is the diameter of a round mouth with area equal to the rounded rectangle of the test mannequins.

Aspirated mass concentration tests allowed longer sample times, but variability between replicates still existed. The results of the six pairs of replicate experiments conducted at each of the three velocity-ratio conditions are shown in Figure 2.9. Despite the unfortunately large replicate variability (mean coefficient of variation = 30%), the mass concentration inhaled by the anatomical mannequin was consistently and significantly less than that of the elliptical mannequin for each set of velocity conditions, as indicated in Table 2.4.

The significantly higher mass concentrations aspirated by the elliptical form indicates that there may be a trend of more larger-particles inhaled by the elliptical form compared to the anatomical mannequin. A closer look at the tails of the size distribution curve from optical counting at R = 0.11, acknowledging the limitations of the low number counts in these ranges, provides some evidence of this trend. The anatomical mannequin inhaled more smaller particles than did the elliptical form: 19 of the 1004 of the inhaled particles

counted, nearly 2%, were smaller than 44 μm, yet no particles smaller than 44 μm were measured with the elliptical form, given the same relative position between the aerosol source and inhaling mouth. At the other end of the spectrum, the elliptical form inhaled more larger particles than the anatomical mannequin: of particles counted for the elliptical form, 9 (1.6%) were larger than 86 μm and 3 (0.5%) were larger than 95 μm, compared to 5 (0.5%) larger than 86 μm and none (0%) larger than 95 μm for the anatomical mannequin. These represented only a few particles over a short sample duration, but data indicated a trend for aspirating smaller particles by the anatomical mannequin and larger particles by the elliptical form, even though the median diameters for the size distributions were the same.

2.4 Discussion

The facial features of the inhaling anatomical mannequin were associated with a significantly different velocity field compared to that of an inhaling elliptical cylinder at distances less than 30 mm anterior to the mouth. In addition, the mass of particles aspirated by the anatomical form was significantly less than that of the elliptical form at the tested indoor air velocity conditions with the facing-the-wind orientation.

One key reason for these differences was the projection of the anatomical mannequin's facial features in front of the mouth opening. While the surface of the elliptical cylinder was flush with the mouth opening and devoid of facial features such as nose, lips and chin protruding upstream of the surface, the anatomical mannequin's facial features projected up to 10.2 mm into the upstream flow field, relative to the position of the mouth opening. As expected, the nose projection resulted in decreased horizontal velocity upstream of the nose, but this effect was limited to within 10 mm in front of the nose tip (X = -20 mm). Above the nose, the anatomical mannequin's horizontal and vertical velocity components were greater than that of the elliptical form. At these heights, the anatomical mannequin's face began to recess behind the X = 0 mm surface of the elliptical form. Under the chin, the neck also recessed behind the X = 0 mouth-opening plane, resulting in obvious velocity differences. As air was allowed to pass under the chin, the horizontal velocity was greater and the vertical velocity was lesser with the anatomical mannequin as compared to the ellipse. In the similar region on the

elliptical mannequin, the velocity was forced to turn upward and laterally to pass the bluff body. The horizontal velocity differences were significant through 20 mm in front of the plane of the mouth opening, but vertical effects were significant only at the closest measurement location, X = -11 mm.

More important to contaminant transport into the inhaling mannequin were velocity field differences into the mouth. By reviewing the mannequin profiles illustrated in Figure 2.2, air into the elliptical mannequin was restricted only by the flat surface of the mannequin, a 180° arc from top to bottom surfaces at the midsagittal (Y=0) plane. However, the lips of the anatomical mannequin restricted the incoming air to 60°, a significant volume reduction. Given the same inhalation rate and mouth orifice area for the two mannequins, the velocity immediately upstream of the anatomical mouth would be greater in magnitude due to this physically restricted volume. Lateral motion was not as restricted in either form, as both forms were open to the sides of the mouth opening.

The effects of velocity differences into the mouth were limited to lateral distances just wider than the mouth opening, at +/-0.6 times the mouth orifice width. Where velocities near the mouth were greater with the anatomical mannequin, these effects were limited to vertical distances +/-2.5 times the mouth orifice height.

The identified velocity field differences into the mouth occurred within a small volume, approximately 30 mm high by 20 mm wide within 20 mm upstream of the mouth. However, velocity field differences identified above the mouth could affect particle seeding into the inhalation region. At and above the nose tip near centerline, the fluid flow field was less towards the mouth for the anatomical mannequin: the lateral velocity was more away from centerline, vertical velocity was more upward, and streamwise velocity was smaller towards the face. Velocity differences at streamwise distances closer to the mouth opening were not obtainable, but as approaching the elliptical cylinder, there was more volume through which particles could fall into the inhalation stream tube, a volume blocked by the facial features of the anatomical mannequin. In low velocity environments where gravity dominates large particle motion, the nose and lips serve as a surface for particle impaction and interception on its way to the inhaling mouth.

Particle experiments were not conducted to explore fully the issue of particle inhalability, as no attempts were made to generate a uniform aerosol distribution. However, the tests were conducted so that aspirated concentration could be compared between two similarly dimensioned mannequins with the same relative distance to an aerosol source. Variability in the particle aspiration experiments can be attributed to the short sample duration. In these short periods, small fluctuations in the velocity field in the 2.4 m long wind tunnel operating at 0.3 m s^{-1} would have a large impact on aspiration in the facing-the-wind orientation. With a slightly taller wind tunnel, the position of the aerosol source relative to the inhaling mouth could have been better optimized to allow for longer test time, which may have resulted in less variability between tests. In addition, the aerosol generator has not been evaluated for generation rate stability, and any temporal variation in aerosol output may contribute to the identified particle aspiration variability.

For a given test velocity ratio, the sample durations were the same for both test mannequins, yet the variation in particle mass concentrations was greater for the elliptical form than for the anatomical form. Preliminary visualizations studies using incense upstream of the inhaling mannequin indicated that aspiration of incense smoke by the elliptical form was more sensitive to the generation position: the incense stick was positioned horizontally, burning from right to left, and the time over which the incense was captured by the anatomical mannequin was, qualitatively, longer than that of the elliptical form, over multiple days. Hence, small temporal changes in the velocity field in the open-entrance wind tunnel may have affected particle aspiration by the elliptical form more than the anatomical form, resulting in more variability in the elliptical form's aspiration of the oil aerosol generated from a fixed position upstream and above the inhaling mouth.

Regardless of this variability, in each paired aspiration test, the mass inhaled by the elliptical form was always greater than that of the anatomical mannequin, by at least 20% (mean = 88%), regardless of the velocity ratio examined. With aerosol generation at the same fixed location relative to the mouth opening, aerosol impaction by the mannequin face during gravitational settling anterior to the nose and lips is a plausible reason for the reduced aspirated mass.

These study conditions can be scaled to human-scale, using Reynolds number for the fluid field and Stokes number for particle motion. However, the gravitational effects on particles cannot be directly scaled to the larger system (Froude = 0.096 in this study, but 0.028 in full-scale system). Thus, the applicability of the particle findings of this study to an inhaling human is limited. Ignoring gravitational effects, the median particle size of 60 μm in these tests scaled to 90 μm in a human-scale system, using Stokes number. This particle size lies within the scope of inhalable particles, but the gravitational effects on an aerosol in the equivalent full-scale system would be greater than this study's system.

In addition to scaling and feature dimension issues, this study simplified the complexity of conditions needed to fully explore particle inhalability. Specifically, the neglect of the natural convective layer associated with a real human, the continuous rather than cyclical inhalation, and the sole orientation of facing-the-wind provided only a limited evaluation of the appropriateness of using an elliptical surrogate in lieu of a more complex anatomical form. In low velocity environments, the natural convection boundary layer surrounding a real human creates upward velocity component that may affect particle inhalability in the velocity range studied here, specifically for smaller particles (Heist *et al.*, 2003a), and this effect on the performance differences between these two mannequins was not addressed here. In addition, the effect of inhalation pattern, specifically continuous inhalation versus a more realistic cyclical breathing, was reported by Kennedy and Hinds (2002) to have little or no effect on mouth inhalability. The differences found between particle aspiration of the two mannequins tested here may be on the same order of magnitude as the continuous inhalation simplification. Finally, the facing-the-wind orientation used here has the highest aspiration efficiency of all orientations (*e.g.,* Armbruster and Breuer, 1982; Kennedy and Hinds, 2002) and contributes appreciably to the orientation-averaged inhaled particulate mass. Even if other orientations were investigated and had less significant differences between the two mannequin shapes, it is the facing-the-wind orientation that contributes most to the inhaled particulate mass. Therefore, significant differences in both velocity field and particle aspiration between the anatomical mannequin and the elliptical form in the facing-the-wind orientation, regardless of the inhalation pattern, indicate that the elliptical

cylinder may be insufficient to represent the human form for large particle aspiration efficiency studies.

2.5 Conclusions

This paper described a method for evaluating velocity field and particle aspiration differences between two scaled inhaling mannequins in a low velocity environment. Although limitations in the laser Doppler system prevented velocity field measurements close to the mannequin surface, significant differences were identified. These differences were in the region where air was directed into the inhaling mouth, as well as above the mouth and below the chin. Velocity differences were insignificant beyond 20 mm upstream of the mouth opening, indicating that the facial features affected the flow field only near the mannequin surface.

Particle studies used a fixed aerosol source rather than generating a uniform aerosol concentration, which released liquid aerosol upstream and above the same two inhaling mannequins. The median count diameter aspirated by both mannequins for the baseline condition (R = 0.11) was 60 μm, equivalent to a Stokes number of 0.03. In each of the three different velocity ratio conditions tested (R=0.056, 0.11, 0.33), the particle mass concentration aspirated by the anatomical form was significantly less than that of the elliptical form. This particle study indicates that an elliptical cylinder may be a poor surrogate for a human form and may overestimate particle inhalability, specifically for the facing-the-wind and low freestream velocity condition tested.

The mannequins investigated were selected to represent human forms: the simplified elliptical form was selected because of the potential ease of its use in computational fluid dynamics modeling, whereas the anatomical mannequin was commercially available yet reasonably realistic example of human geometry. The lip and nose features were associated with larger horizontal velocity and larger lateral velocity towards the inhaling mouth at distances less than 20 mm anterior to the mouth opening. Although only one anatomical form was examined, the facial features were associated with different velocity fields and could be associated with reduced aspiration concentration as compared to an elliptical cylinder. Future three-dimensional computational fluid dynamics and numerical simulations to investigate human aspiration of particles should incorporate the complex

features of the human face, including nose, lips and chin as well as a rounded head, to adequately investigate particle aspiration in low velocity environments. Details in the lateral dimensions, such as cheeks and ears, are less critical.

2.6 References

2004 TLVs and BEIs: Based on the documentation of the threshold limit values for chemical substances and physical agents and biological exposure indices. ACGIH Worldwide, Cincinnati, OH.

Aitken,. R.J., P.E.J. Baldwin, G.C. Beaumont, L.C. Kenny, and A.D. Maynard (1999) Aerosol inhalability in low air movement environments. *J. Aerosol Sci.* 30(5): 613-626.

Armbruster, L. and H. Breuer (1982) Investigations into defining inhalable dust *Ann. Occup. Hyg.* 26(1): 21-32.

Baldwin, P.E.J. and A.D. Maynard (1998) A survey of wind speeds in indoor workplaces. *Ann. Occup. Hyg.* 42(5): 303-313.

Carlton, G.N. and M.R. Flynn (1997) Influence of spray painting parameters on breathing zone particle size distributions. *Appl. Occup. Environ. Hyg.* 12(11): 743-750.

Chung, I.P. and D. Dunn-Rankin (1992) Numerical simulation of two-dimensional blunt body sampling in viscous flow. *J. Aerosol Sci.* 23(3): 217-232.

Chung, I.P., T. Trinh and D. Dunn-Rankin (1994) Experimental investigation of a two-dimensional cylindrical sampler. *J. Aerosol Sci.* 25(5): 935-955.

Chung, I.P. and D. Dunn-Rankin (1997) Experimental investigation of air flow around sampling in viscous flow. *J. Aerosol Sci.* 28(2): 289-305.

Dunnett, S.J. and D.B. Ingham (1986) A mathematical theory to two-dimensional blunt body sampling. *J. Aerosol Sci.* 17(5): 839-853.

Dunnett, S.J. (1997) A numerical study of the flow field in the vicinity of a bluff body with aspiration oriented to the flow. *Atmospheric Environment* 31(22): 3745-3752.

Dunnett, S.J. (1999) An analytical investigation into the nature of the airflow near a spherical bluff body with suction. *J. Aerosol Sci.* 30(2): 163-171.

Dunnett and Vincent (2000) A mathematical study of aerosol sampling by an idealised blunt sampler oriented at an angle to the wind: the role of gravity. *J. Aerosol Sci.* 31(10): 1187-1203.

Dunnett, S.J. and D.B. Ingham (1988) The human head as a blunt aerosol sampler. *J. Aerosol Sci.* 19(3): 365-380.

Erdal, S. and N.A. Esmen (1995) Human head model as an aerosol sampler: calculation of aspiration efficiencies for coarse particles using an idealized human head model facing the wind. *J. Aerosol Sci.*, 26(2): 253-272.

Heist, D.K., A.D. Eisner, W. Mitchel, and R. Wiener (2003a): Airflow around a child-size manikin in a low-speed wind environment. *Aerosol Sci. and Tech.* 37(4): 303-314.

Heist, D.K., J. Richmond-Bryant, A. Eisner, and T. Conner (2003b) Development of a versatile aerosol generation system for use in a large wind tunnel. *Aerosol Sci and Tech*; 37: 293-301.

Hsu, D.J, and D.L. Swift (1999) The measurement of human inhalability of ultralarge aerosols in calm air using manikins. *J. Aerosol Sci.* 30(10): 1331-1343.

Ingham, D.B. and M.L. Hildyard (1991) The fluid-flow into a blunt aerosol sampler oriented at an angle to the oncoming flow. *J of Aerosol Sci.* 22(3): 235-252.

Kennedy, N.J. and W.C. Hinds (2002) Inhalability of large solid particles. *J. of Aerosol Sci.* 33: 237-255.

Leith, D. and M.W. First (1976) Uncertainty in particle counting and sizing procedures, *Am. Ind. Hyg. Assoc. J*, 37(2): 103-176.

Ogden, T.L. and J.L. Birkett (1977) The human head as a dust sampler. In Halton, W.H. editor. Inhaled particles IV: proceedings of an international symposium organized by the British Occupational Hygiene Society. Oxford: Pergamon Press. p. 93-105. ISBN 0080205607

Odgen, T.L. and J.L. Birkett (1978) An inhalable-dust sampler, for measuring the hazard from total airborne particulate. *Ann. Occup. Hyg.* 21: 41-50.

Prabhu, P. Determination of Particle Size Distribution for Aerosol Generated by Lechler's Ultrasonic Atomizer. Masters Thesis, The University of North Carolina, Chapel Hill, NC, May 2003.

Tilley, A.R. *The Measure of Man and Woman: Human Factors in Design.* John Wiley and Son, NY, 1993.

U.S. EPA. (1997) EPA/600/P-95/002Fa. Exposure Factors Handbook. Washington, D.C.: U.S. Environmental Protection Agency, Office of Research and Development, National Center for Environmental Assessment

Vincent, J.H. and L. Armbruster (1981) On the quantitative definition of the inhalability of airborne dust. *Ann. Occup. Hyg.* 24: 245-248.

Vincent, J.H. and D. Mark (1982) Applications of blunt sampler theory to the definition and measurement of inhalable dust. *Ann. Occup. Hyg.* 26(1): 3-19.

Vincent, J.H., D. Mark, B.G. Miller, L. Armbruster, and T.L. Ogden (1990) Aerosol inhalability at higher windspeeds. *J. Aerosol Sci.* 21: 577-586.

2.7 Nomenclature

d_{ae}	particle aerodynamic diameter (μm)
D_{head}	diameter of the mannequin head, ear to ear (mm)
D_1	lateral (side-to-side) diameter of mouth (mm)
D_2	vertical (top-to-bottom) diameter of mouth (mm)
D_{eq}	equivalent (round) diameter of mannequin mouth, determined as the diameter of a round opening with area equivalent to that of the rounded rectangular mouth opening (mm)
g	gravitational acceleration (9.8 m s^{-1})
p	probability that the two values being compared are the same
R	velocity ratio, U_o/U_s
Re	Reynolds number, a dimensionless ratio of viscous to inertial forces; using a specified velocity (U) and characteristic length, and dynamic viscosity (μ), $Re = UD/\mu$
s.d.	standard deviation
	dynamic viscosity
U_o	freestream velocity (m s^{-1})
U_s	average inhalation (or suction) velocity at the plane of the mouth opening, determined from inhalation flow rate divided by mouth area (m s^{-1})
U_x	horizontal velocity component, defined as positive in the direction of into the mouth (m s^{-1})
U_y	lateral velocity component, defined as positive to the right of the mannequin (m s^{-1})
U_z	vertical velocity component, defined as positive upward (m s^{-1})
$U_{i,j}^{E}$	i velocity component associated with the Elliptical form, at location j
$U_{i,j}^{A}$	i velocity component associated with the Anatomical mannequin, at location j

Table 2.1 Critical dimensions of anatomical mannequin and 50th percentile human female-US. (Tilley, 1993). Measurements that are in bold were used to create the elliptical form.

Dimension	Anatomical Mannequin (cm)	50th percentile female (cm)	Mannequin: Human (unitless)
Overall Height with truncation at feet	75.5	n/a	n/a
Head			
Fontal D, head width (D_{head})	**9.6**	14.5	0.66
Side D, head depth	**10.8**	18	0.60
Location of mouth center, relative to top of head	**11.5**	17.3	0.66
Top of head to shoulders	**18**	30	0.60
Top of head to chin	14.5	21.6	0.67
Neck (chin to shoulders)	4.5	8.1	0.56
Torso			
Frontal Chest (to shoulder)	20.5	40.9	0.50
Frontal Chest (under arm) (D_{torso})	**15.5**	26.4	0.59
Dorsal Chest (bust)	**11.5**	25.4	0.45
Frontal Chest (waist)	14.2	22.9	0.62
Hip breadth	18	36.8	0.49
Abdominal depth	10.3	25.4	0.41
Mouth (measured on Anatomical, calculated equivalence for 50th % female)			
Horizontal axis (D_1)	**1.645**	2.485	0.66
Vertical axis (D_2)	**0.396**	0.598	0.66
Equivalent Diameter (round) (D_{eq})	0.887	1.34	0.66
Hydraulic Radius (D_{hydr})	0.66	1.00	0.66
Mouth Area (rounded rectangle)	0.618 (cm^2)	1.409 (cm^2)	0.44

Table 2.2 Dimension and velocity scaling for baseline condition (R = 0.11).

Scaled Form Parameters	Mannequin		Full-scale human (50th percentile female)		Ratio of Mannequin/ Human
Relative Dimensions					
Mouth Equivalent Diameters	0.887	cm	1.340	cm	0.66
Mouth D_1/D_2	4.154	-	4.154	-	1.00
Breathing Simulation					
Inhalation rate	10	Lpm	15.11	Lpm	0.66
Average velocity at mouth, U_s	2.70	m s^{-1}	1.79	m s^{-1}	1.51
$Re_{mouth}=U_sD_{eq}/\nu$	1590	-	1590	-	1.00
Freestream Conditions					
Freestream Velocity, U_o	0.3	m s^{-1}	0.199	m s^{-1}	1.51
$Re_{freestream}=U_oD_{head}/\nu$	1910	-	1909	-	1.00
$Re_{freestream}=U_oD_{torso}/\nu$	3080	-	3480	-	0.89
$R = U_o/U_s$	0.111	-	0.111	-	1.00
kinematic viscosity (ν)=1.51x10^{-5} m^2 s^{-1}					

Table 2.3 Regions of significant velocity difference (R = 0.11). P-values are given for two-tailed t-test for velocity differences between mannequins, paired by location. A indicates velocity associated with the anatomical mannequin, E indicates velocity associated with the elliptical form.

Finding	X (mm)	Y (mm)	Z (mm)	Ave U_{iA} (m s^{-1})	Ave U_{iE} (m s^{-1})	U_{iE}/U_{iA} (%)	p-value
Mouth							
U_x: A is greater than E	-11, -15	-5 to 10	-5, 0	0.252	0.199	80	0.0017
U_z: A more downward than E	-11, -15	-10 to 15	0 to 10	-0.033	0.002	-90	0.017
U_z: A more upward than E	-11	-5 to 10	-10, -5	0.102	0.074	74	0.036
Chin and Neck							
U_x: A is greater than E	-11, -15, -20	-30 to 30	-20, -25, -30	0.183	0.150	81	<0.0001
U_z: A less upward than E	-11	-15 to 10	-20, -25, -30	0.042	0.068	164	0.0028
Above Mouth							
U_x: A is less than E	-11, -15	-5 to 5	10, 15 (20 at nose tip only)	0.114	0.147	132	0.005
U_z: A more upward than E	-11, -15, -20	-30 to 30	20, 25, 30	0.048	0.022	47	<0.0001
Asymmetrical Areas of Significance							
U_x: A is less than E	-15	5 to 30	10 to 30	0.139	0.164	117	0.006
U_y: A is less away than E	-11	5 to 30	-30 to 30	0.039	0.067	224	<0.0001
U_x: A is greater than E	-11, -15	-30 to -10	-5 to -15	0.195	0.117	87	<0.0001
U_y: A is less away than E	-11, -15, -20	-30 to -20	-30 to -20	-0.058	-0.081	142	0.009
U_x: A is greater than E	-11	-10, (-5)	25, 30	0.132	0.107	81	0.025
U_y: A is more away than E	-11, -15	-10 to 0	10 to 30	-0.046	-0.015	23	0.0002
U_y: A is more to left than E	-11, -15	-5 to 5	-30 to -20	-0.018	0.005	*n/a*	0.012

Table 2.4 Mass concentration comparison between forms. Two-tailed paired t-test p-values given.

Velocity Ratio	Anatomical		Elliptical		p-value
	Mean mg/m^3	Stdev mg/m^3	Mean mg/m^3	Stdev mg/m^3	
0.33	6.99	2.95	10.34	3.26	0.0029
0.11	7.14	1.92	15.72	4.27	0.0042
0.056	5.38	0.53	9.56	3.08	0.027
All	6.44	2.2	11.7	4.6	<0.0001

Figure 2.1 Test shapes and axis orientation of (a) anatomical mannequin and (b) elliptical form.

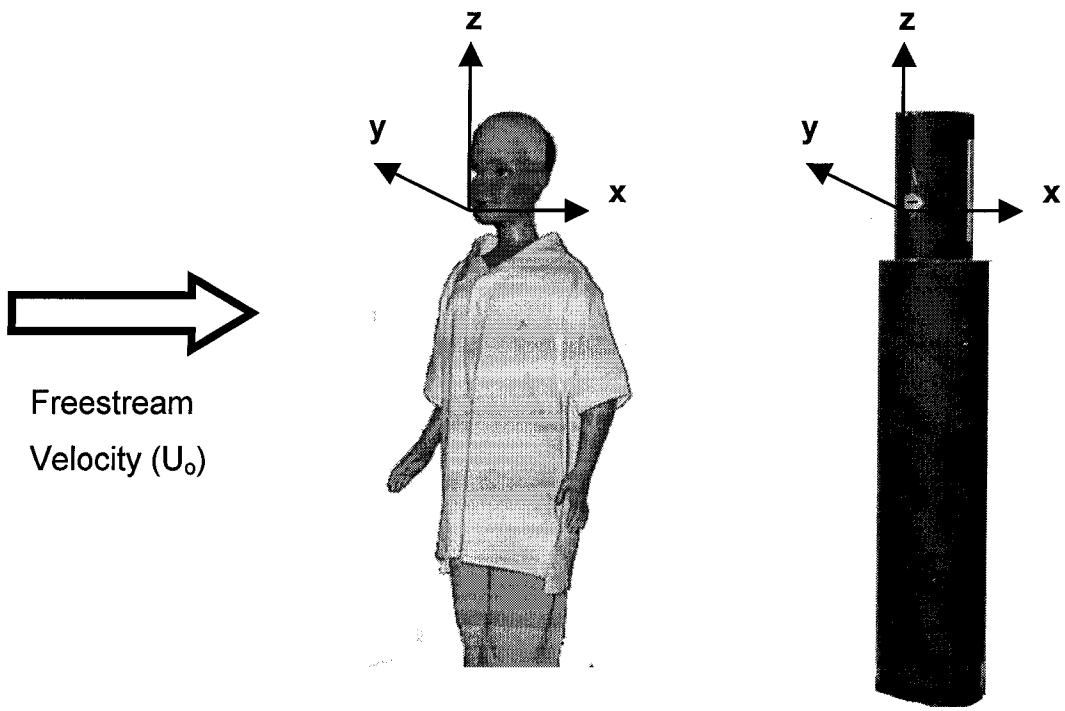

Figure 2.2 Mannequin profile at midsagittal plane. Solid line shows the profile of the anatomical mannequin, whereas the vertical dashed line represents the elliptical mannequin profile.

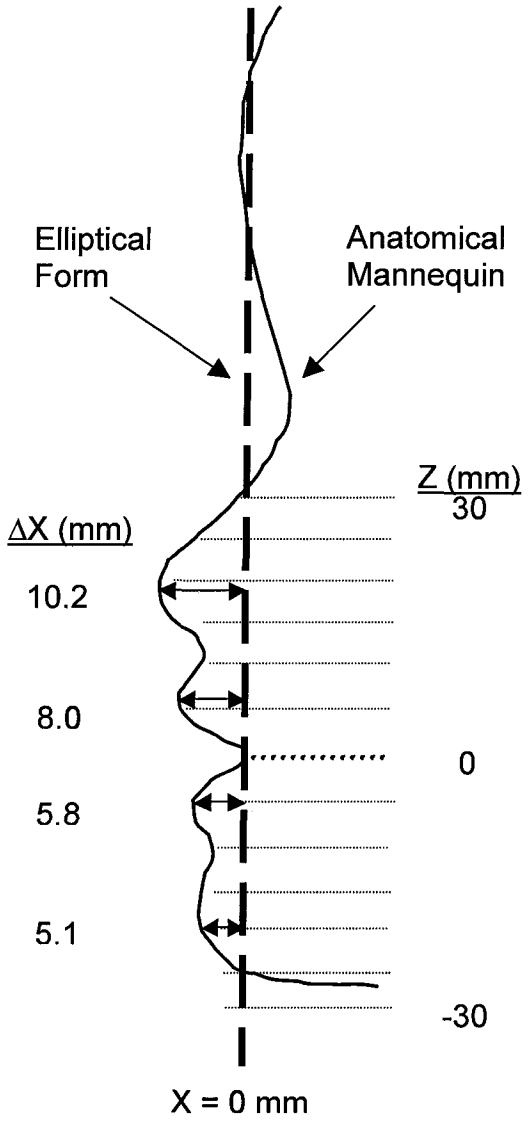

Figure 2.3 Velocity field in midsagittal plane at Y = 0 mm (R = 0.11). Difference between fields was insignificant further upstream than 20 mm. Measurement location indicated by arrow tail; arrows in legend are scaled to 0.3 m s^{-1}. Velocities at 5 mm anterior to the mouth opening were available only with the elliptical form.

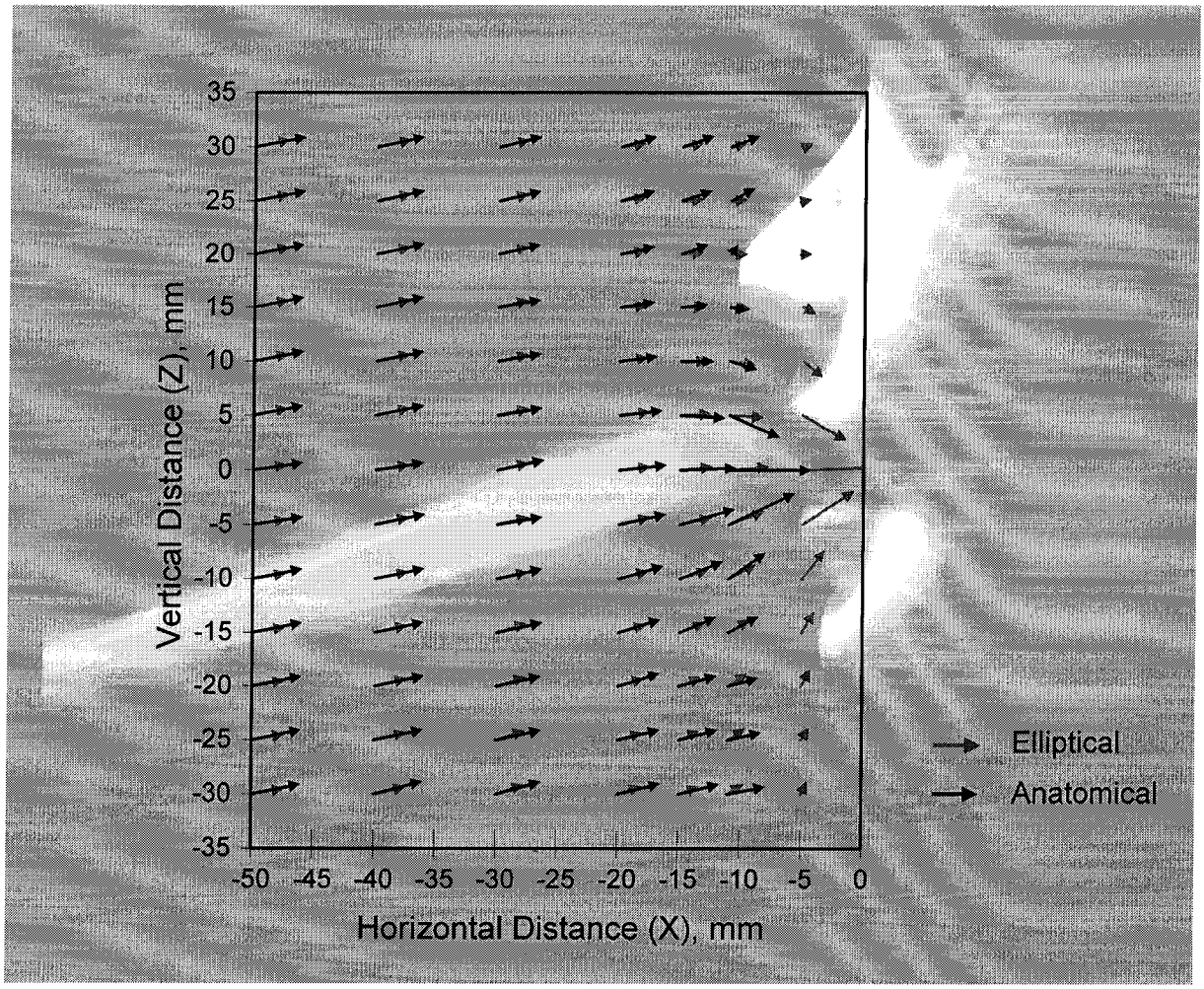

Figure 2.4 Radial velocity = 0 contours at (a) X = -11 mm, (b) X = -15 mm for both test forms, with scaled photo of anatomical mannequin (R = 0.11).

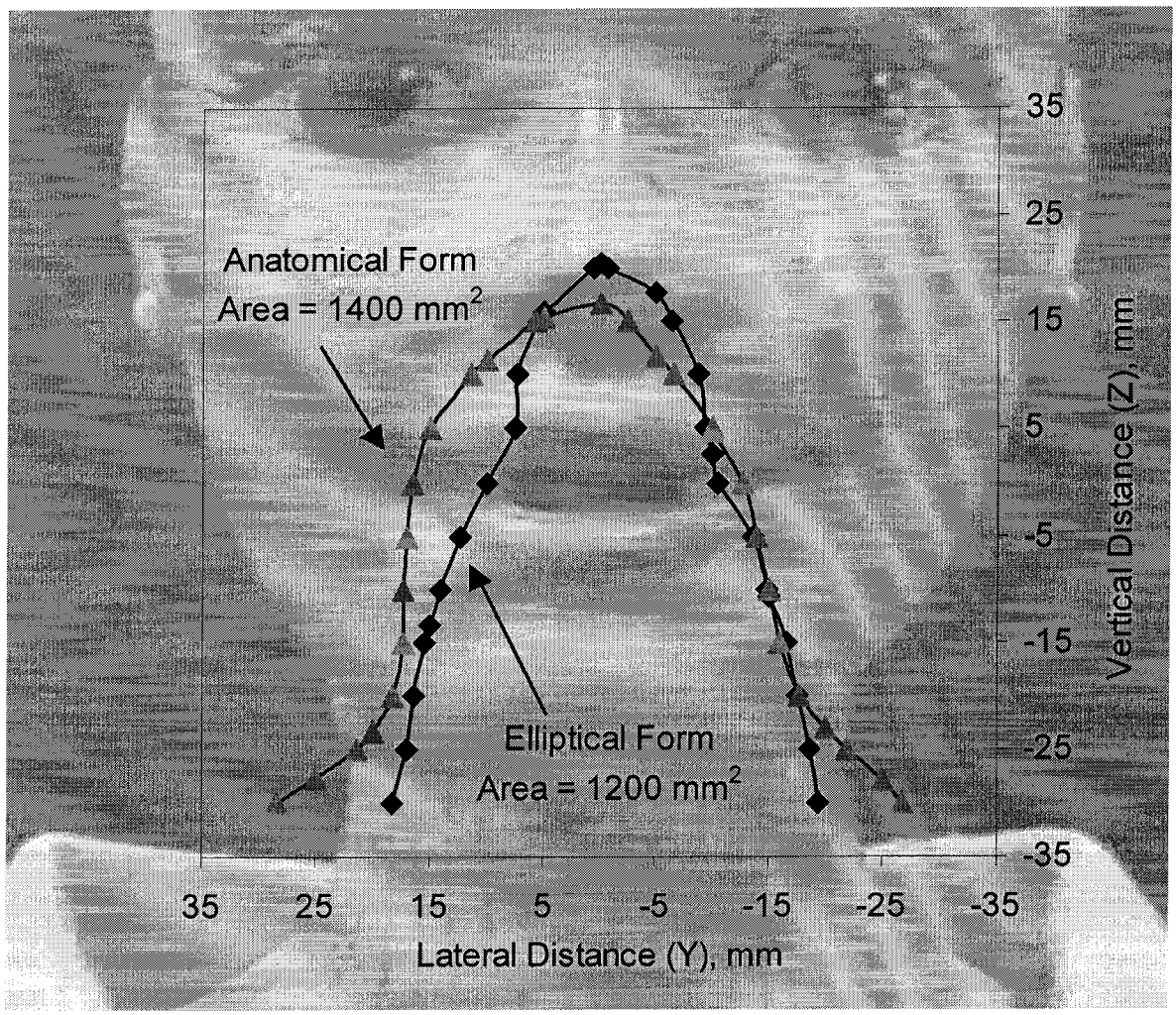

(a)

Figure 2.4 Radial velocity = 0 contours at (a) X = -11 mm, (b) X = -15 mm for both mannequins, with scaled photo of anatomical mannequin (R = 0.11)

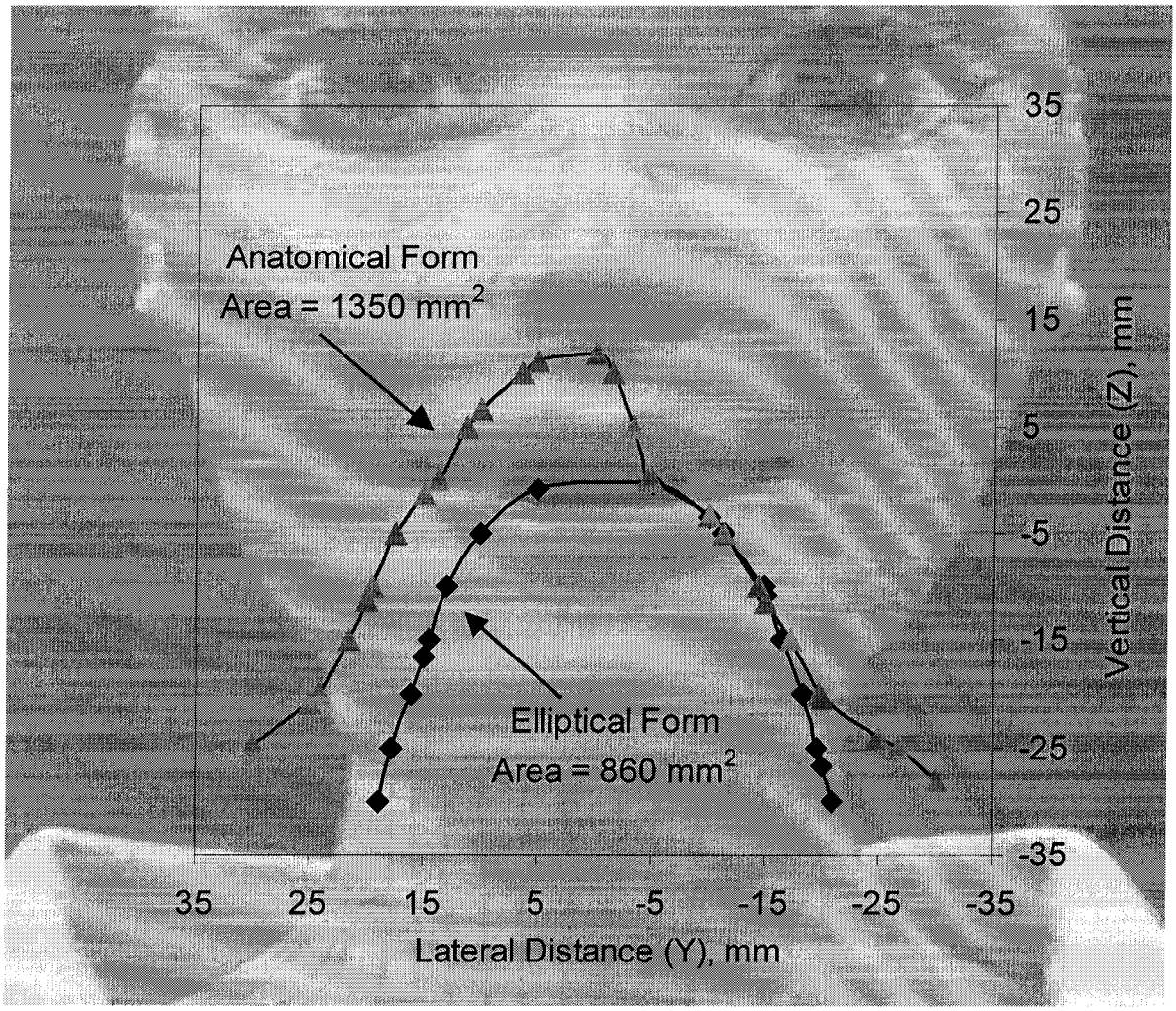

(b)

Figure 2.5 Regions of significant streamwise velocity differences (R = 0.11). All values are average U_{xE}/U_{xA} within the region indicated over X = -11 to -15 mm, except for: under the chin (81%), which also includes X = -20 mm, and above the nose (81%), which is only for X = -11 mm.

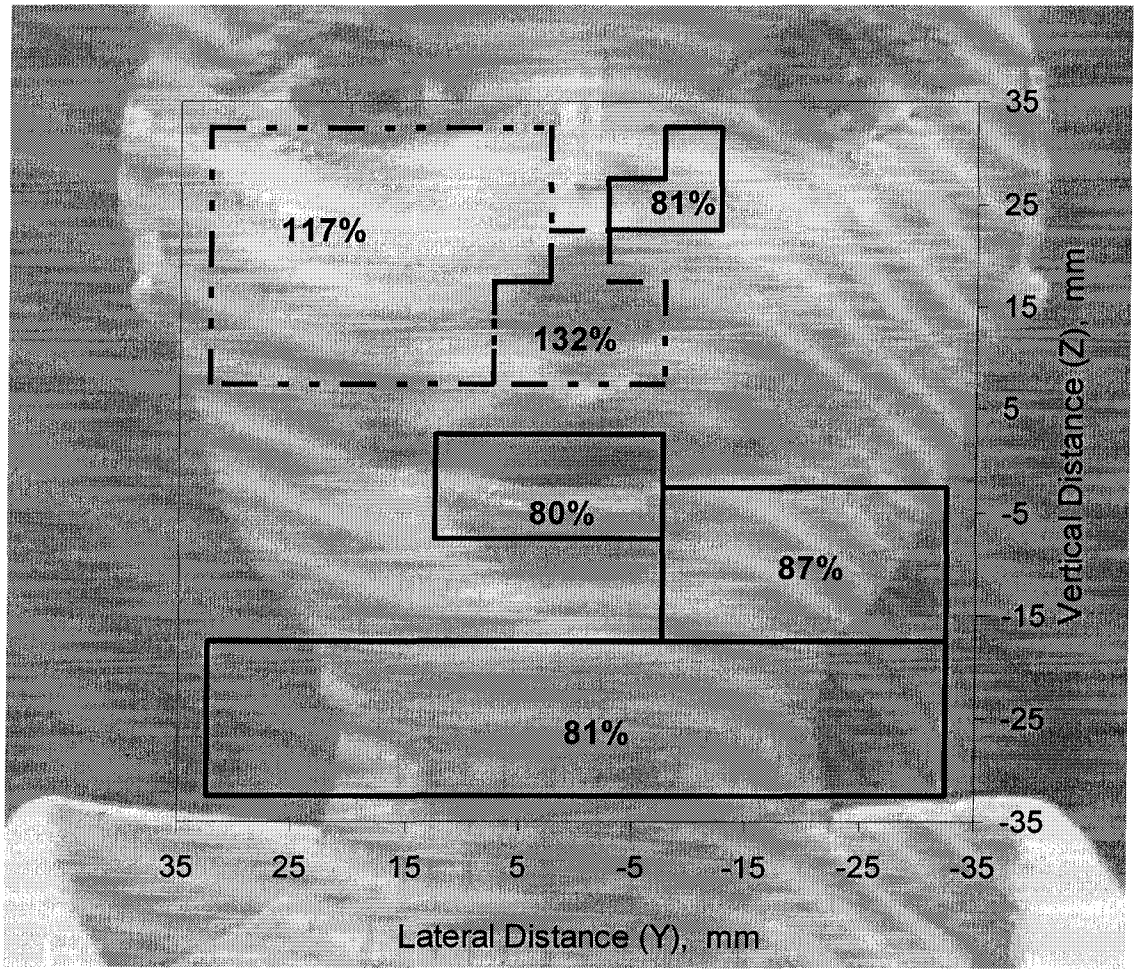

Figure 2.6 Regions of significant vertical velocity differences (R = 0.11). All values are average U_{zE}/U_{zA} within the region indicated over the following upstream distances: X = -11 mm under the chin (164%), X = -11 and -15 mm under the mouth (74%), X = -11 mm at/above the mouth (-90%), and X = -11, -15, -20 for above the nose (47%).

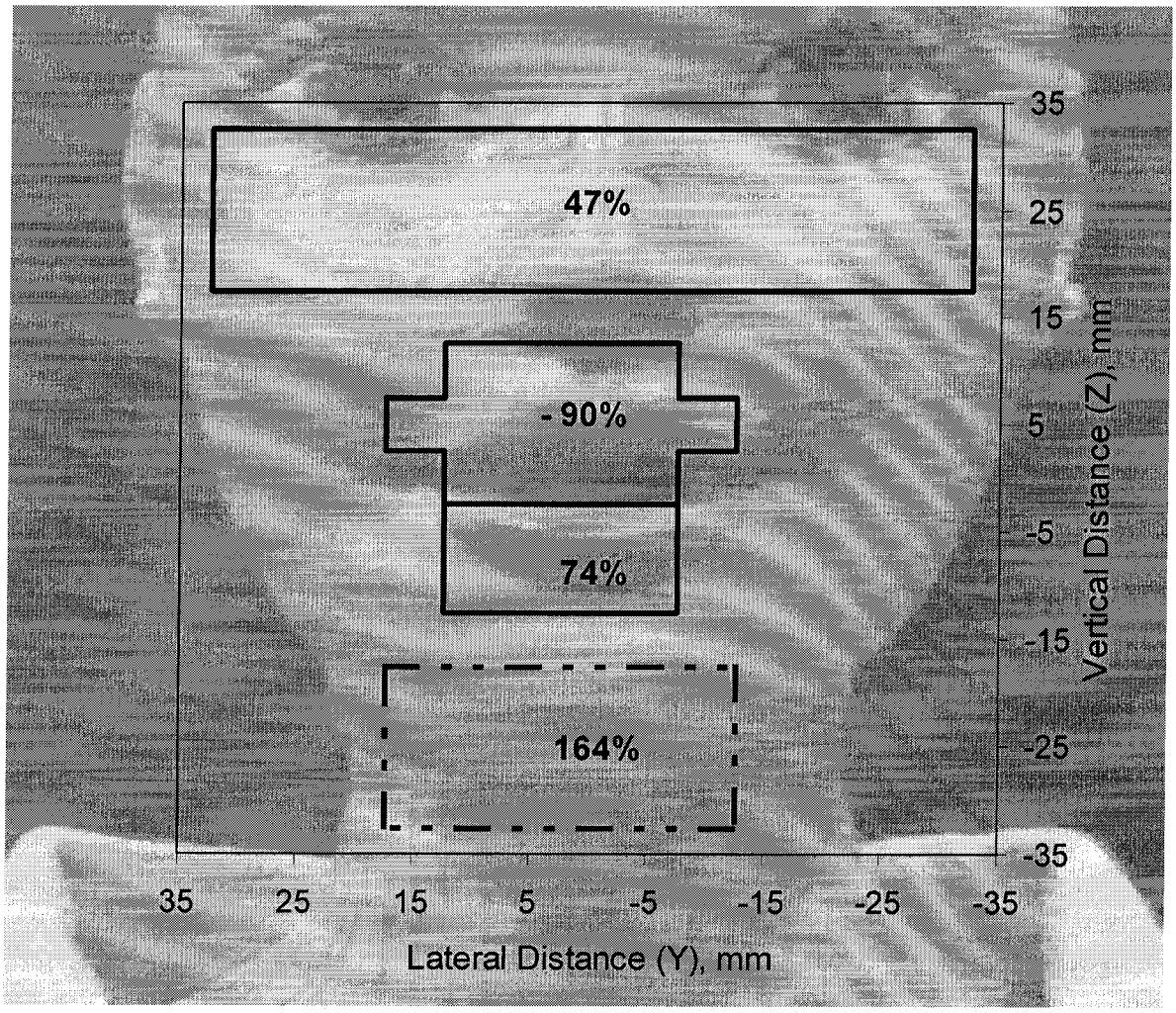

Figure 2.7 Regions of significant lateral velocity differences (R = 0.11). All values are average U_{yE}/U_{yA} within the region indicated over X = -11 to -15 mm, except for the regions under the left (142%) and right (191%) chin, which also include X = -20 mm. The center location under the chin is significant, but the average ratio is insufficient to describe behavior here.

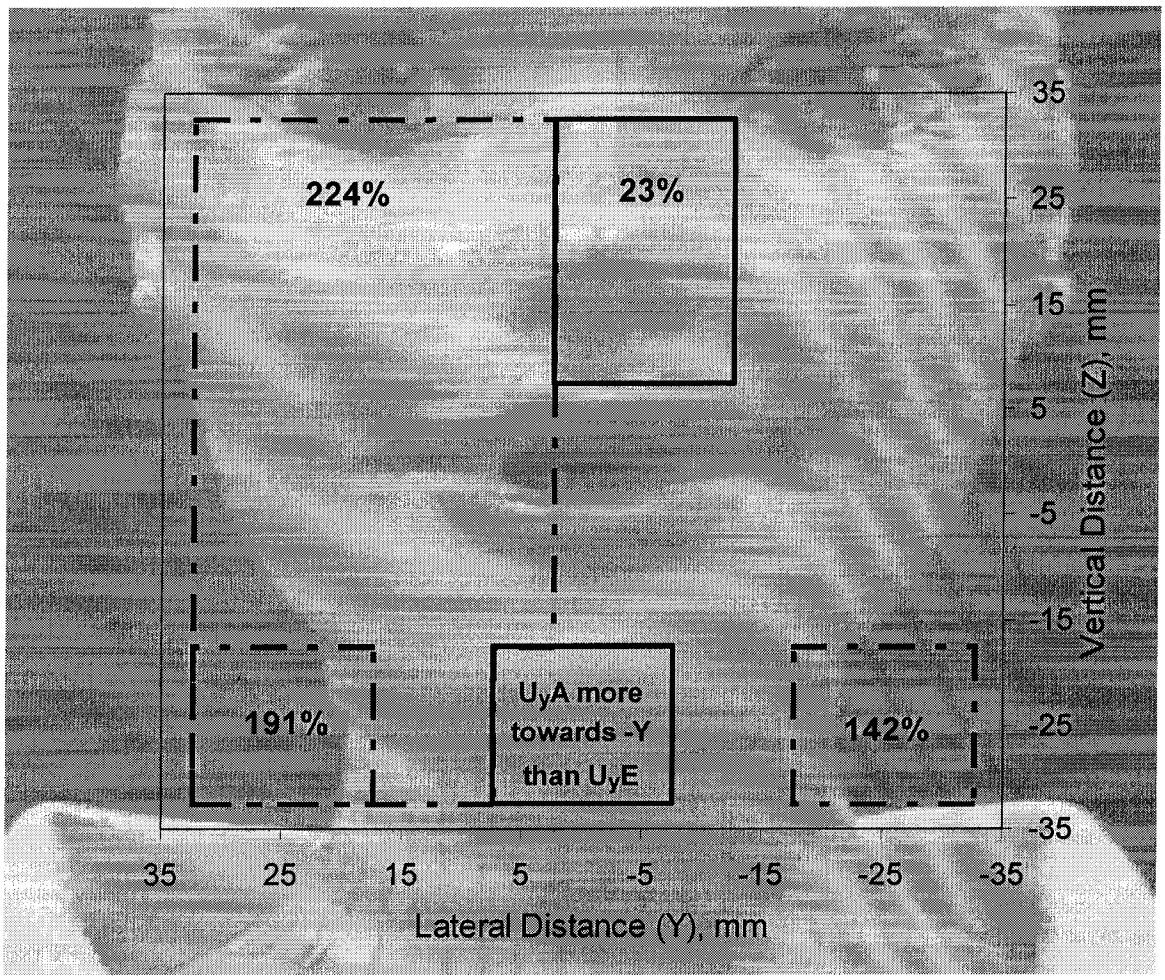

Figure 2.8 Particle size distribution at R = 0.11, horizontal distance between mouth and nozzle = 91.5 cm, vertical distance between mouth and nozzle = 36.7 cm.

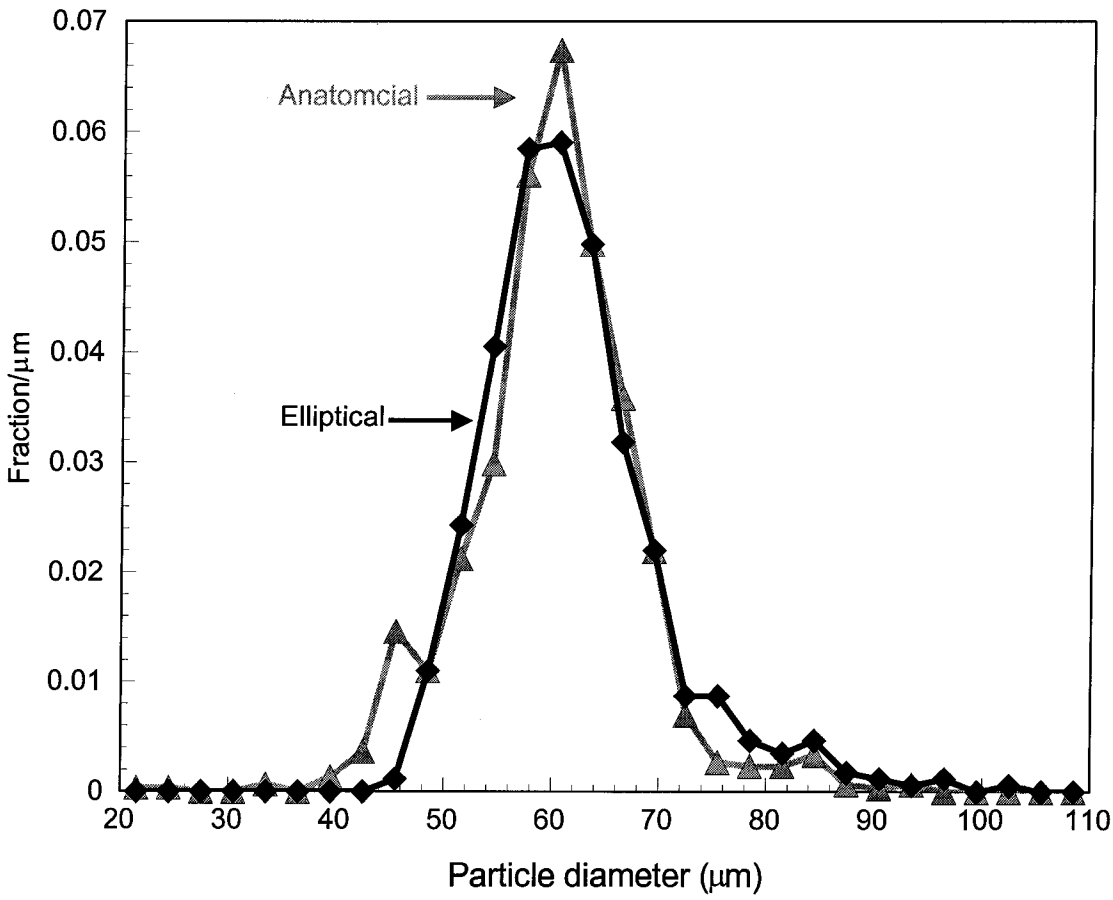

Figure 2.9 Mean paired inhaled mass concentration for all velocity ratios. Error bars indicate +/-95% confidence interval. For all conditions, mass inhaled by elliptical form exceeded mass inhaled by anatomical mannequin.

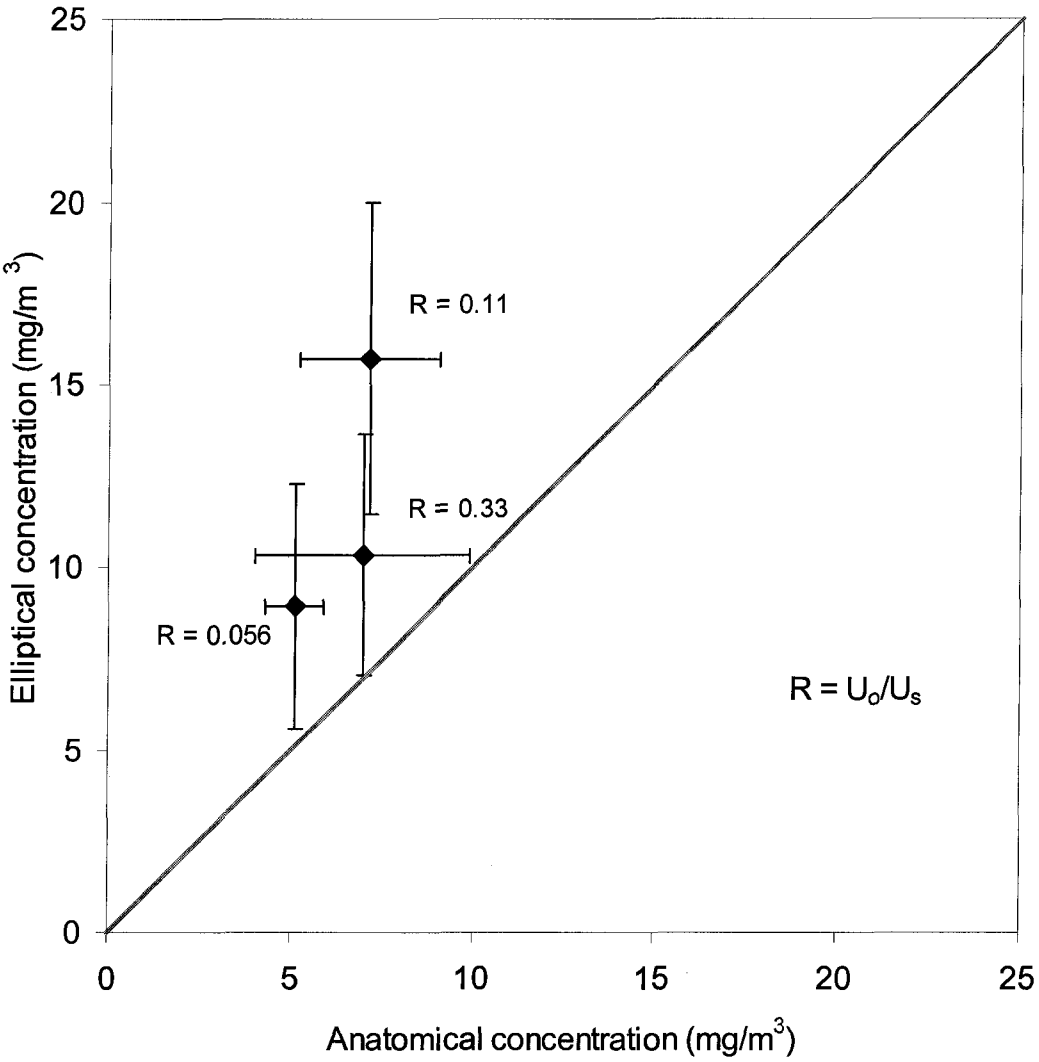

CHAPTER 3:
CFD MODEL FOR A 3-D INHALING MANNEQUIN: VERIFICATION AND VALIDATION

3.0 Abstract

This work investigates the use of computational fluid dynamics (CFD) to model air flow and particle transport associated with an inhaling anatomical mannequin. The studied condition represents typical of occupational velocities (Re = 1920) and at-rest breathing ($R = U_o/U_m = 0.11$). Methods to verify and validate CFD simulations are detailed to demonstrate convergence and describe the model's uncertainties. The standard *k*-epsilon model provided a reasonable flow field, although vertical velocity components were consistently smaller than the experimental validation data, due to truncation of the computational model at hip height. Laminar particle trajectory studies indicated that the modeled velocity field resulted in a shift of particle aspiration fractions toward particles smaller than those determined experimentally, consistent with the vertical velocity field differences.

3.1 Introduction

Particle inhalability, or aspiration efficiency, is defined by the ratio of the inhaled particle concentration to the uniform freestream particle concentration. This ratio varies with particle size and is affected by the freestream velocity, breathing rate and pattern, and orientation of the breather relative to the flow field. Traditional studies to investigate these ratios rely on wind tunnel experiments where mannequins inhale particles uniformly distributed in the wind tunnel. However, as particle sizes increase and freestream velocities decrease, the ability to ensure spatially uniform particle distributions becomes difficult. Hence, the denominator in the particle inhalability calculation becomes more uncertain. Computational fluid dynamic (CFD) modeling of

particle aspiration circumvents this fundamental problem inherent in wind tunnel experiments.

Numerical simulations have been used for the past 24 years to explore particle inhalability; see Table 3.1. Initial studies used simple, two-dimensional shapes to represent the human form (Ingham, 1981; Dunnet and Ingham, 1986; Ingham and Hildyard, 1991; Chung and Dunn-Rankin, 1992). With advances in computer speed and memory, researchers performed three-dimensional simulations by representing the human head as a sphere (Dunnett and Ingham, 1988; Dunnett, 1997, 1999; Dunnett and Vincent, 2000) with a circular opening for the mouth. However, these models ignore the bluff body effect of the human torso, in which the velocity of the approaching freestream under the head decreases streamwise but increases laterally and vertically. Erdal and Esmen (1995) added a torso effect by using a circular cylinder with a hemispherical top to investigate particle aspiration through a circular mouth opening using potential flow simulations. To date, these models typically examined high-velocity conditions rather than the low velocity (< 0.3 m s^{-1}) freestream representative of occupational environments (Baldwin and Maynard, 1998).

Dunnet and Ingham (1988) used the boundary integral equation method to investigate aspiration efficiency of a human head by studying inhalation of a sphere dimensioned to match the mannequin head used in the wind tunnel experiments of Ogden and Birkett (1977). They found that the sphere provided similar results to the head studies, except at low suction (suction velocity = 1.07 m s^{-1}, freestream velocity = 2.75 m s^{-1}), where the facial features created greater effects on the fluid flow near the mannequin. Recent experimental work comparing aspiration differences between simple geometric and more complex anatomical mannequins indicated that, in low freestream environments, both the velocity fields and the concentrations of aspirated particles were significantly different between these mannequins (Anthony *et al.*, 2005). The authors recommended using a three-dimensional model with facial details to investigate particle inhalability in computational fluid dynamic (CFD) studies.

Other recent CFD investigations of flow past heated mannequins have successfully used more realistic shapes to represent humans (*e.g.*, Hyun and Kleinstreuer, 2001; Hayashi *et al.*, 2002), an improvement over the cubic-mannequin forms and estimated

inhalation volume used in Brohus and Neilsen (1996) and Brohus (1997). However, these studies are of limited use to particle inhalability studies due to the unrealistic breathing simulations. Murakami *et al.* (1999) ignored breathing and used a Launder-Sharma low-Reynolds *k*-epsilon model to examine the thickness of the boundary layer as a function of freestream velocity (0.25 and 2.5 m s^{-1}) and turbulence intensity (6% and 29%). Hayashi *et al.* (2002) used a standard *k*-epsilon turbulence model with inhalation to examine the effects of body positions on the rising thermal plume. Because this model focused on room ventilation, it is of limited use to inhalability studies requiring uniform particle concentration and freestream conditions. Hyun and Kleinstreuer (2001) used the RNG *k*-epsilon turbulent model to study inhaled concentrations of tracer gases by the most realistic of humanoid shapes in these studies. Although they considered respiration, thermal heating, and room ventilation conditions, their mannequin head was devoid of facial features that affect particle transport and inhalation.

The goal of this work is to develop a CFD model to examine particle inhalability associated with a human-shaped mannequin, with emphasis on quantifying the numerical uncertainties. This paper investigates the fluid dynamics associated with an inhaling humanoid mannequin and discusses the adequacy of the standard *k*-epsilon turbulence model in low velocity environments. Model verification includes a detailed discussion of the two major sources of computational error: non-linear iteration and mesh convergence (Roache, 1998; Stern *et al.*, 2000). The uncertainties of numerical velocity prediction are assessed using the grid convergence index (Roache, 1998). Experimental velocity measures are used to validate the numerical model by examining where the uncertainty bands of predicted and measured velocities overlap. Subsequently, both laminar and turbulent particle trajectories are studied to explore the particle transport model.

3.2 Methods

The three-dimensional air velocity field associated with an inhaling mannequin facing the wind was measured using laser Doppler anemometry in a wind tunnel and was subsequently simulated numerically using Fidap v. 8.7.2 (Fluent, Inc., Lebanon, NH). Details of the experimental conditions have been discussed (Anthony *et al.*, 2005), but a

summary is provided here for clarity. Figure 3.1 illustrates the geometry, coordinate system, and nomenclature used throughout this study.

3.2.1 Experimental

The test mannequin, modified to match the anthropometric dimensions of a full-scale female, was a commercially available doll, My Size Barbie™ (Mattel Inc., El Segundo, CA). The mouth opening was shaped within the lips as a rounded-edged rectangle (0.01645 m wide by 0.00396 m tall, area = 3.09×10^{-5} m^2). The origin of the co-ordinate system was at the mouth center for both numerical and experimental work. The mannequin was positioned in the wind tunnel to face the wind. The ratio of inhalation velocity (2.7 m s^{-1}) to freestream velocity (0.3 m s^{-1}) was 0.11. The Reynold's number, using the head diameter (0.096 m) as the length scale, was approximately 1910 and represents a person in a low velocity (0.2 m s^{-1}) environment.

The investigation of the fluid flow field was conducted in a closed-loop wind tunnel, measuring 1.2 m high by 1.5 m wide, with a 7 m glass-walled test section. The mannequin blocked less than 6% of the wind tunnel cross section. Velocity measurements were obtained using a laser Doppler anemometer (LDA) (Dantec 41N10 Traversing Amplifier, 58N10 PDA Signal Processor, and Sizeware 2.0 software, Dantec Dynamics A/S, Solvlunde, Denmark). A theatrical smoke generator (Martin Magnum Pro 2000, Martin Professional, Denmark) was used to seed the flow for the measurements.

The LDA used a Coherent Innova 306 argon-ion laser (Laser Innovations, Moorpark, CA) to generate laser light that was split into the three wavelengths for velocity measures: 488.0 nm (blue, for streamwise velocity), 514.5 nm (green, for lateral velocity), and 476.5 nm (violet, for vertical velocity). The Dantec FiberFlow optical system split each of these beams in two, passing one of each pair through a Bragg cell, thereby shifting the frequency by 40 MHz to eliminate the ambiguity in velocity direction measurements. Doppler burst signals from the photomultiplier tubes were analyzed to obtain velocity measurements.

Three-dimensional, time-averaged velocity components were measured upstream of the inhaling mannequin. Measurements were taken in 0.005 m increments laterally and

vertically to distances +/- 0.030 m and at distances of 0.011, 0.015, 0.020, 0.030, 0.040, 0.050, and 0.100 m upstream of the mouth opening for a total of 1171 locations. Because only half the velocity field was investigated in the numerical simulation, velocities on the two sides of the symmetric plane of the test mannequin were treated as replicate samples, yielding a total of 636 measurement locations to validate the CFD model.

Particle experiments were conducted using a Lechler ultrasonic spray system [US 1 nozzle (710.070.16.50) with a US 1 generator (071.091.01.11), Lechler, Inc., Metzengin, Germany], positioned horizontally upstream of the mannequin mouth at (x, y, z) of (-1.523, 0, 0.3685) m. The size distribution of Inland Oil (density = 0.86 g/cc) aerosol from this ultrasonic nozzle was determined by optical sizing and counting in a settling chamber; the size-specific concentration inhaled into the mouth was also determined by optical sizing. The experimental aspiration fraction was calculated using the ratio: inhaled particle count per mL liquid aerosolized / generated particle count per mL liquid aerosolized, for a given particle diameter. Aspiration fractions were computed for particle sizes of 51.5 to 63.5 μm.

3.2.2 Numerical

Gambit 2.1.6 (Fluent, Inc., Lebanon, NH) was used to generate the computational domain. Vertices from a generic file of a three-dimensional female head formed the basis for the computer representation of this mannequin. Simplifications to this file included the removal of the fine details associated with the ears, eyes, and lips. The vertex coordinates were scaled to match the computer model to the dimensions of the experimental mannequin. Additional adjustments were made to modify the relative positions of the nose, lips, and chin to better match the experimental mannequin. To reduce the size of the computational domain, lateral symmetry was assumed. Hence, a plane bisected the mannequin midsagittally, and only the right side of the mannequin head/neck was used for the numerical study. A total of 339 vertices was used to define the final head and neck geometry. The right half of a cylinder, bisected midsagittally, was dimensioned to the test mannequin to form the rest of the computational human form (Figure 3.1).

The width of the computational domain was 0.762 m to match the half-width of the experimental wind tunnel. The height of the computational domain was 0.8212 m. The distance from the top of the domain to the top of the mannequin head was matched, but the torso was truncated at approximately hip level (0.25 m below the mouth opening) to save computational costs. The domain was 3.050 m long, with the mannequin mouth opening located 1.847 m into the domain, to match experimental particle inhalation conditions. The location of the mannequin was more than 10 head diameters upstream of the wind tunnel exit, sufficient to assume a stress-free boundary at the wind tunnel exit.

Because of the complex geometry associated with the anatomical shape in the wind tunnel, a tetrahedral meshing scheme with paved meshes was necessary. The spacing of nodes along the long edges of the wind tunnel domain was denser near the center of the wind tunnel, where the mannequin was located, and less dense near the wind tunnel entrance and exit to resolve velocity gradients more effectively. Three successively denser meshes were made by increasing the number of nodes on each edge by a factor of approximately 1.3, yielding a mesh-coarsening factor, r, of approximately 1.24. The three meshes contained approximately 159,900 (coarse), 308,300 (mid), and 591,300 (fine) nodes. Figure 3.2 illustrates the computational domain of the coarsest mesh.

The equations used to model the airflow were steady state, incompressible, turbulent, Navier-Stokes equations:

$$\nabla \cdot \mathbf{u} = 0 \tag{3.1}$$

$$\mathbf{u} \cdot \nabla \mathbf{u} = \nabla \cdot [(1/\rho)(\mu + \mu_t)(\nabla \mathbf{u} + \nabla \mathbf{u}^T)] - (1/\rho)\nabla P \tag{3.2}$$

The Boussinesq constitutive relationship was used to model the Reynolds stresses; the eddy viscosity was defined by:

$$\mu_t = \rho c_\mu k^2/\varepsilon \tag{3.3}$$

The standard two-equation k-epsilon model equations were used:

$$\rho (\mathbf{u} \cdot \nabla k) = \nabla \cdot (\mu + (\mu_t/\sigma_k) \nabla k) + \mu_t \Phi - \rho\varepsilon \tag{3.4}$$

$$\rho (\mathbf{u} \cdot \nabla \varepsilon) = \nabla \cdot (\mu + (\mu_t/\sigma_\varepsilon) \nabla \varepsilon) + c_1(\varepsilon / k) \mu_t \Phi + c_2 (\varepsilon / k) \Phi - c_2 \rho (\varepsilon^2/ k) \tag{3.5}$$

where Φ is the viscious dissipation function and the standard constants are:

c_μ=0.09, σ_k = 1.00, σ_ε=1.30, c_1 = 1.44, c_2=1.92.

Table 3.2 provides a summary of the boundary conditions assigned to these simulations. On the domain inlet, a uniform velocity of 0.30 m s^{-1} with turbulence kinetic energy of 3.2912 x 10^{-5} m^2 s^{-2} and dissipation of 3.58183 x 10^{-7} m^2 s^{-3} were specified. These values were based on the experimental measurements of turbulence intensity (1.55%) and the assumption of 25 as R_u, the ratio of eddy viscosity to laminar viscosity. The outlet was specified as no-stress; the lateral wall and top of the domain were specified as no-slip walls; and the symmetry plane that bisected the mannequin laterally was specified to have zero normal velocity and zero tangential stress. Because the bottom of the computational domain was not at the same height as the floor of the wind tunnel, it was specified as having zero normal velocity and zero tangential stress to enhance the model's ability to produce the upwards velocity as air approached the bluff body.

The mouth inlet was specified with normal velocity to achieve 10 LPM inhalation across the mouth inlet area and zero lateral and vertical velocity in that plane. For all other surfaces that defined the mannequin, the no-slip wall condition was assigned. Normal derivatives of turbulence kinetic energy (k) and turbulent dissipation (ε) were set to zero at the mouth inlet. Because mesh refinement made slight adjustments to the mouth inlet size, minor modifications were made to the assigned normal velocity at the mouth to ensure identical flow rates for each mesh.

The simulations were conducted using the segregated solver with pressure projection and an element-Reynolds number relaxation scheme. Streamline-upwinding was used to stabilize the convective terms, yielding a nearly second-order accurate method with no crosswind artificial dissipation. The iterative solvers for the linear systems were conjugate gradient squared and conjugate residual methods. The clip was set to 10^{12} to account for the range of turbulence kinetic energy and dissipation in this system. Steady-state solutions for three meshes at three sequentially lower global solution error norm (GSE) tolerance levels required a total of approximately 120 hours of computational time using a 3 GHz, 2 GB RAM computer (Windows 2000). Solutions to coarser mesh simulations were used as initial conditions for finer mesh simulations.

The solutions to the fluid flow model were then used to conduct particle aspiration studies using both laminar and turbulent particle trajectory methods. Particles were

released from a position matching the location of the experimental nozzle relative to the mouth entrance (-1.523 m upstream and 0.3685 m above the mouth). Although particles from the experimental nozzle were emitted from a circular annulus, the corresponding simulations released particles from a horizontal line extending from the nozzle center (Y=0 m) to 0.004646 m, the distance from the experimental nozzle's center to the edge of the annulus. No attempt was made to include the ultrasonic nozzle itself in the computational domain; thus, the turbulent wake behind the nozzle was ignored. Because experiments were conducted with 2 Lpm air through the nozzle, an initial release velocity of 1.802 m s^{-1} was assigned to the particles to match the experimental air velocity at the outlet. Time steps of 0.00065 sec were used in particle transport calculations. Durations of 6.5 seconds allowed particles to travel from the nozzle to the mouth or to bypass the mannequin head, sufficient to determine whether a particle was inhaled or not. Sensitivity to both the release location (+5 mm vertically, -5 mm streamwise) and to initial velocity (+/- 11%) was examined to determine if fairly large experimental errors would result in significantly different numerical predictions of particle aspiration. For turbulent particle simulations at a given particle size, counts of aspirated particles and total particles released were accumulated until the addition of more particles had insignificant (< 0.5%) changes to the aspiration fraction. For most particle sizes, 2000 particle releases were adequate.

3.3 Experimental Fluid Flow Results

The experimental data (U, V, W, and K) were summarized by a mean and standard deviation based on replicate measurements for each of the 636 measurement locations. For each location, 2 to 6 replicate measures were available (mean = 2.2); these data include actual replicate measurements as well as the reflected velocity measurements from the left (-Y) to the right (+Y) side of the mannequin. Although dependence between the right and left side measurements exists, the impact is expected to be minimal and was considered a useful trade-off to data acquisition. Despite data reflection, the low sample sizes at each measurement location required correction for the computed standard deviations (Sokal and Rohlf, 1981).

Table 3.3 presents the minimum and maximum values for each degree of freedom, along with the fraction of measurement locations that had coefficients of variation (cv) less than 0.1, 0.25, and 1.0. The streamwise velocity (U) and the vertical velocity (W) were more precise than lateral velocity (V) and kinetic energy (K). The lateral velocities were often near zero, which contributed to the larger cv. In addition, when centered on the nose tip, the mannequin head was 2 mm wider on right (+Y) side compared to the left (-Y) side. Because the mouth opening was centered on the nose tip, this anthropometric discrepancy may account for greater variability in the replicate measures of lateral velocity.

3.4 Computational Verification

Verification studies were performed on three sequentially denser meshes. For each mesh, the non-linear iterative convergence limit was established. Next, mesh convergence was assessed to determine the independence of the solutions with respect to the fine mesh. Locations were investigated to assess monotonic convergence by examining local orders of accuracy; grid convergence indices were calculated to estimate the numerical uncertainty for the validation studies.

3.4.1 Non-linear Convergence

Using the traditional L_2 error norm, the Fidap software monitored the non-linear convergence for all nodes in the computational domain. Convergence for a simulation was achieved and a solution to the fluid flow domain was provided when this global solution error norm (GSE) for each degree of freedom over all computational nodes reached a specified level (default = 10^{-3}). To evaluate the adequacy of this global solution tolerance, the GSE was reduced an order of magnitude, and the fluid flow field was recomputed to achieve the lower GSE tolerance. The resulting flow data were then assessed to determine whether the reduction of this tolerance affected the fluid flow field in the area of interest. The comparison between the fluid flow field at two tolerance levels was made by calculating a local L_2 error norm. For this study, two local areas were investigated. The "velocity measurement" area matched the 636 locations where experimental measures were made. The "nozzle region" area was defined by 2533

upstream locations to incorporate a region where particle transport would occur (X = 0 to –1.6 m, Y = 0 to 0.5 m, Z = -0.3 to 0.12 m).

The global solution tolerance was reduced successively until insignificant changes occurred in the local relative L_2 error norms for these regions. Table 3.4 provides the relative L_2 error norms for each degree of freedom between solutions at GSEs of 10^{-3} and 10^{-4} and GSEs of 10^{-4} and 10^{-5} for these two regions. For a given mesh density, the local relative L_2 error norm decreased with reductions in GSEs, although minor oscillations for the finest mesh were identified. The local L_2 error norms for the velocity measurement region were less than 5% for each degree of freedom, which was small relative to any mesh errors when the global solution tolerance was set to 10^{-5}. The error norms for the velocity measurement locations were less than for the nozzle locations, where the mesh was less refined.

3.4.2 Mesh Convergence

After an iterative convergence tolerance limit was established at 10^{-5}, a local mesh convergence ratio, R_2, was calculated for each degree of freedom based on the absolute L_2 error norm. This error norm was computed by comparing the differences in the three meshes, using the equation from Stern *et al.* (2001):

$$R_2 = ||\varepsilon_{mid,fine}||_2 / ||\varepsilon_{coarse,mid}||_2 \qquad (3.6)$$

where $||\varepsilon||_2 = (\Sigma\varepsilon_{j,k}^2)^{0.5}$

The term $\varepsilon_{j,k}$ is the difference between the coarser (j) and finer (k) mesh level values for a given degree of freedom.

Table 3.5 provides the mesh convergence ratios for the series of three meshes at the same two study locations within the calculation domain. For the velocity measurement region, near the head, the regional mesh convergence ratios for all degrees of freedom were between 0 and 1, indicating monotonic convergence for solutions at both 10^{-4} and 10^{-5} global tolerance limits. For the upstream nozzle locations, the mesh convergence is monotonic for all terms except pressure and dissipation, which indicates that the upstream meshes are too coarse to solve the equations accurately.

Even though mesh convergence ratios for the local data indicate convergence near the head, locally divergent or oscillatory behavior may also occur at specific locations (Stern

et al., 2001). Thus, local mesh convergence ratios were calculated at each of the locations previously grouped. Of the 3816 possible local convergence ratios from the velocity measurement location, 17% exhibited monotonic convergence, while 73% remained oscillatory and 10% were divergent. The minimum local $|R_1|$ was 8.5×10^{-5}, indicating that no node was considered completely converged using the convergence criteria of $|R_1| < 10^{-16}$ (Stern *et al., 2001*). Of the points that exhibited monotonic convergence, 10% had orders of accuracy (p) within the theoretical range of 1 to 2, where:

$$p = \ln(\varepsilon_{coarse,mid}/\varepsilon_{mid,fine}) / \ln(r) \quad (3.7)$$

For the nozzle location, 68% indicated monotonic convergence.

The subjective, statistical approach presented by Flynn and Eisner (2004) was also used to investigate convergence by fitting regression equations to the data from sequential mesh solutions. The relationship between predicted streamwise velocity in the finest and middle mesh is shown in Figure 3.3, while Table 3.6 provides regression data for all degrees of freedom. Figure 3.3d illustrates that the disagreement between the predicted velocities occurred mainly in the higher velocity measures, which occurred near the mouth inlet. With the sequential mesh refinement, the slopes, intercepts, and coefficient of determination (R^2) all approach the ideal values of 1, 0, 1, respectively, with very tight confidence intervals. The greatest residual error occurred near the mannequin head with the dissipation term. These results indicate that little changes in velocity and turbulence kinetic energy were evident between the middle and finest meshes, which demonstrates good "mesh independence."

3.5 Validation

3.5.1 Velocity Validation

"Validation" of a computational model is achieved when the numerical predictions agree with experimental measurements. Because both numerical and experimental uncertainties exist, validation is achieved when the uncertainty intervals of both predicted and measured values overlap for all degrees of freedom. For a given position, the experimental uncertainty is defined by the standard deviation of the measured velocity, whereas the numerical uncertainty is defined by the computed grid convergence index

(GCI) for the finest mesh (Roach, 1998). These GCIs are available only for locations where monotonic convergence is observed.

Table 3.7 provides information on the fraction of monotonically convergent locations where the simulated variable was within one, two, or three standard deviations of the measured velocity component. The lateral velocity (V) had the strongest agreement: 82% of the simulated values were within 3 standard deviations of the experimental data. This finding is attributable to the larger experimental variability discussed earlier, which contributed to more locations having overlapping confidence intervals. The streamwise velocity (U) near the mannequin face exhibited reasonable agreement with the experimental velocity measurements: of the monotonically converging locations, 54% of predicted U were within 3 standard deviations of the experimental data. Of the monotonically converging locations, only 12% of predicted W were within 3 standard deviations of the experimental data.

The agreements between the measured and simulated velocity data are illustrated graphically in Figures 3.4 through 3.6. In each plot, the dashed diagonal line indicates perfect agreement between measured and simulated velocities while the solid line indicates the least-squares fit between the numerical and experimental data, regardless of monotonicity (*i.e.,* all 636 paired data). The error bars indicate +/-1 standard deviation for the experimental velocity measurements and +/- 1 GCI for the numerically simulated velocities. The simulated streamwise velocities over-estimated the experimental U at values above 0.13 m s^{-1}; the simulated lateral velocities over-estimated the experimental V above 0 m s^{-1}; and the simulated vertical velocities under-estimated the experimental W for all but the very large vertical velocity measurements, *i.e.*, above 0.11 m s^{-1}. Even though the simulated velocities tended to over- or under-estimate experimental results, the trends were well captured with coefficients of determination (R^2) of 0.91, 0.90, and 0.84 for U, V, and W, respectively. When all velocity component data are combined and analyzed together, as shown in Figure 3.7, it is apparent that the central portion of the curve, where the bulk of the data exists, illustrates agreement between measured and predicted velocities. Table 3.8 provides regression statistics for the individual and combined velocity data, indicating that the slope is 14% greater than perfect agreement and the intercept is –0.011 for the combined data. The coefficient of determination is

improved to 97% for the combined data, indicating a strong predictive relationship for the model. Although the model was not able to predict all velocities within experimental accuracy, the model predicted the trends in the velocity field well, thereby indicating the usefulness of the model (Lasher, 2001).

Possible explanations for disagreement between the modeled and measured velocity flow include: (1) inappropriate truncation at the bottom of the calculation domain; (2) differences between the computational face and the experimental mannequin; and (3) errors positioning the laser Doppler anemometer at mouth center, resulting in a systematic bias in the experimental measurements. The first error is likely a noteworthy contributor to the poor agreement among the vertical velocity data. The truncation of the mannequin at hip level and the subsequent assignment of zero vertical velocity at this bottom plane may have prevented the upward flow near the bluff body that occurred experimentally. If the differences in facial detail represent a significant contribution to velocity field differences, then a larger problem exists: this finding implies that the large variability in facial features of real people has a greater impact on the velocity field than other factors.

The third possible explanation, an LDA positioning error bias, was examined using the numerical model. Because the traverse system that moved the laser and optics through the experimental wind tunnel was capable of moving in 1 mm increments, the positioning sensitivity was investigated at half this distance. Therefore, the simulated flow field was examined at locations +/- 0.5 mm laterally, vertically, and streamwise from each of the velocity measurement positions (*e.g.*, $x' = x + 0.0005$ m, $y' = y - 0.0005$ m, $z' = z$). For each of the 636 validation locations, 27 nearby locations were investigated numerically. No single velocity field from these 27 sets of data performed any better than the original velocity measurement set. For each of the 636 velocity measurement locations, a position-based standard deviation (σ_p) was calculated using the predicted velocity components for the 27 adjusted positions. The standard deviations associated with the 27 adjusted-position velocity averages were less than the numerical uncertainty defined by the GCI. Paired t-tests revealed these differences were significant for the vertical velocity field ($p = 0.0008$). These uncertainties were incorporated into the uncertainty analysis by adding $1\sigma_p$ and $3\sigma_p$ to the GCI uncertainty term. Results are

incorporated into Table 3.7. The inclusion of positional uncertainty into the numerical prediction uncertainty provided only moderate improvements in the fraction of validated locations for the velocity field. Thus, positional bias is not sufficient to address the differences in predicted versus measured velocity fields.

3.5.2 Kinetic Energy Validation

Within the velocity measurement locations, the simulated turbulence kinetic energy (KE) was orders of magnitude larger than the experimental values (mean experimental = 4.2×10^{-6} $m^2 s^{-2}$, mean numerical = 2.6×10^{-3} $m^2 s^{-2}$), as illustrated in Figure 3.7. Only four of the 158 monotonically converging locations were successfully validated: these four locations had numerical uncertainties that were greater than the predicted turbulence kinetic energy, so that their confidence intervals included zero. These are illustrated in Figure 3.7 for data with large horizontal error bars. These large numerical uncertainties were sufficient to allow for overlapping of measured and predicted uncertainty intervals for kinetic energy.

The fraction of validated locations increased from 3 to 80% when including the additional 0.5 mm positioning uncertainty to turbulence kinetic energy estimates. Using positional uncertainty (σ_p) and numerical uncertainty (GCI), 126 of the 158 monotonically converging locations had uncertainties larger than the mean predicted KE for the given location. This again resulted in the inclusion of zero in the uncertainty intervals, sufficient to include the measured kinetic energy within the confidence intervals of numeric predictions, despite the orders of magnitude differences in predicted versus experimental kinetic energy. More distressing is the lack of correlation between the predicted and measured values of the turbulence kinetic energy ($R^2 = 0.0009$). Simulations at higher turbulence intensity (3%, with $R_u = 10$) were also conducted for these mesh series, and similar poor correlations were found ($R^2 = 0.0006$).

The discrepancy between measured and simulated turbulence kinetic energy is likely attributable to the low particle seeding in experimental velocity measurements. A mere 10 Doppler bursts were recorded per second, resulting in a filter cut-off frequency of 1.5 Hz, using the equation

$$\text{filter cut-off frequency} = \text{mean particle rate}/(2\pi) \tag{3.8}$$

For this low particle-seeding rate, the true kinetic energy has been under-reported by laser Doppler anemometry (Noback *et al.*, 1998).

As a result of the experimental uncertainties, the turbulence kinetic energy from the CFD simulations remains unvalidated. Concerns of the thickness of the boundary layer associated with the high Reynolds number model are unresolved: in this low Reynolds number regime, the facial features of the human form may have been contained within the relatively thick viscous boundary layer present in low Reynolds number regimes, making resolution of kinetic energy near the walls difficult. Initial simulations using the low Reynolds number *k*-omega turbulence equations resulted in unachievable convergence at these same mesh densities. Finer near-wall meshes are required, and sensitivities to free-stream values of turbulent frequency (ω) have not been resolved at this time.

3.5.3 Particle Aspiration Validation

Simulated particle releases occurred at locations representing experimental conditions: 1.523 m upstream and 0.3685 m above the mouth center, along a line from the plane of symmetry (Y = 0 m) to 0.004636 m laterally. Table 3.9 provides the aspiration fraction for experimental measurements as well as both laminar and turbulent particle aspiration simulations. For laminar particle simulations, no particles smaller than 55.0 μm and no particle larger than 58.0 μm released along this line were aspirated. This range was smaller than both the median aspirated particle size (60.2 μm) and the particle size with the maximum experimental aspiration fraction (66.5 μm).

To compare numerical aspiration fractions with experimental results, turbulent particle motion was examined for 51.5, 54.5, 57.5, 60.5 and 63.5 μm oil particles (density = 0.86 g/cc). These sizes matched binned data from optical particle count concentrations from experimental studies. Particles outside this range had negligible simulated aspiration fractions. The maximum simulated aspiration was 11.8% for 57.5 μm, within the range of the particle sizes inhaled in laminar simulations. The peak aspiration fraction for the experimental study occurred for 66.5 μm particles. Sensitivity tests indicated that neither moving the source upwards 5 mm nor changing the initial particle velocity magnitude would shift the simulated aspiration fraction curve toward larger

particles. The particle size differences between the measured and simulated aspiration curves are consistent with the under-prediction of vertical velocity identified earlier. The differences in the aspirated particle sizes indicate that differences between the modeled and measured velocity fields limit the model's usefulness to study aspiration efficiency from a point source.

Table 3.9 also illustrates that the simulated aspiration fraction was nearly two orders of magnitude greater than those observed experimentally. Poorly modeled turbulence kinetic energy and the oversimplification of the nozzle in the particle simulation study contributed to this finding. Because the fluid flow model over-estimated kinetic energy near the head of the mannequin, turbulent particle motion is expected to be more random and should result in fewer inhaled particles. However, this outcome is opposite of the trend observed, and the kinetic energy discrepancies in the model are not the cause of these over-estimations in aspiration.

Therefore, the major contribution to the poor agreement between the magnitudes of aspiration fractions is likely the oversimplification of the particle generation mechanism. The source of air exiting the nozzle was represented only with the assignment of initial velocity to the particle, under-representing particle momentum. In addition, the lack of a realistic physical representation of the nozzle in the fluid flow field ignored the effect of the wake turbulence downstream of the nozzle. This wake effect increased particle dispersion experimentally, resulting in decreased particle aspiration at the downstream inhaling mannequin. Re-solving the fluid flow field would be necessary to fully capture this event. However, while better representation of the nozzle would probably yield better agreement between the magnitudes of the aspiration efficiency, it is not anticipated to produce better agreement in the shape of the aspiration fraction curves. The maximum aspirated particle size would still be smaller for the model than what was found experimentally.

3.6 Conclusions

The simplifications in the CFD model may have prevented better agreement between the experimental and simulated data. First, and perhaps most important, the truncation of the mannequin at hip height led to a consistent under-estimation of vertical velocity. The

bottom of the computational domain presented here restricted the flow to zero-vertical velocity, allowing for streamwise and lateral velocity, unlike the no-slip condition of an actual wind tunnel floor. However, the location of this plane was insufficient to represent the vertical velocity field found in the experimental studies with a non-truncated mannequin. It is this velocity field difference that contributed to the shift in the particle aspiration curve toward smaller particles by approximately 9 μm.

Previous work in particle inhalability proved the importance of the torso to induce upward particle flow in front of an inhaling mannequin (Vincent and Mark, 1982). Results from the present study indicate that the truncation of the mannequin at hip height may not adequately represent the velocity field associated with the full-height mannequin. As such, particle motion through this field may be affected by this reduction in upward velocity, even for the relatively large particles and low freestream velocity. Fortunately, the traditional method to determine numerical and experimental aspiration efficiency relies on the assumption of uniformly distributed particles within the wind tunnel. In this case, the sensitivity of the source position is avoided while still allowing examination of particle inhalability.

The second over-simplification was the particle release simulations, which led to over-estimation of the fraction of particles aspirated by the human form downstream of the ultrasonic nozzle. Additional modeling efforts to represent the aerosol source from this nozzle are necessary to validate the particle transport portion of this research. Fortunately, the particle sizes that were aspirated in the simulations were in the size range of those aspirated experimentally. The 9-μm shift to smaller aspirated particle sizes was consistent with the decreased vertical velocity field identified earlier.

The final simplification of the complex reality associated with particle inhalation studies was the selection of the computational mannequin shape. The computational human shape was a generic form, modified to match several key dimensions of the experimental mannequin, including lip location, mouth opening, head height and width, and location of shoulders. However, the specific facial details were not addressed, and, in light of the results discussed above, the effects of using the generic face shape could not be specifically addressed.

The greatest concern for this model is the lack of agreement between turbulence kinetic energies, but this is likely attributable to the measurement errors associated with low particle seeding. Validation is incomplete for turbulence kinetic energy simulations at this time.

Finally, this work provides recommendations for future CFD investigations that model airflow around an inhaling mannequin. First, the difficulties of obtaining appropriate mesh densities near the mouth and in the freestream are unavoidable. The average element dimension was 0.4 mm at the mouth and was 5.81 mm at the domain inlet. Verification studies found that discretization near the mouth and head was sufficient, but because upstream verification was incomplete, future studies should examine smaller discretization for the freestream. This would require either reducing the computational domain's size or using software that can access more than the 2GB Ram. In addition, setting the proper clip in these simulations was key to obtaining converged meshes. The default of 10^{8} was insufficient for this flow regime, and a value of 10^{12} was needed to achieve convergence to 10^{-5} GSE; this information should save valuable time in future computational studies with a complex human form.

Future CFD studies to investigate particle aspiration from a point source should include the full mannequin height and additional discretization for sources more than 10 head diameters upstream. However, the model developed here may still be useful for investigations that target information on particle concentration where the exact location of particle source is not significant. Particularly, the aspiration efficiency studies could use this model as they rely on the assumption of uniform particle concentrations upstream of the inhaling human but do not rely on the specific particle source location. Therefore, a human-scale version of this model may still provide insights into inhalable particle studies.

3.7 References

Anthony, TR, M.R. Flynn, A.Eisner (2005). Evaluation of facial features on particle inhalation. *Ann. Occup. Hyg.* 49(2): 179-193.

Baldwin, P.E.J. and A.D. Maynard (1998). A survey of wind speeds in indoor workplaces. *Ann. Occup. Hyg.* 42(5): 303-313.

Brohus, H. and P.V. Nielsen (1996). CFD models of persons evaluated by full-scale wind channel experiments" **Proceedings of Roomvent '96, 5th International Conference on Air Distribution in Rooms**, Yokohama, Japan, July 17-19, 1996, 2:137-144.

Brohus, H. (1997). CFD simulation of personal exposure to contaminant sources in ventilated rooms. **Proceedings of Ventilation '97**, The 5th International Symposium on Ventilation for Contaminant Control, Global Developments in Industrial Ventilation, Ottawa, Canada, Vol. 1, September 14-17, 1997, pp. 215-226.

Chung, I.P. and D. Dunn-Rankin (1992). Numerical simulation of two-dimensional blunt body sampling in viscous flow. *J. Aerosol Sci.* 23(3): 217-232.

Dunnett, S.J. (1997). A numerical study of the flow field in the vicinity of a bluff body with aspiration oriented to the flow. *Atmospheric Environment* 31(22): 3745-3752.

Dunnett, S.J. (1999). An analytical investigation into the nature of the airflow near a spherical bluff body with suction. *J. Aerosol Sci.* 30(2): 163-171.

Dunnett, S.J. and D.B. Ingham (1986). A mathematical theory to two-dimensional blunt body sampling. *J. Aerosol Sci.* 17(5): 839-853.

Dunnett, S.J. and D.B. Ingham (1988). The human head as a blunt aerosol sampler. *J. Aerosol Sci.* 19(3): 365-380.

Dunnett, S.J. and J.H. Vincent (2000). A mathematical study of aerosol sampling by an idealised blunt sampler oriented at an angle to the wind: the role of gravity. *J. Aerosol Sci.* 31(10): 1187-1203.

Erdal, S. and N.A. Esmen (1995). Human head model as an aerosol sampler: calculation of aspiration efficiencies for coarse particles using an idealized human head model facing the wind. *J. Aerosol Sci.* 26: 253-272.

Flynn, M.R. and A.D. Eisner (2004). Verification and validation studies of the time-averaged velocity field in the very near-wake of a finite elliptical cylinder. *Fluid Dynamics Research* 34:273-288.

Hyun, S. and C. Kleinstreuer (2001). Numerical simulation of mixed convection heat and mass transfer in a human inhalation test chamber. *Int. J. Heat Mass Transfer* 44: 2247-2260.

Hayashi, T., I. Yoshiaki, K.S. Kato, and S. Murkami (2002). CFD analysis of characteristics of contaminated indoor air ventilation and its application in the evaluation of the effects of contaminant inhalation by a human occupant. *Building and Env.* 37: 219-230.

Ingham, D.B and M.L. Hildyard (1991). The fluid-flow into a blunt aerosol sampler oriented at an angle to the oncoming flow. *J. Aerosol Sci.* 22:235-252.

Lasher, W.C. (2001). Computation of two-dimensional blocked flow normal to a flat plate. *J. Wind Engin.*; 89: 493-513.

Murakami, S., J. Zeng, T. Hayashi (1999). CFD analysis of wind environment around a human body. *J. Wind Engin.*; 83: 393-408.

Nobach, H., E. Müller, C. Tropea (1998). Efficient estimation of power spectral density from laser Doppler anemometry. *Experiments in Fluids*; 24: 499-509.

Ogden, T.L. and J.L. Birkett (1977). The human head as a dust sampler. In Halton, W.H. editor. Inhaled particles IV: proceedings of an international symposium organized by the British Occupational Hygiene Society. Oxford: Pergamon Press. p. 93-105. ISBN 0080205607

Roache, P.J. (1998). **Validation in Computational Science and Engineering.** Hermosa Publishers, Albuquerque, NM.

Sokal, RR, and Rohlf, F.J. (1981). **Biometry**, 2nd Edition. W.H. Freeman and Co., San Francisco, CA.

Stern, F., Wilson, R.V., Coleman, H.W., Patterson, E.G. (2001). Comprehensive approach to verification and validation of CFD simulations – part 1: methodology and procedures. *J. Fluids Engin.*, 123:793-802.

Vincent, J.H. and D. Mark (1982). Applications of blunt sampler theory to the definition and measurement of inhalable dust. *Ann. Occup. Hyg.* 26(1): 3-19

3.8 Nomenclature

c_μ empirical coefficient for standard *k*-epsilon turbulence model, 0.09

c_1 empirical coefficient for standard *k*-epsilon turbulence model, 1.44

c_2 empirical coefficient for standard *k*-epsilon turbulence model, 1.92

GSE global solution error

K kinetic energy, measured, $\frac{1}{2}(\overline{u_i'u_i'})$, $m^2\ s^{-2}$

N_i number of nodes in mesh i

P pressure

p computed order of accuracy from simulation

r mesh coarsening factor, $(N_{finer}/N_{coarser})^{1/3}$

R_2 mesh convergence ratio, equation (3.6)

R^2 coefficient of determination

R_u ratio of eddy viscosity to laminar viscosity, used to relate dissipation to kinetic energy, with $\varepsilon = \rho c_\mu k^2/(R_u \mu)$

u velocity vector

U streamwise velocity component, $m\ s^{-1}$

V lateral velocity component, $m\ s^{-1}$

W vertical velocity component, $m\ s^{-1}$

ε turbulent dissipation, $m^2\ s^{-3}$

$\varepsilon_{i,j}$ degree of freedom's difference between conditions i and j

k turbulence kinetic energy, $m^2\ s^{-2}$

ρ air density, 1.205 $kg\ m^{-3}$

σ_ε Prandtl number for ε, used in standard *k*-epsilon model, 1.30

σ_k Prandtl number for *k*, used in standard *k*-epsilon model, 1.00

σ_m standard deviation for a give degree of freedom over replicate measurements

σ_p standard deviation for a given degree of freedom over positions within +/- 0.5 mm from the velocity measurement location

μ dynamic viscosity of air, $1.82 \times 10^{-3}\ kg\ m^{-1}\ s^{-1}$

μ_t turbulent dynamic viscosity of air

Φ viscous dissipation function

Table 3.1 Review of existing computational simulations of particle inhalability. Zero-degree orientation indicates the geometry "mouth" was facing the wind.

Author	Year	Dimension	Geometry	Orientation	Method	Turbulence	Gravity	Comments
Numerical Particle Inhalability Studies								
Ingham	1981	2	Cylinder	0°	Potential	no	no	Only good for small particles in large velocities
Dunnett and Ingham	1986	2	Cylinder and Rectangle	0°	Potential	no	no	Method gave "accurate flow description near sampler"
Dunnett and Ingham	1987	2	Cylinder	0°	Potential	no	no	Particle Re is important
Dunnett and Ingham	1988	3	Sphere	0°	Potential	no	no	Compared to Ogden & Birkett; good agreement except low suction
Ingham and Hildyard	1991	2	Cylinder	0° to 180°	Potential	High Re	no	Only good in some high Re conditions
Chung and Dunn-Rankin	1992	2	Cylinder	0°	Navier-Stokes	no	no	Investigated $R=U_o/U_s$; δ/D; viscous and inviscous calculations
Erdal and Esmen	1995	3	Rounded-top cylinder	0°	Potential	no	yes	0.5 to 9 m s^{-1}; round mouth, cyclical inhalation
Velocity Field Studies								
Brohus, Nielsen	1996	3	3 Cubic mannequins	0°	CFD: Standard k-e turbulence	yes	n/a	Respiration not simulated
Brohus	1997	3	Cubic mannequin	Ventilated room	CFD: Standard k-e turbulence	yes	n/a	Hemisphere inhalation region
Bjorn, Nielsen	1998	3	Cubic mannequin	Ventilated room	CFD: Standard k-e turbulence	yes	n/a	Respiration simulated (one mannequin inhaled, other exhaled)
Murakai, Zeng, Hayashi	1999	3	Heated mannequin	0, 180°	CFD: Launder-Sharma low RE k-e turbulence	yes	n/a	Thermal boundary layer thickness increased with height (0.25 and 2.5 m/s); non-breathing
Hayashi, Ishizu, Kato, Murakami	2001	3	CFD heated mannequin in room	sit, stand, lie	CFD: Standard k-e turbulence	yes	n/a	Steady inhalation for heated mannequin
Hyun, Kleinstreuer	2001	3	Realistic mannequin (no face)	0, 90, 180°	CFD: RNG k-e turbulence	yes	n/a	Thermal effects

Table 3.2 Boundary conditions for numerical simulation

Surface	Normal Velocity ($m\ s^{-1}$)	Tangential Velocity ($m\ s^{-1}$)	Turbulence Kinetic Energy ($m^2\ s^{-2}$)	Turbulent Dissipation ($m^2\ s^{-3}$)
Inbox	0.3 (mean)	0	3.2912×10^{-5}	2.582×10^{-7}
Outbox	$\partial \mathbf{u}/\partial n = 0$	$\partial \mathbf{u}/\partial \tau = 0$	$\partial k/\partial n = 0$	$\partial \varepsilon/\partial n = 0$
Top of Box	0	0	0	0
Y-Box	0	0	0	0
Bottom of Box	0	$\partial \mathbf{u}/\partial \tau = 0$	$\partial k/\partial n = 0$	$\partial \varepsilon/\partial n = 0$
Midsagittal Plane	0	$\partial \mathbf{u}/\partial \tau = 0$	$\partial k/\partial n = 0$	$\partial \varepsilon/\partial n = 0$
Mouth Inlet	2.7 (mean)	0	$\partial k/\partial n = 0$	$\partial \varepsilon/\partial n = 0$
Head/Torso Surfaces	0	0	$\partial k/\partial n = 0$	$\partial \varepsilon/\partial n = 0$

Table 3.3 Ranges and fraction of measurements below the indicated coefficient of variation (cv)

Degree of Freedom	minimum, maximum	$cv \leq 0.1$	$cv \leq 0.25$	$cv \leq 1.0$
U	0.018, 0.364 ($m\ s^{-1}$)	0.86	1.00	1.00
V	-0.044, 0.098 ($m\ s^{-1}$)	0.24	0.47	0.85
W	-0.106, 0.154 ($m\ s^{-1}$)	0.86	0.99	0.99
KE	5.05×10^{-6}, 0.00316 ($m^2\ s^{-2}$)	0.29	0.63	0.97

Table 3.4 Relative L_2 error norms for non-linear convergence tolerance for (a) velocity measurement region and (b) nozzle region upstream of inhaling mannequin

(a) Velocity measurement locations

Mesh	GSE Levels	U	V	W	P	KE	ε
Coarse	$10^{-3} - 10^{-4}$	0.024	0.020	0.271	0.031	0.107	0.082
	$10^{-4} - 10^{-5}$	0.002	0.003	0.009	0.001	0.009	0.010
Moderate	$10^{-3} - 10^{-4}$	0.029	0.021	0.333	0.031	0.163	0.189
	$10^{-4} - 10^{-5}$	0.003	0.004	0.020	0.003	0.008	0.012
Fine	$10^{-3} - 10^{-4}$	0.001	0.003	0.006	0.003	0.008	0.007
	$10^{-4} - 10^{-5}$	0.001	0.005	0.015	0.003	0.012	0.011

(b) Nozzle locations

Mesh	GSE Levels	U	V	W	P	KE	ε
Coarse	$10^{-3} - 10^{-4}$	0.002	0.033	0.053	0.124	0.081	0.095
	$10^{-4} - 10^{-5}$	0.000	0.002	0.004	0.002	0.003	0.004
Moderate	$10^{-3} - 10^{-4}$	0.003	0.042	0.079	0.122	0.132	0.098
	$10^{-4} - 10^{-5}$	0.000	0.002	0.005	0.010	0.004	0.006
Fine	$10^{-3} - 10^{-4}$	0.001	0.025	0.019	0.027	0.017	0.022
	$10^{-4} - 10^{-5}$	0.003	0.024	0.021	0.021	0.006	0.002

Table 3.5 Three-mesh convergence ratios, R_2, at sequential global solution errors (GSE), for Velocity Measurement and Nozzle locations. Values greater than 1 are bolded and indicate mesh independence is not yet achieved.

GSE	U	V	W	P	KE	ε
Velocity Measurement Locations (n=636)						
10^{-3}	**2.119**	0.905	**2.922**	**1.087**	0.820	**1.103**
10^{-4}	0.941	0.850	0.696	0.342	0.342	0.744
10^{-5}	0.913	0.833	0.593	0.702	0.312	0.761
Nozzle Locations (n=2541)						
10^{-3}	0.663	**1.315**	0.789	**2.854**	0.698	**2.469**
10^{-4}	0.485	0.896	0.411	0.564	0.470	**1.908**
10^{-5}	0.671	0.760	0.368	**1.039**	0.466	**1.842**

Table 3.6 Verification regression statistics for (a) velocity measurement locations and (b) nozzle locations. Bolded values highlight the degrees of freedom and meshes that yielded less than ideal values of Slope = 1, Intercept = 0, $R^2 = 1$.

(a)

Degree of Freedom	Meshes Compared	Slope	Slope 95% CI	Intercept	Intercept 95% CI	R^2
U	5 and 4	0.998312	0.99831, 0.99831	0.00025	0.00023, 0.00026	0.995
U	4 and 3	0.975439	0.97544, 0.97544	0.00471	0.00468, 0.00473	0.995
V	5 and 4	1.000131	1.00013, 1.00013	0.00061	0.00059, 0.00063	0.995
V	4 and 3	1.006897	1.00690, 1.00690	-0.00062	-0.00064, -0.00059	0.995
W	5 and 4	0.994507	0.99451, 0.99451	0.00081	0.00077, 0.00084	0.993
W	4 and 3	0.962434	0.96243, 0.96243	0.00176	0.00169, 0.00184	0.993
P	5 and 4	0.997877	0.99788, 0.99788	0.00018	0.00016, 0.00020	0.994
P	4 and 3	0.963632	0.96363, 0.96363	0.00165	0.00158, 0.00173	0.994
KE	5 and 4	1.018339	1.01834, 1.01834	0.00003	-0.00003, 0.00009	0.986
KE	4 and 3	**0.782393**	0.78239, 0.78239	0.00029	-0.00078, 0.00136	0.986
E	5 and 4	**0.805228**	0.80523, 0.80523	0.00093	0.00035, 0.00152	**0.881**
E	4 and 3	**0.714250**	0.71425, 0.71425	0.00045	-0.00110, 0.00200	**0.881**

(b)

Degree of Freedom	Meshes Compared	Slope	Slope 95% CI	Intercept	Intercept 95% CI	R^2
U	5 and 4	1.01689	1.01689, 1.01690	-0.00430	-0.00436, -0.00424	0.998
U	4 and 3	1.07440	1.07438, 1.07442	-0.02172	**-0.02191, -0.02153**	**0.992**
V	5 and 4	1.01926	1.01926, 1.01926	0.00001	0.00000, 0.00001	0.999
V	4 and 3	1.00664	1.00664, 1.00664	0.00006	0.00005, 0.00006	0.998
W	5 and 4	0.99038	0.99038, 0.99038	0.00008	0.00007, 0.00008	0.998
W	4 and 3	0.96532	0.96532, 0.96532	0.00020	0.00018, 0.00021	0.985
P	5 and 4	0.99908	0.99908, 0.99908	-0.00016	-0.00019, -0.00014	0.996
P	4 and 3	1.02747	1.02747, 1.02747	-0.00010	-0.00012, -0.00009	0.991
KE	5 and 4	0.97171	0.97171, 0.97171	0.00000	-0.00001, 0.00001	0.989
KE	4 and 3	0.97286	0.97286, 0.97286	0.00000	-0.00006, 0.00006	0.944
E	5 and 4	**0.72313**	0.72313, 0.72313	0.00000	-0.00033, 0.00034	0.998
E	4 and 3	**0.79246**	0.79246, 0.79246	0.00000	-0.01046, 0.01046	0.999

Table 3.7 Fraction of numerical predictions within the indicated experimental uncertainty (σ_m) for monotonically convergent locations, regardless of order of accuracy. Uncertainty for the numerical simulation considers the GCI, GCI plus 1 standard deviation of position uncertainty (GCI +/- σ_p), and GCI plus 3 standard deviations of position uncertainty (GCI +/- $3\sigma_p$); n = the number of locations that displayed monotonic convergence for the indicated degree of freedom.

	Degree of Freedom	Experimental confidence based on replicate error (σ_m)		
		Mean +/- σ_m	Mean +/- $2\sigma_m$	Mean +/- $3\sigma_m$
Numerical confidence based on GCI and +/-0.5mm positioning error variability (σ_p)	**U** (n = 117)			
	GCI	**0.17**	**0.36**	**0.54**
	GCI +/- σ_p	0.19	0.39	0.57
	GCI +/- $3\sigma_p$	0.24	0.41	0.59
	V (n = 115)			
	GCI	**0.62**	**0.77**	**0.82**
	GCI +/- σ_p	0.66	0.78	0.85
	GCI +/- $3\sigma_p$	0.72	0.80	0.89
	W (n = 281)			
	GCI	**0.04**	**0.06**	**0.12**
	GCI +/- σ_p	0.04	0.07	0.12
	GCI +/- $3\sigma_p$	0.05	0.08	0.13
	KE (n = 158)			
	GCI	**0.03**	**0.03**	**0.03**
	GCI +/- σ_p	0.80	0.80	0.80
	GCI +/- $3\sigma_p$	0.80	0.80	0.80

Table 3.8 Regression statistics for measured versus simulated velocity, for the equation: Numerical = slope (Measured) + intercept.

Degree of Freedom	Slope	95% CI for Slope			Intercept	95% CI for Intercept			R^2
U	1.16194	1.16192	,	1.16196	-0.01301	-0.01344	,	-0.01257	0.906
V	1.13796	1.13796	,	1.13796	0.00291	0.00245	,	0.00336	0.898
W	1.11489	1.11489	,	1.11489	-0.02590	-0.02665	,	-0.02515	0.836
All 3	1.14266	1.14266	,	1.14266	-0.01118	-0.01134	,	-0.01102	0.972

Table 3.9 Particle aspiration fraction comparison. Simulated releases occurred at (-1.523, 0 to 0.004636, 0.3685) m. The maximum capture efficiency for each of the three methods is provided in bold.

Particle Diameter (μm)	Aspiration Fraction		
	Experimental	Laminar Simulations	Turbulent Simulations
51.5	0.00010	0.0	0.015
54.5	0.00022	0.0	0.081
57.5	0.00049	**1.0**	**0.118**
60.5	0.00114	0.0	0.038
63.5	0.00136	0.0	0.020
66.5	**0.00227**	0.0	0.0
69.5	0.00094	0.0	0.0

Figure 3.1 Geometry, coordinate system, and nomenclature used throughout this study

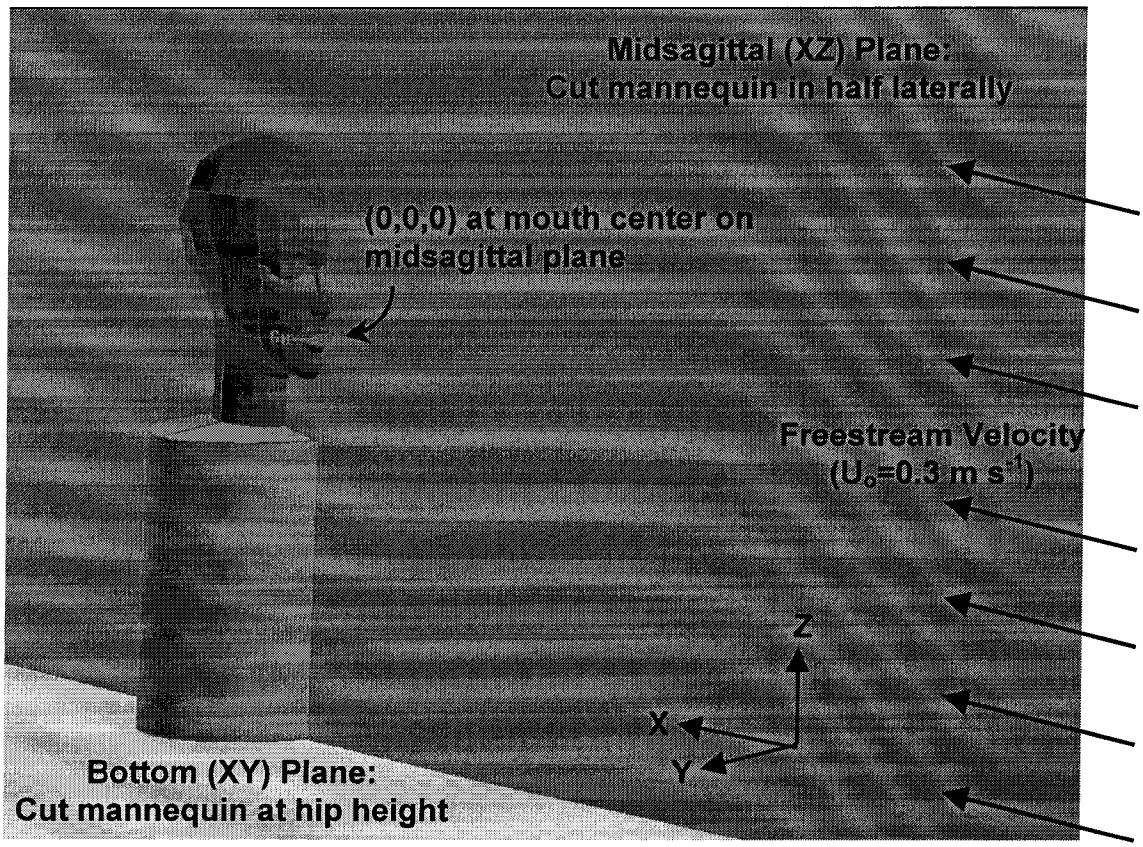

Figure 3.2 Illustration of coarsest mesh, N=159,900 (a) domain, (b) close-up of face (a)

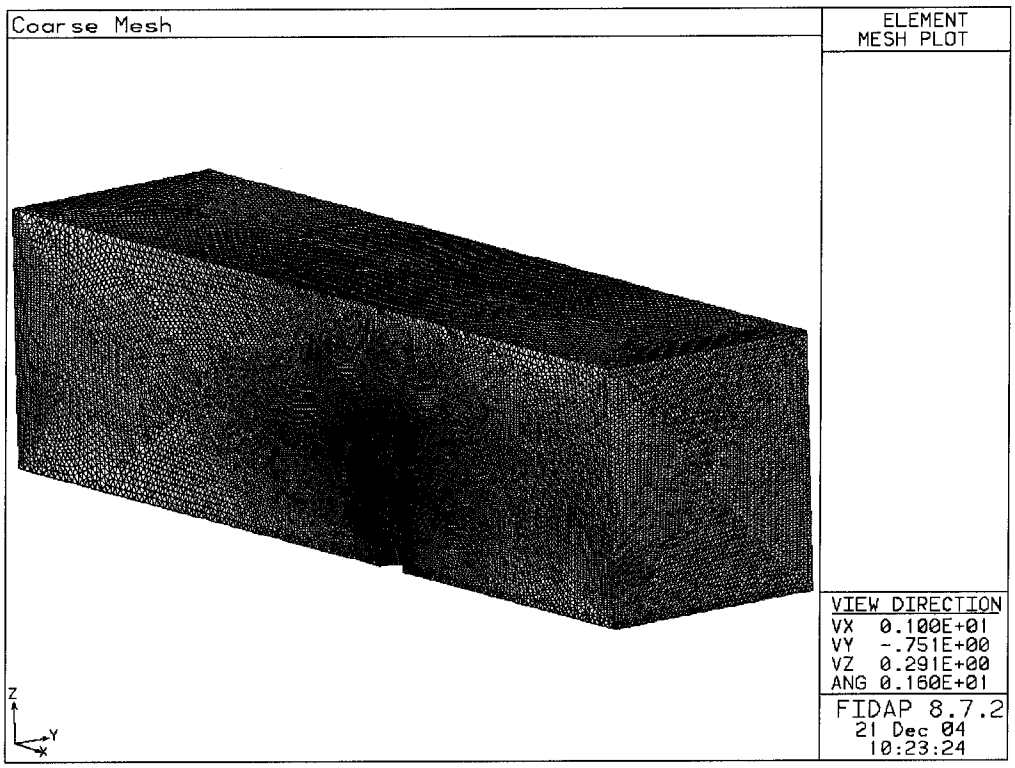

(b)

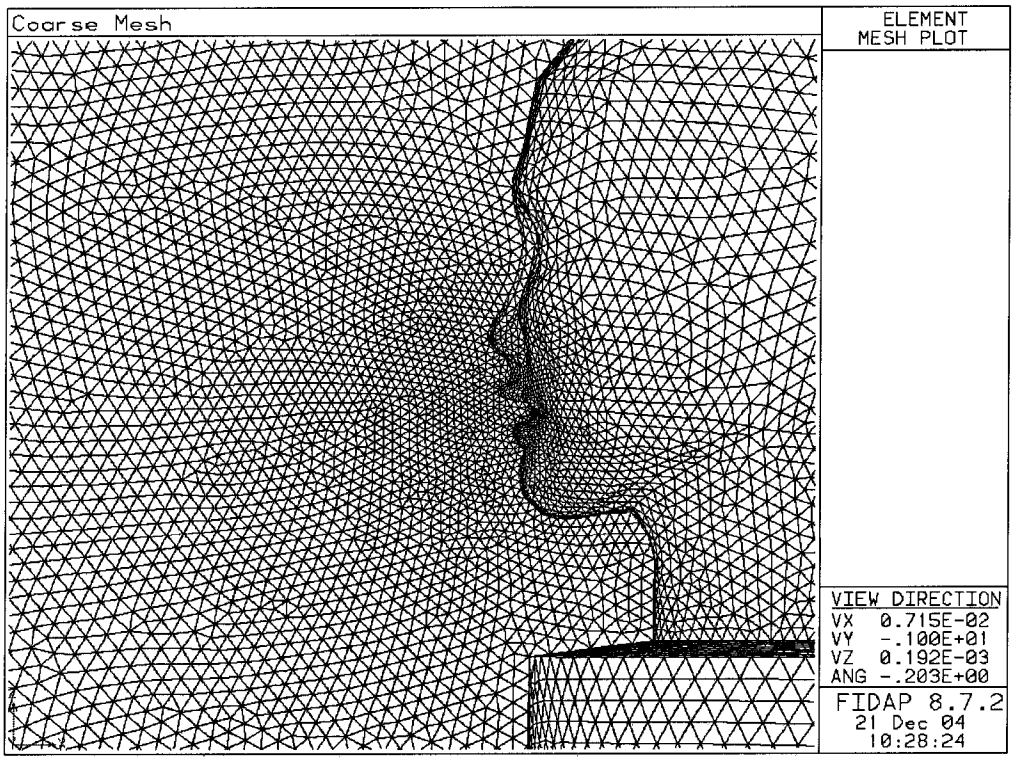

Figure 3.3 Comparison of numerically predicted streamwise velocity between middle and fine mesh at velocity measurement locations (GSE = 10^{-5})

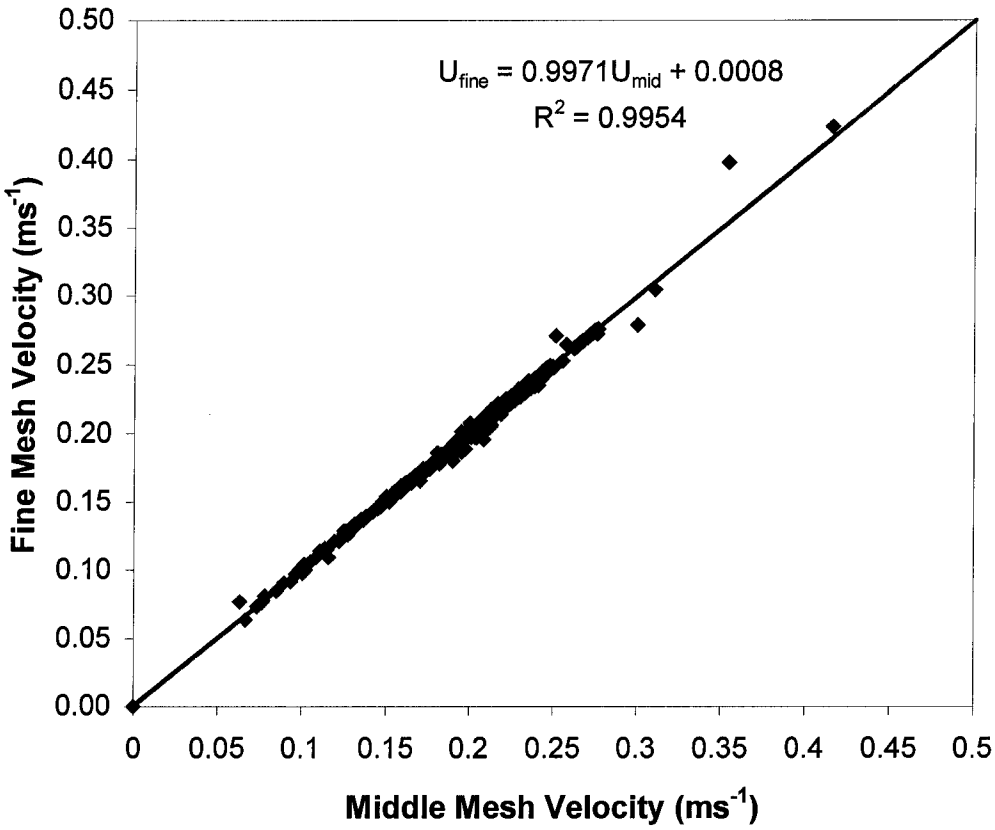

Figure 3.4 Comparison of numerically predicted and experimentally measured streamwise velocity (U)

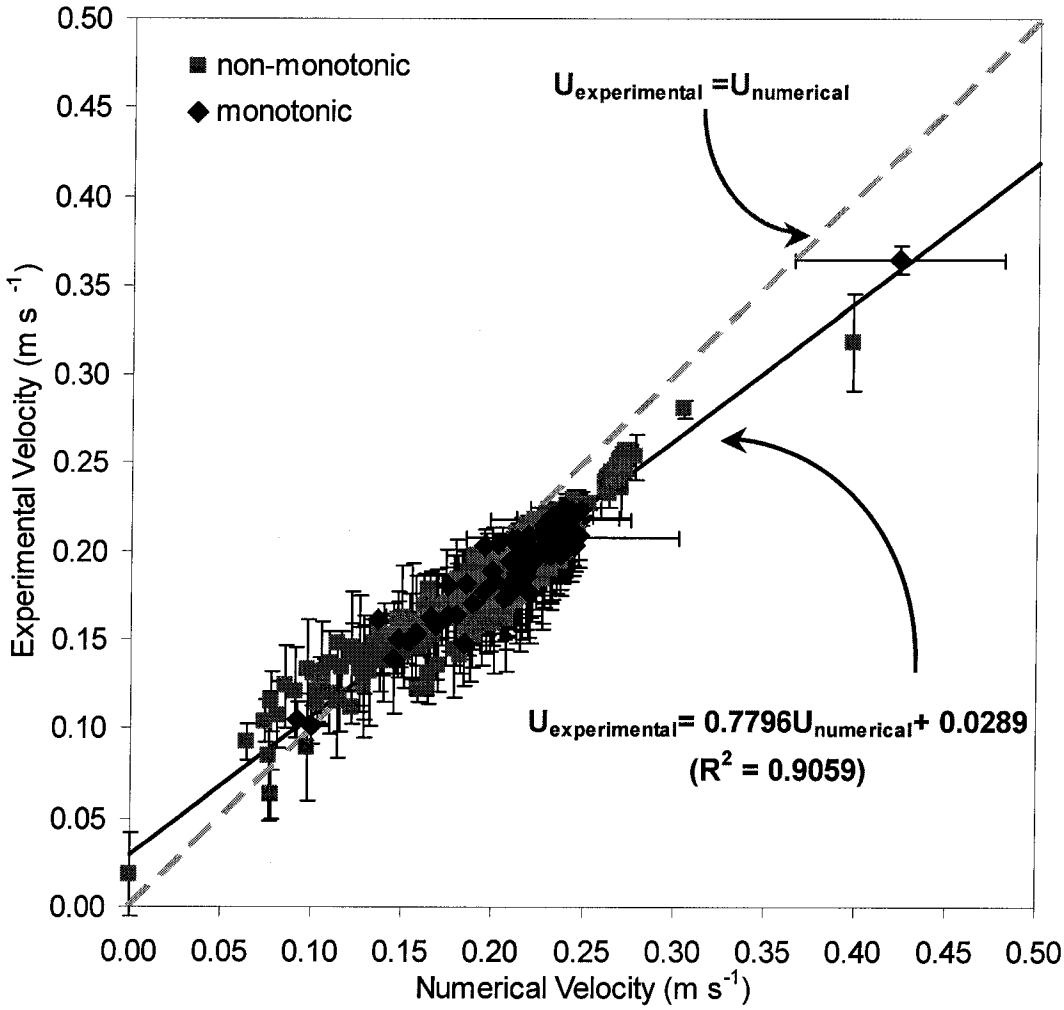

Figure 3.5 Comparison of numerically predicted and experimentally measured lateral velocity (V)

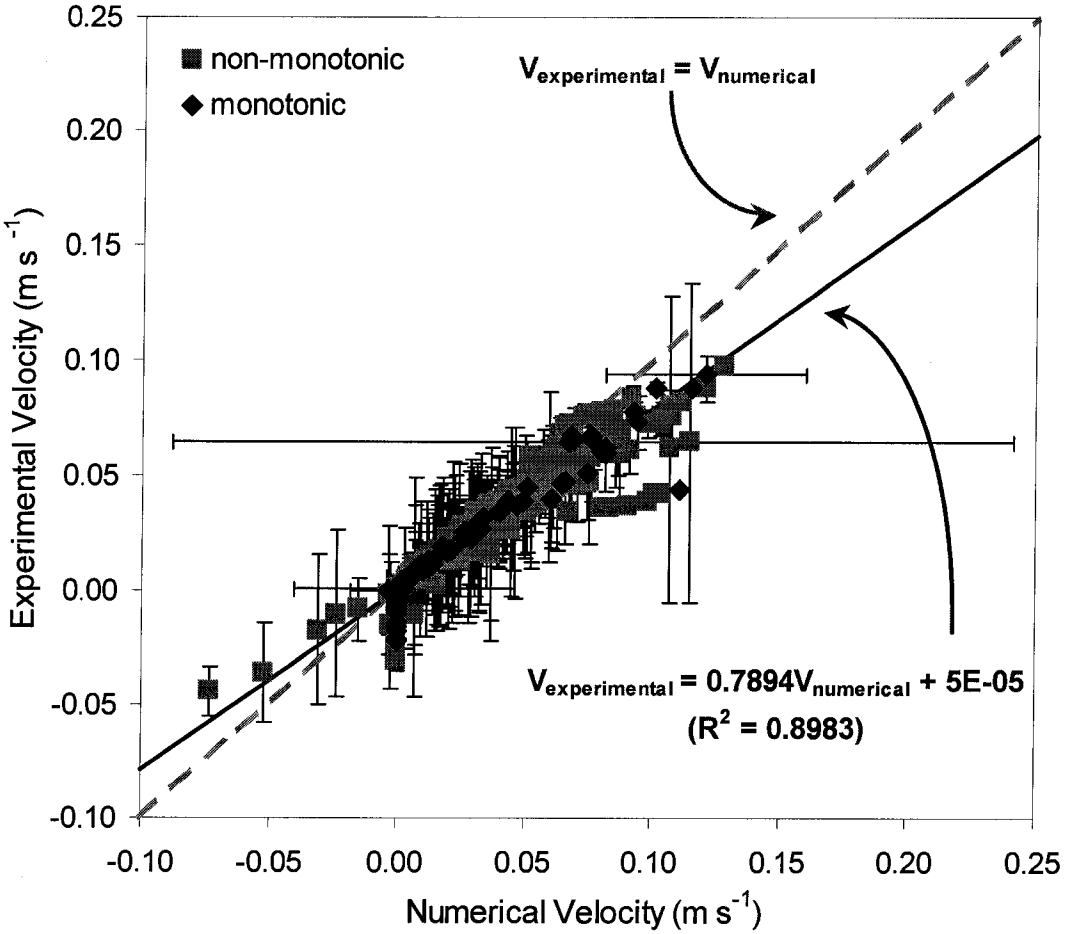

Figure 3.6 Comparison of numerically predicted and experimentally measured vertical velocity (W)

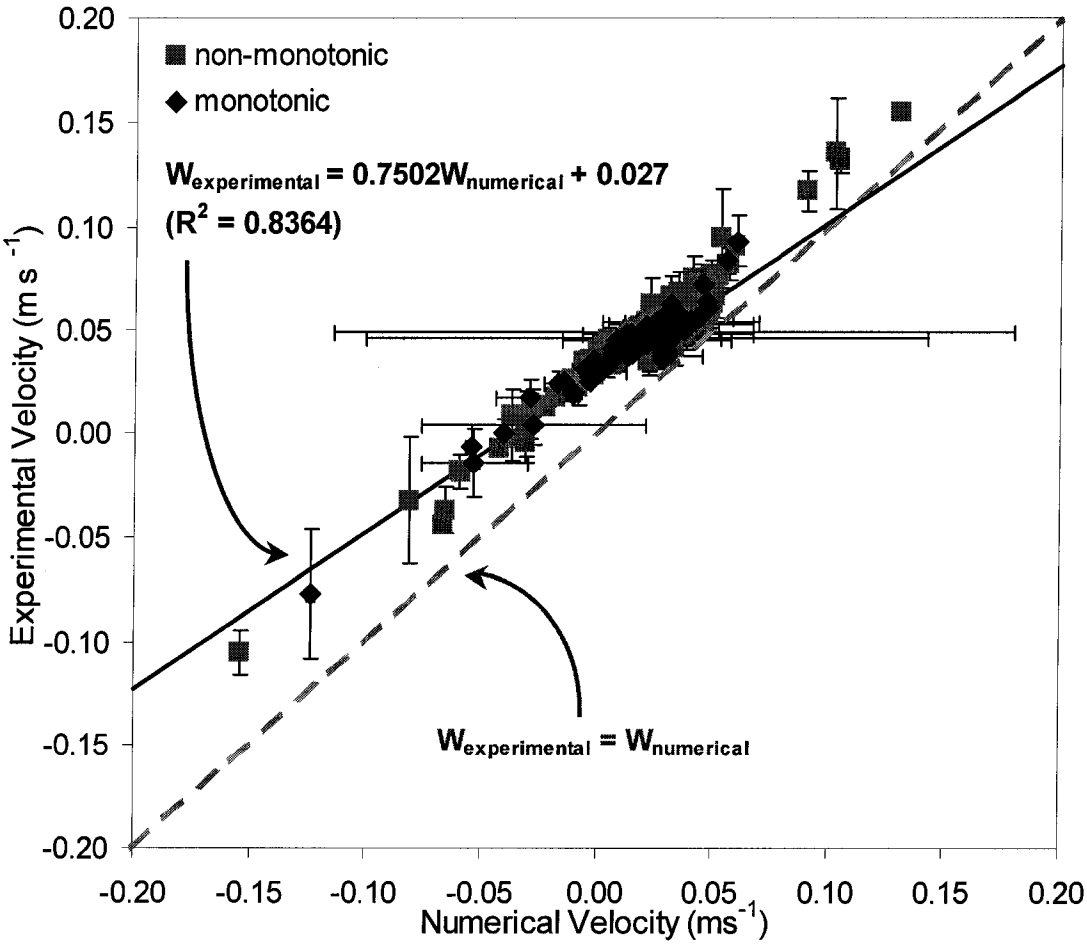

Figure 3.7 Velocity comparison using all velocity components

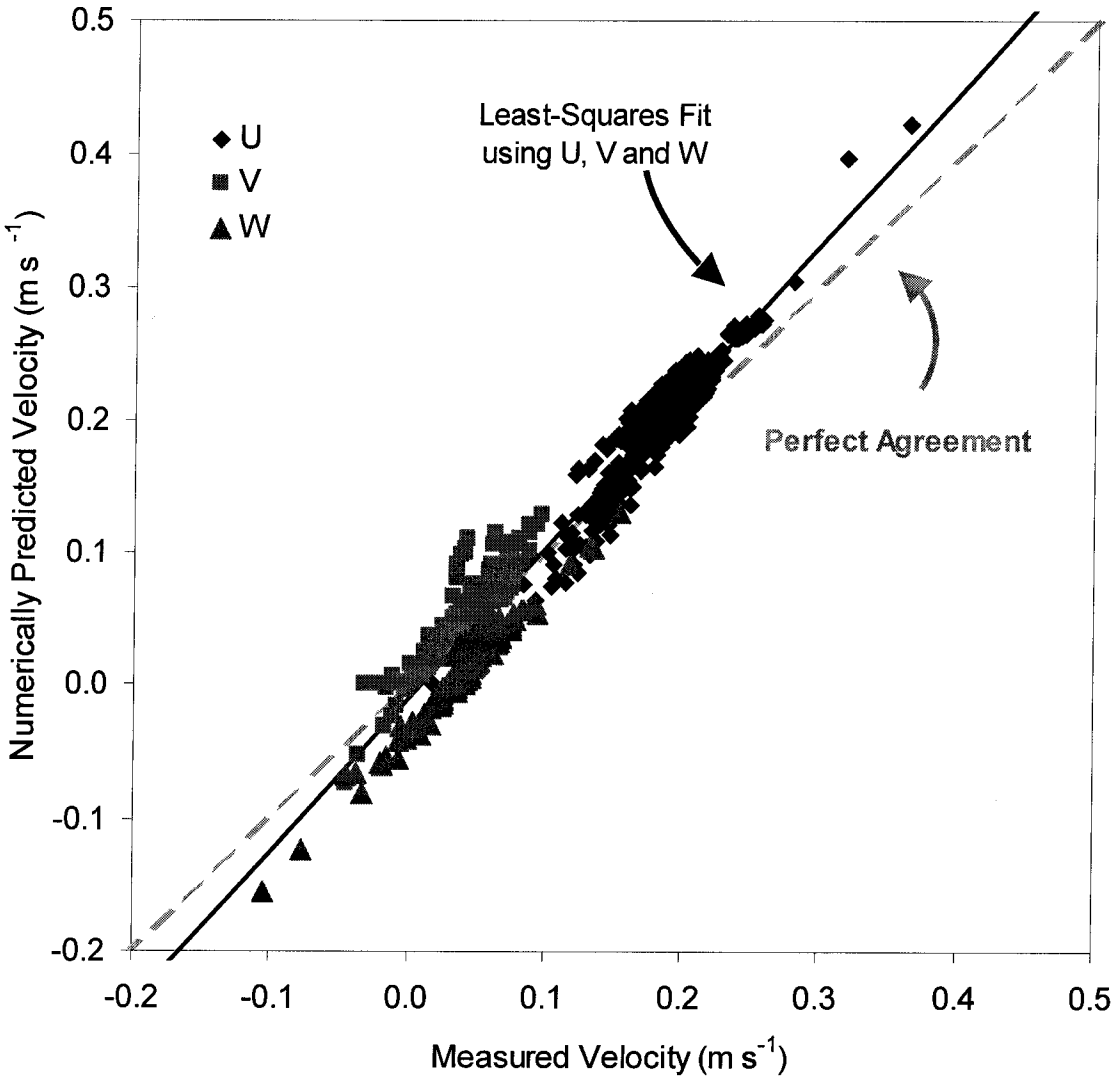

Figure 3.8 Comparison of numerically predicted and experimentally measured kinetic energy (KE)

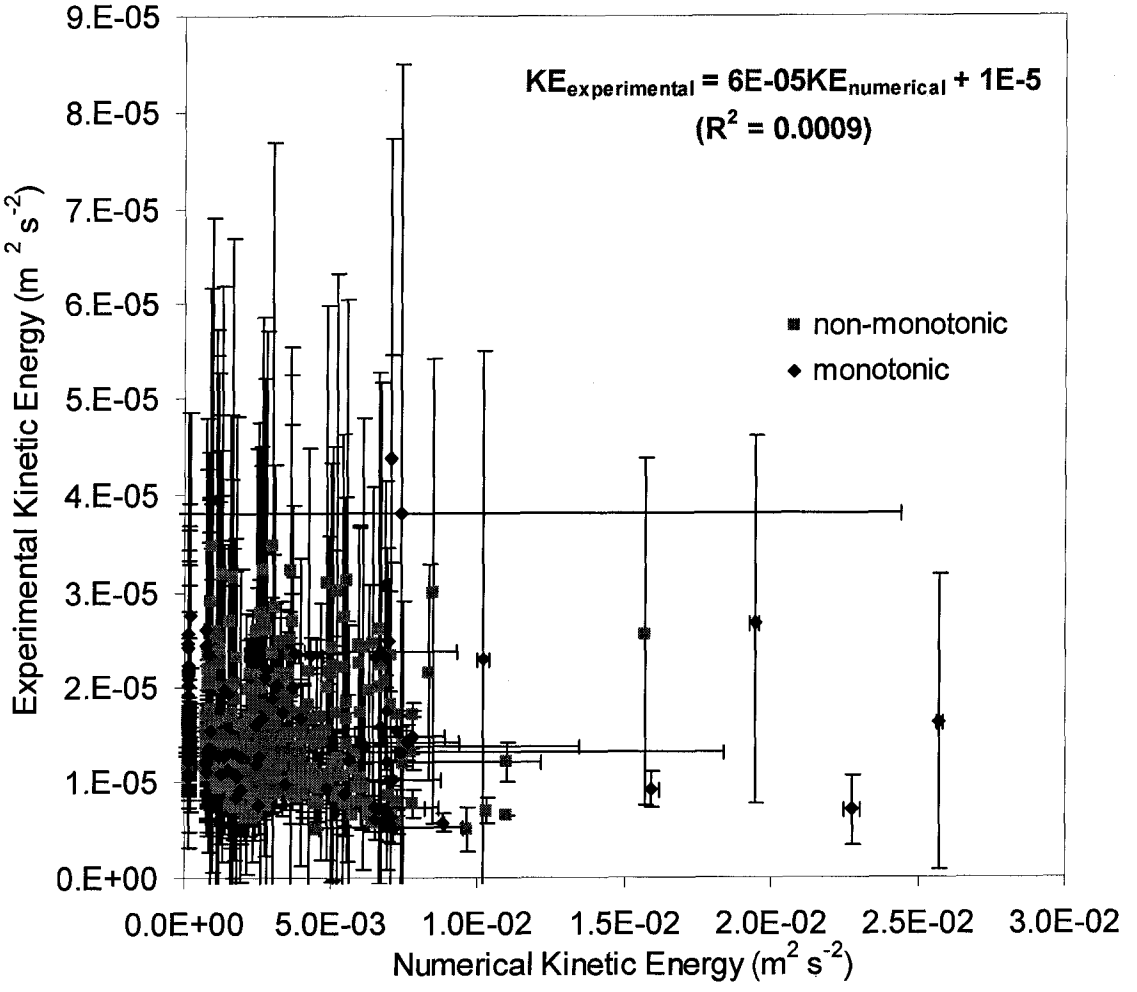

CHAPTER 4:
COMPUTATIONAL FLUID DYNAMIC INVESTIGATION OF PARTICLE INHALABILITY

4.0 Abstract

This study uses computational fluid dynamics to investigate particle aspiration at the low air velocities typical of occupational settings. A realistic representation of a human head on a simpler geometric torso was positioned facing the wind (0.2, 0.4 m s^{-1}), and breathing was simulated using constant inhalation (1.8, 4.3 m s^{-1}). Particles ranging from 0.3 to 116 μm were released from fixed positions, and laminar particle transport was simulated to locate the critical area upstream of the mannequin where particles were inhaled. Results from the 0.4 m s^{-1} freestream (Re = 3780) and 4.3 m s^{-1} inhalation rate compared well with results from the literature for smaller particles. For particles 68 μm and larger, simulations yielded smaller aspiration efficiencies than reported in experiments, and for all velocity conditions studied the aspiration efficiency curve dropped well below the 50% recommended by the ACGIH inhalability curve. While not simulating particle bounce directly, this study also provides an upper limit to particle inhalation due to secondary aspiration. This model is suitable for performing additional investigations at other orientations and breathing rates, which will be useful to provide inhalable particulate mass criterion for large particles in low velocity environments.

4.1 Introduction

Particle inhalability, also referred to as aspiration efficiency, is defined by the ratio of the inhaled particle concentration to the uniform freestream concentration. For particles with deleterious health effects independent of the regional deposition in the respiratory

tract, occupational exposure assessments require monitoring with equipment designed to match the human inhalability curve. In the U.S., the American Conference of Governmental Industrial Hygienists (ACGIH) defines the inhalable particulate mass collection efficiency (IPM) curve as:

$$IPM = 0.5\,(1 + e^{-0.06\,d}), \quad d \leq 100\ \mu m \tag{4.1}$$

where d is the aerodynamic diameter of the particle (ACGIH, 2004). As particle size increases above 50 μm, the IPM plateaus at 50%.

The development of this criterion began with experimental wind tunnel studies (Ogden and Birkett, 1977, 1978; Vincent and Armbruster, 1981; Armbruer and Breuer, 1982; Vincent and Mark, 1982; Vincent *et al.,* 1990; and others). These studies were typically conducted at a freestream velocity of 1 m s^{-1}or greater. With the recent understanding that mean occupational air velocities are 0.3 m s^{-1}, with a mode of 0.05 m s^{-1} (Baldwin and Maynard, 1998), the IPM curve required additional investigation at lower velocities. Kennedy and Hinds (2002) performed wind tunnel experiments using cyclical breathing at freestream velocities of 0.4 m s^{-1}, approaching the occupational mean. Particles greater than 116 μm could not be investigated due to particle suspension problems. Experiments requiring uniform particle suspension at lower velocities would yield similar problems for a wider range of particle sizes.

Numerical simulations of particle aspiration have been conducted using simple geometric surrogates, particularly cylinders (Dunnett and Ingham, 1986, 1987; Ingham and Hildyard, 1991; Chung and Dunn-Rankin,1992), a rounded-top cylinder (Erdal and Esmen, 1995), and a sphere (Dunnett and Ingham, 1988). However, Anthony *et al.* (2005) indicated that a simple geometric cylinder over-aspirates particles when compared to an anatomical mannequin, particularly in the facing-the-wind orientation with continuous inhalation. This finding confirmed the hypothesis from Dunnet and Ingham (1988) that in some flow conditions the facial features could create a significant effect on fluid flow and particle transport.

This study uses computational fluid dynamics to investigate particle aspiration at the low air velocities typical of occupational settings. The verification and validation of the underlying fluid flow field are detailed elsewhere (Anthony and Flynn, 2005). Although the kinetic energy was not validated with the standard *k*-epsilon turbulence model,

laminar particle simulations avoid this problem. For this study, laminar particle transport simulations were conducted to determine the critical upstream area through which particles were aspirated.

The goals of this study are to validate the particle trajectory simulations with published literature using the low velocity data from Kennedy and Hinds (2002), and to provide additional information for the IPM sampling criterion for large particles in low velocity environments.

4.2 Aspiration Theory

The fundamental definition of aspiration efficiency is the ratio of aspirated particle concentration (C) to the ambient freestream particle concentration (C_o):

$$A = C / C_o. \tag{4.2}$$

The aspirated concentration is the number of particles inhaled into the mouth (N_m) divided by the volume of air inhaled. This latter term is expressed as the product of the mouth area (A_m), the average velocity into the mouth (U_m), and time (t):

$$C = N_m / (A_m \ U_m \ t). \tag{4.3}$$

Experimental and numerical aspiration studies assume a uniform particle concentration across the wind tunnel: C_o does not vary spatially upstream of the inhaling human, where the velocity field is unaffected by the presence of the person. Over this upstream cross-sectional area, the particle concentration is the ratio of the number of particles in the freestream, N_o, to the volume of air through the cross-sectional area, which is the product of wind tunnel cross-sectional area (A_w), the average velocity through the cross-section (U_o), and time (t):

$$C_o = N_o / (A_w \ U_o \ t). \tag{4.4}$$

Rather than simulating particle releases that are uniformly distributed across the entire cross-section of the wind tunnel, numerical resources can be focused on the region of the wind tunnel where particles are actually aspirated. For a given particle size, there is a finite area upstream of the breathing person where particles are inhaled: this area is the critical area, A_c. A person will aspirate all particles contained within this area. Outside of this area, particles in the freestream will either impact on or bypass the person. The average velocity normal to the critical area is designated as the freestream critical

velocity, U_c. Thus, the concentration of particles through this area is calculated using the number of particles within this area, N_c:

$$C_o = N_c / (A_c \ U_c \ t). \quad (4.5)$$

The values of C_o from equations (4.4) and (4.5) must be identical to uphold the uniform particle concentration assumption. By substitution, aspiration efficiency becomes

$$A = C / C_o = [N_m / (A_m \ U_m \ t)] / [N_c / (A_c \ U_c \ t)]. \quad (4.6)$$

By locating the critical area where all particles are aspirated, the number of particles within the area (N_c) equals the number of inhaled particles (N_m), thereby equation (4.6) is reduced to:

$$A = [A_c \ U_c] / [A_m \ U_m]. \quad (4.7)$$

Equation (4.7) provides the definition of aspiration efficiency used in numerical studies. The mouth area remained constant throughout this study, and the inhalation velocity (U_m) and freestream velocity (U_o and, therefore, U_c) were varied by test condition. Particle simulations were performed to determine the values of A_c and the associated freestream critical velocity, U_c.

4.3 Methods

4.3.1 Fluid Flow and Particle Simulation

Geometry from earlier small-scale experiments and velocity simulations (Anthony and Flynn, 2005) was scaled to full-human size. The geometry was scaled by a factor of 1.5, and the Reynolds numbers were matched to one of the test conditions studied here. In addition, a more dense mesh at the mouth orifice was needed to achieve iterative convergence for the full-scale system. Figure 4.1 provides an illustration of the simulated geometry, where the coordinate system originates at the center of the mouth orifice. Lateral symmetry was assumed, so that only the right half of the mannequin was represented in the computational domain. The top of the domain extended 0.857 m above the mouth center, and the floor was 0.375 m below the mouth center, indicating truncation of the mannequin at approximately hip level, typical of wind tunnel study conditions. Relative to the center of the mouth, the computational domain extended 2.77 m upstream, 1.80 m downstream, and laterally 1.14 m.

The aspiration efficiency data reported by Kennedy and Hinds (2004) served as the experimental comparison for this study, and any references to experimental work refer to the 0.4 m s^{-1} freestream velocity data provided in their Figure 8. A comparison between test conditions of the experimental work and this computer simulation are provided in Table 4.1. The simulated head was 4% shorter and 6% wider than the experimental mannequin. To match the average flowrate of the cyclical breathing pattern in the experimental work, an average mouth velocity of 4.33 m s^{-1} was assigned to the comparable simulation (20.8 Lpm inhaled over 30 seconds of a 1 minute period through the 1.6 cm^2 mouth opening).

Three sets of velocity conditions were explored to investigate the relationship between aspiration efficiency and both freestream and inhalation velocities. The condition matching the published experimental work was 0.4 m s^{-1} freestream with 4.33 m s^{-1} inhalation velocity, yielding a velocity ratio ($R = U_o/U_m$) of 0.092. The velocity conditions matching the Reynolds numbers in the experimental work of Anthony *et al.* (2005) were also studied, using a freestream velocity of 0.2 m s^{-1} and inhalation velocity of 1.81 m s^{-1} ($R = 0.11$). A third velocity condition matching the low freestream and higher inhalation velocity conditions ($U_o = 0.2$ m s^{-1}, $U_m = 4.33$ m s^{-1}, $R = 0.046$) was also investigated to examine the interaction of breathing and freestream velocities. Given the mouth dimensions in this study, the lower and higher inhalation velocities are equivalent to the mean velocities associated with at rest (7.5 Lpm minute volume) and moderate (18 Lpm) cyclical breathing rates, respectively.

Fidap v. 8.7.2 (Fluent, Inc., Lebanon, NH) was used to conduct the computational study. Details of the fluid flow field simulation are provided elsewhere (Anthony and Flynn, 2005), but key conditions are provided here, for clarity. The standard *k*-epsilon equations were solved, using the Boussinesq constitutive relationship to model Reynolds stresses, with a segregated solver, pressure projection, and an element-Reynolds number relaxation scheme. Streamline-upwinding was used to stabilize the convective term. The iterative solvers for the linear systems were conjugate gradient squared and conjugate residual methods. A ratio of eddy viscosity to laminar viscosity of 10 was assigned, typical of wind tunnel studies, and a turbulence intensity of 8% was used. With identical geometries and mesh densities, fluid flow simulations were conducted for each of the

three velocity conditions. Six degrees of freedom (U_x, U_y, U_z, pressure, kinetic energy, and dissipation) were solved on three sequentially refined meshes to an iterative convergence tolerance of 10^{-5}. Mesh convergence was examined for the three velocity conditions using local mesh convergence ratios, discussed by Roache, 1998:

$$R_2 = \| \varepsilon_{mid,fine}\|^2 / \|\varepsilon_{coarse,mid}\|^2$$

where $\|\varepsilon\|^2 = (\Sigma \varepsilon_{j,k}^2)^{0.5}$.

The term $\varepsilon_{j,k}$ is the difference between the coarser (j) and finer (k) mesh level values for a given degree of freedom. Mesh convergence is indicated when local R_2 are less than one for all degrees of freedom.

Solving particle transport equations after solving the fluid flow field required the reasonable assumption that interfacial forces between the air and particles were negligible. Particle transport calculations were conducted on the middle mesh because the computational memory allocated by Fidap was insufficient on the densest meshes. Relative L_2 error norms between the middle and finest meshes ranged from 0.003 (U_x) to 0.096 (U_y) for velocity components, indicating small relative differences in velocity magnitudes between these meshes.

Particle momentum was described by equation (4.8):

$$du_i^P / dt = (u_i - u_i^P)/\tau + (\rho_p - \rho)\, g_i / \rho_p + f_i^P \qquad (4.8)$$

where

u_i^P = particle velocity

u_i = fluid velocity

ρ_p = particle density

ρ = fluid density

f_i^P = forces acting on the fluid

τ = particle relaxation time, given by

$\tau = 4\rho_p d_p^2 / (3\mu C_D Re^P)$

μ = fluid viscosity

d_p = particle diameter

Re^P = particle Reynolds number = $d_p |u_i - u_i^P| / \mu$

C_D = drag coefficient (a function of Re)

The implicit backward Euler method was used to solve equation (4.8). This is a first-order accurate method, selected for its stability over the range of particles to be investigated. Sensitivity to the time step and number of iterations allowed per time step were investigated to ensure convergence. Simulations used a time step of 5×10^{-5} seconds, where no difference in particle termination locations was observed in replicate trials. Fidap's default of a maximum of 10 iterations within a time step was sufficient.

Particle simulations were performed for the 8 particle sizes reported by Kennedy and Hinds (2002): 7, 17, 22, 37, 52, 68, 82 and 116 μm diameters of unit density (1 g/cm^3). In addition, smaller 0.3 μm particles were investigated as their trajectories should closely follow the airflow and allow for an investigation of the streamlines. Calculations used generalized Stokes drag, and buoyancy was included to account for gravitational forces.

4.3.2 Critical Area Determinations

Release locations for all but the largest particle size were 0.75 m upstream of the inhaling mannequin (X = -0.75 m). This distance was more than 4 head-diameters upstream of the human form, sufficient to ensure negligible bluff-body effects on the freestream (Chung and Dunn-Rankin, 1997). Gravitational settling of the 116 μm particles in the 0.2 m s^{-1} freestream required releases closer to the human form (0.4 m upstream), but these locations were above the head where the influence of the human form was also inconsequential.

To simulate the uniform particle concentration assumption, initial velocity was assigned to particles at the point of release. The initial streamwise particle velocity was set to the freestream velocity at the release location. The initial vertical particle velocity included both the vertical freestream component at the release location and the terminal settling velocity.

The release plane was vertical and normal to the main direction of flow: that is, X was constant at -0.75 m for a given critical area investigation. To identify the upstream locations that defined the critical aspiration area, particle releases were simulated at sequential lateral (Y) locations. For a given Y, 20 particles were released along a 1 cm line extending in the vertical (Z) direction. Along this line, some particles entered the

mouth and other particles did not. The initial position of the last particle to enter the mouth and the next particle that did not enter the mouth were recorded. For example, twenty 52-μm unit density particles were released at Y = 0 m from Z = 0.1375 to 0.1275 m. The particle released at Z = 0.1328 m was inhaled, but the particle released at Z = 0.1333 m was intercepted by the upper lip and was not inhaled. The value of Z = 0.1328 m defined the upper bound of the critical area. At the same Y, finding the last particle to cross into the mouth by passing the lower lip identified the lower bound of the critical area. Similar particle releases were repeated at a lateral distance 0.00025 m away from the last position ($Y_{i+1} = Y_i + 0.00025$ m). This process was repeated to identify the series of positions where particles just entered the mouth, defining the upstream area within which all particles were aspirated, *i.e.*, the critical area (A_c). The size of the critical area was determined by summing the areas of rectangles defined by upper ($Z_{U,i}$) and a lower ($Z_{L,i}$) vertical coordinate for a given Y_i, using the following equation:

$$A_c = \sum_{i=1}^{N} 0.5\,(Y_{i+1} - Y_{i-1})\,(Z_{U,i} - Z_{L,i}) \qquad (4.9)$$

where

N = the total number of Y positions where particle inhalation was observed

Y_i = the lateral coordinate of the i^{th} position

$Z_{U,i}$ = the upper vertical particle release location associated with Y_i where a particle is inhaled

$Z_{L,i}$ = the lower vertical particle release location associated with Y_i where a particle is inhaled

The particle release method resulted in a vertical distance of 0.00052 m between the initial locations of the inhaled and the adjacent non-inhaled particle. Critical areas were calculated for the positions where all particles were inhaled and the slightly larger area that included the next particle that was not inhaled. The average of these two areas provided the critical area for a given test condition, with uncertainty assigned as the difference between the average and the inhaled particle's critical area. Using this method, the maximum aspiration uncertainty was +/- 1.4% over all particle sizes and velocity conditions.

Additional uncertainty in the definition of critical area was considered by investigating particle deposition and bounce. The critical area discussed above is referred to as the "through orifice" critical area, as all particles included in this determination passed between the lips and into the rounded rectangular orifice, directly into the mouth. In some simulations, particles deposited on the internal surfaces of the lips prior to reaching the mouth orifice. Because the location of the mouth orifice recessed behind the lips was somewhat arbitrary, it was prudent to include particles depositing within the lips in the determination of the simulated aspiration efficiency. The associated critical area designated as "between lips" reflects where upstream particles passed through the orifice or deposited on the inside lip surface. As will be discussed later, these designated areas are the basis of aspiration efficiency determinations, defining the inhalable particle curves for this study.

Although particle bounce was not investigated directly, simulations were conducted to determine where particles moved toward the mouth but terminated on the face. These particles are associated with the outer layer of what Dunnett and Ingham (1987) call the "spring onion" shape that describes the approaching path lines where particles moved toward the mouth. Particles released just outside this critical area diverged from the inhaled trajectories and moved away from the mouth. Because of the complexity of the facial features, particles near the edges of the volume containing these path lines moved toward the mouth. However, they were not inhaled because they either deposited on the outer lip surfaces or were numerically trapped in the boundary layer. Although particles terminating here may contribute to secondary aspiration via particle bounce, they were not inhaled during these simulations because they did not terminate between the lips. The critical areas associated with particles traveling within this path-tube are referred to as "directed toward mouth" and provide the maximum limit of aspiration efficiency.

4.4 Results

4.4.1 Fluid Flow Field Validation

Table 4.2 provides a summary of the mesh convergence ratios for the three meshes, at locations close to the head (636 locations, $-0.15 \leq X < 0$ m) and farther away (2533 locations, $-2.4 \leq X < 0$ m). Where the local R_2 is less than unity, the solutions are

generally converging and uncertainty can be evaluated. Results are similar to what was found in earlier small-scale investigations with these mesh densities: convergence was achieved near the head of the mannequin, as indicated by the mesh convergence ratios in the "close" region but was less well demonstrated farther upstream, indicating further mesh refinement needs near the wind tunnel entrance.

4.4.2 Critical Areas

Given reasonable convergence near the head of the inhaling human form, particle aspiration simulations were performed using the three solved fluid flow fields. Critical areas were determined for the three criteria (through orifice, between lips, and directed toward mouth). Figure 4.2 illustrates the locations and shapes of critical areas associated with all particles that passed between the lips and were considered inhaled. These areas represent half of the critical area, as simulated. To accommodate all particle sizes on these graphs, the scale of the vertical axis is compressed. Figure 4.3 illustrates the uncompressed shapes of the critical areas associated with particles that terminate between the lips for 7, 22, and 82 μm particles. The shapes of the critical areas are taller than they are wide, similar to the egg-shaped limiting particle trajectories described by Dunnett and Vincent (2000) who simulated aspiration efficiency associated with a sphere.

The mouth extended laterally 0.0123 m from centerline, and the width of the critical areas extend beyond the mouth width only for particles smaller than 68 μm for all velocity conditions investigated. Therefore, suction affected the width of the critical area for the smaller range of particle sizes.

Near the midsagittal plane (Y = 0 m), particles released upstream of the human form traveled toward the head but impacted on the surface of the nose or lips and were not aspirated. This impaction is illustrated by a reduction in critical area height near the centerline (Y=0 m). At the edges of these notched areas, the critical area has an irregular shape for smaller particles: small particles were affected more by the minute details of the facial features and in some locations could pass over smaller obstacles to be aspirated. For clarity, both the "notch" and irregular shapes for the 82 μm particle are highlighted in Figure 4.2(a). These irregular shapes were related to the shape and dimensions of the computational human form; likewise, great interpersonal variability would exist in the

real world. However, the contributions of these irregularly shaped portions of the critical areas were generally less than 1% of the overall critical aspiration area.

For larger particles, where gravitational settling dominated particle motion, suction was insufficient to move particles toward the mouth and between the lips. None of the 116 μm particles were transported through the mouth orifice or deposited between the lips for the low suction, low velocity condition (R = 0.11). At the low velocity, high suction condition (R = 0.046), a few particles passed into the mouth orifice (critical area = 1.05×10^{-6} m^2) and between the lips (1.50×10^{-4} m^2). At the higher freestream and higher suction (R=0.092), a larger critical area existed where particles passed into the orifice (1.59×10^{-5} m^2), and essentially an equal critical area existed where particles passed between the lips (1.26×10^{-4} m^2).

4.4.3 Aspiration Efficiencies

From the critical area data, aspiration efficiencies were calculated using equation (4.7). Results from the three definitions of critical area are presented in Table 4.3 along with the reference experimental data. The coefficients of variation for the three velocity ratios studied were below 5% for particles < 52 μm, indicating relatively little difference in aspiration efficiencies for the smaller particles. However, with larger particles, the aspiration efficiencies had greater dependence on the velocity conditions, even within the relatively small freestream range studied.

For the condition matching the experimental data (R = 0.092), agreement was within the reported experimental uncertainty for particles through 52 μm, as shown in Figure 4.4(a). However, simulations of larger particles yielded lower aspiration efficiencies than were reported experimentally. It is important to note that the simulations excluded particle bounce, but the comparative experimental work used solid aluminum oxide particles with a fiberglass mannequin, where bounce could have contributed to secondary aspiration. For this reason, the additional investigation of the "toward the mouth" area was included in the analysis. Figure 4.4(b) provides aspiration efficiencies based on this larger critical upstream area. While improving agreement with the larger particles, the simulations now significantly over-estimate the middle portion of the aspiration efficiency curve.

4.5 Discussion

4.5.1 Critical Area Definition Evaluation

For particle sizes ≤ 52 μm, an average of 1.3% difference in aspiration efficiencies were identified between the "through orifice" and "between lips definition." These differences are in the same range as aspiration efficiency differences between the studied velocities. Thus, for small particles, negligible difference existed between these two definitions of critical areas. As the particle size increased, more particles deposited on the inside surface of the lips, and the "between lips" critical area and the associated aspiration efficiency increased. The "between lips" criteria would over-estimate particle aspiration if deposition between the lips did not result in a bounce into the aspiration orifice. However, as discussed earlier, the location of the mouth orifice relative to the lips was not based on anatomical criteria, so the critical area of most relevance is that associated with particles passing between the lips. Thus, the "between lip" critical areas define the inhaled particles.

The aspiration efficiencies designated as "directed toward mouth" represent the upper bound of aspiration anticipated by the inhaling human. Here, the critical area includes both inhaled particles, as discussed above, as well as particles that traveled toward the inhaling mouth but which terminated on the outside of the lips. If these particles were allowed to bounce, their trajectories may be directed into the streamlines moving toward the mouth and may be aspirated. Particles released outside of these critical areas were directed away from the mannequin mouth surface, such as below the lower lip and directed downward or to the side of the mouth and directed around the head. Thus, any resulting bounce from these particles would likely be directed away from the mouth.

Some smaller particles depositing on the facial features within the "directed toward mouth" critical area may in fact be trapped within the numerical boundary layer and some fraction of them may contribute to primary aspiration. However, as the particle size increases, particles terminating on the lips are unlikely to enter the mouth without the benefit of particle bounce.

4.5.2 Comparisons Between Velocity Conditions

At conditions representative of occupational air velocities studied here, gravitational settling dominated large "inhalable" particle motion. Figure 4.5 illustrates path-tubes for small (7 μm) particle aspiration, and Figure 4.6 illustrates path-tubes for large (116 μm) particle aspiration. Particle trajectories were predominantly horizontal for the 7 μm particles, which were unaffected by gravity in each velocity condition studied, Figures 4.5(a) – 4.5(c). The larger critical streamtube associated with the lowest velocity ratio is visible in Figure 4.5(b).

For larger particles, gravity is the predominant force, and the trajectories are mostly downward, as illustrated in Figures 4.6(a) – 4.6(c) with 116 μm particles. Figure 4.6(a) illustrates that particles in the 0.4 m s^{-1} freestream velocity had more horizontal motion than in the 0.2 m s^{-1} freestream conditions. As such, particle releases for the 0.4 m s^{-1} freestream velocity condition in Figure 4.6(a) were at X = -0.75 m, but the 0.2 m s^{-1} freestream required particle releases closer to the mouth at X = -0.4 m. The large particles in the at-rest breathing simulation, Figure 4.6(c), were incapable of both passing the nose and upper lip and turning into the mouth to be inhaled; hence, zero aspiration was identified. As the breathing rate increased to 4.33 m s^{-1}, suction began to affect particle transport, illustrated by Figure 4.6(b) at the low 0.2 m s^{-1} freestream velocity as well as the higher 0.4 m s^{-1} freestream velocity in Figure 4.6(a).

The largest particle investigated was 116 μm. At the low freestream and low inhalation velocity condition, aspiration efficiency for 116 μm particles was 0%. Based on the shape of the curve in Figure 4.4(a), aspiration efficiency probably reaches 0% for particles smaller than 116 μm. For the two conditions with inhalation velocity of 4.33 m s^{-1}, the smaller freestream velocity (0.2 m s^{-1}) data indicated a sharper decrease in aspiration efficiency for large particles compared to the larger freestream velocity (0.4 m s^{-1}). In the latter case, particle trajectories were slightly more horizontal and the facial features had slightly less influence on the upstream critical areas, resulting in higher aspiration efficiencies. Extrapolation suggests that 0% aspiration efficiency would occur for a smaller particle size in the lower freestream, given the same inhalation velocity.

4.5.3 Comparison to Experimental Data

Fundamental differences between the wind tunnel studies of Kennedy and Hinds and these simulations included breathing patterns, slightly different head and mouth dimensions, particle bounce, and turbulent particle transport. The peak cyclical inhalation velocity for the experimental study was greater than the 4.33 m s^{-1} average used in the comparative set of steady-state simulations for this study. These short-duration peaks could contribute to increased aspiration of large particles that had difficulty moving into the region between the lips due to the dominance of gravitational settling relative to the convective forces associated with inhalation. Differences in head dimensions should have minimal effects on particle transport, although the size of the nose and lips relative to the location of the mouth orifice may affect aspiration. However, if these facial feature differences contributed significantly to aspiration efficiency differences between studies, the anthropometric variability of human facial features would be difficult to examine fully. Earlier studies identified that geometric surrogates over-aspirated particles compared to anatomical mannequins, and additional investigation of the significance of these facial dimensions is warranted.

Particle bounce simulations for the 116-μm particles under-predicted aspiration efficiency compared to Kennedy and Hinds experiments, but were within numerical and experimental uncertainties. For all other particle sizes, simulations of bounce yielded significantly larger aspiration efficiencies than Kennedy and Hinds measured. These results indicated that not all particles that terminated on the mannequin lips would bounce and result in secondary aspiration. As such, the critical areas defined by the path-tubes directed toward the mouth should only be used to provide an upper limit of aspiration efficiency. Actual simulations of particle bounce are necessary to test whether the critical area defined here is sufficient to describe bounce.

These simulations considered only laminar particle transport, ignoring the effects of turbulence. Significantly more computational resources would be required to ensure particle convergence with turbulent particle transport simulations. This work would require the investigation of larger critical areas coupled with a probabilistic term for particle aspiration to address the randomness of turbulent particle transport. For the low freestream/low inhalation velocity condition studied, turbulent simulations of large

particle aspiration may result in aspirated particles, where none were aspirated in laminar simulations. Additional research is required to examine the significance of turbulent particle transport on aspiration efficiency.

Potential sampling bias of large particles in low velocity air may also contribute to the disagreement between the experimental data and these simulations. Kennedy and Hinds provided good documentation on the temporal and spatial variability of particles in the wind tunnel, and the difficulties maintaining and measuring the reference concentrations of large particles in low velocity environments are well known. In experimental work, the assumption of uniform particle concentration is essential to conducting aspiration studies. With these human-scale simulations, the largest inhalation critical area was 13.76 cm^2, equivalent to a circle with a 2.1 cm radius. For the 116 μm particle, the smallest area through which particles were aspirated was 1.33 cm^2, equivalent to a 0.65 cm radius circle. Ensuring both spatially and temporally uniform particle concentrations on these small scales poses obvious experimental challenges.

Finally, concerns arise regarding particle transport into the isokinetic reference samplers for particles larger than 68 μm. These samplers were positioned laterally relative to the mannequin, with a horizontal alignment facing the freestream. However, motion for large particles in 0.4 m s^{-1} freestream is profoundly influenced by gravity. Numerical simulations revealed that trajectories were toward the mouth at an angle of 16° below the horizon for 68 μm particles, 22° for 82 μm particles and 38° for 116 μm particles. Isokinetic sampling theory indicates that alignment with the freestream and operation at the same sampling velocity as the freestream would yield 100% aspiration efficiency for these reference samplers. Confirmation of this at the nearly calm-air conditions of the wind tunnel for the large particles of interest has not been identified. If the horizontal alignment of the isokinetic samplers for these larger particles resulted in under-aspiration of the reference concentration, then higher aspiration efficiencies would be reported. Although this bias is consistent with the data presented here, additional investigation of such a hypothesis would be needed.

4.6 Conclusions

Aspiration efficiency of particles in low velocity environments has been investigated using CFD to simulate particle transport with a breathing human form. Particle releases upstream of the inhaling form required initial velocities equivalent to the freestream velocity and any additional downward velocity equal to the terminal settling velocity of the corresponding particle size. Aspiration efficiency was described with the upstream critical area defined as the location where all released particles terminate between the lips of the inhaling human form. Results from particles 52 μm and smaller compared well with experimental work of others, but simulations of larger particles yielded smaller aspiration efficiencies than have been published in wind tunnel studies. Differences may be associated with differences in facial features, turbulence, and breathing patterns, which require additional investigation.

Using a smooth-surfaced cylinder and cyclical breathing in 0.5 m s^{-1} freestream velocity, Erdal and Esmen (1995) indicated that aspiration efficiency would not go to zero for the particle range in this study. However, this study found particle transport around the facial features becomes difficult for large particles in low velocities. With at-rest breathing in 0.2 m s^{-1} velocity, typical of occupational environments, the aspiration efficiency of 116 μm particles was zero and rose to less than 10% at moderate breathing rates.

Although the results of this study are limited to the facing-the-wind orientation and a continuous inhalation simplification, the aspiration efficiencies predicted in low velocity conditions indicate that aspiration efficiency is less than the orientation-averaged ACGIH inhalable particulate mass criterion, which specifies that aspiration efficiency remains at 50% for particle sizes greater than approximately 50 μm. Additional numerical investigations of aspiration efficiencies at other orientations and higher breathing rates are recommended to further the development of an inhalable particulate mass criterion for occupational environments.

4.7 References

American Conference of Governmental Industrial Hygienists (2004). **TLVs and BEIs Based on the Documentation of the Threshold Limit Values for Chemical Substances and Physical Agents and Biological Exposure Indices.** ACGIH Worlkwide, Cincinnati, OH, 2004.

Anthony, TR, M.R. Flynn, and A.Eisner (2005). Evaluation of facial features on particle inhalation. *Ann. Occup. Hyg.* 49(2):179-193.

Anthony, T.R., and M.R. Flynn (2005). CFD Model for a 3-D Inhaling Mannequin: Verification and Validation. Submitted to *Ann. Occup. Hyg.*

Armbruster, L. and H.Breuer (1982). Investigations into defining inhalable dust. *Ann. Occup Hyg* 26: 21-32.

Baldwin, P.E.J. and A.D. Maynard (1998). A survey of wind speeds in indoor workplaces. *Ann. Occup. Hyg.* 42(5): 303-313.

Chung, I.P. and D. Dunn-Rankin (1992). Numerical simulation of two-dimensional blunt body sampling in viscous flow. *J. Aerosol Sci.* 23(3): 217-232.

Chung, I.P. and D. Dunn-Rankin (1997). Experimental investigation fo a two-dimensional cylindrical sampler. *J. Aerosol Sci.* 25: 935-955.

Dunnett, S.J. (1997). A numerical study of the flow field in the vicinity of a bluff body with aspiration oriented to the flow. *Atmospheric Environment* 31(22): 3745-3752.

Dunnett, S.J. (1999). An analytical investigation into the nature of the airflow near a spherical bluff body with suction. *J. Aerosol Sci.* 30(2): 163-171.

Dunnett, S.J. and D.B. Ingham (1986). A mathematical theory to two-dimensional blunt body sampling. *J. Aerosol Sci.* 17(5): 839-853.

Dunnett, S.J. and D.B. Ingham (1987). The effects of finite Reynolds number on the aspiration of particles into a bulky sampling head. *J. Aerosol Sci.* 18(5): 553-561.

Dunnett, S.J. and D.B. Ingham (1988). The human head as a blunt aerosol sampler. *J. Aerosol Sci.* 19(3): 365-380.

Dunnett, S.J. and J.H. Vincent (2000). A mathematical study of aerosol sampling by an idealised blunt sampler oriented at an angle to the wind: the role of gravity. *J. Aerosol Sci.* 31(10): 1187-1203.

Erdal, S. and N.A. Esmen (1995). Human head model as an aerosol sampler: calculation of aspiration efficiencies for coarse particles using an idealized human head model facing the wind. *J. Aerosol Sci.* 26: 253-272.

Ingham, D.B and M.L. Hildyard (1991). The fluid-flow into a blunt aerosol sampler oriented at an angle to the oncoming flow. *J. Aerosol Sci.* 22: 235-252.

Kennedy, N.J. and W.C. Hinds (2002). Inhalability of large solid particles. *J. Aerosol Sci.* 33: 237-255.

Ogden, T.L. and J.L. Birkett (1977). The human head as a dust sampler. In Halton, W.H. editor. *Inhaled particles IV: Proceedings of an international symposium organized by the British Occupational Hygiene Society.* Oxford: Pergamon Press. p. 93-105. ISBN 0080205607.

Ogden, T.L. and J.L.Birkett (1978). An inhalable-dust sampler for measuring the hazard from total airborne particulate. *Ann. Occup. Hyg.* 21: 41-50.

Roache, P.J. (1998). *Validation in Computational Science and Engineering.* Hermosa Publishers, Albuquerque, NM.

Vincent, J.H. and D. Mark (1982). Applications of blunt sampler theory to the definition and measurement of inhalable dust. *Ann. Occup. Hyg.* 26(1): 3-19.

Vincent, J.H. and L. Armbruster (1981). On the quantitative definition of the inhalability of airborne dust. *Ann. Occup. Hyg.* 24: 245-248.

Vincent, J.H., D. Mark, B.G. Miller, L. Armbruster, and T.L. Ogden (1990). Aerosol inhalability at higher windspeeds. *J. Aerosol Sci.* 21(4): 577-586.

Table 4.1 Dimensions and flow conditions.

Dimension	Simulation	Kennedy & Hinds (2002)
Head – half width (m)	0.0712	0.067
Head – height (m)	0.216	0.225
Mouth – half width (m)	0.0123	0.015
Mouth – height (m)	0.006	0.006
Mouth area- full (cm^2)	1.386	1.6
Mouth shape	Rounded-end rectangle	Ellipse
Freestream velocity ($m\ s^{-1}$)	0.4 (0.2)	0.4
Inhalation velocity ($m\ s^{-1}$)	4.33 (1.81)	4.33

Table 4.2 Mesh convergence ratios (R_2) for three velocity conditions at locations close to the head and farther upstream. Italicized numbers exceed unity and indicate non-convergence.

Degree of Freedom	$U_m = 4.33$ m s^{-1} $U_o = 0.2$ m s^{-1} (R = 0.046)	$U_m = 4.33$ m s^{-1} $U_o = 0.4$ m s^{-1} (R = 0.092)	$U_m = 1.81$ m s^{-1} $U_o = 0.2$ m s^{-1} (R = 0.11)
Close Locations (n=636)			
U_x (streamwise velocity)	0.672	0.727	0.688
U_y (lateral velocity)	0.574	0.674	0.636
U_z (vertical velocity)	0.483	0.545	0.583
Pressure	0.507	0.524	0.482
Kinetic Energy	0.787	0.590	0.442
Dissipation	0.846	0.612	0.447
Far Locations (n=2533)			
U_x (streamwise velocity)	0.629	0.703	0.626
U_y (lateral velocity)	*1.203*	*1.193*	*1.129*
U_z (vertical velocity)	0.643	0.729	0.632
Pressure	*1.110*	0.856	0.962
Kinetic Energy	0.906	*1.179*	0.810
Dissipation	0.751	0.648	0.759

Table 4.3 Aspiration Efficiency Results.

Particle size (μm)	$U_m = 4.33$ m s^{-1} $U_o = 0.2$ m s^{-1} (R = 0.046)	$U_m = 4.33$ m s^{-1} $U_o = 0.4$ m s^{-1} (R = 0.092)	$U_m = 1.81$ m s^{-1} $U_o = 0.2$ m s^{-1} (R = 0.11)	Mean	C.V.
Critical Area = Through Orifice					
0.3	87.9%	85.8%	86.3%	86.7%	0.012
7	90.3%	88.3%	88.0%	88.9%	0.014
17	90.9%	88.6%	88.2%	89.2%	0.016
22	91.0%	88.0%	87.7%	88.9%	0.020
37	89.4%	85.9%	84.9%	86.8%	0.027
52	87.1%	79.9%	78.5%	81.8%	0.056
68	78.0%	63.9%	59.5%	67.1%	0.144
82	53.5%	35.5%	26.9%	38.6%	0.352
116	0.1%	2.2%	0.0%	0.8%	1.648
Critical Area = Between Lips					
0.3	89.0%	88.0%	88.0%	88.3%	0.007
7	91.7%	90.0%	88.1%	89.9%	0.020
17	92.0%	90.3%	88.9%	90.4%	0.017
22	91.9%	88.6%	88.8%	89.8%	0.020
37	89.6%	86.7%	86.4%	87.6%	0.021
52	87.3%	81.6%	80.2%	83.0%	0.045
68	78.0%	66.7%	63.2%	69.3%	0.111
82	53.7%	48.9%	30.2%	44.3%	0.281
116	10.6%	17.4%	0.0%	9.3%	0.941
Critical Area = Directed Toward Mouth					
0.3	100.5%	99.0%	99.3%	99.6%	0.008
7	100.4%	99.6%	99.2%	99.7%	0.006
17	99.8%	98.9%	99.5%	99.4%	0.005
22	99.1%	98.2%	98.1%	98.5%	0.006
37	96.9%	95.9%	94.0%	95.6%	0.015
52	92.0%	92.2%	88.7%	90.9%	0.022
68	86.2%	86.4%	79.3%	84.0%	0.048
82	75.1%	77.4%	60.4%	70.9%	0.130
116	32.1%	45.8%	13.8%	30.6%	0.524
Kennedy & Hinds (2002) Figure 8					
0.3	-	-	-	-	-
7	-	100%	-	-	0.2000
17	-	96%	-	-	0.0833
22	-	92%	-	-	0.0870
37	-	80%	-	-	0.0625
52	-	74%	-	-	0.0946
68	-	75%	-	-	0.0667
82	-	60%	-	-	0.1333
116	-	52%	-	-	0.0769

Figure 4.1 Geometry of simulated human.

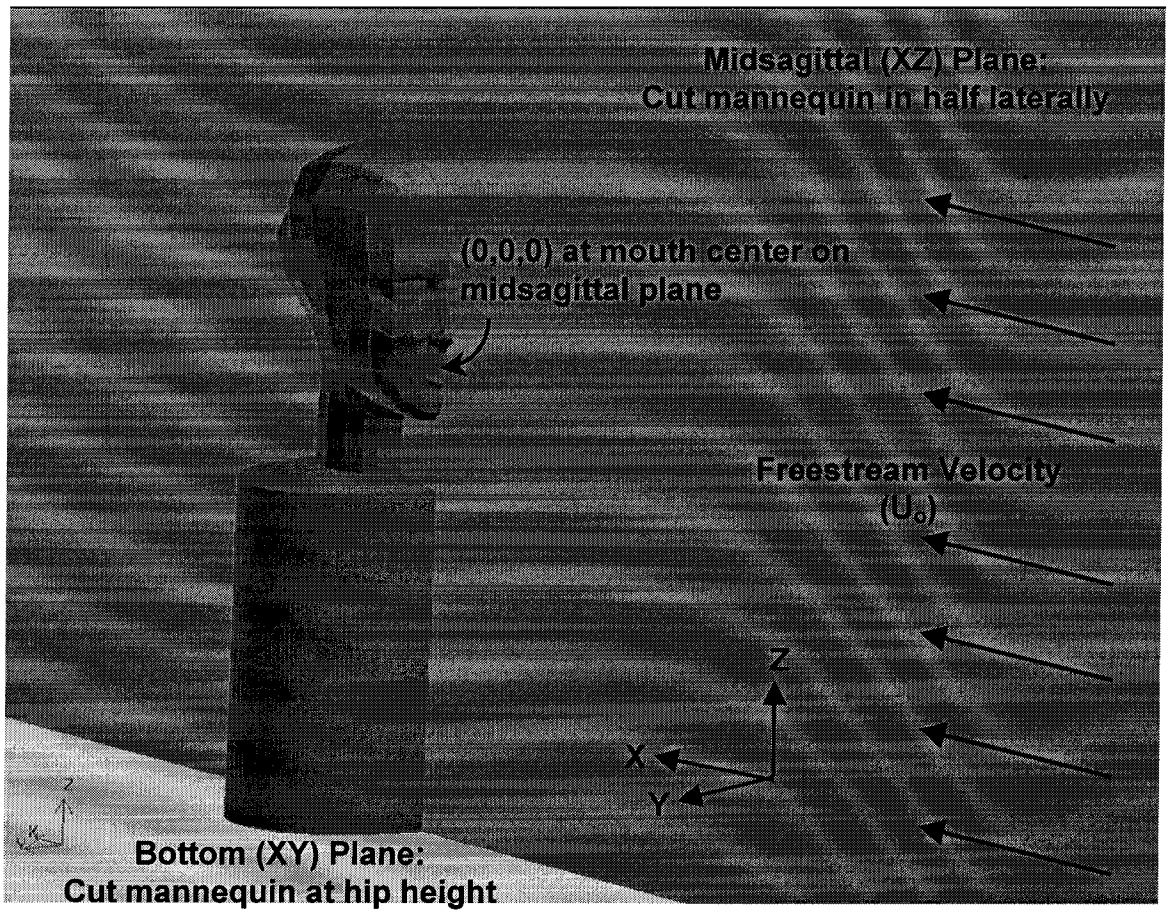

Figure 4.2 Critical areas (between lips) for (a) $U_m = 4.33$ m s^{-1}, $U_o = 0.4$ m s^{-1}, (b) $U_m = 1.81$ m s^{-1}, $U_o = 0.2$ m s^{-1}, (c) $U_m = 4.33$ m s^{-1}, $U_o = 0.2$ m s^{-1}. Note: different scales are used for horizontal and vertical axes.

4(a)

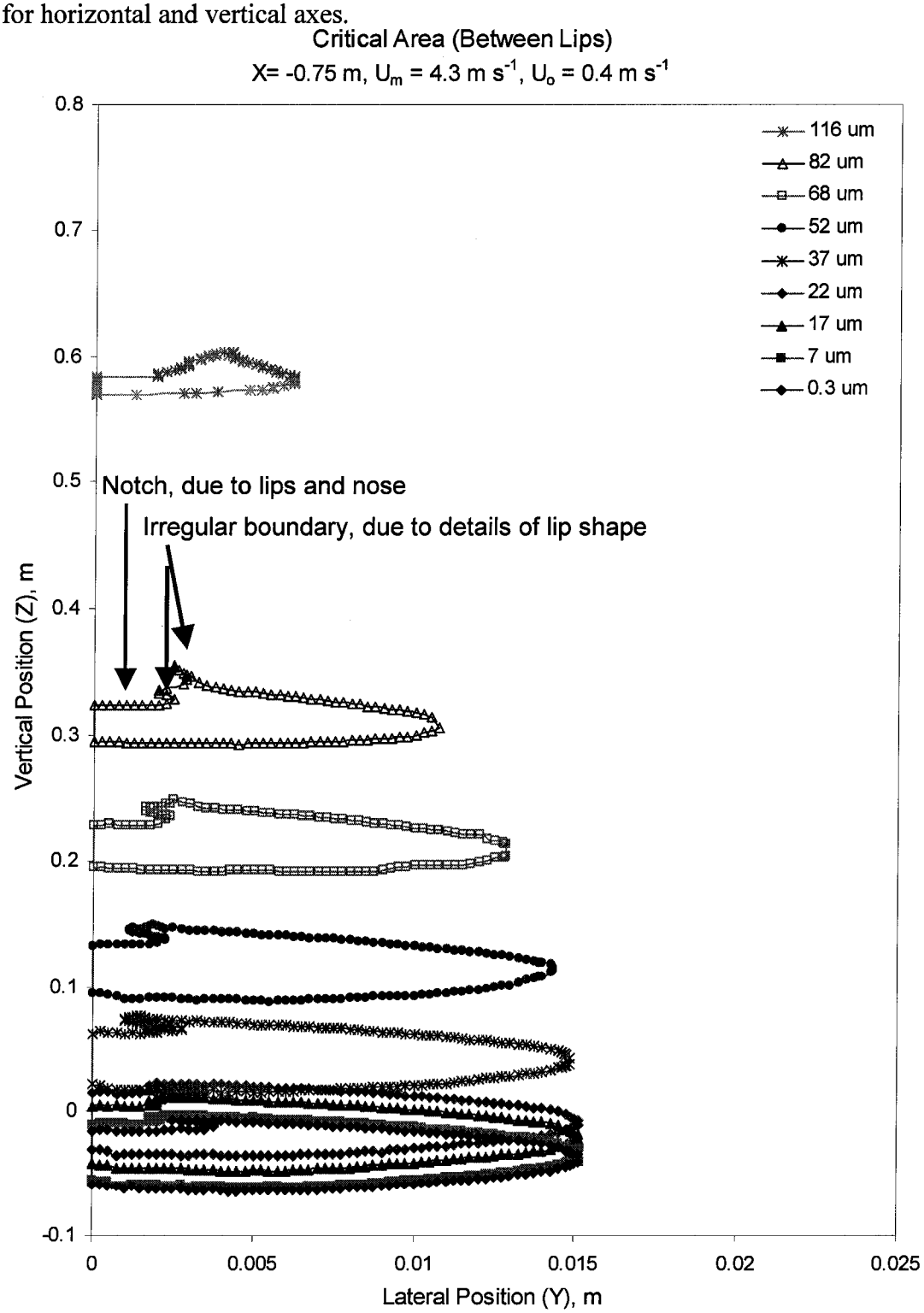

Figure 4.2 Critical areas (between lips) for (a) $U_m = 4.33$ m s^{-1}, $U_o = 0.4$ m s^{-1}, (b) $U_m = 1.81$ m s^{-1}, $U_o = 0.2$ m s^{-1}, (c) $U_m = 4.33$ m s^{-1}, $U_o = 0.2$ m s^{-1}. Note: different scales are used for horizontal and vertical axes.

4.2(b)

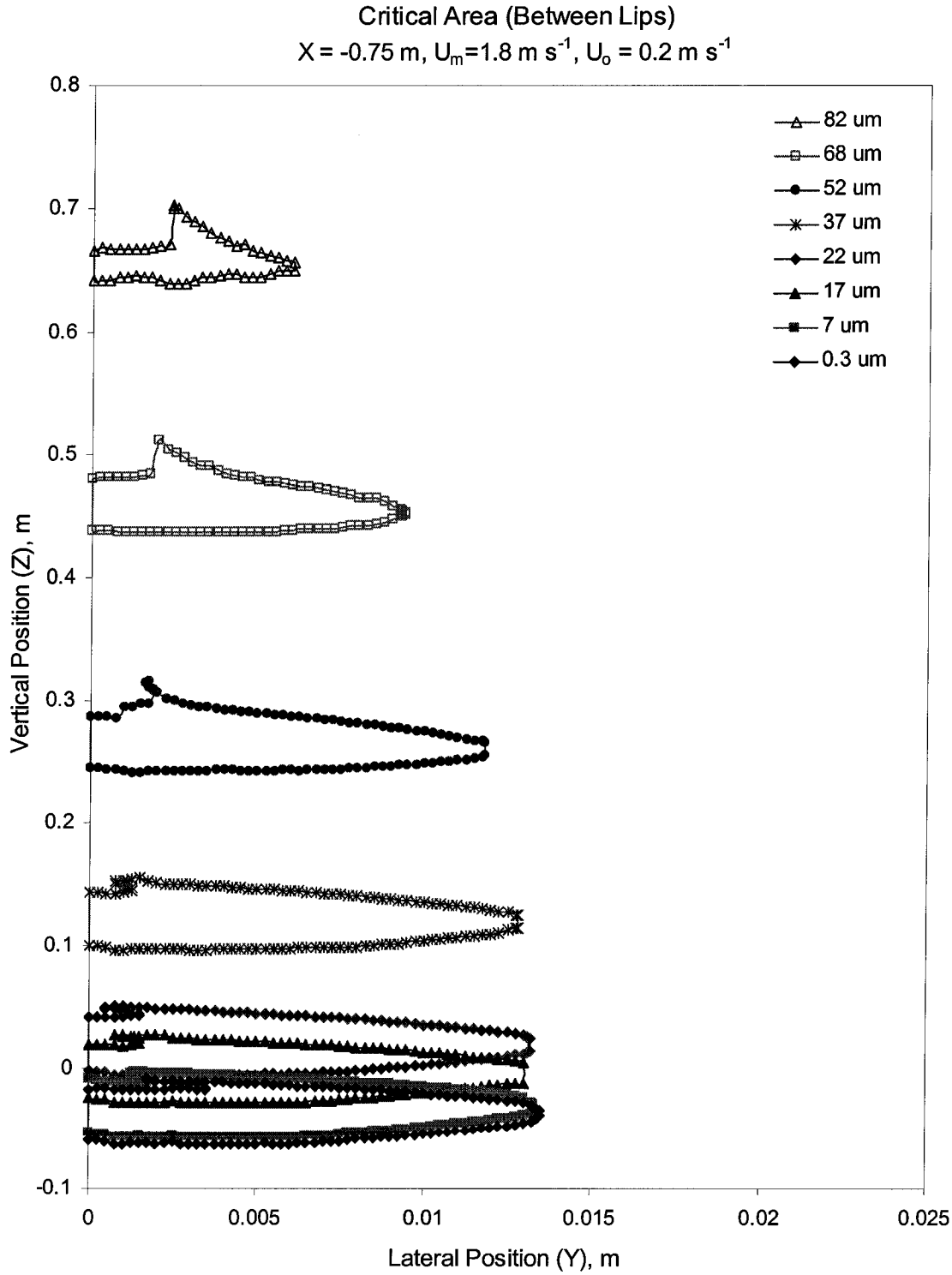

Figure 4.2 Critical areas (between lips) for (a) $U_m = 4.33$ m s^{-1}, $U_o = 0.4$ m s^{-1}, (b) $U_m = 1.81$ m s^{-1}, $U_o = 0.2$ m s^{-1}, (c) $U_m = 4.33$ m s^{-1}, $U_o = 0.2$ m s^{-1}. Note: different scales are used for horizontal and vertical axes.

4.2(c)

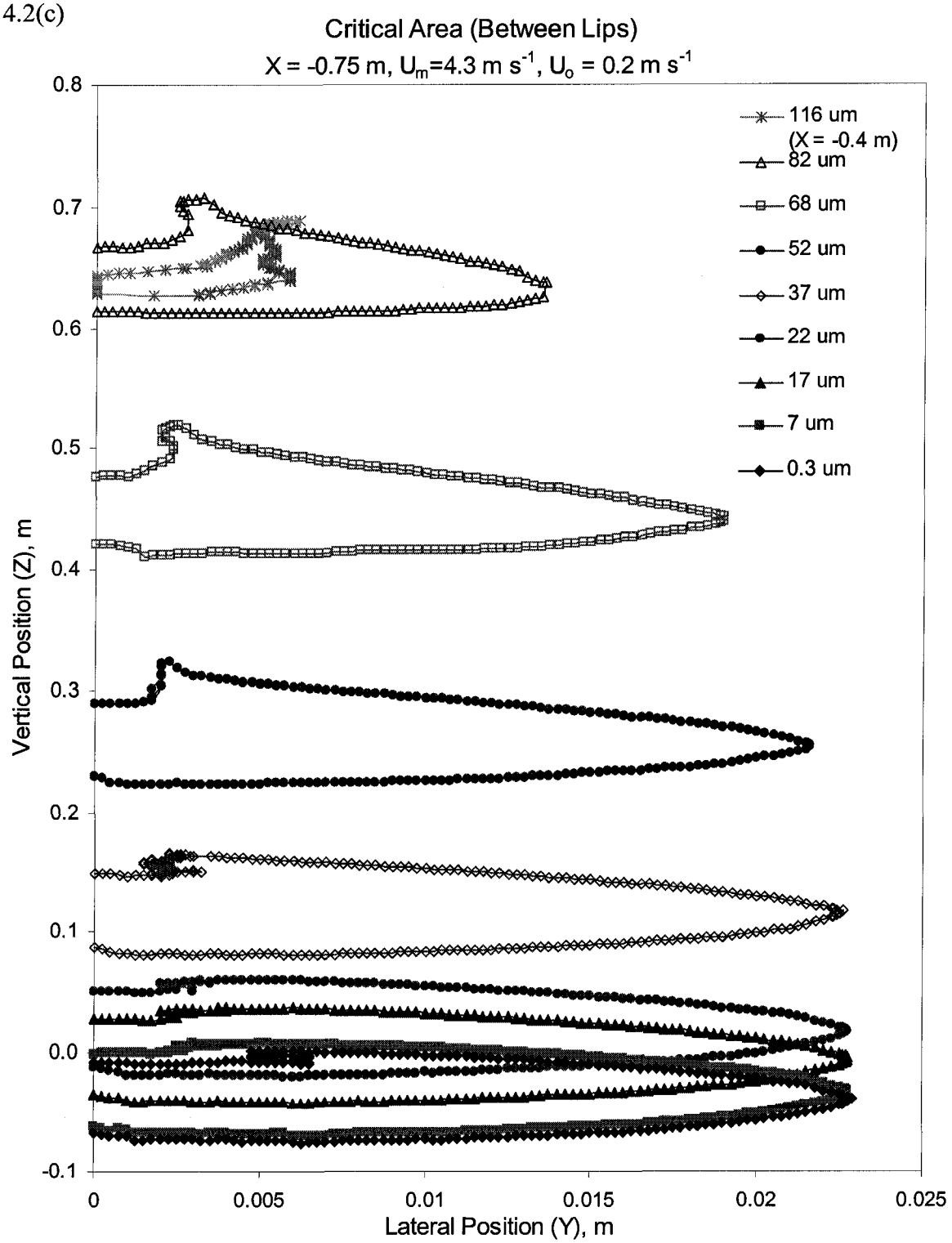

Figure 4.3 Scaled critical areas for (a) 7 μm, (b) 22 μm, and (c) 82 μm.

4.3(a)

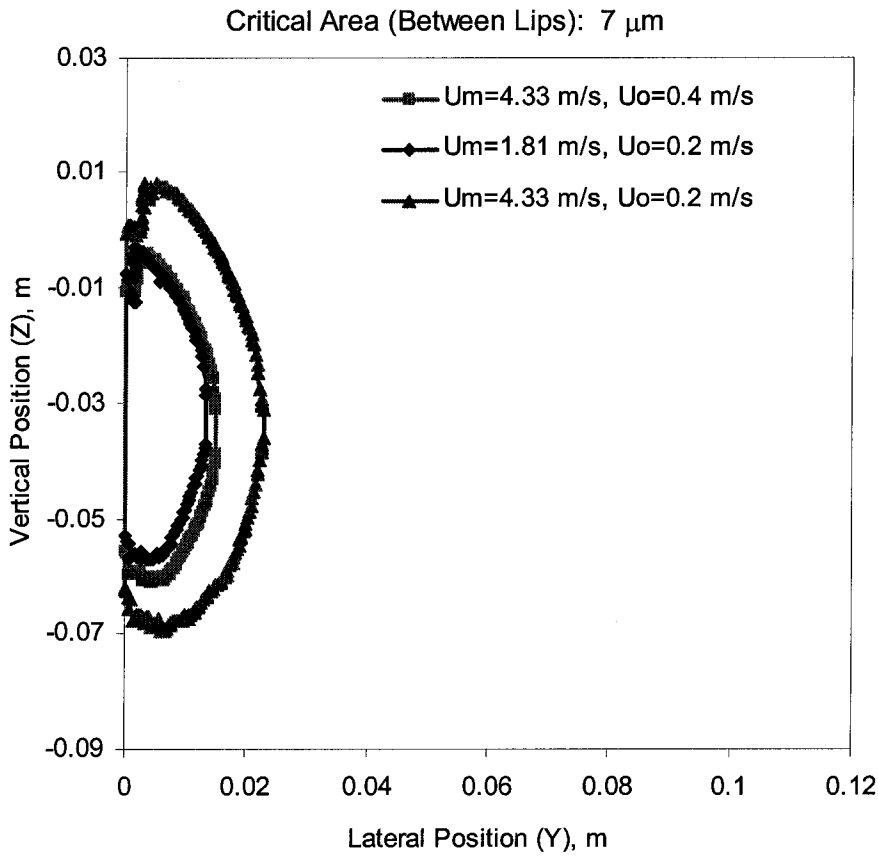

Figure 4.3 Scaled critical areas for (a) 7 μm, (b) 22 μm, and (c) 82 μm.

4.3(b)

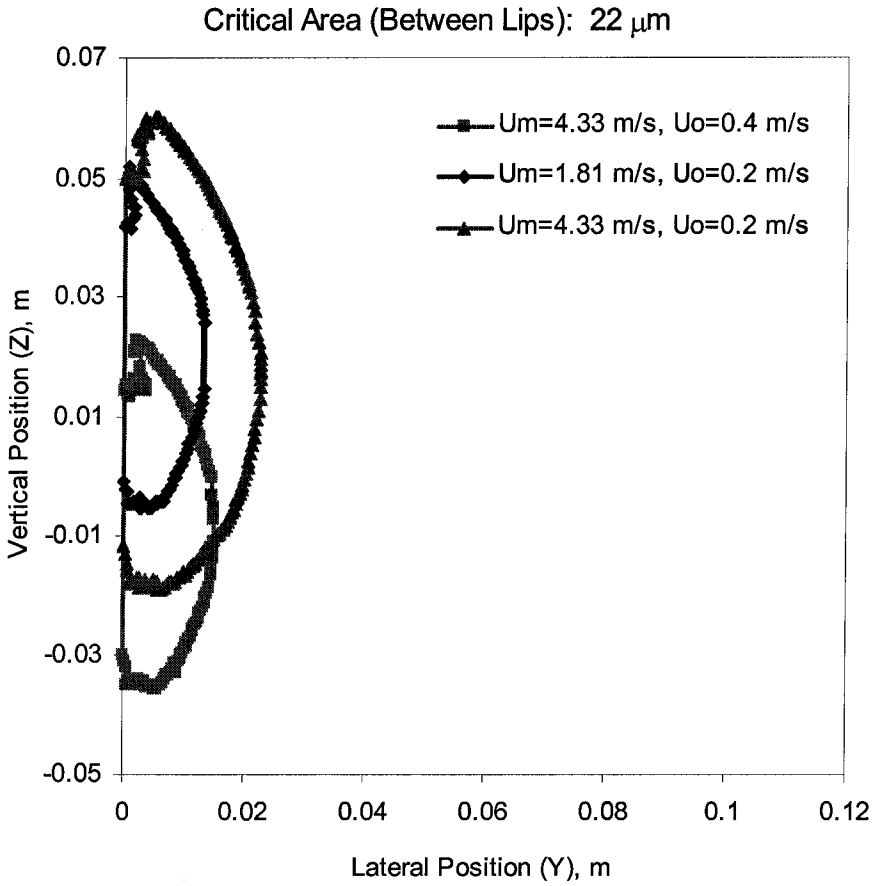

Figure 4.3 Scaled critical areas for (a) 7 μm, (b) 22 μm, and (c) 82 μm.

4.3(c)

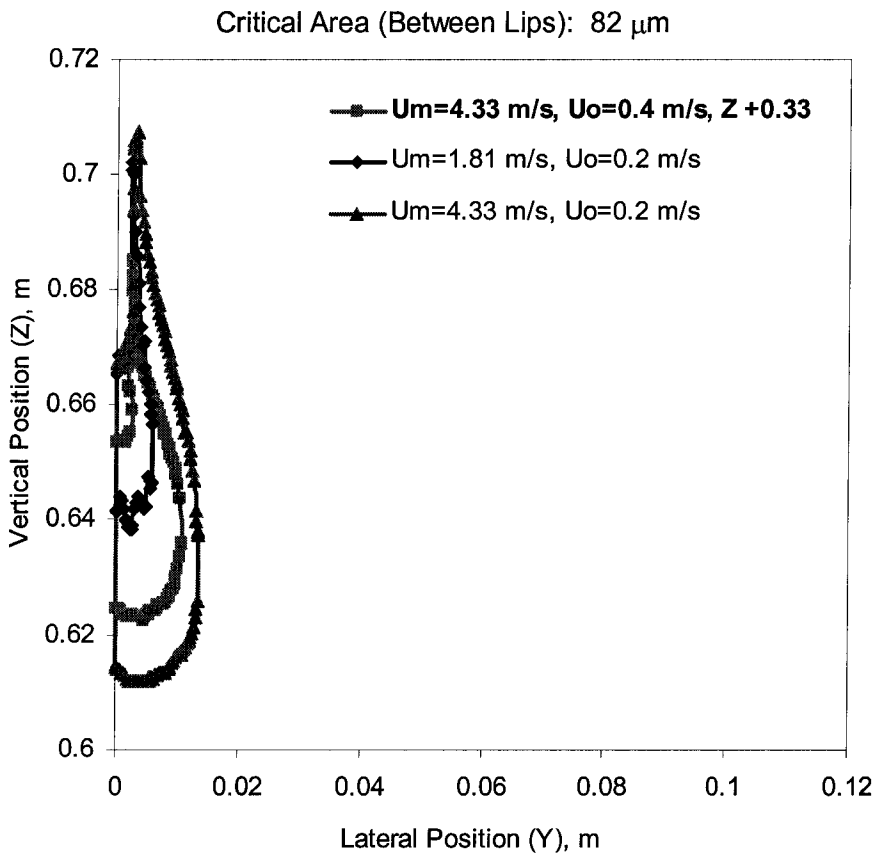

Figure 4.4 Aspiration efficiencies based on the (a) between-lip and (b) directed toward mouth definitions for critical area. Error bars for simulated aspiration efficiencies are based on the uncertainty of the particle critical area that was associated with the particle spacing in simulations. The dashed horizontal line indicates 50% aspiration efficiency.

4.4(a)

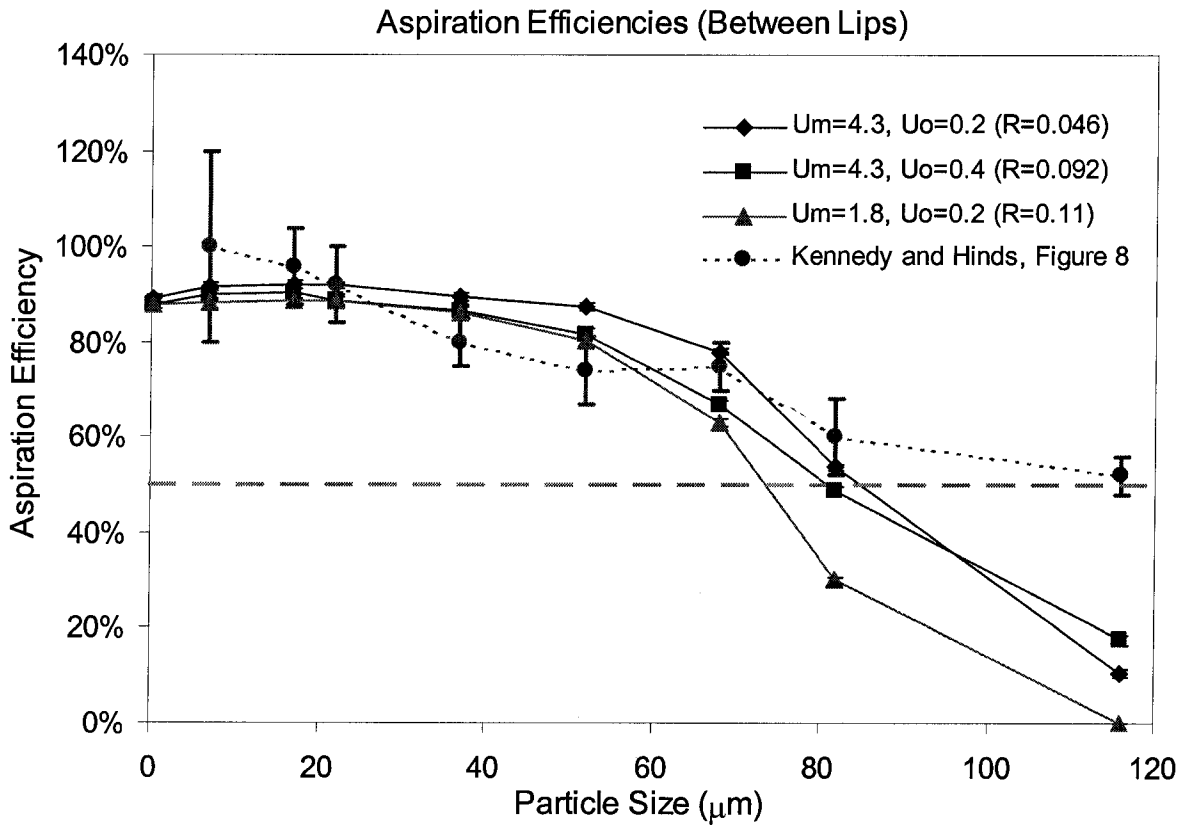

Figure 4.4 Aspiration efficiencies based on the (a) between-lip and (b) directed toward mouth definitions for critical area. Error bars for simulated aspiration efficiencies are based on the uncertainty of the particle critical area that was associated with the particle spacing in simulations. The dashed horizontal line indicates 50% aspiration efficiency.

4.4(b)

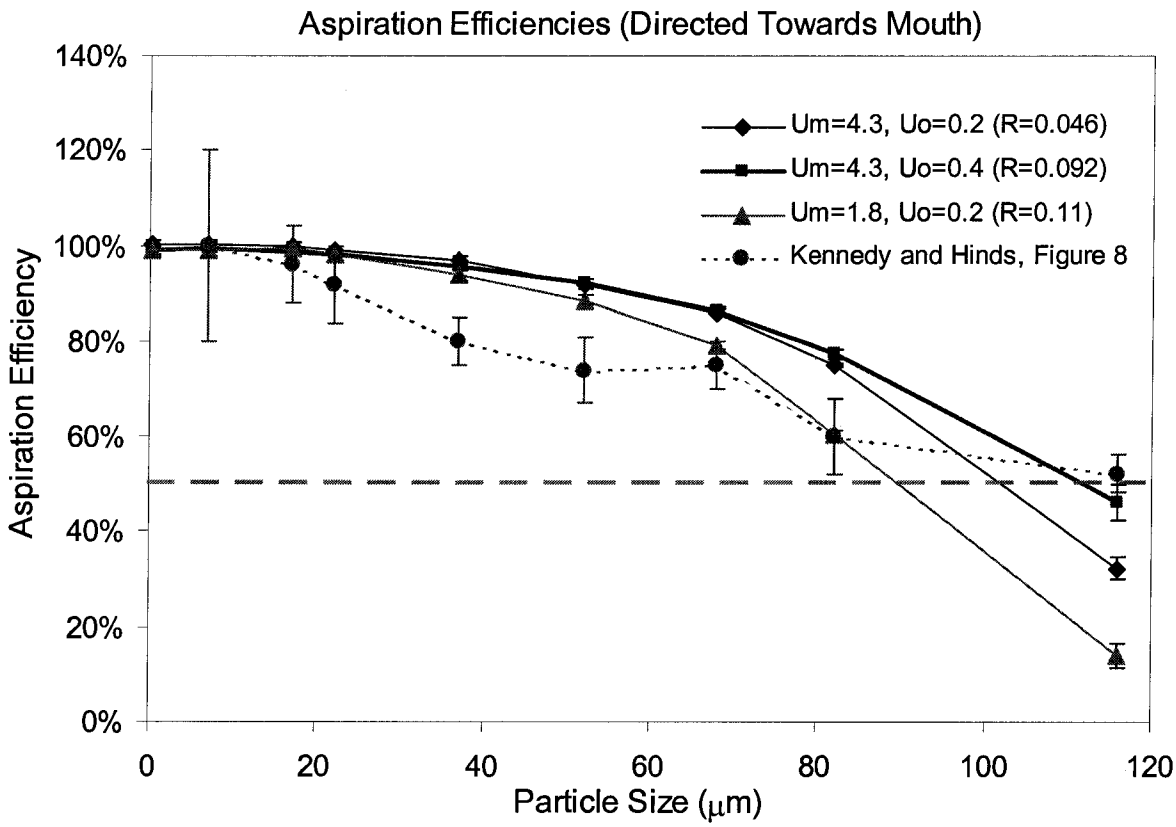

Figure 4.5 Particle aspiration illustrations for 7 μm particles (a) $U_o = 0.4$ m s^{-1}, $U_m = 4.33$ m s^{-1}, (b) $U_o = 0.2$ m s^{-1}, $U_m = 4.33$ m s^{-1}, and (c) $U_o = 0.2$ m s^{-1}, $U_m = 1.81$ m s^{-1}.

4.5(a)

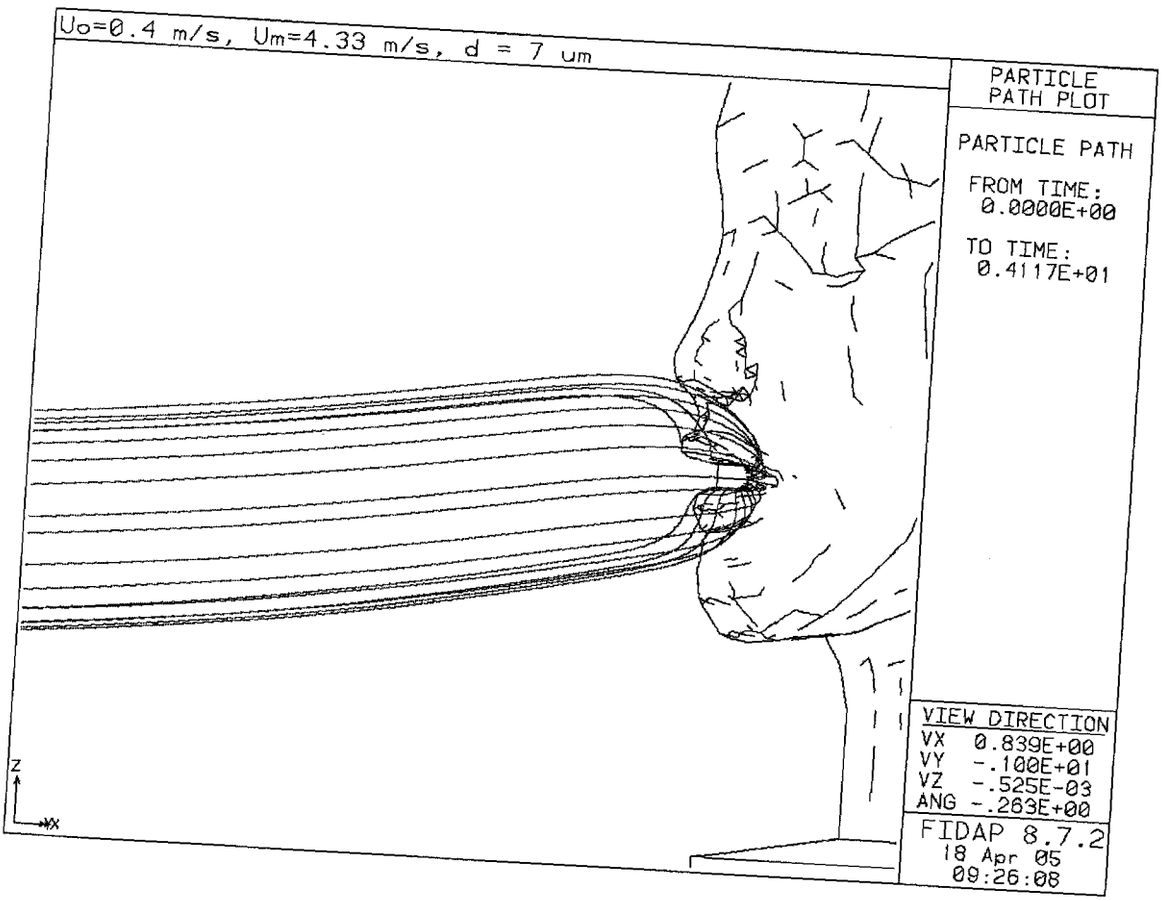

Figure 4.5 Particle aspiration illustrations for 7 μm particles (a) U_o = 0.4 m s^{-1},U_m = 4.33 m s^{-1}, (b) U_o = 0.2 m s^{-1}, U_m = 4.33 m s^{-1}, and (c) U_o = 0.2 m s^{-1}, U_m = 1.81 m s^{-1}.

4.5(b)

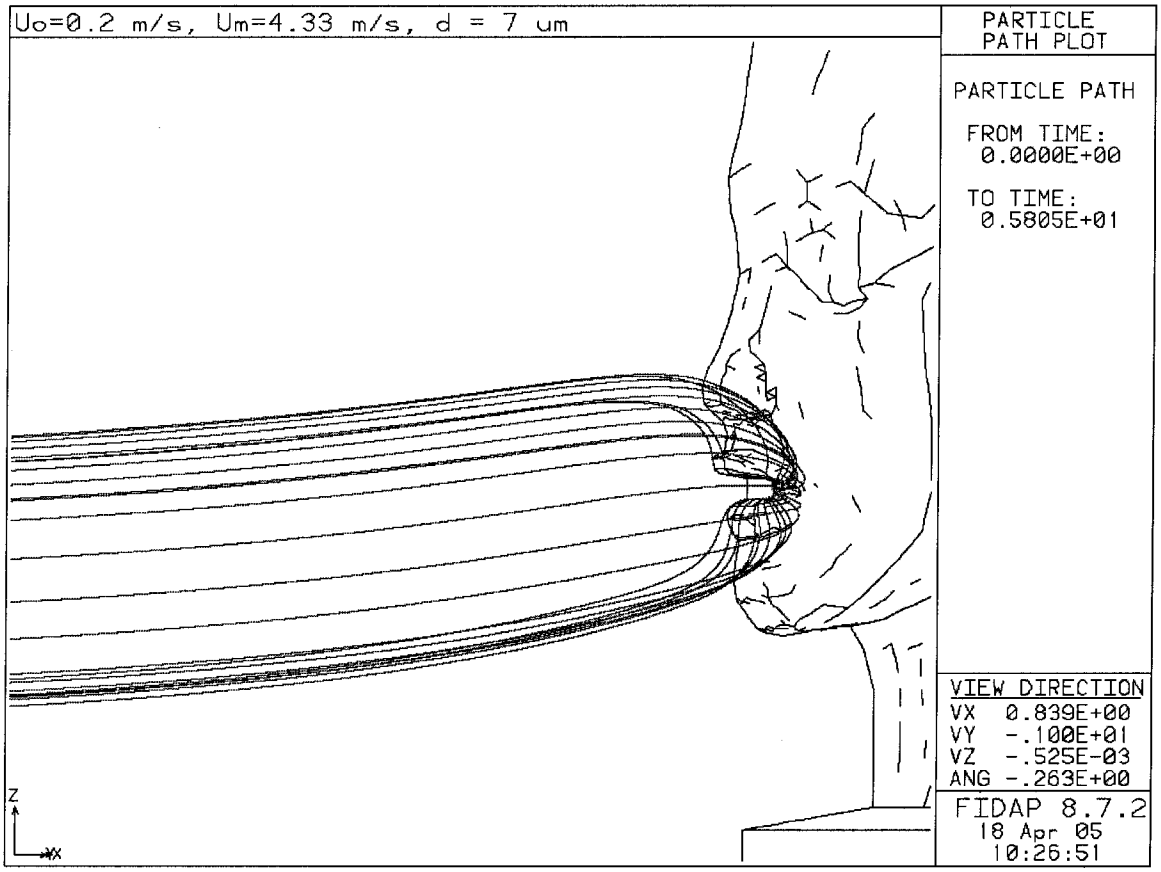

Figure 4.5 Particle aspiration illustrations for 7 μm particles (a) $U_o = 0.4$ m s^{-1},$U_m = 4.33$ m s^{-1}, (b) $U_o = 0.2$ m s^{-1}, $U_m = 4.33$ m s^{-1}, and (c) $U_o = 0.2$ m s^{-1}, $U_m = 1.81$ m s^{-1}.

4.5(c)

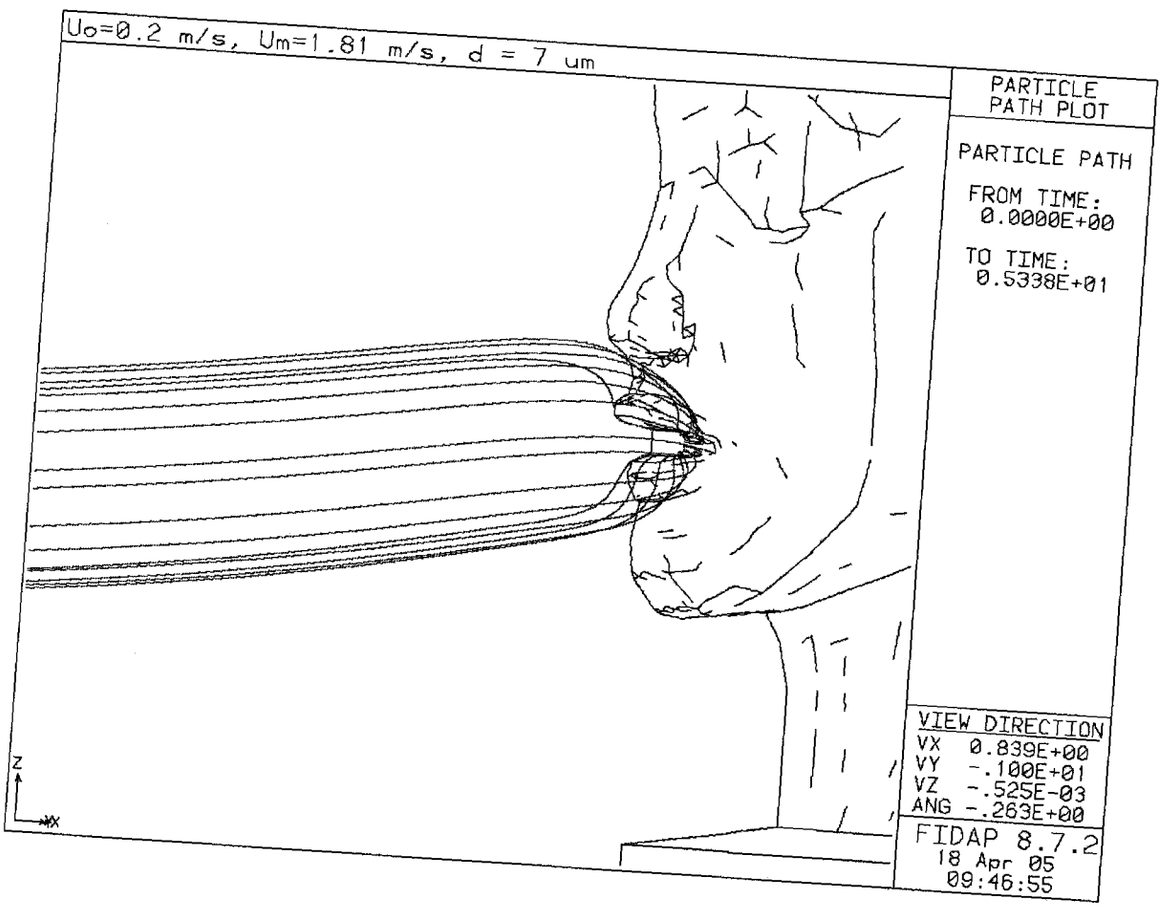

Figure 4.6 Particle aspiration illustrations for 116 μm particles (a) $U_o = 0.4$ m s^{-1},$U_m =$ 4.33 m s^{-1}, (b) $U_o = 0.2$ m s^{-1}, $U_m = 4.33$ m s^{-1}, and (c) $U_o = 0.2$ m s^{-1}, $U_m = 1.81$ m s^{-1}.

4.6(a)

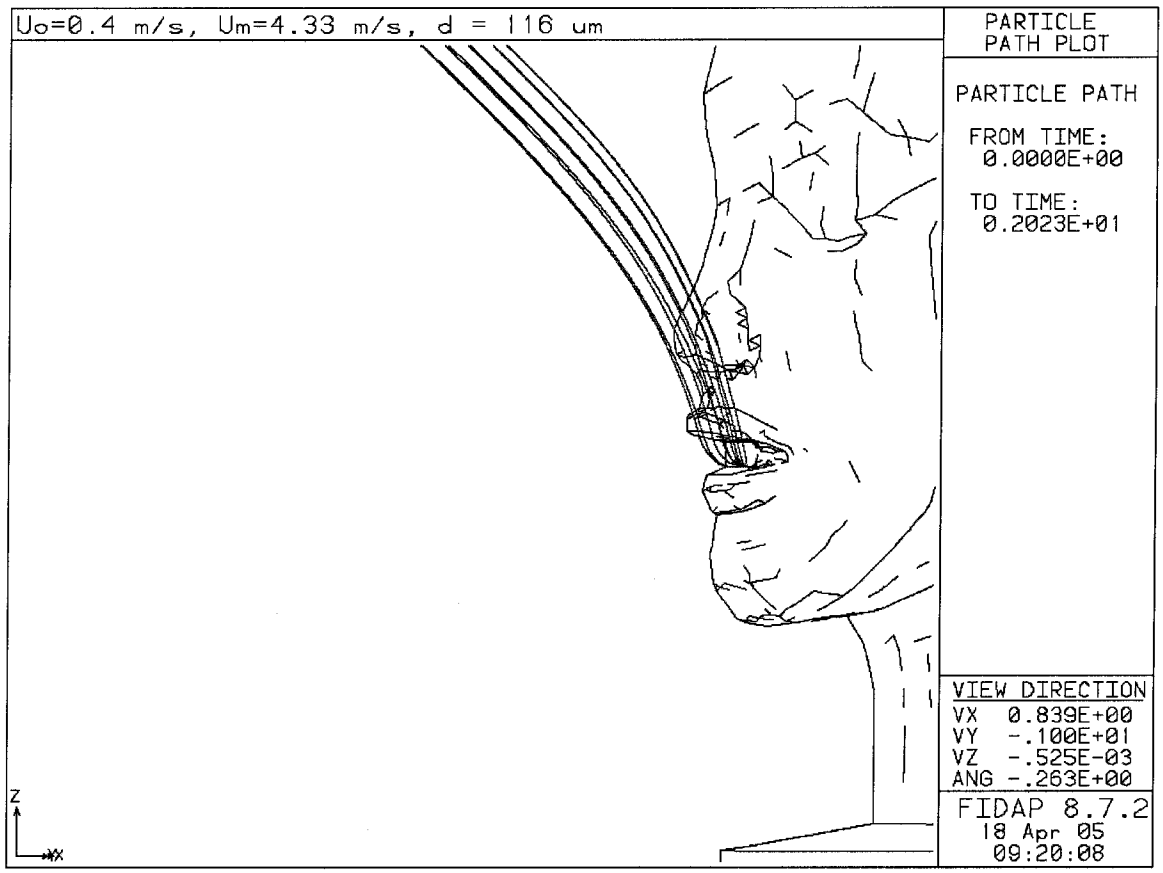

Figure 4.6 Particle aspiration illustrations for 116 μm particles (a) $U_o = 0.4$ m s^{-1},$U_m =$ 4.33 m s^{-1}, (b) $U_o = 0.2$ m s^{-1}, $U_m = 4.33$ m s^{-1}, and (c) $U_o = 0.2$ m s^{-1}, $U_m = 1.81$ m s^{-1}.

4.6(b)

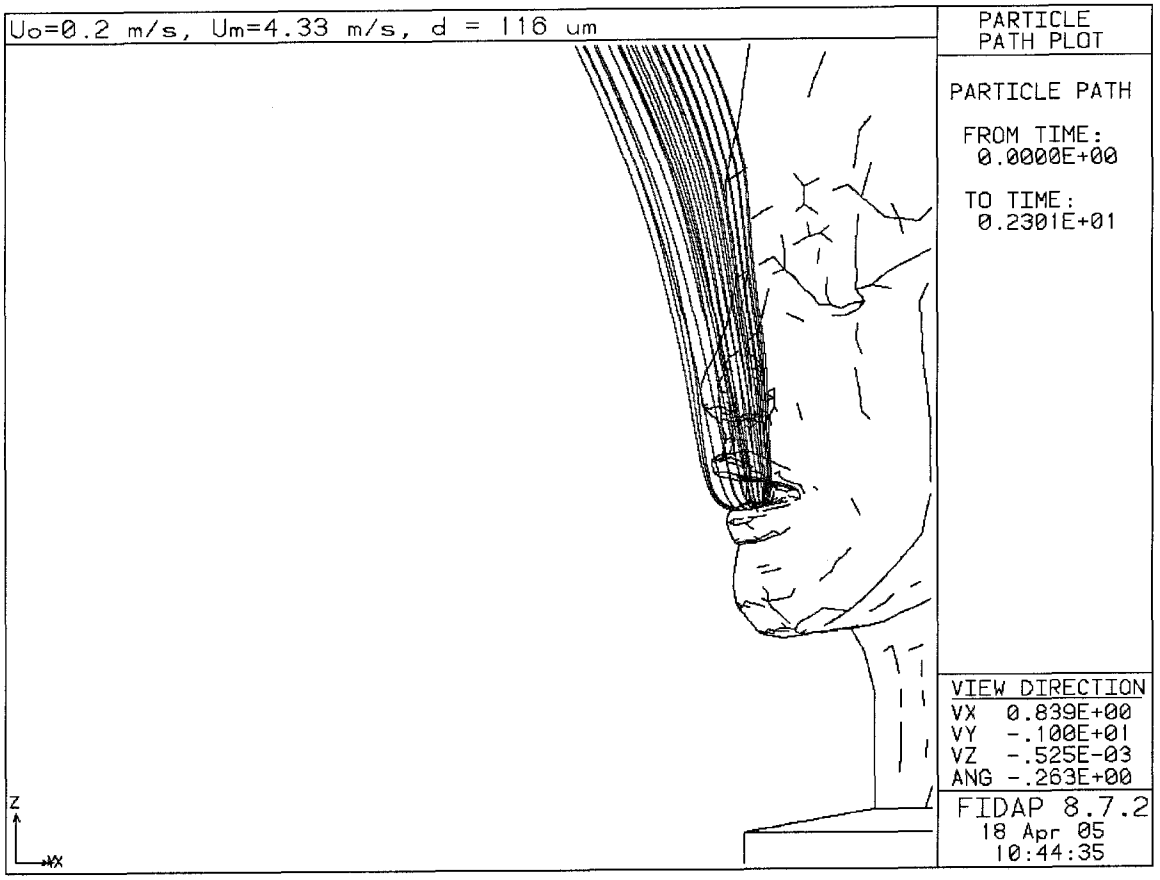

Figure 4.6 Particle aspiration illustrations for 116 μm particles (a) $U_o = 0.4$ m s^{-1},$U_m =$ 4.33 m s^{-1}, (b) $U_o = 0.2$ m s^{-1}, $U_m = 4.33$ m s^{-1}, and (c) $U_o = 0.2$ m s^{-1}, $U_m = 1.81$ m s^{-1}.

4.6(c)

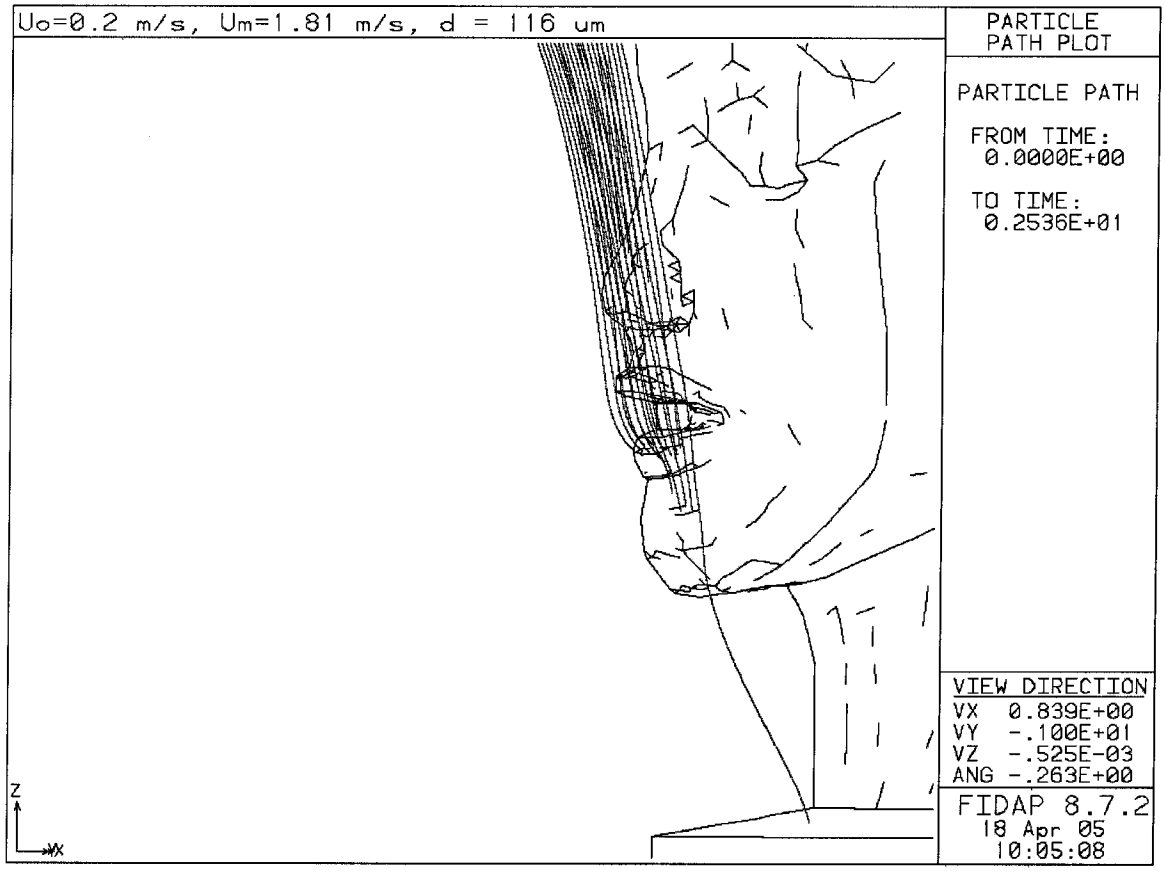

APPENDIX A: EQUIPMENT CALIBRATION

Experimental work required the calibration of equipment to ensure the designed flow conditions were achieved. Calibration of the experimental wind tunnel in the Baity Air Laboratory first required the calibration of velocity measuring devices, including an experimental orifice, a thermal anemometer, and a rotating vane anemometer. Additionally, rotameters were calibrated with primary standards to set air flowrates for breathing simulation and the aerosol generator. The liquid flow rate through the aerosol generator was also determined. The process and results are detailed in this appendix. Supporting data are found in the data disc accompanying this dissertation, described in Table A.1.

Table A.1 Data files supporting Appendix A

File Name	Description	Discussion Section
A1-Cal 4 inch Orifice.xls	Calibration of 4" orifice used as the primary standard for velocity measuring equipment	A.1.b
A2-TSI RV Cal – all.xls	Rotating vane calibration (TSI Velocicalc 8324)	A.1.c
A3-TSI Probe 87_87 July 10.xls	Calibration of TSI-IFA probe #87-87 using 6.684" orifice	A.1.d
A4-TSI Probe 87_87 July 16.xls	Calibration of TSI-IFA probe #87-87 using 4" orifice, and combined data analysis	A.1.d
A5-WT Cal with Filters.xls	Calibration of Baity Laboratory Wind tunnel's hood static pressure	A.2
A6-Rotameter Calibrations.xls	Calibration of rotating vanes used to set breathing and aerosol generator flowrates	A.3
A7-Masterflex Cal.xls	Calibration of masterflex pump used to meter liquid to aerosol generator	A.4

A.1 Velocity Measurement Equipment

To conduct studies in the Baity Lab wind tunnel, a series of calibration steps were required. The relationship between the measured hood static pressure and the wind tunnel volumetric flow rate was investigated to determine settings for the operation of the wind tunnel. To do this, anemometers required calibration. First, the pressure drop

across an orifice was calibrated using a pitot-tube traverse upstream of the orifice. Secondly, the voltage signal from the thermal anemometer and the readings from the rotating vane anemometer were calibrated against the orifice pressure difference readings.

A.1.a Calibration System

To calibrate all velocity measurement equipment, a calibration system consisting of a fan, an 8-inch duct with orifice, and a calibration wind tunnel were used. An industrial fan, exhausted to the outside, was used to pull air through the system. A controllable butterfly-valve was used to adjust the flow over an established range. An orifice was positioned in the 8-inch duct, sharp edge to the upstream direction, and a Dwyer Manometer, Model 400-10 (SN S436), was used to measure the change in static pressure across the orifice. Velocity measurement equipment was located centrally in the open-ended calibration wind tunnel (cross sectional area of 2.54 ft^2).

A.1.b Orifice Calibration

The first step of calibration was to determine the relationship between the change in static pressure across an orifice and the volumetric flow through an 8-inch duct. A small 4-inch orifice was needed to allow for future anemometer calibrations in low velocity conditions. The square root of the change in static pressure across this orifice was proportional to the volumetric flow rate through the orifice:

$$Q = K(\Delta h)^{1/2} \quad \text{(A.1)}$$

where:

Q = volumetric flow rate (cfm)

Δh = static pressure difference across the orifice (inch water)

K = constant

The theoretical calibration of a 4-inch orifice in an 8-inch duct, using factors published in the Industrial Ventilation: A Manual of Recommended Practice (23rd Edition, page 9-13, Table 9-4) indicated the following relationship:

$$Q\ (cfm) = 219\ (\Delta h)^{1/2} \quad \text{(A.2)}$$

Because mass was conserved throughout the duct, the volumetric flow rate at any point in the system was the same as that through the orifice. As such, velocity readings

were made upstream of the orifice using a pitot tube with ten-point traverses, both horizontal and vertical. Velocity pressure was measured using the pitot tube and was converted to velocity using the following:

$$V = 1096(VP/\rho)^{1/2} \quad \text{(A.3)}$$

where:

V = velocity (fpm)

VP = velocity pressure (inch water)

ρ = density of air (0.075 lb/ft^2)

For the 4-inch orifice calibration, a 95-inch straight run section of 4-inch duct was located upstream of the orifice to obtain reliable velocity pressure readings with pitot tube traverses (January 26 and 27, 2003). Traverse measurements were collected at 64 inches (16 duct diameters) downstream of the transitional contraction following the entry hood, which was sufficient to allow for stable velocity profiles in the duct.

Seven different flow rates were investigated to ensure that the desired velocity of 0.3 m s^{-1} (59 ft/min) would be achievable in the calibration wind tunnel. A least-squares regression of the square root of the pressure change across the orifice and the volumetric flow rate was conducted, forcing the intercept through zero, to obtain the best fit for the equation in the form above (A.1). This calibration process yielded a slope of 216, indicating that the calibration equation of the orifice was:

$$Q\ (\text{cfm}) = 216\ (\Delta h)^{1/2} \quad \text{(A.4)}$$

This equation is valid over the range of 96 to 207 cfm. Summary data for the above regression are given in Table A.2, which is presented graphically in Figure A.1 *(data file: A1).*

In addition to the 4-inch orifice for calibrating anemometers in low velocities, a larger orifice was needed to calibrate the rotating vane in higher velocities. This work relies on the thorough calibration by of a 6.784 inch orifice (Kovitz). The relationship between volumetric flowrate (cfm) and pressure difference (inch water) across the orifice was given by Kovitz as:

$$Q\ (\text{cfm}) = 796(\Delta h)^{1/2} + 22 \qquad (R^2=0.9969) \quad \text{(A.5)}$$

This calibration had been performed over the range of 100 to 650 cfm.

A.1.c Rotating Vane Anemometer Calibration

A TSI Velocicalc (model 8324, SN 03060423) rotating vane anemometer was calibrated using both the 4-inch and the 6.784-inch orifice in the 8-inch duct. The rotating vane was suspended in the center of the calibration wind tunnel (cross-setional area = 2.54 ft^2) and static pressure difference measurements were made across the orifice.

Using both low velocities associated with the 4-inch orifice plate from July 14 and 16 and higher velocities with the 6.784-inch orifice from July 16, the relationship between the velocity indicated by the rotating vane (fpm_{meas}) and the true velocity (fpm_{true}) is given as:

$$fpm_{true} = 0.9318 fpm_{tsi} - 14.838 \qquad (R^2=0.998) \qquad (A.6)$$

This calibration was valid over the rotating vane readings of 77 to 348 fpm, or true velocities ranging from 58 to 306 fpm. The calibration curve is provided in Figure A.2 *(data file: A2).*

A.1.d Thermal Anemometer Calibration

Velocity measurements inside the Baity Air Lab wind tunnel were also made using TSI® 1210-06 platinum hot wire probes and a TSI IFA-100 flow analyzer. These probes required calibration in the calibration wind tunnel in low velocity conditions, using the 4-inch orifice. Each probe used required its own calibration, as the resistivity of each varies slightly. The anemometer consists of a thin wire suspended on thin, rigid supports, connected to a cable and the flow analyzer. The wire is heated to a constant temperature, and the cooling effect of moving air requires additional voltage to be applied to the wire to maintain this temperature. King's law, simplified for the condition of operating at a constant elevated temperature, is:

$$H = A + Bv^{0.45} \qquad (A.7)$$

where:

H = rate of heat loss per unit length of wire

A, B = constants of calibration

v = fluid velocity

Velocity measurements were made by placing the sensor at right angles to the oncoming wind, with the probe positioned horizontally. Both signal and transducer

voltages were recorded, and the relationship between the voltage and the true velocity was determined for the probe. Because the range of measured signal voltages is wider than for transducer voltages, calibrations were performed using the signal voltages. The system was operated with an offset of 1, a gain of 6, and a filter of $5x10^{-4}$, which allows for a relationship to be determined between the transducer and signal voltages:

$$Voltage_{trans}=(Voltage_{signal} / gain) + offset \quad (A.8)$$

A summary of calibration data for the probe (#87-87) is provided in Table A.3 (*data files: A3 and A4).* Figure A.3 provides the calibration curve relating the signal voltage from the TSI IFA-100 to the true velocity, as determined from velocity measures across the orifice located in the calibration system.

A.2 Wind Tunnel at Baity Air Laboratory

The calibrations above were performed so that the flow rate through the Baity Air Lab wind tunnel could be known. The study wind tunnel had a 5 foot by 5 foot entrance and a depth of 8 feet; however, a false floor was positioned 1 foot above the existing floor to match the cross-sectional dimensions of the wind tunnel used at the U.S. EPA wind tunnel at Research Triangle Park, NC. To minimize turbulence within the wind tunnel, a continuous 6.3 cm thick fiberglass filter (Hess Industries, Astonia, NY) was placed at the tunnel entrance, behind which was a thin-walled, turbulence-reducing grid with openings 15.25 by 15.25 cm and 15.25 cm deep. Behind the tunnel was a contraction leading to the fan, into which a pitot tube was inserted centrally. Following this short duct and transition, the air handler with a variable controller (Tosvert) was located. Air was exhausted through a rectangular duct to the outside, through louvers that were fixed in the open position during experiments to minimize temporal fluctuations associated with transient wind outside the building.

Velocity measures were made using a twenty-point tranverse, illustrated by Figure A.4. These locations represented the centers of twenty equally sized rectangular areas across the wind tunnel cross section. Using the rotating vane, velocity traverse measurements were made 18" inside of the wind tunnel entrance for six hood static pressures. A 0.045" static pressure provided the target mean velocity needed for this study. At this pressure, additional velocity measurements were made at 49¾ and 72

inches into the wind tunnel. The mean and standard deviation of replicate measurements are provided in Tables A.4 through A.12, and the summary data used for the wind tunnel calibration curve are provided in Table A.13 *(data file: A5)*. The calibration curve for this wind tunnel is provided in Figure A.5, where the 0.045" hood static pressure data were pooled. The relationship between the average wind tunnel velocity and the hood static pressure was given by:

$$V_{ave} = 348.6(SP^{1/2}) - 15.368$$

where V_{ave} is the cross sectional average velocity in fpm, and SP is the hood static pressure, in inches of water.

Also included in this figure are previous calibration data for the wind tunnel without the fiberglass filter on the inlet. The addition of this filter not only not only reduced turbulence intensities within the wind tunnel, but allowed us to operate at slightly larger hood static pressures to achieve the desired low velocities, assisting with system stability.

A.3 Rotameters

The inhalation flowrate through the mannequin mouth and the flowrate through the ultrasonic nozzle used to generate particles also required accurate calibration. Dwyer rotameters were used during experiments to monitor these flow conditions during particle aspiration experiments. Hence, their calibration to a traceable primary standard was critical. All rotameter readings were taken at the center of the ball.

A.3.a Calibration of Breathing Simulation

A vacuum pump was used to simulate mannequin inhalation. The pump pulled air through a treated 2 μm pore-size polycarbonate filter positioned within the mannequin mouth, requiring significant pressure. Because of this, primary electronic calibrators, such as the BIOS DryCal, were ill-suited for calibrating this flow. Instead, a rotameter was used to set and monitor the mannequin inhalation rate. The rotameter was calibrated with chain-compensated gasometer (Warren E. Collins, Inc., SN2382, calibration of 134.0 cc/min) connected to a sampling train that included a treated polycarbonate filter, the rotameter to be calibrated, and the vacuum pump, with a sampling line of similar length used in the study. Ten flowrates were examined, and results are provided in

Figure A.6. Target flowrates of 10 and 20 Lpm were achieved using this rotameter's setting of 21.9 and 43.7 scfh *(data file: A6).*

A.3.b Calibration of Air through Ultrasonic Nozzle

To move particles out of the wake of the ultrasonic nozzle, compressed air was metered through the nozzle at 2 Lpm. The flowrate was monitored using a Dwyer rotameter, calibrated with a BIOS DryCal calibrator in line with the supplied air, filter, flow valve, rotameter and ultrasonic nozzle. Calibration was examined from 1.0 to 5.0 scfh on the rotameter, and a operation at setting of 4.2 provided the 2 Lpm needed for the experiments. Next, repeatability and stability of the supplied air were investigated. Table A.14 indicates that repeated settings of 4.2 resulted in a mean flowrate of 2.01 Lpm (s.d. = 0.015 Lpm), and Figure A.7 indicates the system decayed 0.02 Lpm over a 30 minute period, sufficient for the 10 minute tests that were run with this nozzle *(data file: A6).*

A.4 Masterflex Pump

The liquid flowrate was metered through the ultrasonic nozzle using a Masterflex pump using two cartridges. Liquid was pumped to a tared graduated cylinder, where the weight of the oil, the time of liquid dispensing, and the density of the oil were used to calculate the flowrate through the system. Calibration was performed over a range of settings, and experiments were operated at a setting of 0.24, where the aerosol generation appeared to be stable. Table A.15 provides the results of setting sensitivity at this reading *(data file A7).* For this study, the setting was adjusted before each run.

Table A.2 Orifice Calibration Summary

Run Ref.	Mean Velocity from Pitot Traverse (ft/min)	Mean CFM from Pitot Traverse	Average Δh across Orifice (in wg)	Average $(\Delta h)^{1/2}$ across Orifice (in wg)
1/27-a	1092	95	0.18	0.43
1/26-c	1075	94	0.19	0.43
1/27-b	1349	118	0.30	0.55
1/26-b	1710	149	0.49	0.70
1/27-c	1809	158	0.52	0.72
1/26-d	2255	197	0.85	0.92
1/27-d	2370	207	0.91	0.95

Table A.3 Thermal Anemometer Calibration 87-87
Settings: offset = 1, gain = 6, filter =0.0005
Calibration wind tunnel area = 2.54 ft^2

Orifice Diameter	Date	Δh	+/- Δh	CFM	Vtrue	$Vtrue^{1/2}$	Ave Vsig	$Vsig^2$	Stdev (Vsig)	$stdv(Vs^2)$
4"	16-Jul-03	3.25	0.05	389	151	12.3	2.8669	8.2256	0.0793	0.4512
4"	16-Jul-03	4.8	0.1	473	184	13.6	3.0487	9.3057	0.1065	0.6487
4"	16-Jul-03	5.8	0.1	520	202	14.2	3.1411	9.8756	0.0942	0.5912
4"	16-Jul-03	6.65	0.1	557	216	14.7	3.2032	10.2666	0.0771	0.4930
4"	16-Jul-03	3.95	0.05	429	167	12.9	2.9485	8.7026	0.0934	0.5419
4"	16-Jul-03	2.3	0.025	328	127	11.3	2.6910	7.2537	0.1099	0.5850
6.684"	10-Jul-04	0.025	-	148	58	7.59	1.9701	3.8871	0.0765	0.2986
6.684"	10-Jul-04	0.05	-	200	78	8.82	2.1944	4.8257	0.1017	0.4360
6.684"	10-Jul-04	0.09	-	261	101	10.07	2.3620	5.5910	0.1092	0.5057
6.684"	10-Jul-04	0.19	-	369	144	11.98	2.7490	7.5622	0.0721	0.3995
6.684"	10-Jul-04	0.305	-	462	180	13.40	3.0165	9.1103	0.1048	0.6352
6.684"	10-Jul-04	0.42	-	538	209	14.47	3.1360	9.8469	0.1122	0.7060
6.684"	10-Jul-04	0.57	-	623	242	15.57	3.2973	10.8801	0.0877	0.5810
6.684"	10-Jul-04	0.61	-	644	250	15.83	3.3835	11.4519	0.0647	0.4367
6.684"	10-Jul-04	0.785	-	727	283	16.82	3.5051	12.2941	0.0900	0.6325
6.684"	10-Jul-04	0.89	-	773	301	17.34	3.5863	12.8653	0.0623	0.4465
6.684"	10-Jul-04	1.3	-	930	362	19.02	3.8340	14.7017	0.0452	0.3464

Table A.4 Velocity averages at traverse locations

SP = 0.032 inch water, 18" into wind tunnel

True Velocity	a	b	c	d	e		
1	43.7	46.7	47.9	39.7	36.9	47	mean
2	38.9	48.7	51.9	49.5	46.9	37	min
3	44.8	46.3	51.0	52.0	52.2	54	max
4	47.6	46.2	52.5	54.0	51.4	5	stdev

True Stdev	a	b	c	d	e		
1	1.2	0.4	1.9	0.6	1.4	1.5	mean
2	2.1	0.7	2.3	1.1	0.9	0.4	min
3	1.7	1.8	1.5	2.1	1.2	4.2	max
4	1.4	1.0	4.2	0.8	0.9	0.8	stdev

Table A.5 Velocity averages at traverse locations

SP = 0.045 inch water, 18" into wind tunnel (Oct 24)

True Velocity	a	b	c	d	e		
1	51.3	55.6	57.8	51.6	51.4	58	mean
2	53.4	54.0	64.4	61.8	55.0	51	min
3	58.4	55.0	56.0	63.7	61.8	67	max
4	59.8	64.9	67.3	62.8	59.1	5	stdev

True Stdev	a	b	c	d	e		
1	0.6	1.1	1.0	1.2	0.8	1.2	mean
2	1.4	0.5	0.2	0.8	0.8	0.2	min
3	0.6	2.5	4.3	1.0	1.1	4.3	max
4	1.2	0.7	1.7	2.4	0.5	0.9	stdev

Table A.6 Velocity averages at traverse locations

SP = 0.045 inch water, 18" into tunnel (replicate, Oct 27)

True Velocity	a	b	c	d	e		
1	58.5	56.1	59.8	49.3	49.3	59	mean
2	55.1	56.1	66.1	57.1	55.3	49	min
3	60.2	58.7	65.3	63.8	60.7	69	max
4	62.6	62.7	68.7	61.8	55.7	5	stdev

True Stdev	a	b	c	d	e		
1	0.5	0.3	0.3	0.6	0.3	0.7	mean
2	0.5	0.3	0.8	0.4	0.7	0.3	min
3	0.7	0.7	0.7	0.8	1.3	2.3	max
4	0.7	0.4	0.5	1.7	2.3	0.5	stdev

Table A.7 Velocity averages at traverse locations

SP = 0.045 inch water, 49 ¾ inch into tunnel (Oct. 27)

True Velocity	a	b	c	d	e		
1	52.3	52.1	55.7	47.7	51.4	58	mean
2	51.7	58.4	59.5	62.0	56.9	48	min
3	55.3	57.4	64.5	63.2	57.4	69	max
4	59.8	64.2	64.3	68.9	60.2	5.5	stdev

True Stdev	a	b	c	d	e		
1	0.2	0.8	0.4	0.8	2.5	0.8	mean
2	0.5	0.6	1.3	0.5	0.4	0.2	min
3	0.5	0.9	1.3	0.7	1.1	2.5	max
4	0.4	0.8	0.6	0.4	0.6	0.5	stdev

Table A.8 Velocity averages at traverse locations

SP = 0.045 inch water, 72 inch into tunnel (Oct. 27)

True Velocity	a	b	c	d	e		
1	52.3	53.9	65.1	61.2	59.1	62	mean
2	53.0	53.4	67.3	66.3	60.7	52	min
3	61.2	54.9	65.4	65.3	65.3	69	max
4	67.3	60.0	66.4	69.0	64.4	5.5	stdev

True Stdev	a	b	c	d	e		
1	0.9	1.0	0.4	1.5	0.6	0.7	mean
2	1.0	0.4	0.4	0.5	0.8	0.4	min
3	1.2	0.4	0.5	0.5	0.8	1.5	max
4	0.8	0.9	0.9	0.6	0.6	0.3	stdev

Table A.9 Velocity averages at traverse locations

SP = 0.080 inch water, 18" into wind tunnel

True Velocity	a	b	c	d	e		
1	77.7	76.8	83.2	74.0	70.0	81	mean
2	75.9	76.9	88.3	84.5	77.5	70	min
3	81.5	82.4	89.6	82.6	81.2	90	max
4	82.6	82.6	88.9	88.8	82.9	5	stdev

Stdev True Velocity	a	b	c	d	e		
1	0.8	0.7	1.0	0.5	0.6	0.9	mean
2	0.5	1.2	0.7	1.6	0.6	0.5	min
3	1.1	0.7	0.7	3.3	0.7	3.3	max
4	1.1	0.6	0.7	0.7	0.8	0.6	stdev

Table A.10 Velocity averages at traverse locations

SP = 0.127 inch water, 18" into wind tunnel

True Velocity	a	b	c	d	e		
1	94.1	98.6	103.5	93.7	91.3	107	mean
2	101.4	101.7	118.5	109.9	98.8	91	min
3	105.5	108.8	114.2	114.4	109.0	122	max
4	113.4	115.9	121.6	121.0	113.0	9	stdev

True Stdev	a	b	c	d	e		
1	1.8	0.5	0.5	0.6	1.0	0.8	mean
2	1.0	0.4	0.6	1.1	0.4	0.4	min
3	0.6	0.5	1.3	1.6	1.1	1.8	max
4	0.6	0.6	1.1	0.7	0.5	0.4	stdev

Table A.11 Velocity averages at traverse locations

SP = 0.199 inch water, 18" into wind tunnel

True Velocity	a	b	c	d	e		
1	128.3	132.8	136.2	123.3	118.1	139	mean
2	128.7	135.0	152.7	143.3	126.9	118	min
3	141.2	142.2	150.6	146.3	141.8	153	max
4	143.9	146.2	151.5	151.6	147.7	10	stdev

True Stdev	a	b	c	d	e		
1	0.6	1.1	0.5	1.0	0.8	0.9	mean
2	0.6	0.8	1.2	0.6	1.6	0.5	min
3	1.2	0.6	0.5	1.5	1.5	1.6	max
4	0.8	1.0	0.5	0.7	1.1	0.4	stdev

Table A.12 Velocity averages at traverse locations

SP = 0.319 inch water, 18" into wind tunnel

True Velocity	a	b	c	d	e		
1	170.1	174.7	173.0	162.5	153.7	183	mean
2	173.3	178.0	198.6	186.6	167.8	154	min
3	173.3	185.9	196.5	195.0	184.3	203	max
4	193.6	198.9	203.4	200.5	189.9	14	stdev

True Stdev	a	b	c	d	e		
1	0.9	0.6	1.0	0.7	0.7	0.8	mean
2	1.1	0.7	0.9	0.8	0.5	0.5	min
3	1.1	1.4	0.6	0.6	1.3	1.4	max
4	0.9	0.5	0.8	1.0	0.9	0.3	stdev

Table A.13 Wind tunnel calibration summary data

Test Date	Hood static pressure (inch water) of wind tunnel			True V (fpm)	
	Average over duration	Range / 2	(Average SP)$^{1/2}$	Spatial Average	Std. dev.
24-Oct-03	0.045	0.0025	0.212	58.2	5
24-Oct-03	0.08025	0.0025	0.283	81	5
24-Oct-03	0.1267	0.00125	0.356	107	9
27-Oct-03	0.318875	0.00375	0.565	183	14
27-Oct-03	0.199125	0.00375	0.446229	139	10
27-Oct-03	0.03223	0.0025	0.17944	47	5
30-Oct-03	0.045	-	0.212132	59	5
30-Oct-03	0.045255	-	0.212728	58	5
30-Oct-03	0.045255	-	0.212728	62	5

Table A.14 Repeatability tests for setting air flowrate through nozzle

30-Jan-04		
Dwyer Rotameter: "093" = manufacturer's id (faint)		
Scale:	1 to 5 scfh	
Location:	Center of ball at 4.2 (red line placed)	
Direction Moved	**Run #**	**Lpm (from Gilibrator)**
Down	1	2.018
Up	2	2.021
Down	3	2.01
Up	4	2.014
Down	5	2.012
Up	6	2.033
Down	7	2.038
Up	8	1.996
Down	9	1.999
Up	10	2
run 1	11	2.003
run2	12	1.995
run3	13	1.992
	Average Lpm:	2.010
	stdev Lpm	0.015

Table A.15 Calibration of flow through ultrasonic nozzle

MasterFlex Calibration							
Pump Motor:	7520-35 (SN: 393810)				***Date:***	***10-Mar-04***	
Pump Head:	7519-10 (SN L02002207)				***Conditions:***	***68.6 F, 30%RH***	
Cartridges:	7519-75						
Two cartridges, in opposite direction of each other							
Occlusion setting for both: 3.5							
Density of oil (from MSDS) g/mL: 0.86							
Run #	Setting	Tare Wt.	Time	End Wt.	Net Wt.	g/min	mL/min
1	0.24	53.1	420.88	55.7	2.6	0.37	0.43
2	0.24	55.7	421.21	58.6	2.9	0.41	0.48
3	0.24	58.6	421.09	61.3	2.7	0.38	0.45
4	0.24	61.3	421.69	64.05	2.75	0.39	0.45
5	0.24	64.15	420.41	66.8	2.65	0.38	0.44
6	0.24	53	419.47	55.65	2.65	0.38	0.44
7	0.24	55.65	424	58.4	2.75	0.39	0.45
8	0.24	58.4	420.43	61.2	2.8	0.40	0.46
						Mean:	0.45
						Stdev:	0.016

Figure A.1 4-inch Orifice Calibration Curve

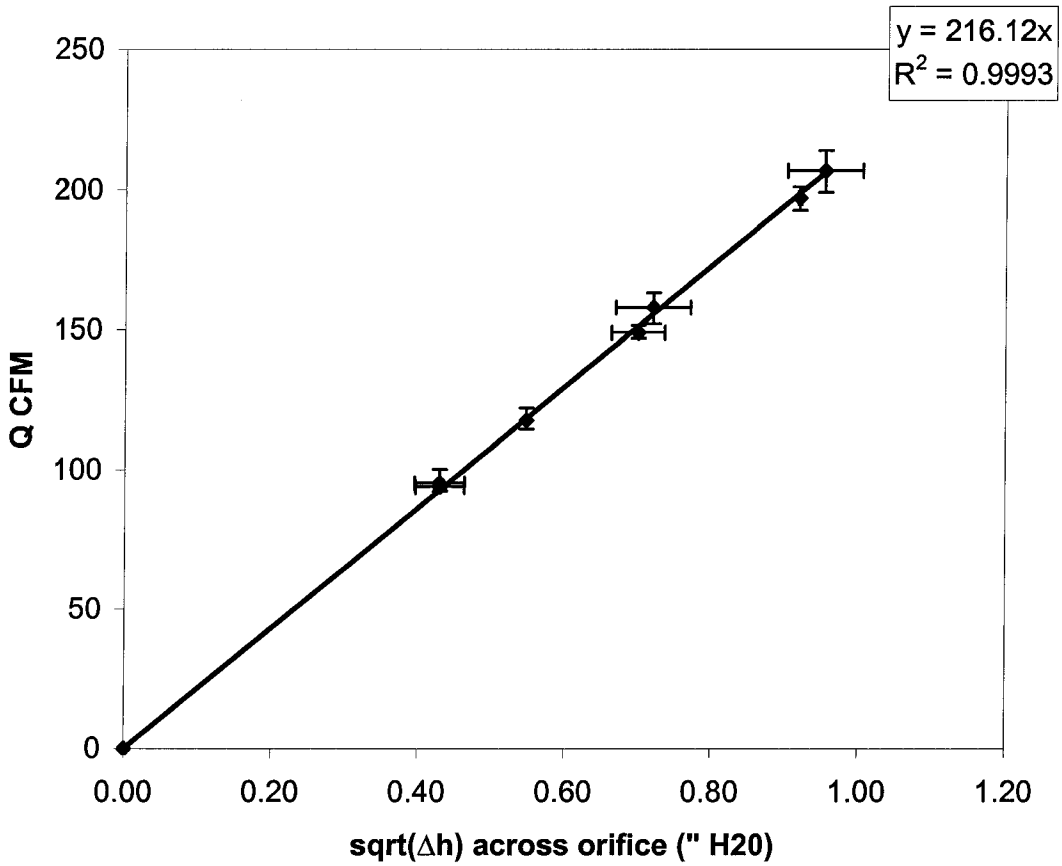

Figure A.2 Rotating Vane (TSI VelociCalc) calibration

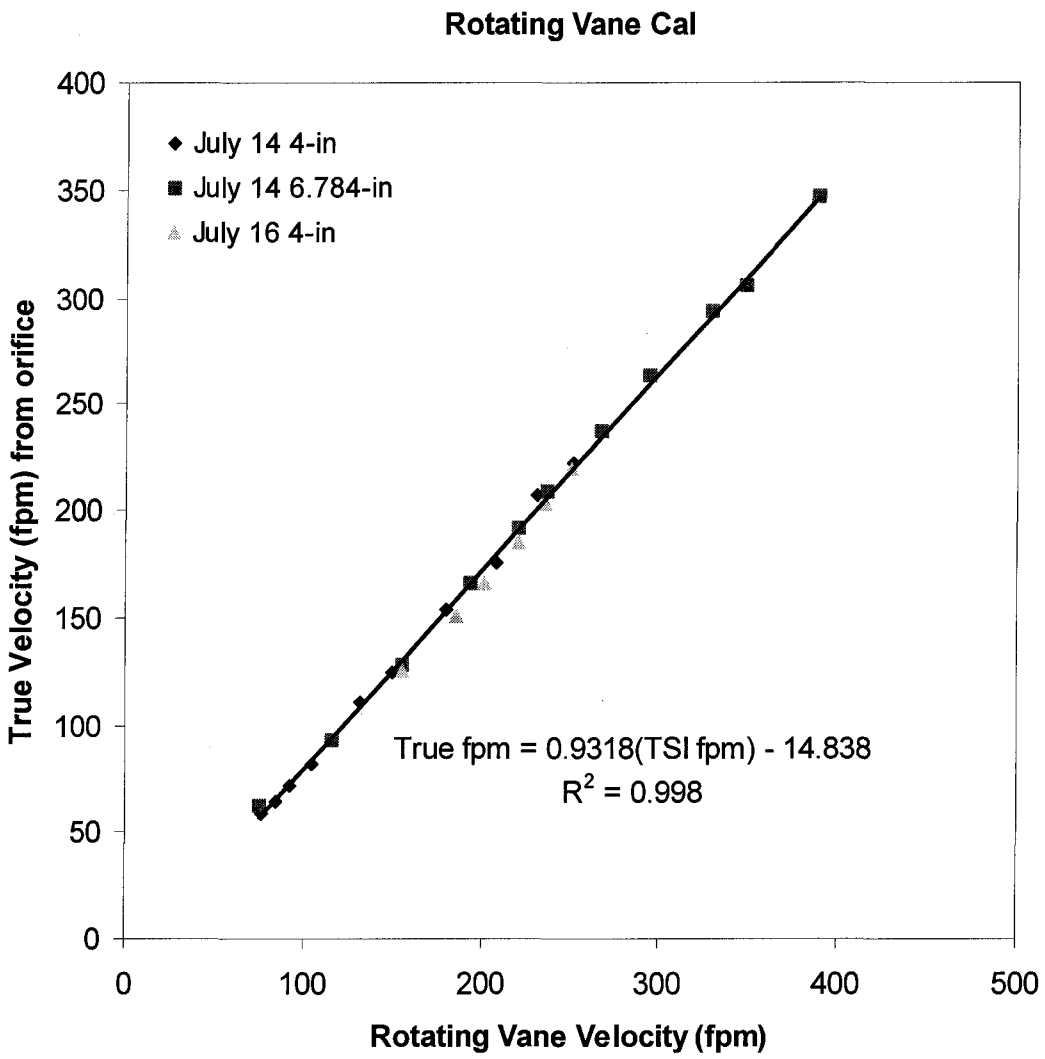

Figure A.3 Calibration of Probe 87-87 for TSI-IFA100

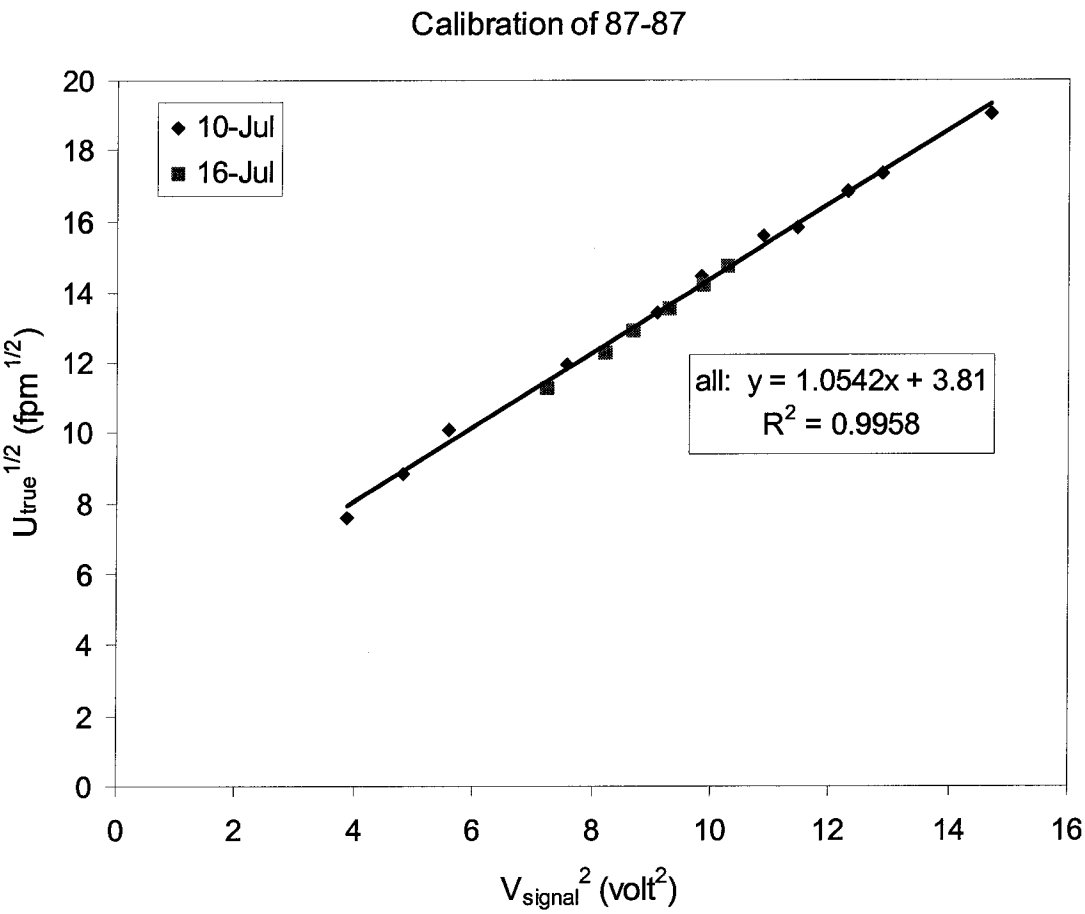

Figure A.4 Locations of Baity Air Lab wind tunnel velocity measurement traverse

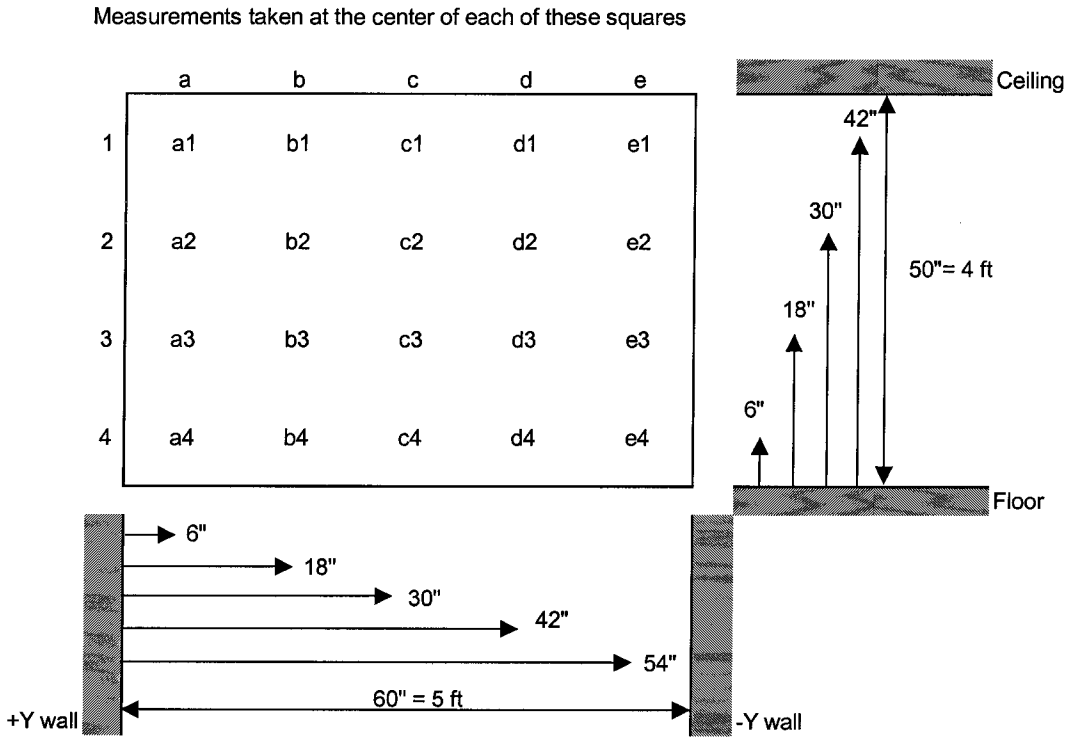

Figure A.5 Velocity measurement traverse

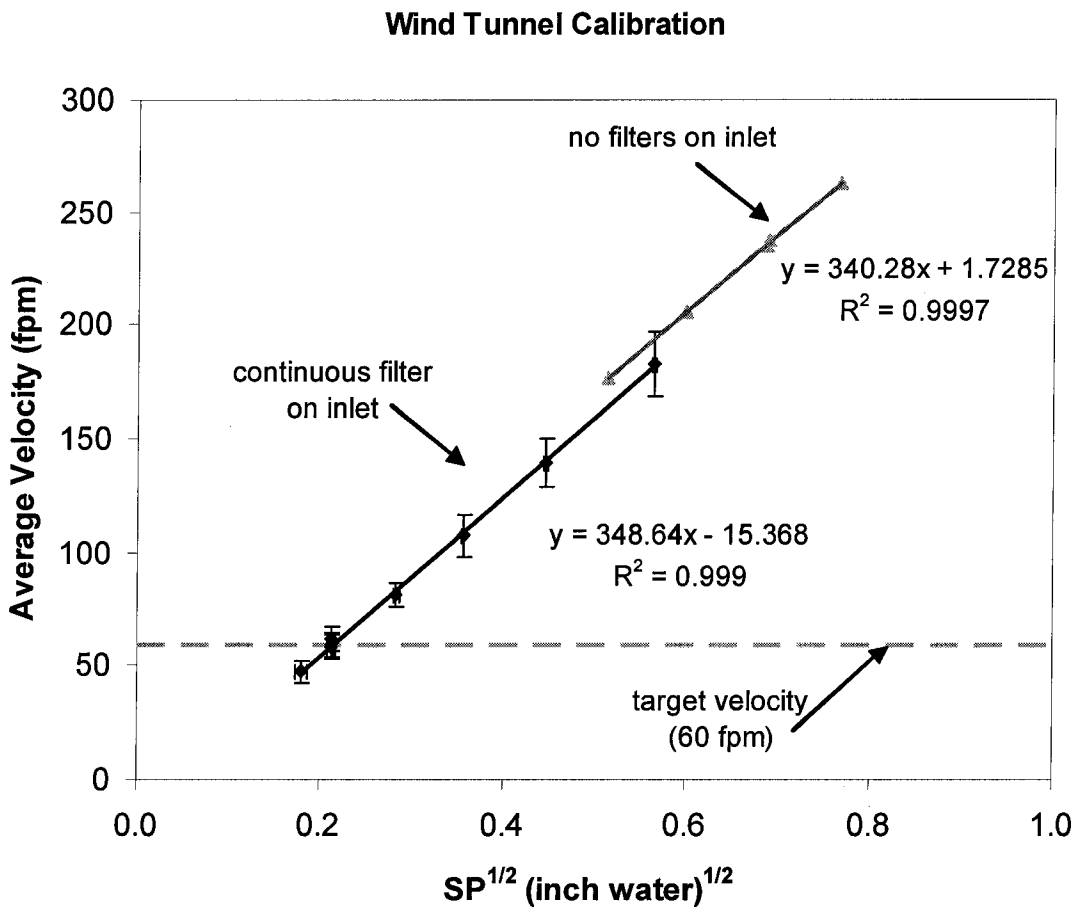

Figure A.6 Calibration of Rotameter used to monitor breathing rate (operation indicated by dashed horizontal lines)

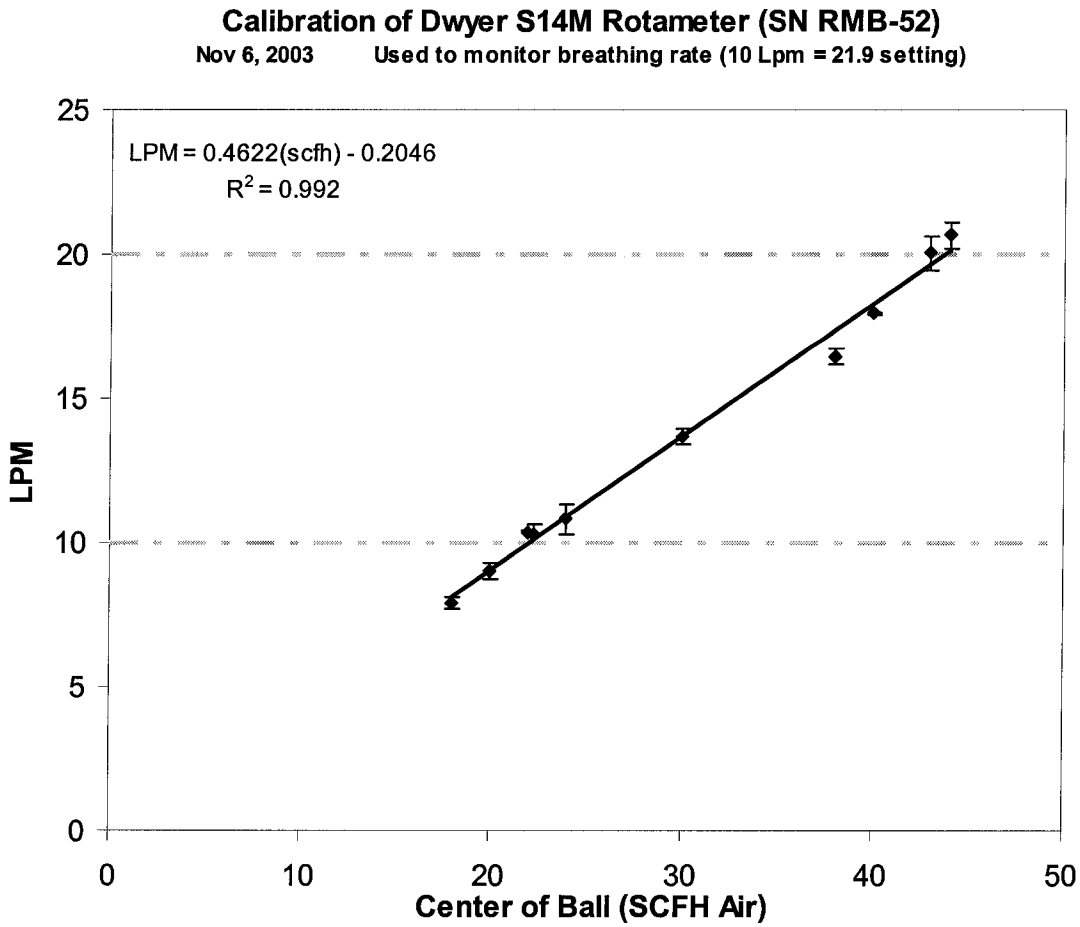

Figure A.7 Stability of supply air to nozzle

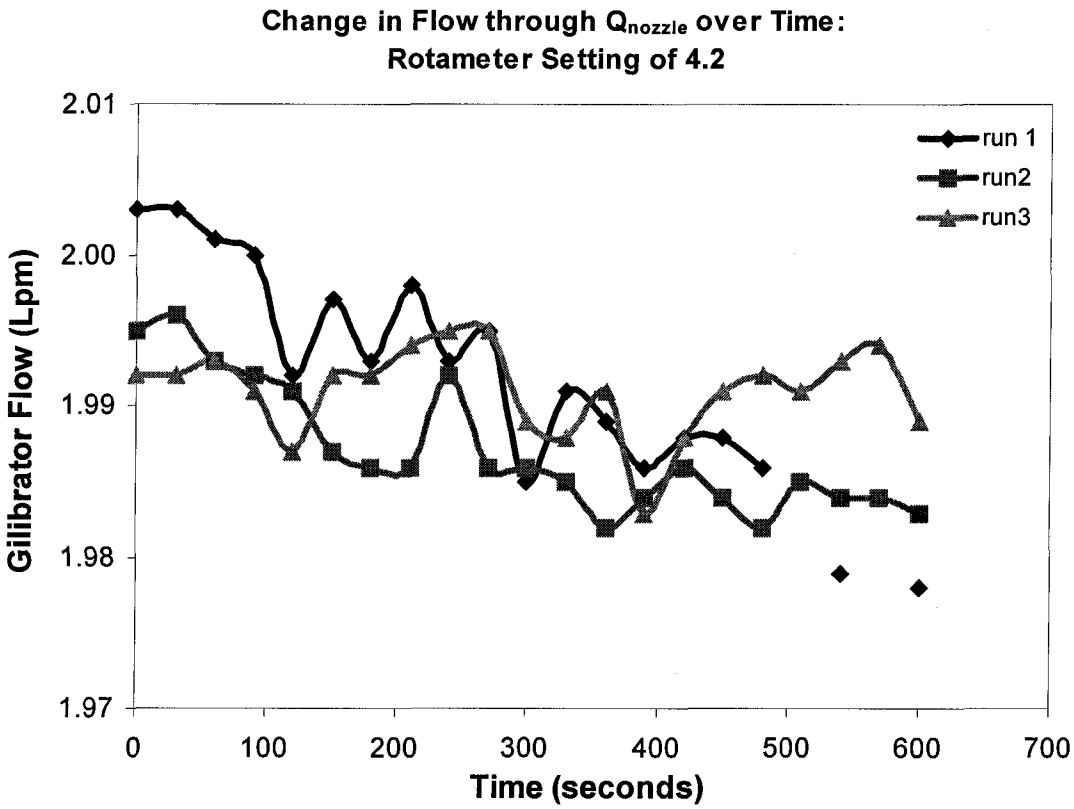

APPENDIX B:
VELOCITY DATA AND CALCULATIONS FOR CHAPTER 2

This appendix details analyses of data from laser Doppler anemometry study conducted in the U.S. EPA wind tunnel in Research Triangle Park, NC. The operational variability is examined, both for wind tunnel measures and breathing simulations. An examination of the measurement repeatability is discussed. Finally, the method used to conduct the comparative study of the mannequin velocity fields is detailed. The supporting data files accompanying this work are summarized in Table B.1.

Table B.1 Data files for Appendix B

File Name	Description	Discussion Section
B1-BigFree.xls	Large grid freestream velocity data and summary.	B.1.a
B2-All Freestream.xls	Freestream velocity data over study period. Contains spatial velocity summary.	B.1.a
B3-Setting History.xls	Daily freestream velocity summary and inhalation calibration data.	B.1.a, B.1.b
B4-Alldatawith turbulence.xls	Spreadsheet with all velocity data, including turbulence. Contains assessment of replicate data.	B.2.1, B.3
B5-Vel diff testing.xls	Statistical testing of velocity differences, by region.	B.3
B6-Zero radial velocity data.xls	Radial velocity contour determination data.	B.3.b

B.1 Operational Variations

Small differences in experimental conditions over time would affect velocity field measurements and subsequent comparisons. The primary contributors to experimental variability included temporal differences in the freestream velocity, changes in volumetric flow through the inhaling mannequin, and slight changes in the relative position of the mannequin and LDA. The following discusses the variability in these conditions that contributed to errors in the velocity measurements.

B.1.a Freestream Velocity

Freestream velocity measurements were made in the empty EPA wind tunnel to evaluate spatial and temporal velocity variation over the course of the study. Because the goal of this study was to compare the velocity fields associated with the two mannequins, the freestream velocity was carefully monitored to minimize its impact on the mannequin velocity fields. Thus, before collecting data, freestream velocity measurements were made. If the mean streamwise velocity was not 0.3 m s^{-1}, the wind tunnel flowrate was readjusted prior to beginning mannequin studies. Table B.2 summarizes the results of these freestream studies, detailed below.

Freestream Spatial Variation: Large Grid

In the empty wind tunnel, the large spatial variation study (N = 255) was performed once in the vertical plane of the mouth (X = 0) during mannequin studies. This plane extended +/- 175 mm laterally and 100 to –300 mm vertically, relative to the center of the mouth. This measurement surface did not extend all the way to the wind tunnel floor due to limitations of the optics. Due to problems with the laser system, the vertical velocity component (U_z) was not available during this analysis. The streamwise velocity, U_x, was greater at lower torso heights, nearer the wind tunnel floor, than at the head, although there was less than 6% variation across this plane. The mean horizontal velocity across this grid during this test was 0.302 m s^{-1}, with a standard deviation (s.d.) of 0.004 m s^{-1}. The turbulence intensity for the horizontal velocity component in this measurement area was 2.1%, with a standard deviation of 0.36%. The lateral component of velocity, U_y, also varied across this measurement area: more negative velocity measures occurred in the torso region of the mannequin's left side (-y) and more positive velocity measures occurred to the mannequin's right side (+y). The mean lateral velocity over this measurement area on this day was 0.004 m s^{-1}, with a standard deviation of 0.005 m s^{-1}. *(Data file: B1)*

Freestream Spatial Variation: Average over Study Duration

At the start and end of each of the 18 study days, velocity measurements in the empty wind tunnel were obtained and averaged by location to investigate the mean velocity at 32 locations, covering lateral distances +/-50 mm and vertical distances 50 to –100 mm,

relative to the mouth center. These measures were taken at two vertical planes: at the mouth center (X = 0 m) and upstream at X= -150 mm. Over the duration of the study, the mean lateral velocity across these areas was slightly positive, or to the mannequin's right side, at 0.005 m s^{-1}, and the mean vertical component was slightly negative, or downward, at –0.008 m s^{-1}. *(Data file: B2)*

Freestream Temporal Variation

Temporal variations within the wind tunnel were assessed over the 18 day study period. The velocity was averaged over the measurement volume for each test and evaluated over time. Over the duration of this study, the mean horizontal velocity within the wind tunnel was 0.300 (s.d. = 0.003) m s^{-1}. When analyzing freestream data by mannequin, no difference was observed in the mean study freestream velocity of each form (mean = 0.300 m s^{-1}, s.d. = 0.003 m s^{-1}, p=0.858, t-test, 2-tailed, homoscedastic). *(Data file: B3)*

B.1.b Breathing Simulation Variability

The volumetric flow rate through the inhaling mannequin was monitored throughout the study using a Bios DryCal. Time-weighted average inhalation rates over these study periods were 10.07 (s.d. = 0.017) Lpm for the anatomical mannequin and 10.06 (s.d. = 0.021) Lpm for the elliptical mannequin, sufficiently similar for the comparative analysis that followed. *(Data file: B3)*

B.2 Replicate Sampling Measurement Errors

Replicate velocity measurements were made at multiple locations throughout the study. The differences in replicate velocity data provided information on the system variability attributable to wind tunnel flowrate, inhalation flowrate, mannequin positioning, and initial positioning of the LDA measurement volume, all of which could vary throughout the study. Because replicate measurements were made on different days at 175 and 212 locations for the elliptical and anatomical form, respectively, differences between velocity measures at matched locations were analyzed. Table B.3 summarizes the mean, maximum, and minimum measurement difference in these sets of replicate data. Table B.3 (a) presents velocity differences in Cartesian coordinates, whereas Table

B.3 (b) uses the cylindrical coordinate system, useful in analyzing the lateral and vertical velocity profiles *(data file: B4).*

When considering all replicate data, the maximum measurement difference in velocity measurements at any one location was 0.020 m/s, approximately 6% of the freestream streamwise velocity. Thus, when comparing velocities between the mannequins, differences of less than 0.020 m/s at any one location may be due to measurement errors and, hence, should not indicate significant velocity differences between mannequins. Upon compilation of the 387 replicate measures, the mean measurement error for each velocity component was determined to be 0.006 m s^{-1} (s.d. = 0.005 m s^{-1}), in the cylindrical coordinate system. Thus, over a range of locations where velocity differences were investigated, a mean velocity difference of less than 0.006 m s^{-1} should not indicate significantly different velocity fields, useful in conducting t-tests. We would be 95% confident that a velocity difference less than 0.016 m s^{-1} (2 s.d.) was not attributable to measurement error, and 99% confident that differences less than 0.021 m s^{-1} (3 s.d.) were attributable to measurement errors.

The location near the surface of the anatomical mannequin's nose (-11, 0, 20 mm) had a larger repeatability problems (maximum measurement difference of 0.027 m s^{-1}). LDA positioning differences of fractions of a millimeter between days would provide significantly different measurements this close to the mannequin surface. Even though the replicate measurement error at this one location was higher than elsewhere, the difference of streamwise velocity (U_x) between the two mannequins more than exceeded the measurement error observed at this location: ($U_{X,A} - U_{X,E}$) was -0.087 m s^{-1}, nearly four times the maximum measurement error. Thus, the effect of the high measurement error at this one location was minimal in the overall analysis.

B.3 Velocity Comparison Methodology

Velocity data from the two mannequins were paired by sample location *(data file: B5).* Where replicate data existed, the mean of each velocity component was used. The magnitude of velocity differences and the size of the approaching streamtube were examined statistically to evaluate differences between the two mannequin's flow fields.

B.3.a Velocity Comparison

Individual and grouped velocity difference data were examined using the three criteria, using two-tailed t-tests:

(a) Mean velocity difference was not zero (H_o: p = Pr [mean difference = 0])

(b) Mean velocity difference exceeded 0.006 (H_o: p = Pr [mean difference $\leq$ 0.006])

(c) Mean velocity difference exceeded 0.020 (H_o: p = Pr [mean difference $\leq$ 0.020])

For a given region, if the difference in mean velocities between the two mannequins was significantly greater than 0.006 m s^{-1}, statistical significance was identified. If the velocity difference between of the two forms was also significantly greater than 0.020 m s^{-1}, the maximum measurement error throughout the study, more significance was given to the finding.

These tests were conducted first for regions within a coronal plane (*i.e.*, X = constant) and within regions across multiple planes. For instance, in the X = -11 mm coronal plane, the average streamwise velocity difference was 0.0147 m s^{-1}, with a standard deviation of 0.0294 m s^{-1}. T-tests indicated velocities were significantly different from 0 m s^{-1} ($p < 0.00001$) and from 0.006 m s^{-1} ($p = 0.0013$), but were not significantly different from 0.020 m s^{-1} ($p = 0.99$). However, when considering locations only in the region of the chin ($Z \leq -20$ mm), significance was identified for each of the three test criteria at X = -11 mm at all Y = -30 to +30 mm ($p < 0.00001$). Velocity differences were also assessed over the region including X = -11, -15 and -20 mm, over the same $Z \leq -20$ mm, and significant differences for all criteria were again identified ($p < 0.00001$). However, the streamwise velocity differences at similar locations at X = -30 mm were not significantly different from 0.020 m s^{-1}, so these were not included in the significant region.

Even though statistically significant differences between velocities were identified, the significance of the *magnitude* of the difference in velocity was also needed to understand the physical importance of the velocity difference. Thus, after significant velocity differences relative to the measurement errors were identified, these locations were evaluated to determine if the velocity magnitude associated with the elliptical form was +/-10% the value of the anatomical form. The value of 10% was established because

the mean turbulence intensity over all velocity measurements was 3.1% (s.d. = 2.1). Hence, 99% of the time, the turbulence intensity at any one location was < 9.4%. A measured velocity difference of 10% or more would indicate that the velocity difference was significantly greater than the turbulence intensity.

Once a region was identified as having significantly different velocities relative to the measurement error, the mean velocity ratio was calculated over this region, using the velocity difference divided by the velocity associated with the anatomical form. If this velocity difference, and the majority of locations within the region under study, exceeded +/-10%, the region was identified as having significantly different velocity and reported. These results have been presented graphically in Figures 2.5 through 2.7.

B.3.b Zero Radial Velocity Contours

A second method to evaluate velocity field differences used velocity contour lines to investigate differences in the size and shape of the streamtube of air approaching the mannequin mouth. At a given coronal plane, *i.e.*, constant X-values, coordinates were identified where velocity was directed radially toward the mouth. These positions defined the "streamtube" of inhaled air. These contours were generated using cubic spline interpolations of the velocity field data *(data file: B6)*. The cross-sectional area of this streamtube was compared between forms. A significantly larger streamtube for a given mannequin would indicate differences in the flow field, which could impact particle transport into the inhaling mannequin. If the streamtubes were sufficiently similar in size and shape, then the simpler elliptical cylinder would be sufficient for modeling particle inhalability; however, if the streamtubes were significantly different, the simplified elliptical form representing a human form would be inadequate to reflect the flow field of an inhaling human.

Paired t-tests were conducted for the height and width of the zero radial velocity curves *(data file: B4)*. Only two planes exhibited radially inward velocity above the mouth for both mannequins: X = -11 and -15 mm. At X = -11 mm, the zero radial velocity contours were not significantly different in height ($p = 0.36$) but it was significantly wider for the anatomical form ($p = 0.0007$). At X = -15 mm, the zero radial

velocity contour was significantly taller ($p = 0.0007$) and wider ($p = 0.0002$) with the anatomical form. Summary information is provided in Table B.4.

Table B.2 Freestream velocities in empty wind tunnel, mean (standard deviation)

	U_x (m s^{-1})	U_y (m s^{-1})	U_z (m s^{-1})
Spatial Variation: Large Grid (255 locations)	0.302 (0.004)	0.004 (0.005)	n/a
Spatial Variation: Average of freestream over duration of tests (18 days, 36 measurement locations each)	0.301 (0.002)	0.005 (0.003)	-0.008 (0.005)
Temporal Variation (18 days, mean per day)	0.300 (0.003)	0.004 (0.005)	-0.006 (0.008)
Temporal Variation: Elliptical mannequin (11 days)	0.300 (0.003)	0.002 (0.004)	-0.001 (0.007)
Temporal Variation: Anatomical mannequin (7 days)	0.300 (0.003)	0.006 (0.006)	-0.011 (0.007)

Table B.3 Velocity measurement differences between replicate data (m s^{-1}) using (a) Cartesian coordinate and (b) cylindrical coordinate systems

(a)

	Elliptical Mannequin (175 replicate locations)			Anatomical Mannequin* (212 replicate locations)			Both Forms (387 replicate locations)		
	U_x	U_y	U_z	U_x	U_y	U_z	U_x	U_y	U_z
Maximum difference	0.020	0.019	0.017	0.018* (0.027 w/nose)	0.016	0.018	0.020	0.018	0.018
Minimum difference	0.000	0.000	0.000	0.000	0.000	0.000	0.000	0.000	0.000
Mean of differences (s.d.)	0.006 (0.005)	0.006 (0.004)	0.007 (0.005)	0.005 (0.004)	0.004 (0.003)	0.003 (0.003)	0.005 (0.004)	0.005 (0.004)	0.003 (0.003)
Mean over all measures	0.006 (0.005)			0.004 (0.004)			0.005 (0.004)		

*data from (-11,0,20) = nose was excluded from this data

(b)

	Elliptical Mannequin (175 replicate locations)			Anatomical Mannequin* (212 replicate locations)			Both Forms (387 replicate locations)		
	U_x	U_r	U_t	U_x	U_r	U_t	U_x	U_r	U_t
Maximum difference	0.020	0.019	0.018	0.018*	0.015	0.016	0.020	0.019	0.018
Minimum difference	0.000	0.000	0.000	0.000	0.000	0.000	0.000	0.000	0.000
Mean of differences (s.d.)	0.006 (0.005)	0.009 (0.005)	0.009 (0.005)	0.005 (0.004)	0.004 (0.003)	0.003 (0.003)	0.005 (0.004)	0.006 (0.005)	0.006 (0.006)
Mean over all measures	0.008 (0.005)			0.004 (0.004)			0.006 (0.005) mean+2sd = 0.016 mean+3sd=0.021		

Table B.4 Zero-radial velocity curve differences for (a) X = -11 mm, (b) X = -15 mm.

(a) X = -11 mm

Width Test				Height Test			
z (mm)	Elliptic ΔY	Anatomic ΔY	$\Delta Y_A - \Delta Y_E$	y (mm)	Elliptic ΔZ	Anatomic ΔZ	$\Delta Z_A - \Delta Z_E$
-30	37.49	55.17	17.68	25		2.3333	2.3333
-25	35.55	43.18	7.63	20		6.6667	6.6667
-20	33.82	35.93	2.10	15	16.5385	35	18.4615
-15	32.07	33.09	1.02	10	30	41.3889	11.3889
-10	28.82	32.26	3.44	5	45.9091	45.3509	-0.5582
-5	25.84	30.88	5.04	0	50.4545	46.6393	-3.8152
0	20.37	29.06	8.69	-5	47.6923	41.7742	-5.9181
5	16.88	24.88	8.01	-10	32.5	34.75	2.25
10	15.96	17.92	1.95	-15	19.2308	20	0.7692
15	11.82	8.17	-3.65	-20		7	7
20	1.21	0.00	-1.21	-25		2.0833	2.0833
t-test p-value:			0.025198	t-test p-value:			0.364094

(b) X = -15 mm

Width Test				Height Test			
z (mm)	Elliptic ΔY	Anatomic ΔY	$\Delta Y_A - \Delta Y_E$	y (mm)	Elliptic ΔZ	Anatomic ΔZ	$\Delta Z_A - \Delta Z_E$
30	-	-	-	30	0	5.3333	5.3333
25	-	-	-	25	0	9.1667	9.1667
20	-	-	-	20	0	18.75	18.75
15	-	-	-	15	13.3333	28.61111	15.27781
10	0	7.92892	7.92892	10	25	36.66667	11.66667
5	0	14.52586	14.52586	5	29.16667	41.1905	12.02383
0	0	18.35495	18.35495	0	30	41.8421	11.8421
-5	21.3636	28.85	7.4864	-5	29.74359	29.87805	0.134459
-10	27.8214	34.0643	6.2429	-10	26.5	26.66667	0.16667
-15	31.0588	38.8011	7.7423	-15	19.2857	18.6364	-0.6493
-20	34.372	43.9367	9.5647	-20	0	9.6667	9.6667
-25	37.3	56.6667	19.3667	-25	0	6	6
-30	39.8674	60	20.1326	-30	0	2	2
t-test p-value:			0.000186	t-test p-value:			0.000686

APPENDIX C:
PARTICLE DATA AND CALCULATIONS FOR CHAPTER 2

This appendix details the particle aspiration studies presented in Chapter 2. A discussion of experiment preparation is provided, followed by a discussion on the optical particle counting method. Finally, the methods to determine aspirated mass and particle size calculations are detailed. Table C.1 summarizes the supporting data found on the data disc accompanying this dissertation.

Table C.1 Data files for Appendix C

File Name	Description	Discussion Section
/Images	Particle images from optical concentration studies	C.2
C1-Optical Particle Feb 23.xls	Optical particle count concentration studies data and analysis for Feb 23 run	C.2
C2-Optical Particle Feb 24.xls	Optical particle count concentration studies data and analysis for Feb 24 run and combined data	C.2
C3-Baseline mass.xls	Baseline mass concentration study (U_o=0.3 m s^{-1}, Q_m=10 Lpm) data and analysis	C.3
C4-High Uo mass.xls	High freestream velocity mass concentration study (U_o=0.6 m s^{-1}, Q_m=10 Lpm) data and analysis	C.3
C5-High Qm mass.xls	High breathing rate mass concentration study (U_o=0.3 m s^{-1}, Q_m=20 Lpm) data and analysis	C.3
C6-Mass Summary.xls	Summary of mass study conditions	C.3

C.1 Particle Aspiration Experiments

Particle aspirations experiments were conducted in the Baity Air Laboratory wind tunnel. Details of the calibration of this system are provided in Appendix A. The two small-scale mannequins were alternately placed in the wind tunnel, facing the wind, to measure aspirated concentrations for three test conditions. The Lechler ultrasonic nozzle generated the test aerosol, with the same position relative to the mannequin mouth for comparative studies. The nozzle was oriented horizontally, as illustrated in Figure C.1. Test conditions are detailed in Table C.2. Optical sizing and concentration measurements

were made on the baseline condition only. Mass concentration studies were conducted at all test conditions. For each test condition, a total of six replicate experiments were conducted, with three replicate tests for each mannequin on a given day. The mannequins were rotated into the wind tunnel for study following a test schedule of E-A-A-E-E-A or A-E-E-A-A-E, depending on the given day.

For all tests, inhaled aerosol was collected onto treated polycarbonate filters with a 2-μm pore size. Filters were pre-treated with Nyebar Q to allow the liquid particles to bead onto the surface of the filter for subsequent optical counting. Filters were prepared at least 24 hours prior to use to allow for the carrier solvent in Nyebar to completely evaporate prior to use.

The aerosol generator was operated prior to experiments to maximize system stability, but power to the generator was stopped when the filters were placed into the filter holder fitted inside the mannequin mouth. As soon as the filter was seated into the mannequin mouth, flow from the vacuum pump was started and adjusted to the appropriate rate: stability was assessed before introducing particles into the system. Once the operating conditions for inhalation, wind tunnel, and air through nozzle were confirmed, the power was supplied to the ultrasonic nozzle and the liquid pump. The recorded duration of the experiment was the time that aerosol was generated in the wind tunnel. There was about a 3 second delay between applying power to the nozzle / liquid pump and actual aerosol generation: the latter was the start time. When the desired sampling duration was reached, power to the aerosol generator and its liquid pump was cut, stopping aerosol generation. However, the mannequin continued to inhale for one additional minute, sufficient to allow any aerosol to travel to the exit of the wind tunnel. After the wind tunnel was purged, the sample was retrieved from the mannequin filter holder and, if scheduled, the mannequins were swapped and positioning reconfirmed.

C.2 Optical Particle Counting

To minimize particle overloading on the 25-mm diameter filters, short one-minute sample times were required. Because the spread factor for the oil aerosol collected on the Nyebar treated filter could change over time (Prabhu, 2003), samples destined for optical analysis were analyzed the same day.

These transparent filters were transported to the UNC Microscopy Lab and prepared for bright field analysis. The filters were placed on a glass slide. On the underside of the slide, a sampling grid was attached, where 5 rings of equal area were divided into 12 wedges. Figure C.2 illustrates this sampling grid. Images were made of particles at the center of each of these 60 equal areas for analysis (*Data file:\Images subdirectory to Appendix C.*) The file names for the images reference the wedge number (1 through 12) and the ring letter (a = outermost through e = innermost). A 4x magnification objective was used, and a calibration of 0.416 pixels per mm was provided. The area of each image was 1.77 mm^2, and the total area of the 60 images counted was 1.0612 cm^2, resulting in the examination of nearly 22% of the total filter area. Figure C.3 illustrates an image (anatomical, baseline, wedge 10, ring a) along with the image of the scale used to calibrate the SCION software, used to process the images. The dark circles are the liquid particles, whereas the smaller dots represent the filter pores.

Imaging software (SCION) was used to measure each particle's area and minimum and maximum diameters. Only particles with centers located on the image area were included in particle counts. For particles wholly contained within the image, the particle diameter was calculated from the area information directly. Because the collected liquid particles were round, size estimation was possible for particles on the edge of the image. Less than full particles were identified during image processing, and the ratio of the maximum to minimum diameters was used to determine how much of the particle was in the image field, as illustrated in Figure C.4. If the diameter ratio exceeded 2.05, the center of the particle was not be on the image and the particle was excluded. If the diameter ratio was less than 2.05, the center of the particle was judged to be on the image and the maximum diameter was assigned to the particle.

Because liquid droplets flatten as they deposit onto the collection filter, adjustments to the measured particle size were needed. The spread factor, defined as the ratio of flattened particle to airborne particle diameter, had been determined by Prahbu (2003) as 1.31 for the materials used in this study. The measured particle diameter was divided by this value to provide the size of the airborne particle that was aspirated by the study mannequin. Particle size and count data were totaled for each filter analyzed, and was multiplied by the ratio of filter area to total sampled area to determine the total aspirated

particle count *(Data files: C1 and C2).* Data were pooled over all replicate tests, and the count median diameters were identified as 60.6 μm and 60.2 μm for the elliptical and anatomical mannequin, respectively, illustrated by Figure C.5. Tables C.3 and C.4 summarize the binned particle frequency data, illustrated in Figure C.6.

C.3 Aspirated Mass Concentration

Because the short sample time required for optical analysis of inhaled particles, additional comparative tests were conducted using gravimetric measures of inhaled particle concentration. These aspiration tests lasted between 5 to 7 minutes. Blanks were collected prior to each mannequin test, to ensure stability in treated filter mass and to evaluate whether any particulates were contaminating the wind tunnel. The average blank "concentration" over all samples was a loss of 0.007 mg m^{-3}, orders of magnitude less than the aerosol concentrations measured. Table C.5 presents the mass concentration data for the velocity conditions studied *(Data file: C6).* Even with the large variability within a given test condition, the mass aspirated by the elliptical mannequin was greater than that of the anatomical mannequin. Two-tailed t-tests were conducted both within test condition (n=6) and over all test conditions, and significant differences in aspirated particle concentration were identified ($p = 0.00002$ to 0.02).

Table C.2 Aerosol aspiration test conditions. X locations were measured from wind tunnel entrance, and Z locations were measured from wind tunnel floor.

Test Reference	Freestream velocity, m s^{-1} (hood SP, in wg)	Breathing Rate Lpm (Rotameter Setting, scfh)	Coordinates of Nozzle Center (cm)	Mannequin Mouth (cm)
Baseline	0.3 (0.045)	10 (22.3)	X = 30.9 Z = 101.6	X = 184.7 Z = 64.8
High U_o	0.9 (0.3)	10 (22.3)	X = 30.9 Z = 80.05	X = 184.7 Z = 64.8
High Q_m	0.3 (0.045)	20 (43)	X = 30.9 Z = 101.6	X = 184.7 Z = 64.8

Table C.3 Pooled and binned particle count distribution data for elliptical mannequin

Particle Range (μm)	Midpoint (μm)	Number of particles in range	Fraction of particles	Fraction of particles/ 3 μm bin
20 to 23	21.5	0	0	0.00000
23 to 26	24.5	0	0	0.00000
26 to 29	27.5	0	0	0.00000
29 to 32	30.5	0	0	0.00000
32 to 35	33.5	0	0	0.00000
35 to 38	36.5	0	0	0.00000
38 to 41	39.5	0	0	0.00000
41 to 44	42.5	0	0	0.00000
44 to 47	45.5	2	0.003472	0.00116
47 to 50	48.5	19	0.032986	0.01100
50 to 53	51.5	42	0.072917	0.02431
53 to 56	54.5	70	0.121528	0.04051
56 to 59	57.5	101	0.175347	0.05845
59 to 62	60.5	102	0.177083	0.05903
62 to 65	63.5	86	0.149306	0.04977
65 to 68	66.5	55	0.095486	0.03183
68 to 71	69.5	38	0.065972	0.02199
71 to 74	72.5	15	0.026042	0.00868
74 to 77	75.5	15	0.026042	0.00868
77 to 80	78.5	8	0.013889	0.00463
80 to 83	81.5	6	0.010417	0.00347
83 to 86	84.5	8	0.013889	0.00463
86 to 89	87.5	3	0.005208	0.00174
89 to 92	90.5	2	0.003472	0.00116
92 to 95	93.5	1	0.001736	0.00058
95 to 98	96.5	2	0.003472	0.00116
98 to 101	99.5	0	0	0.00000
101 to 104	102.5	1	0.001736	0.00058
104 to 107	105.5	0	0	0.00000
107 to 110	108.5	0	0	0.00000
Total:		576	1	0.33333

Table C.4 Pooled and binned particle count distribution data for anatomical mannequin

Particle Range (mm)	Midpoint (mm)	Number of particles in range	Fraction of particles	Fraction of particles/ 3 mm bin
20 to 23	21.5	1	0.000996	0.00033
23 to 26	24.5	1	0.000996	0.00033
26 to 29	27.5	0	0	0.00000
29 to 32	30.5	0	0	0.00000
32 to 35	33.5	2	0.001992	0.00066
35 to 38	36.5	0	0	0.00000
38 to 41	39.5	4	0.003984	0.00133
41 to 44	42.5	11	0.010956	0.00365
44 to 47	45.5	44	0.043825	0.01461
47 to 50	48.5	33	0.032869	0.01096
50 to 53	51.5	64	0.063745	0.02125
53 to 56	54.5	90	0.089641	0.02988
56 to 59	57.5	169	0.168327	0.05611
59 to 62	60.5	203	0.202191	0.06740
62 to 65	63.5	150	0.149402	0.04980
65 to 68	66.5	108	0.10757	0.03586
68 to 71	69.5	66	0.065737	0.02191
71 to 74	72.5	21	0.020916	0.00697
74 to 77	75.5	8	0.007968	0.00266
77 to 80	78.5	7	0.006972	0.00232
80 to 83	81.5	7	0.006972	0.00232
83 to 86	84.5	10	0.00996	0.00332
86 to 89	87.5	2	0.001992	0.00066
89 to 92	90.5	1	0.000996	0.00033
92 to 95	93.5	2	0.001992	0.00066
95 to 98	96.5	0	0	0.00000
98 to 101	99.5	0	0	0.00000
101 to 104	102.5	0	0	0.00000
104 to 107	105.5	0	0	0.00000
107 to 110	108.5	0	0	0.00000
Total:		1004	1	0.33333

Table C.5 Particle mass concentration aspirated by mannequins

U_o, fpm	Q_s, Lpm	Aspirated Concentration, mg m^{-3}			Ave. Difference	p-value (2-tailed t-test)
		Anatomical	Elliptical	E – A		
177	10	11.0	13.3	2.3	3.4	0.0029
177	10	6.7	12.2	5.5		
177	10	10.3	13.8	3.5		
177	10	4.8	9.6	4.8		
177	10	4.5	6.1	1.6		
177	10	4.7	7.1	2.4		
59	10	9.2	18.0	8.8	8.6	0.0042
59	10	6.0	9.6	3.6		
59	10	4.0	16.8	12.8		
59	10	8.9	15.6	6.8		
59	10	7.3	12.5	5.3		
59	10	7.5	21.8	14.3		
59	20	4.9	13.1	8.1	3.8	0.0268
59	20	5.3	8.3	3.1		
59	20	6.0	7.3	1.3		
59	20	3.9	6.3	2.4		
59	20	4.6	5.6	1.0		
59	20	6.0	13.0	7.0		
Average:		6.4	11.7	5.3	5.3	1.94E-05
Standard deviation:		2.2	4.6	3.8		

Figure C.1 Nozzle orientation in wind tunnel (tubes and cords were fixed to top of wind tunnel during experiments)

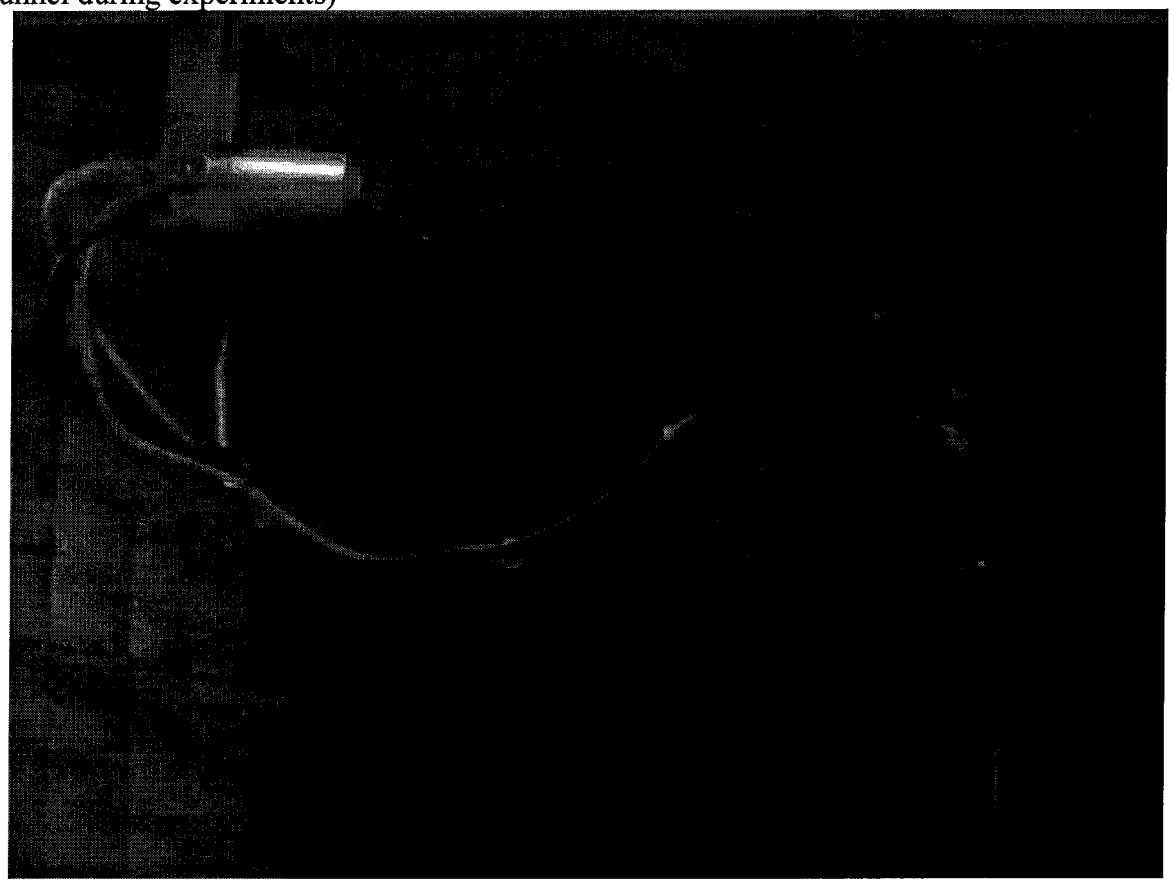

Figure C.2 Sampling grid for 25 mm filter. Boxes indicate the locations of the 60 images.

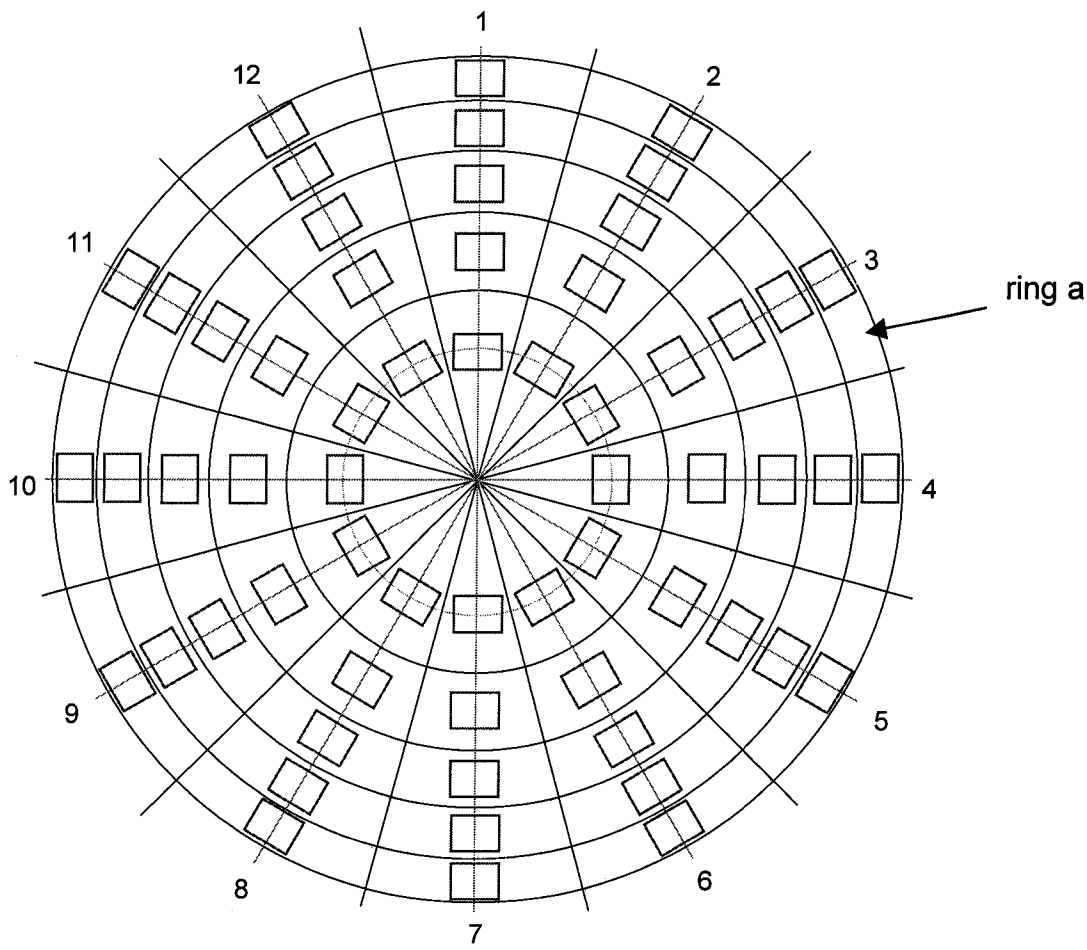

Figure C.3 Particle image (filename: 2_24-1 10d) and BF FXA_DEI-750 4x calibration scale (distance between small lines = 10 μm)

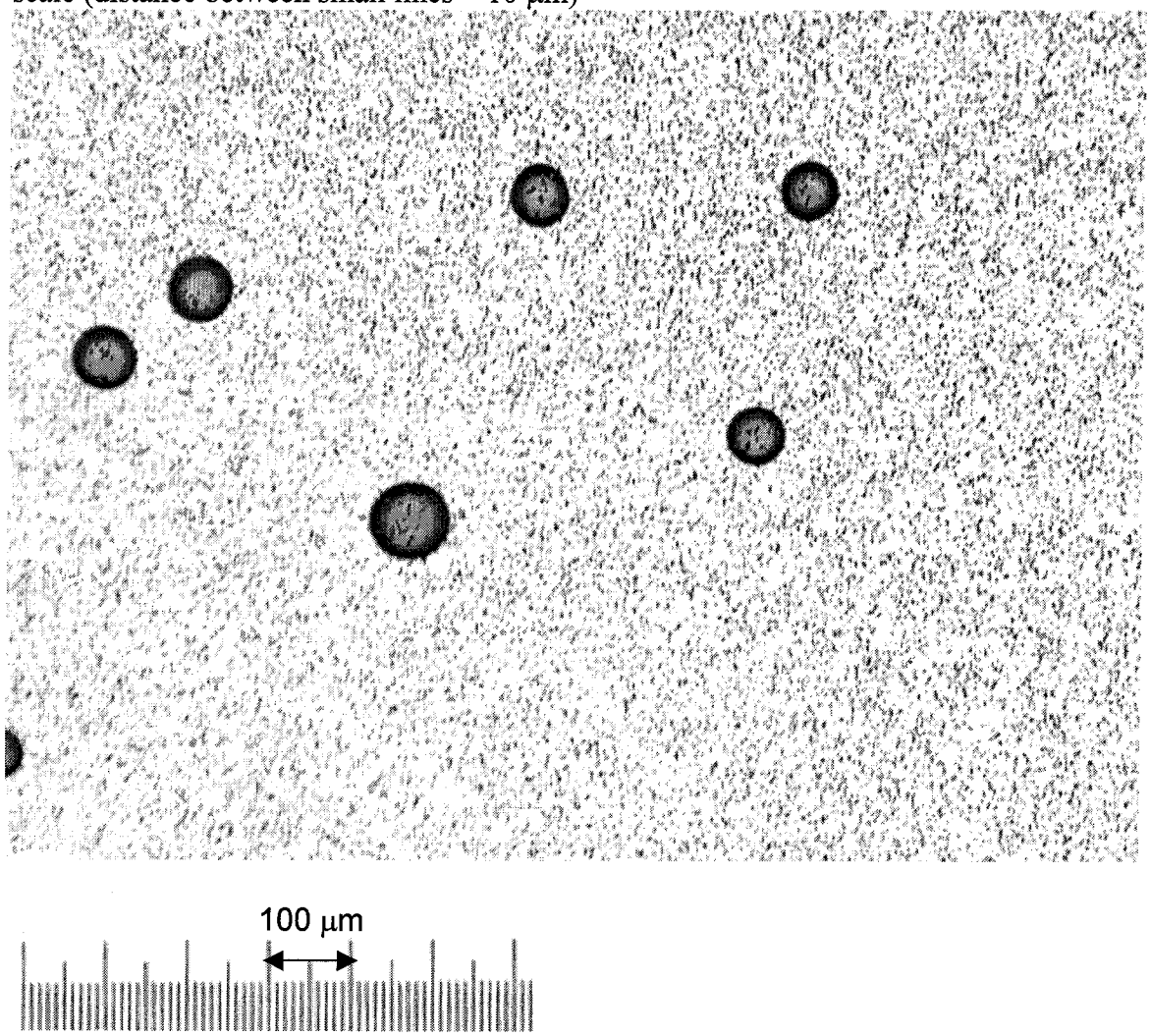

Figure C.4 Illustration of analysis for particles on the edge of the image

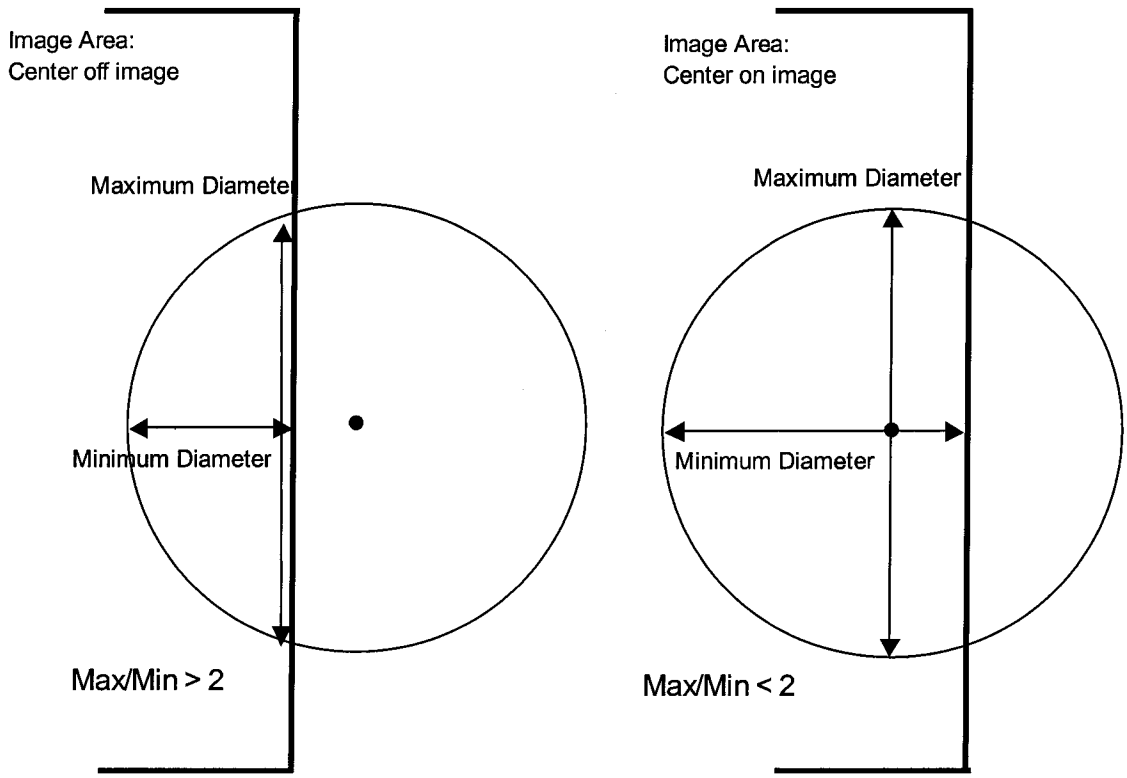

Figure C.5 Particle size distribution for pooled replicate data.

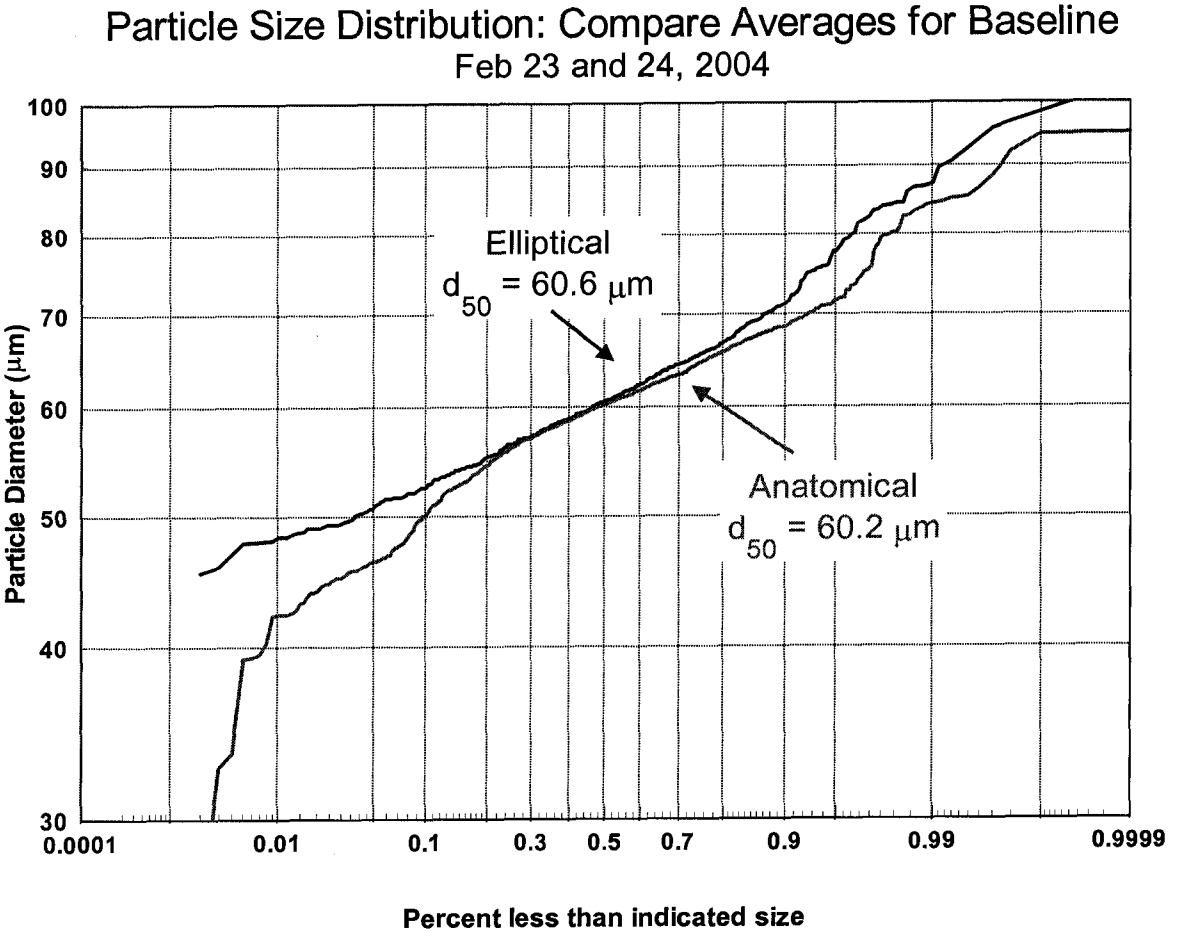

Figure C.6 Particle frequency distribution

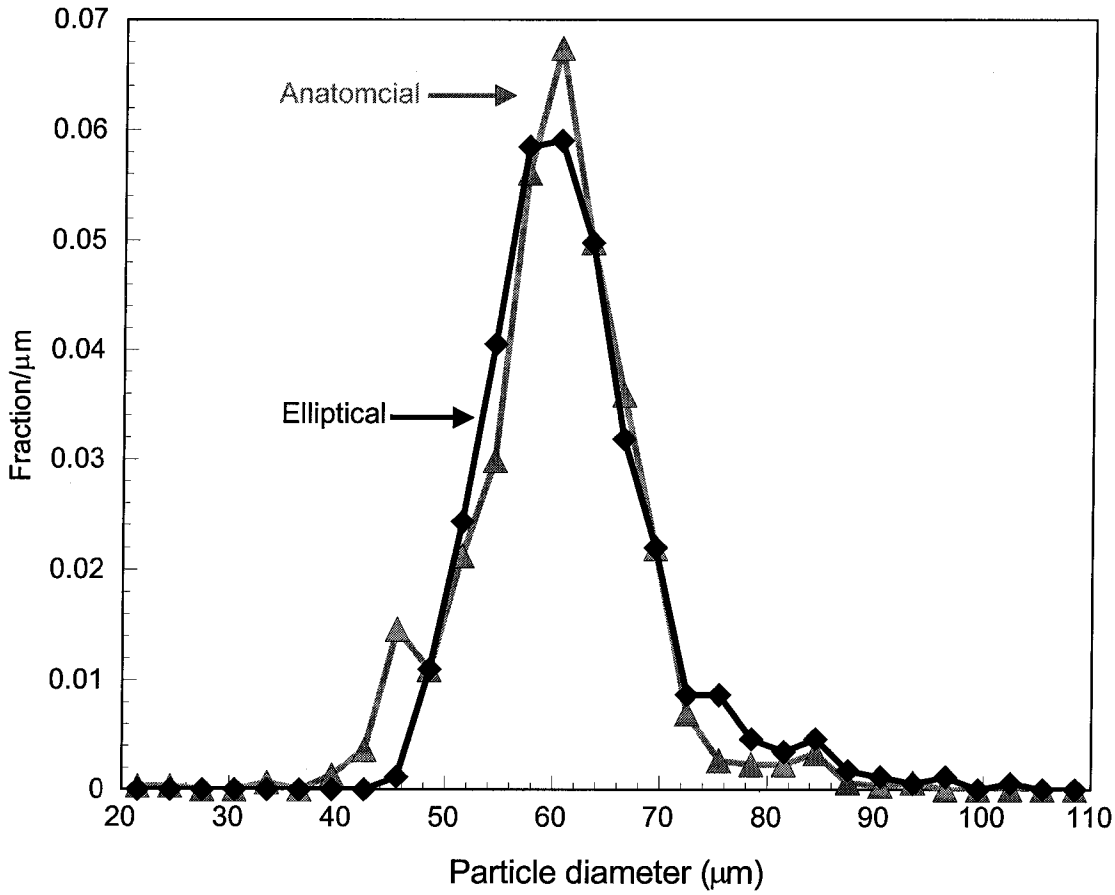

APPENDIX D: MESH DETAILS AND FIDAP CODES

This appendix details the meshes and simulation codes used for this study. Section D.1 provides information on the vertices and mesh spacing assigned to these simulations. Section D.2 provides the FIPREP file used for simulations. Section D.3 provides the particle simulation code used in particle simulations. Supporting data are found in the data disc accompanying this dissertation, described in Table D.1.

Table D.1 Data files supporting Appendix D

File Name	Description	Discussion Section
D1-Vertex Locations.doc	Vertex coordinates defining the computational domain and human form	D.1
Gambit\	This directory contains mesh files (*.dbs) for the small- and human-scale system as generated from Gambit, 3 mesh densities each	D.1
D2-v2hm3d.FIPREP	FIPREP code used to set-up and solve fluid dynamic problem (edit in text format)	D.2
SmallScale\	This directory contains both FDBASE and FIPOST files for the small-scale system, as defined in Table D.2	D.2
HumanScale\	This directory contains both FDBASE and FIPOST files for the human-scale system, as defined in Table D.2	D.2

D.1 File Naming Scheme

Because multiple mesh scales, densities, and velocity conditions were studied, Table D.2 is provided to clarify the attached FDBASE and FIPOST files to support this dissertation. Files beginning with "M" were used for the small-scale simulations detailed in Chapter 3. Both 1.55% and 3% turbulence intensities were investigated, to match the turbulence intensities of the EPA wind tunnel and Baity Air Laboratory wind tunnels, respectively. Because of the low turbulence intensities in the corresponding experiments, the ratio of eddy to laminar viscosity (R_u) was set to 25. The other files, designated with an "H" were the human-scale equivalents to the small-scale system, where different freestream and inhalation velocities were explored for the work described in Chapter 4. In these human-scaled systems, the turbulence intensity was not critical and a reasonable

value of 8% was assigned. In these systems, the value of R_u did not have to be inflated to minimize cell Reynolds numbers, so the typical value of 10 was used.

Table D.2 Naming scheme for simulation files

File Name	Scale	Mesh Density	Target mean U_o (m s^{-1})	Target mean U_m (m s^{-1})	TI (%)	R_u
M3kDC	small	coarse	0.3	1.07	1.55	25
M4kDC	small	middle	0.3	1.07	1.55	25
M5kDC	small	fine	0.3	1.07	1.55	25
M3C12	small	coarse	0.3	1.07	3	25
M4C12	small	middle	0.3	1.07	3	25
M5C12	small	fine	0.3	1.07	3	25
V2hm3D	human	coarse	0.2	1.81	8	10
V2hm4D	human	middle	0.2	1.81	8	10
V2hm5D	human	fine	0.2	1.81	8	10
V4hm3D	human	coarse	0.4	4.33	8	10
V4hm4D	human	middle	0.4	4.33	8	10
V4hm5D	human	fine	0.4	4.33	8	10
24hm3D	human	coarse	0.2	4.33	8	10
24hm4D	human	middle	0.2	4.33	8	10
24hm5D	human	fine	0.2	4.33	8	10

The files with a DBS extension are Gambit files that contain the geometry and mesh and are located in the Gambit\ subdirectory. Files that end with the FDBASE extension are Fidap files that contain the mesh information and settings for simulations. Files that end with FIPOST are Fidap files that contain the simulation solutions. For all files, solutions for the lowest iterative convergence tolerance (10^{-5}) are provided.

Since particle simulations required the use of solutions converged to 10^{-4}, these are provided in a sub-folder named "10-4 Solutions" on the included disk.

D.2 Mesh Details

Three hundred forty nine vertices represented the physical geometry of the realistic humanoid shape and the surrounding domain. These coordinates are provided in attached data file *D1*, corresponding to the human-scale dimensions discussed in Chapter 4. Coordinates for the small-scale system are 2/3 the values provided. These vertices were imported into Gambit (Fluent, Inc., Lebanon, NH) for manipulation to generate the computational domain. Gambit generates a DBS file, which can be converted into an FDNEUT file in the Gambit software. This FDNEUT file can be imported directly into

Fidap to investigate fluid flow. One DBS file for each mesh density and both scales was needed, and these are included on the supporting data disc, consistent with the naming scheme in Table D.2.

The imported vertices were connected by edges, and adjacent edges were combined into small faces. These small faces were combined into the 23 entities that ultimately defined the system. Fourteen entities defined the head; 3 defined the torso, generated from a bisected cylinder; and 6 defined the domain, representing the experimental wind tunnel. The edge of each entity shared vertices of adjacent entities, allowing all to be connected to define a volume, which is the 24th entity, designated as "fluid." Surface meshes were assigned to each individual face, which Gambit used to generate the volume mesh needed to simulate the fluid flow field in Fidap. Table D.3 lists the names of each entity, as referenced in the FIPREP code, along with a brief description of each. Figures D.1 and D.2 illustrate these entities on the simulated human form.

Table D.4 summarizes the number of mesh elements for each of the 24 entities on the three mesh densities evaluated in this study, specific to the human-scale system. For the small-scale system, the mesh density of the mouth inlet and its adjoining faces (v_ulipin, v_llipin, and v_midsag) is slightly smaller. Table D.5 presents information on the mouth densities for both small- and human-scaled system, along with Figure D.3 that provides the edge reference information. Line "a" is along the midsagittal plane, lines "b" and "e" are the horizontal top and bottom, and arcs "c" and "d" are two halves of the semicircular edge making up the lateral mouth corner.

D.3 FIPREP Code

The code used to define the fluid flow field problem is provided in Table D.6. To run this code, a mesh with the entities discussed above must be available in an FDNEUT format. Table D.7 summarizes the velocity conditions assigned to the FIPREP code for the streamwise (U_x) velocity component at both the mouth and domain inlets: as mesh densities were changed, the exact area of these inlets changed subtlety, and these velocity changes were needed to ensure identical flowrates between meshes.

This FIPREP file was read into FIDAP using the READFILE option in –gui. The FIPREP code converted an FDNEUT file into an FDBASE file containing the mesh, its

boundary conditions, and the simulation equations and methods to run the model discussed in Chapters 3 and 4. Activation of FISOLV is required once the FDBASE file is generated.

D.4 Particle Simulation Code

Both laminar and turbulent particle simulations were conducted in these studies. Table D.8 presents the particle code for laminar simulations.

The PARTICLE command given is for 7 μm particles, with initial release velocity of 0.2024 m s^{-1} in the streamwise direction (UX) and a downward velocity of 4.0172×10^{-5} m s^{-1} (UZ), used in Chapter 3. Solid, monodisperse particles with 1000 kg m^{-3} densities were simulated (SOLI, MONO, DENS). One particle was released per location (PARC = 1).

Because the COORdinate keyword was selected but none specified, the user must enter the particle release coordinates. In this research, line releases were simulated, where the beginning and end coordinates were entered and the number of intervals between these releases is entered. For example, "-0.75, 0, 0.1375, -0.75, 0, 0.1275, 18" would result in a release of 20 particles along a line extending from Z = 0.1275 to 0.1375 m at X = -0.75 m, Y = 0 m.

The TWOPHASE command specifies that the solutions from FIPOST file will be used, the particle method is LAGRangian, and that an IMPLicit method of FIXEd time steps will be used. The number of time steps (NTSE) was 130,000, sufficient to cover the 6.5 second time period (TEND), with the size of the time step set to 0.00005 seconds (TSTE). Generalized stokes drag was simulated (GENE), using monodisperse, non-evaporating particles (MDNO). Buoyancy was included (BUOY), with gravity set to 9.8 m s^{-2} in the downward direction (PHI=0). This code specifies laminar particle trajectory simulations (LAMI), but turbulent simulations substituted TURB for the LAMI keyword.

The PATH command specifies plotting details, such as plotting all particles along a continuous path, by particle release location over the period of 0 (TSTA) to 6.5 (TEND) seconds. Results from this code were plotted and not saved to file (PLOT).

Table D.3 Description of Entities

Entity	Description
Head Entities	
tophead	top of the head
bneck	back of the neck
bhead	back of the head
fneck	front of the neck
temporal	temporal region, on the side of head connecting to the tophead
uchin	underneath side of the chin, connecting to front neck
eyefh	eye and forhead
fchin	front of the chin, below the lip and superior to the uchin
v_llipface	lower lip that connects to the face ("outside of the lower lip")
ulipface	upper lip that connects to the face ("outside upper lip")
v_ulipin	inside mouth attached to the upper lip
v_llipin	inside mouth attached to the lower lip
v_milet	the rounded-edge rectangle that defines the mouth orifice
nosezyg	region including nose and zygomatic arch, between eyefh and upper lip
Torso Entities	
torso	the surface of the half-cylinder defining the torso
transfr	transition from the front of the neck to the torso
transbk	transition from the back of the neck to the torso
Wind Tunnel Entities	
outbox	wind tunnel exit
inbox	entrance to the wind tunnel
Ybox	side wall of the wind tunnel
topbox	top of the wind tunnel
v_midsag	plane of symmetry located at the midsagittal plane of the mannequin, effectively bisecting the mannequin
v_botbox	bottom of the wind tunnel

Table D.4 The number of mesh elements on each entity, by mesh density for the human-scale system.

Group #	Entity	HM3 (coarse)	HM4 (middle)	HM5 (fine)
1	fluid	813,925	1,916,038	3,846,262
2	tophead	463	801	1,330
3	bneck	270	464	786
4	bhead	428	734	1,221
5	fneck	332	547	953
6	temporal	406	685	1,091
7	uchin	228	387	625
8	eyefh	417	695	1,182
9	fchin	382	684	1,292
10	v_llipface	122	308	350
11	ulipface	107	184	283
12	v_ulipin	117	169	249
13	v_llipin	80	117	169
14	v_milet	129	195	305
15	nosezyg	402	698	1,118
16	torso	2,285	3,754	6,457
17	transfr	265	438	755
18	transbk	208	354	620
19	outbox	6,379	10,861	18,072
20	inbox	6,664	11,174	18,516
21	Ybox	12,440	21,150	35,738
22	topbox	12,274	20,864	35,198
23	v_midsag	36,752	62,819	106,900
24	v_botbox	13,830	23,452	39,634
Total # Nodes		160,044	333,772	665,314
3/4/5: $r = (N_{i+1}/N_i)^{(1/3)}$		-	1.278	1.259

Table D.5 Mouth mesh densities for small-scale (M#) and human-scale (HM#) systems. The higher the number, the finer the mesh.

	Mesh Reference			
Edge reference	M3 -	M4 HM3D	M5 HM4D	- HM5D
a	5	7	9	11
b	5	7	9	11
c	4	5	6	7
d	4	5	6	7
e	4	7	9	11
Total Nodes	48	81	118	177
Ratio		1.69	1.46	1.50
$R = (N_{i+1}/N_i)^{0.5}$		1.30	1.20	1.22

Table D.6 FIPREP commands

```
/ ****************************************************************
/ Human scaled mannequin, densest mouth series (D files)
/
/ The midsagittal plane is treated as a plane of symmetry, forcing
/ Uy to be zero along this plane.  The bottom of the box is also
/ treated as a plane of symmetry, leaving the Uz to be zero along this
/ plane (not real, but needed here and a reasonable approximation in
the
/ mouth and nose region).
/
/ This has the full size wind tunnel dimensions (symmetry: only half).
/ For low velocity condition (V2HM#D series):
/     For Coarsest mesh (3):  Ux for v_milet=  2.2331253
/                             Ux for inbox= 0.20226532
/     For Middle mesh   (4):  Ux for v_milet=  2.1524323
/                             Ux for inbox= 0.20152856
/     For Finest mesh   (5):  Ux for v_milet=  2.0802553
/                             Ux for inbox= 0.20096029
/  Kinetic energy is based on 8%:  3.8017e-4
/  Dissipation is based on Ru=10:  8.61218e-5
/ For higher velocity condition (V4HM#D_58 series):
/     For Coarsest mesh (3):  Ux for v_milet=  5.340853729
/                             Ux for inbox= 0.40656357
/     For Middle mesh   (4):  Ux for v_milet=  5.147863287
/                             Ux for inbox= 0.40508254
/     For Finest mesh   (5):  Ux for v_milet=  4.97524316
/                             Ux for inbox= 0.40394023
/  Kinetic energy is based on 8%:  1.536e-3
/  Dissipation is based on Ru=10:  1.4059e-3
/
/ Flow is single phase, as particles will be solved in FIPOST.  This
/ requires the assumption that there is no interaction between the
/ motion of particles and the fluid, which is reasonable
/
/ ****************************************************************
/
/          CONVERSION OF NEUTRAL FILE TO FIDAP Database
/
FICONV( NEUTRAL )
INPUT( FILE="V2HM3D.FDNEUT" )
OUTPUT( DELETE )
END
/
TITLE
V4HM3D
/
FIPREP
/          CONTINUUM ENTITIES
/
ENTITY ( NAME = "fluid", FLUID, PROPERTY = "fluid" )
/
```

Table D.6 FIPREP commands, continued

```
/          BOUNDARY ENTITIES
/
ENTITY ( NAME = "tophead", WALL )
ENTITY ( NAME = "bneck", WALL )
ENTITY ( NAME = "bhead", WALL )
ENTITY ( NAME = "fneck", WALL )
ENTITY ( NAME = "temporal", WALL )
ENTITY ( NAME = "uchin", WALL )
ENTITY ( NAME = "eyefh", WALL )
ENTITY ( NAME = "fchin", WALL )
ENTITY ( NAME = "v_llipface", WALL )
ENTITY ( NAME = "ulipface", WALL )
ENTITY ( NAME = "v_ulipin", WALL )
ENTITY ( NAME = "v_llipin", WALL )
ENTITY ( NAME = "v_milet", PLOT )
ENTITY ( NAME = "nosezyg", WALL )
ENTITY ( NAME = "torso", WALL )
ENTITY ( NAME = "transfr", WALL )
ENTITY ( NAME = "transbk", WALL )
ENTITY ( NAME = "outbox", PLOT )
ENTITY ( NAME = "inbox", PLOT )
ENTITY ( NAME = "Ybox", WALL )
ENTITY ( NAME = "topbox", WALL )
ENTITY ( NAME = "v_midsag", PLOT, RICOCHET, REST=1 )
ENTITY ( NAME = "v_botbox", PLOT )
/
/          PROBLEM SETUP
PROBLEM (3-D, INCO, STEA, TURB, NONL, NEWT, MOME, ISOT, FIXE, SING)
EXECUTION( NEWJOB )
DATAPRINT( CONTROL )
SOLUTION (SEGR=1, VELC=1.0E-5, RESC=0.1E-2, CGS=50000, CR=50000,
NCGC=0.1E-7, SCGC=0.1E-7, PREC=21, PPRO, SCHA=0.0)
DENS ( SET="fluid", CONS=1.205 )
VISC ( SET="fluid", CONS=0.182e-04, CLIP=1E12, TWO- )
/
/          INITIAL AND BOUNDARY CONDITIONS
/boundary conditions
BCNO (UX, ENTI="inbox", CONS=0.20226532, INCL)
BCNO (UY, ENTI="inbox", ZERO, INCL)
BCNO (UZ, ENTI="inbox", ZERO, INCL)
/    k = 1.5(TIfract*UX)^2 = , assumed Turb. Intensity of .08
BCNO (KINE, ENTI="inbox", CONS=3.8017e-4, EXCL)
/    e = 5958.79 K^2/Ru, use Ru=10
BCNO (DISS, ENTI="inbox", CONS=18.61218e-5, EXCL)
/planes of symmetry:
BCNO (UY, ENTI="v_midsag", ZERO, INCL)
BCNO (UZ, ENTI="v_botbox", ZERO, INCL)
```

Table D.6 FIPREP code, continued

```
/mouth inlet (now one face):
BCNO (UX, ENTI="v_milet", CONS=2.2331253, incl)
BCNO (UY, ENTI="v_milet", ZERO, incl)
BCNO (UZ, ENTI="v_milet", ZERO, incl)
/ the following should write over the edges of the mouth except for the
/ midsag location
/
BCNO (VELO, ENTI="Ybox", ZERO)
BCNO (VELO, ENTI="topbox", ZERO)
BCNO (VELO, ENTI="tophead", ZERO)
BCNO (VELO, ENTI="bhead", ZERO)
BCNO (VELO, ENTI="bneck", ZERO)
BCNO (VELO, ENTI="eyefh", ZERO)
BCNO (VELO, ENTI="temporal", ZERO)
BCNO (VELO, ENTI="uchin", ZERO)
BCNO (VELO, ENTI="fneck", ZERO)
BCNO (VELO, ENTI="fchin", ZERO)
BCNO (VELO, ENTI="nosezyg", ZERO)
BCNO (VELO, ENTI="v_llipface", ZERO)
BCNO (VELO, ENTI="ulipface", ZERO)
BCNO (VELO, ENTI="v_ulipin", ZERO)
BCNO (VELO, ENTI="v_llipin", ZERO)
BCNO (VELO, ENTI="torso", ZERO)
BCNO (VELO, ENTI="transfr", ZERO)
BCNO (VELO, ENTI="transbk", ZERO)
/
/ initial conditions:
ICNO (UX, CONS=0.400, ALL, EXCL)
ICNO (UY, ZERO, ALL, EXCL)
ICNO (UZ, ZERO, ALL, EXCL)
ICNO (KINE, CONS=2.16e-4, ALL, EXCL)
ICNO (DISS, CONS=1.11206e-5, ALL, EXCL)
/
/          SOLUTION PARAMETERS
PRESSURE (MIXED=1.E-8, CONTINUOUS, CONSISTENT)
/TURBOPTIONS (STANDARD, CONSISTENT, ORIGINAL, DELAY=5)
/EDDYVISCOSITY (  BOUSSINESQ )
/PRESSURE (MIXED=1.E-8, CONTINUOUS, CONSISTENT, PQUADRATIC)
OPTI (UPWI)
DATA (CONT)
PRINTOUT( NONE )
RELA (ELEMENT, MAXIMUM)
0.5, 0.5, 0.5, 0.7, 0.05, 0.55, 0.55, 0.55
RELA (ELEMENT, MINIMUM)
0.3, 0.3, 0.3, 0.3, 1.E-5, 0.05, 0.05, 0.05
RENU (PROF)
/
END
CREATE( FIPREP,DELETE )
PARAMETER( LIST )
CREATE( FISOLV )
/RUN( FISOLV, BACKGROUND )
```

Table D.7 Velocity assignments to ensure constant volumetric flow rates for more dense meshes. The average target velocities are indicated in the mesh reference, and the assigned horizontal velocity to achieve these averaged are given, by mesh and study condition.

Mesh Reference	Assigned Velocity ($m\ s^{-1}$)	
	v_milet	inbox
Small-scale, U_m= 1.07 $m\ s^{-1}$, U_o = 0.3 $m\ s^{-1}$		
M3keDC (coarse)	3.657198	0.30492300
M4keDC (mid)	3.32535653	0.30382089
M5keDC (fine)	3.20514396	0.30296059
Human-scale, U_m= 1.8 $m\ s^{-1}$, U_o = 0.2 $m\ s^{-1}$		
V2hm3D (coarse)	2.233125300	0.20226532
V2hm4D (mid)	2.15243230	0.20152856
V2hm5D (fine)	2.08025532	0.20096026
Human-scale, U_m= 4.33 $m\ s^{-1}$, U_o = 0.4 $m\ s^{-1}$		
V4hm3D (coarse)	5.340853729	0.40656357
V4hm4D (mid)	5.147863287	0.40508254
V4hm5D (fine)	4.97524316	0.40394023
Human-scale, U_m = 4.33 $m\ s^{-1}$, U_o = 0.2 $m\ s^{-1}$		
24hm3D (coarse)	5.340853729	0.20226532
24hm4D (mid)	5.147863287	0.20152856
24hm5D (fine)	4.97524316	0.20096026

Table D.8 Particle transport coding

PARTICLE(COOR, PSIZ = 7E-006, UX = 0.2024, UZ = -4.0172E-005, MONO, SOLI, DENS = 1000, PARC = 1)

TWOPHASE(FIPO, LAGR, IMPL = 10, FIXE, NTSE = 130000, TSTA = 0, TEND = 6.5, DT = 5E-005, GENE, MDNO, BUOY, GRAV = 9.8, PHI = 0, LAMI)

PATH(CONT, PART, ALL, TSTA = 0, TEND=6.5, PLOT)

Figure D.1 Locations of entities defining the human form

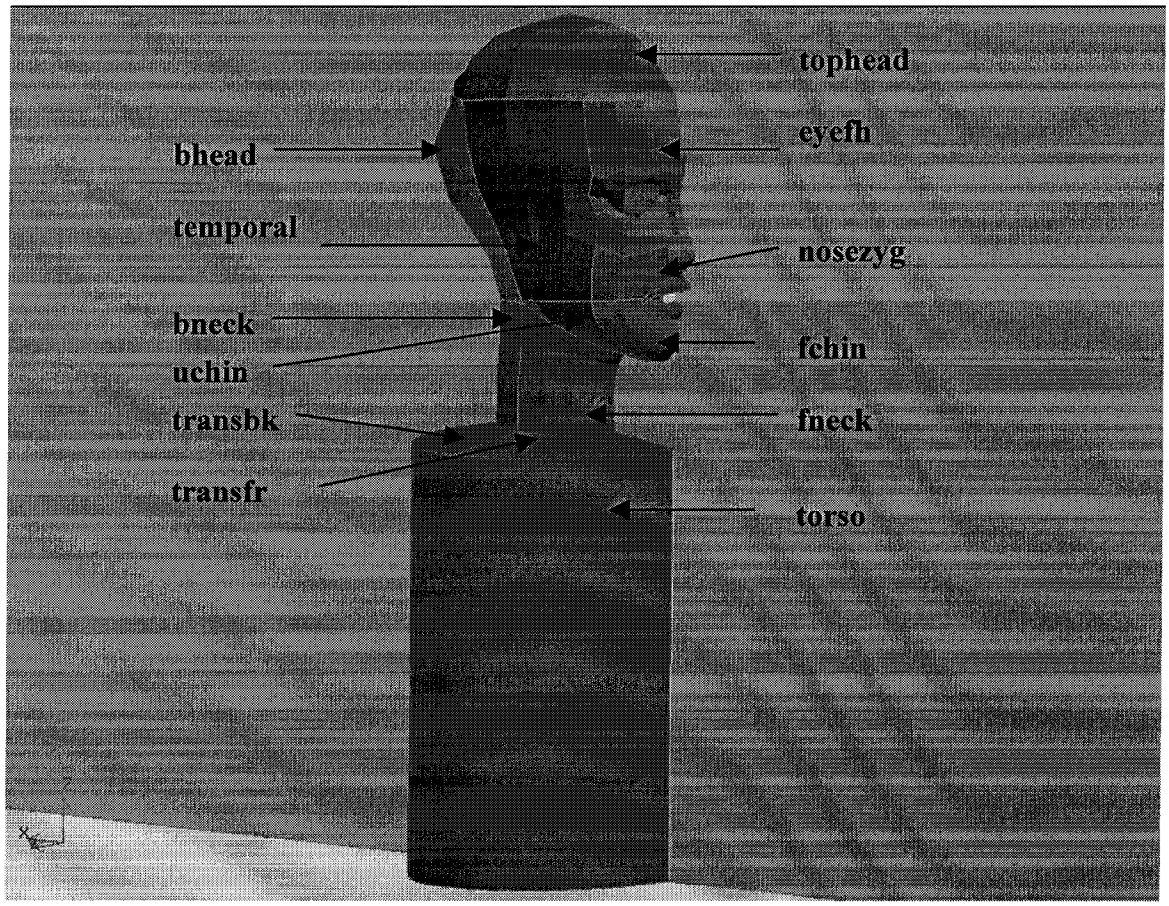

Figure D.2 Locations of entities defining the human form, mouth close-up

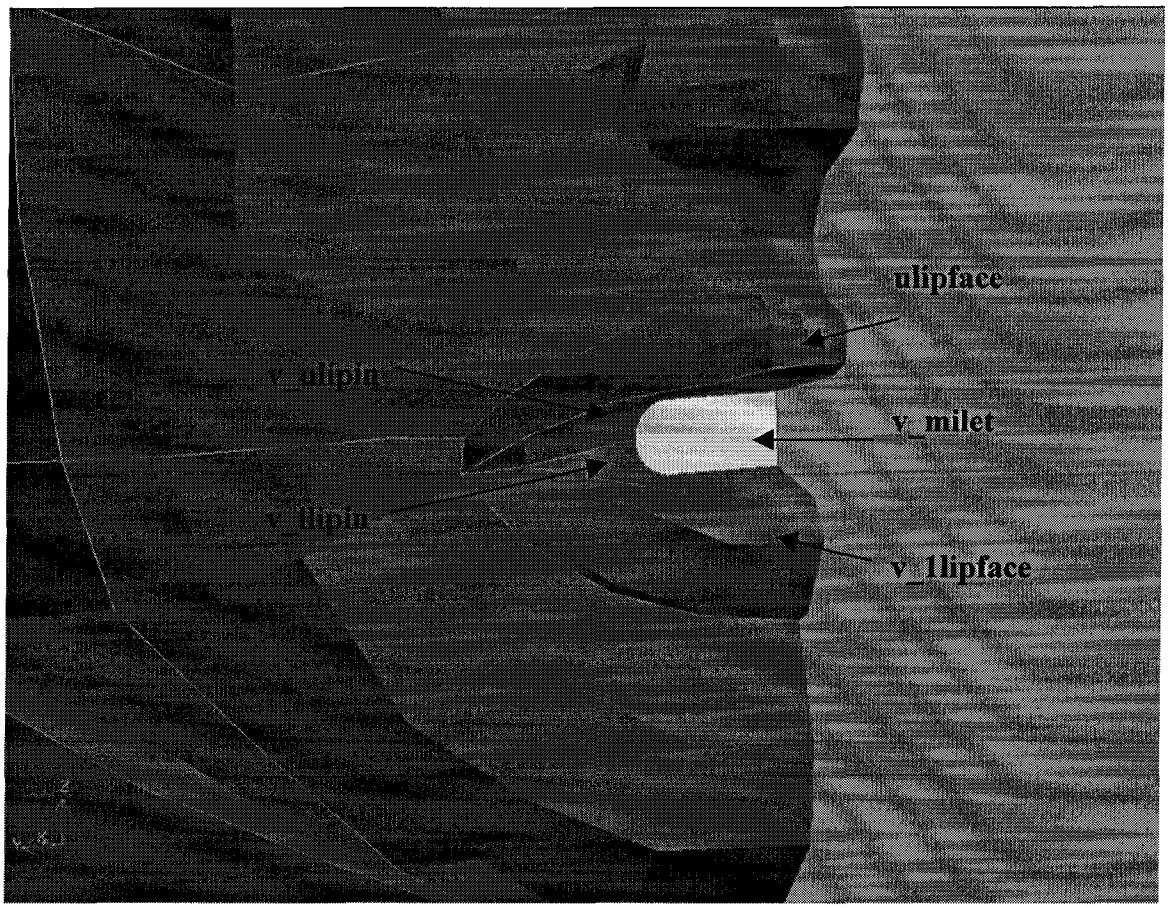

Figure D.3 Edge reference for mouth mesh densities

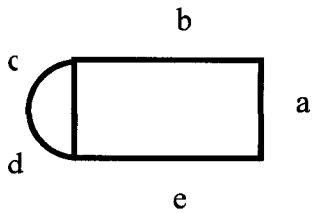

APPENDIX E: DATA AND CALCULATIONS FOR CHAPTER 3

This appendix documents the calculations used to conduct the verification and validation of the computer model discussed in Chapter 3. This developed and evaluated a small-scale computational fluid dynamic (CFD) model appropriate to study particle inhalability. The details of the geometry and mesh are discussed separately in Appendix D. Supporting data are found in the data disc accompanying this dissertation. These files are summarized in Table E.1.

E.1 Flow Verification

Fluid flow simulations were conducted for the small-scale mesh discussed in Appendix D. This section discusses the steps to verify these simulations, specifically the appropriate grid solution error norm and mesh convergence assessments. A 1.55% turbulence intensity was associated with the EPA wind tunnel used to obtain velocity measurements with the laser Doppler anemometer (LDA), and a 3% turbulence intensity was identified with the wind tunnel in the Baity Laboratory. This discussion is based on simulations of the LDA test conditions (*data files: E2 and E3*), but similar analysis and findings are provided in data files for the 3%TI simulations (*data file: E4*).

Verification calculations were performed to determine whether simulations were appropriately converged and to determine numerical uncertainty. Two volumes were assessed for these tests: velocity measurement and nozzle locations. The locations used in the velocity measurement set were matched to the near-head locations where laser Doppler anemometry (LDA) measurements were made in the wind tunnel, excluding the location of the nose (X, Y, Z) = (-0.011, 0, 0.020 m). The nozzle set included locations further upstream of the mannequin near the wind tunnel entrance, above and below the head (X = 0 to -1.5 m, Y = 0 to 0.5 m, Z = -0.03 to 0.15 m, N = 2533).

Table E.1 Data files for Appendix E

File Name	Description	Discussion Section
E1-GSE study.xls	Examination of global solution error tolerance	E.1.a
E2-M#keDC verify valid TI155 near head.xls	Simulations for small-scale meshes at turbulence intensity of 1.55%. Includes verification calculations for each mesh at three GSE values and validation assessments, compared to experimental velocity data. This file includes near-head locations only.	E.1.b-c
E3-M#keDC verify TI155_nozzle.xls	Simulations for small-scale meshes at turbulence intensity of 1.55%. Includes verification calculations for each mesh at three GSE for upstream "nozzle" locations only.	E.1.b-c
E4-Mti3c12 verif valid TI3.xls	Simulations for small-scale meshes at turbulence intensity of 3%. Includes verification calculations for each mesh at three GSE values and validation assessments, compared to experimental velocity data	same method as E.1.b
E5-Experim Vel Data.xls	Manipulations to the experimental velocity data to address lateral symmetry	E.2.a
E6-Slope calcs M#kedc sim vs meas.xls	Slope calculations investigating the simulated and measured velocity fields for the small-scale system	E.2.a
E7-Point locations.xls	Coordinates for numerically investigating positional errors of LDA	E.2.b
E8-Position error investing.xls	Evaluation of velocity fields at 0.5 mm increments from system origin	E.2.b
E9-GCI vs Location.xls	Investigation of uncertainties including measurement errors, GCI and positioning errors	E.2.b
E10-Particle experiments.xls	Summary of experimental particle inhalation experiments conducted in the Baity Lab wind tunnel	E.3.a
E11-Particle simulations small-scale.xls	Results of particle simulations to reflect the experimental conditions in the Baity Lab wind tunnel	E.3.b

E.1.a Non-linear Convergence

Non-linear convergence was assessed for a given mesh density to examine when the global solution error norm (GSE) was sufficiently low for each degree of freedom. The

criterion was set so that the relative L_2 error norm from successively lower GSE solutions was less than 5%. The L_2 error norms were calculated using equation E.1:

$$L_2 = [\sum_{position} (f_i - f_{i+1})^2] \; / \sum_{position} f_i^2 \qquad \text{(E.1)}$$

Where f_i is the value for a degree of freedom at the smaller GSE (e.g., 10^{-5}) and f_{i+1} is the value for the sequentially larger degree of freedom (e.g., 10^{-4}). These are summed over all matched positions in the region being tested. Table E.2 provides a summary of these error norm calculations: error norms are reduced an order of magnitude, to a maximum of 0.024 over all degrees of freedom, when the GSE is reduced to 10^{-5} *(Data file: E1)*.

E.1.b Mesh Convergence

Mesh convergence calculations were performed to determine whether the solutions provided by the model were mesh-independent. Calculations were based on the three types of error norms, given in equations (E.2) through (E.4):

Two-mesh error norm:

$$\text{Relative } L_2 = [\sum_{position} (f_{coarser} - f_{finer})^2] \; / \sum_{position} f_{finer}^2 \qquad \text{(E.2)}$$

Three-mesh error norms:

$$R_2 = [\sum_{position} (f_{mid} - f_{fine})^2] \; / \; [\sum_{position} (f_{coarse} - f_{mid})^2] \qquad \text{(E.3)}$$

$$R_1 = [\sum_{position} (f_{mid} - f_{fine})] \; / \; [\sum_{position} (f_{coarse} - f_{mid})] \qquad \text{(E.4)}$$

where:

f = the degree of freedom and

data are summed over all positions in the region being tested.

Results from error norm calculations are provided in Tables E.3 through E.5 for the velocity measurement locations and Tables E.6 through E.8 for the nozzle locations.

The L_2 error norms for the most accurately solved system of meshes (*i.e.*, GSE = 10^{-5}) identified that between-mesh velocity differences were reduced to less than 0.06 over both regions investigated, indicating a difference in velocity magnitudes of 6%

attributable to the mesh densities. Convergence of kinetic energy and dissipation were higher, indicating mesh dependence is still likely.

The three-mesh error norm, defined by R_2 in equation (E.3), simultaneously compares the differences between the predicted degree of freedom between the three meshes. Monotonic convergence is indicated when R_2 over a given region is less than 1 (Stern *et al.*, 2001). This occurred for all velocity degrees of freedom. For the "nozzle" locations, pressure and kinetic energy R_2 values exceeded unity, confirming the mesh-dependency issues identified with the L_2 error norm assessments.

In addition to investigating a local R_2, individual values of R_1 were calculated for each of the 636 positions in the velocity measurement region, using equation (E.4). These local values were used to assess point-wise convergence. From these values, point-wise convergence was assessed using the criteria by Stern, *et al.* (2001):

Monotonic convergence if: $0 < R_1 < 1$

Oscillatory convergence if: $R_1 < 0$

Divergent convergence if: $R_1 > 1$

For locations that were monotonically convergent, the local order of accuracy, p, was determined using equation (E.5):

$$p = \ln[(f_{coarse}-f_{mid}) / (f_{mid}-f_{fine})] \ / [\ln(r)] \quad \text{(E.5)}$$

where r is the mesh refinement ratio, defined for this three-dimensional model as:

$$r = 0.5 [(N_{fine} / N_{mid})^{1/3} + (N_{mid} / N_{coarse})^{1/3}] \quad \text{(E.6)}$$

where N is the number of nodes in a given mesh.

For locations that were monotonically convergent and displayed an order of accuracy between 1 and 2, the location was identified as converging. For these locations, the grid convergence index (GCI) was calculated to provide uncertainty associated with the value of a given degree of freedom, using equation (E.7) (Roache, 1998).

$$GCI = 1.25 | (f_{mid}-f_{fine}) / (r^p-1) | \quad \text{(E.7)}$$

For monotonically convergent locations that did not display the correct order of accuracy (*i.e.*, $p < 1$ or $p > 2$), a greater safety factor was used to determine the GCI, as also recommended by Roache:

$$GCI = 3 | (f_{mid}-f_{fine}) / (r^p-1) | \quad \text{(E.8)}$$

Tables E.9 through E.11 and E.12 through E.14 summarize the fraction of locations that were converging and behaved in agreement with the theoretical order of accuracy, for velocity measurement and nozzle locations, respectively.

E.1.c Least-Squares Approach

In addition to the rigorous mesh convergence assessments discussed above, a statistically-based comparison of the flow field was also conducted between meshes. Figure E.1 illustrates the relationship between the fine and coarse mesh predicted streamwise velocities for the velocity measurement. Similar agreement was identified for all velocity components, as indicated in Table E.15. The coefficient of determination improved with increased mesh density, and hence less difference existed between the fine and middle mesh relative to the middle and coarse mesh.

E.2 Flow Validation

The small-scale experimental velocity data for the anatomical mannequin, discussed in Chapter 2, were used to validate the model. Validation is achieved when the confidence intervals for measurements overlap with the confidence intervals for the simulated predictions, using the GCI as numerical uncertainty.

E.2.a Experimental Uncertainty

Velocity measurements had been obtained over both the right and left side of the mannequin, but the model was simplified to look at only half of the regime. As such, the data from the mannequin's left side was reflected to the right side, such that no changes were required to the streamwise or vertical velocity data, but a sign change was required for the lateral velocity components (V). For example, the velocity field (u, v, w) at (x, -y, z) m was reflected to (x, +y, z) as (u, -v, w). *(Data file: E5)*

In addition, the value of the experimental turbulence kinetic energy was calculated. Values of turbulence intensity (TI) and the mean velocity were available for each velocity component, and turbulence kinetic energy (KE) was calculated using the relationships in equations E.9 through E.12.

$$U'_x = TI \times U_{x,ave} / 100 \quad \text{(E.9)}$$

$$U'_y = TI \times U_{y,ave} / 100 \quad \text{(E.10)}$$

$$U'_z = TI \times U_{z,ave} / 100 \quad (E.11)$$

$$KE = (U'^2_x + U'^2_y + U'^2_z) / 2 \quad (E.12)$$

Once KE was determined, turbulence dissipation was calculated using $\varepsilon = \rho c_\mu (KE)^2 / R_u \mu$, where ρ = air density =1.205, R_u=25, c_μ = 0.09, μ=1.81 x 10^{-5} N s m^{-2}. However, due to the low particle seeding in the LDA measurements, these calculated turbulence kinetic energies are biased and under-represent actual KE values (Nobach *et al.*, 1998)

At a given location, multiple velocity and kinetic energy data existed, due to repeat measurements and the lateral data reflection. The mean and standard deviation for each degree of freedom were calculated. However, the number of replicates ranged from 2 to 6, requiring adjustments to the standard deviations using the technique found in Sokal and Rohlfs (1981):

$$\text{Adjustment} = [(n-1)/2)]^{0.5} \ \Gamma[(n-1)/2] / \Gamma[n/2] \quad (E.13)$$

The gamma function is defined for integers as $\Gamma[x] = (x-1)!$. For fractions, tables were used to find:

$$\Gamma(0.5) = (\pi/2)^{0.5} \quad (E.14)$$

$$\Gamma(1.5) = 0.5\ (\pi^{0.5}) \quad (E.15)$$

$$\Gamma(2.5) = 3/4(\pi^{0.5}) \quad (E.16)$$

For the values of n= 2 through 6, the values of the adjustment to the standard deviation are given in Table E.16. The computed standard deviation from replicate data was multiplied by the adjustment corresponding to the sample number. Adjustments to the coefficients of variation were also made, in accordance with Sokal and Rohlfs (1981), by using:

$$CV^* = CV\ (1 + 1/(4n)) \quad (E.17)$$

where CV is the unadjusted coefficient of variation (CV = stdev/mean) and n is the number of replicates for that location. Thus, data for each degree of freedom from the measurement locations were represented by a mean and adjusted standard deviation.

E.2.b CFD Simulation Uncertainty

Numerical uncertainty from the simulated velocity and turbulence kinetic energy were obtained from the GCIs, as outlined previously in equations (E.7) and (E.8). These GCIs

were used as the uncertainty surrounding the predicted degree of freedom, for monotonically converged locations.

Additionally, LDA positioning uncertainty was assessed. The traverse system was capable of moving at 1 mm increments, but locations could be off by as much as 0.5 mm. Errors attributable to this positioning bias could not be assessed other than with repeat measurement uncertainty, evaluated earlier. However, the velocity field from the simulated model was queried for positions that were +/- 0.5 mm relative to the velocity measurement locations to arrive at a quantitative estimate of positioning error. Hence, for each of the 636 measurement locations, 27 nearby locations were evaluated within +/- 0.5 mm streamwise (X), laterally (Y) and vertically (Z) (*data file: E7*). Velocity from each of these 27 data sets were compared to experimental measures using least-squares regressions between predicted and measured (Tables E.17-E.19; *data file: E8*). No single set of adjusted velocity locations provided better agreement with the experimental data than that of the unadjusted positions. For each measurement location, a positional uncertainty, σ_p, was assigned based on the standard deviation of the 27 locations within +/- 0.5 mm. This positioning uncertainty was compared to the computed GCI for each measurement location (*data file: E9*). For velocity field data, the numerical GCI was greater in magnitude than the computed positioning error, significantly so for the vertical velocity component ($p = 0.0005$ using paired t-test).

E.2.c Validation Calculations

The simulated fluid field was validated by experimental data at locations where the interval of the predicted degree of freedom +/- the GCI overlapped the interval of the mean +/- standard deviation of the measurement data. These calculations were only possible were mesh convergence studies indicated monotonic convergence, and not all of the 636 velocity measurement locations were monotonically convergent. The fraction of monotonically converged locations that had numerical uncertainty bands overlapping the experimental uncertainty (1, 2, and 3 s.d.) were provided in Table 3.7.

In addition, information from the position uncertainty were incorporated into the uncertainty surrounding the numerical predictions (error band is +/- GCI +/- $1\sigma_p$). For example, at (-0.011,0.030, -0.025), the mean measured streamwise velocity was 0.2091 m

s^{-1} and an adjusted standard deviation (based on small sample size) was 0.0179 m s^{-1}. The predicted velocity at the same location was 0.2467 m s^{-1}, with a GCI of 0.00137 and a computed positional standard deviation of 0.0008 m s^{-1}. The uncertainty intervals were:

experimental +/-:

1 s.d. = (0.1912, 0.2270) m s^{-1}

2 s.d. = (0.1733, 0.24490) m s^{-1}

3 s.d. = (0.1554, 0.2628) m s^{-1}

numerical +/-:

1 GCI = (0.24533, 0.24807) m s^{-1}

1 GCI, 1 σ_p = (0.24453, 0.24887) m s^{-1}

At this location, the uncertainty intervals do not overlap when considering only 1 standard deviation of the experimental data and 1 GCI for the numerical data. However, when 2 s.d. are used for the experimental data, the experimental interval overlaps the numerical +/- (1 GCI, 1 σ_p), indicating a validated location. Further, the 3 s.d. confidence interval for the experimental data overlaps both the uncertainty bands for the numerical predictions. *(Data file: E9)*

Comparisons of experimental and numerical simulations also included least-squares regressions between numerical and experimental velocities, of the form:

Numerical = $b_{y,x}$(Experimental) + intercept.

Included in this evaluation was an attempt to provide a confidence interval for the resulting estimator for the numerical velocity in the above equation. It was hoped that the biconcave confidence belt from the plotted estimated numerical velocity was sufficiently large to include the data. Table E.20 summarizes this regression information, and the resulting confidence interval is given by the equation E.18:

$$95\%CI \text{ for } \mu_{Yi|Xi} = \hat{Y}_i +/- \ t_{0.05,n} \hat{S}_y \qquad (E.18)$$

However, because of the large n, the resulting confidence interval for the estimator of predicted numerical velocity is narrow, as shown in the confidence bounds abutting the associated regression line, shown in Figure E.2.

E.3 Particle Validation

E.3.a Experimental Aspiration

Results from the particle experiments discussed in Appendix C were used as the basis for the validation data for particle aspiration simulations. Additional work conducted by Yoshi Koto provided information on the size-specific particle count generation rate for the Lechler Ultrasonic nozzle used in these experiments *(data file: E10)*. These experiments relied on the gravitational settling of newly generated particles onto a sampling grid. Particles were sized and counted using bright field microscopy to determine the particle count generation rate. Table E.21 provides a summary of the generation rate data for particles in the size range aspirated by the anatomical mannequin, along with the measured particle aspiration count rate, previously discussed in Appendix C. Because the liquid flow rates and sample times were different in the generation rate and aspiration studies, the experimental and generation rate data were normalized by the total liquid volume metered through the pump over each experiment. The capture efficiency was defined as the number of particles aspirated per mL of liquid dispensed divided by the number of particles generated by the nozzle per mL of liquid dispensed.

E.3.b Particle Simulations

Particle simulations were performed on the middle density mesh with 3% turbulence intensity, to match the conditions in the wind tunnel where experimental data was matched. Memory allocation by Fidap was insufficient to perform particle simulations on the finest mesh. Particles were released with a horizontal velocity of 1.802 m s^{-1}, designed to match the mean air velocity exiting the circular annulus, based on a 2 Lpm flowrate supplied to the aerosol generator. Rather than releasing particles along a semi-circular arc representing the generator annulus, particles were released along a line extending from the center of the nozzle to the edge of the annulus. Particles were assigned densities of 860 kg m^{-3} to represent the vacuum pump oil aerosol used in experimental work.

Initially, laminar particle simulations were conducted. Only particles between 55.0 and 58.0 microns were inhaled under these conditions. Next, turbulent particle motion was simulated, allowing for random deviations from the mean particle path. Particles

48.5 to 69.5 were investigated, using the midpoint of the particle diameter bins from earlier optical counting experiments (Table C.3).

Turbulent simulations were conducted at time steps 0.0005 seconds or smaller. Twenty particles were released along a line source, and particles terminating at the mouth orifice were counted as aspirated. This process was repeated in 20-particle increments, and cumulative totals of particles released and aspirated were recorded. The collection efficiency was calculated as the number of particles inhaled divided by the number released. *(Data file: E11)* This differs from aspiration efficiency, but compares to the same aspiration ratio from the experimental work. Typically 2000 particle releases were required to achieve stability, determined when additional releases of particles had little change on the collection efficiency (fraction). Figures E.3 through E.8 provide cumulative aspiration fractions for the 8 particle ranges studied. Similar data are presented for simulations with no initial particle velocity (Figures E.9 and E.10) and for particle releases 5 mm higher than the location of the nozzle centerline (Figures E.11 and E.12) to examine sensitivity to position and release velocity.

Figure E.13 illustrates the comparison of the two capture efficiencies. Note that the left y-axis corresponds to the simulated capture efficiency, the right for the experimental efficiencies. The peaks are off-set by 9 μm, consistent with differences between experimental and simulated velocity fields. In addition, the momentum of particles issued from the nozzle is not well captured: the 2 Lpm of air through the nozzle does not dissipate as soon as it exits from the nozzle, which was what was represented by simply assigning an initial velocity to the generated particles. The differences in the magnitudes are explained by the poor nozzle representation in the CFD model: by excluding the presence of the nozzle in the computational domain, wake turbulence was ignored and less particle dispersion was simulated.

Table E.2 L_2 error norms to examine velocity convergence tolerance (GSE) for (a) velocity measurement locations and (b) nozzle locations

(a) Velocity Measurement Locations

Mesh	GSE Levels	u	v	w	p	k	e
Coarse	$10^{-3} - 10^{-4}$	0.024	0.020	0.271	0.031	0.107	0.082
	$10^{-4} - 10^{-5}$	0.002	0.003	0.009	0.001	0.009	0.010
Moderate	$10^{-3} - 10^{-4}$	0.029	0.021	0.333	0.031	0.164	0.195
	$10^{-4} - 10^{-5}$	0.003	0.004	0.020	0.003	0.008	0.013
Fine	$10^{-3} - 10^{-4}$	0.001	0.003	0.006	0.003	0.008	0.007
	$10^{-4} - 10^{-5}$	0.001	0.005	0.015	0.003	0.012	0.012

(b) Nozzle Locations

Mesh	GSE Levels	u	v	w	p	k	e
Coarse	$10^{-3} - 10^{-4}$	0.002	0.033	0.053	0.124	0.081	0.095
	$10^{-4} - 10^{-5}$	0.000	0.004	0.004	0.002	0.003	0.004
Moderate	$10^{-3} - 10^{-4}$	0.002	0.042	0.079	0.122	0.132	0.098
	$10^{-4} - 10^{-5}$	0.000	0.005	0.005	0.010	0.004	0.006
Fine	$10^{-3} - 10^{-4}$	0.001	0.025	0.019	0.027	0.017	0.022
	$10^{-4} - 10^{-5}$	0.003	0.024	0.021	0.021	0.006	0.002

Table E.3

Error Norm Convergence Tests: M#keDC series, GSE=10^{-3}

U_o= 0.3 m s^{-1}, U_m = 1.07 m s^{-1}

TI=1.55%, Ru=25, Clip = 10^{12}

Locations: "Velocity Measurement" (N=636)

		Degree of Freedom					
		Ux	**Uy**	**Uz**	**P**	**KE**	**E**
Relative L_2 Norm							
	Mesh 3 - 4	0.015	0.056	0.140	0.036	0.218	0.471
	Mesh 4 - 5	0.034	0.052	0.344	0.038	0.157	0.381
Relative L_1 Norm							
	Mesh 3 - 4	-0.00820	-0.01050	0.17428	0.01177	-0.06717	-0.12108
	Mesh 4 - 5	0.02771	0.02140	-0.37885	-0.02243	-0.15593	-0.17003
Absolute L_2 Norm							
	Mesh 3 - 4	0.08922	0.05832	0.09901	0.02912	0.01820	0.21220
	Mesh 4 - 5	0.18843	0.05279	0.28929	0.03165	0.01492	0.23408
Absolute L_1 Norm							
	Mesh 3 - 4	-1.17364	-0.20018	1.79530	0.22908	-0.09629	-0.34222
	Mesh 4 - 5	3.85716	0.39939	-6.28310	-0.44642	-0.26495	-0.60204
3-Mesh Error Norms							
R_2		2.1119	0.9052	2.9217	1.0871	0.8200	1.1031
R_1		-3.2865	-1.9952	-3.4998	-1.9487	2.7516	1.7592

Table E.4

Error Norm Convergence Tests: M#keDC series, GSE=10^{-4}

U_o= 0.3 m s^{-1}, U_m = 1.07 m s^{-1}

TI=1.55%, Ru=25, Clip = 10^{12}

Locations: "Velocity Measurement" (N=636)

		Degree of Freedom					
		Ux	**Uy**	**Uz**	**P**	**KE**	**E**
Relative L_2 Norm							
	Mesh 3 - 4	0.014	0.057	0.082	0.036	0.258	0.493
	Mesh 4 - 5	0.013	0.048	0.048	0.025	0.081	0.331
Relative L_1 Norm							
	Mesh 3 - 4	-0.00381	-0.01426	0.03905	0.01464	-0.11003	-0.19432
	Mesh 4 - 5	0.00186	0.01920	-0.01018	0.00325	0.00809	-0.01514
Absolute L_2 Norm							
	Mesh 3 - 4	0.07857	0.05883	0.06818	0.02998	0.02481	0.26650
	Mesh 4 - 5	0.07175	0.04899	0.04041	0.02105	0.00775	0.20277
Absolute L_1 Norm							
	Mesh 3 - 4	-0.53108	-0.27107	0.63784	0.29286	-0.18871	-0.65713
	Mesh 4 - 5	0.25944	0.35819	-0.16801	0.06471	0.01376	-0.05361
3-Mesh Error Norms							
R_2		0.9132	0.8328	0.5927	0.7022	0.3123	0.7609
R_1		-0.4885	-1.3214	-0.2634	0.2209	-0.0729	0.0816

Table E.5

Error Norm Convergence Tests: M#keDC series, GSE=10^{-5}

U_o= 0.3 m s^{-1}, U_m = 1.07 m s^{-1}

TI=1.55%, Ru=25, Clip = 10^{12}

Locations: "Velocity Measurement" (N=636)

	Degree of Freedom					
	Ux	**Uy**	**Uz**	**P**	**KE**	**E**
Relative L_2 Norm						
Mesh 3 - 4	0.014	0.057	0.078	0.036	0.258	0.494
Mesh 4 - 5	**0.013**	**0.049**	**0.055**	**0.025**	**0.091**	**0.331**
Relative L_1 Norm						
Mesh 3 - 4	-0.00301	-0.01381	0.02996	0.01647	-0.10935	-0.19379
Mesh 4 - 5	-0.00055	0.02116	0.02621	0.00388	0.02983	0.00456
Absolute L_2 Norm						
Mesh 3 - 4	0.07735	0.05879	0.06583	0.03047	0.02497	0.26977
Mesh 4 - 5	0.07281	0.04996	0.04584	0.02115	0.00853	0.20080
Absolute L_1 Norm						
Mesh 3 - 4	-0.41879	-0.26172	0.49866	0.32857	-0.18913	-0.66135
Mesh 4 - 5	-0.07707	0.39274	0.42508	0.07705	0.05011	0.01596
3-Mesh Error Norms						
R_2	0.9414	0.8499	0.6964	0.6941	0.3418	0.7443
R_1	0.1840	-1.5006	0.8525	0.2345	-0.2650	-0.0241

Table E.6

Error Norm Convergence Tests: M#keDC series, GSE=10^{-3}

U_o= 0.3 m s^{-1}, U_m = 1.07 m s^{-1}

TI=1.55%, Ru=25, Clip = 10^{12}

Locations: "Nozzle" (N=2533)

	Degree of Freedom					
	Ux	**Uy**	**Uz**	**P**	**KE**	**E**
Relative L_2 Norm						
Mesh 3 - 4	0.010	0.058	0.148	0.060	0.289	0.206
Mesh 4 - 5	0.003	0.079	0.107	0.167	0.179	0.338
Relative L_1 Norm						
Mesh 3 - 4	0.00379	0.04570	0.07709	-0.00587	0.00285	-0.00052
Mesh 4 - 5	-0.00123	0.00753	-0.04519	-0.17706	-0.01836	-0.00125
Absolute L_2 Norm						
Mesh 3 - 4	0.07266	0.02174	0.05825	0.00992	0.00411	0.01906
Mesh 4 - 5	0.05027	0.02973	0.04622	0.03013	0.00286	0.04707
Absolute L_1 Norm						
Mesh 3 - 4	2.96600	0.25582	0.48711	-0.03792	0.00162	-0.02531
Mesh 4 - 5	-0.96324	0.04186	-0.29969	-1.44568	-0.01082	-0.05176
3-Mesh Error Norms						
R_2	0.6918	1.3673	0.7934	3.0358	0.6978	2.4692
R_1	-0.3248	0.1636	-0.6153	38.1213	-6.6771	2.0449

Table E.7

Error Norm Convergence Tests: M#keDC series, GSE=10^{-4}

U_o= 0.3 m s^{-1}, U_m = 1.07 m s^{-1}

TI=1.55%, Ru=25, Clip = 10^{12}

Locations: "Nozzle" (N=2533)

		Degree of Freedom					
		Ux	**Uy**	**Uz**	**P**	**KE**	**E**
Relative L_2 Norm							
	Mesh 3 - 4	0.009	0.049	0.131	0.052	0.236	0.207
	Mesh 4 - 5	0.002	0.045	0.053	0.029	0.108	0.284
Relative L_1 Norm							
	Mesh 3 - 4	0.00376	0.03363	0.04039	0.00044	-0.00168	-0.00059
	Mesh 4 - 5	0.00038	0.04144	0.02744	0.00415	-0.00601	-0.00097
Absolute L_2 Norm							
	Mesh 3 - 4	0.07069	0.01867	0.05534	0.00960	0.00373	0.02121
	Mesh 4 - 5	0.03427	0.01673	0.02278	0.00541	0.00175	0.04047
Absolute L_1 Norm							
	Mesh 3 - 4	2.94056	0.19405	0.27488	0.00368	-0.00099	-0.02988
	Mesh 4 - 5	0.29777	0.22961	0.18156	0.03553	-0.00356	-0.04040
3-Mesh Error Norms							
R_2		0.4847	0.8962	0.4115	0.5639	0.4700	1.9083
R_1		0.1013	1.1832	0.6605	9.6509	3.5872	1.3520

Table E.8

Error Norm Convergence Tests: M#keDC series, GSE=10^{-5}

U_o= 0.3 m s^{-1}, U_m = 1.07 m s^{-1}

TI=1.55%, Ru=25, Clip = 10^{12}

Locations: "Nozzle" (N=2533)

		Degree of Freedom					
		Ux	**Uy**	**Uz**	**P**	**KE**	**E**
Relative L_2 Norm							
	Mesh 3 - 4	0.009	0.048	0.130	0.054	0.235	0.209
	Mesh 4 - 5	0.003	0.038	0.048	0.056	0.107	0.278
Relative L_1 Norm							
	Mesh 3 - 4	0.00378	0.03119	0.03769	0.01685	-0.00173	-0.00059
	Mesh 4 - 5	0.00286	0.02192	0.01872	-0.04852	-0.00440	-0.00094
Absolute L_2 Norm							
	Mesh 3 - 4	0.07073	0.01842	0.05536	0.00994	0.00372	0.02148
	Mesh 4 - 5	0.04743	0.01400	0.02038	0.01033	0.00174	0.03957
Absolute L_1 Norm							
	Mesh 3 - 4	2.95684	0.18148	0.25888	0.13713	-0.00103	-0.03024
	Mesh 4 - 5	2.23011	0.12482	0.12603	-0.43049	-0.00260	-0.03906
3-Mesh Error Norms							
R_2		0.6706	0.7598	0.3682	1.0393	0.4664	1.8421
R_1		0.7542	0.6877	0.4868	-3.1392	2.5260	1.2918

Table E.9 **Convergence Behavior: M#keDC series, GSE=10^{-5}**
U_o= 0.3 m s^{-1}, U_m = 1.07 m s^{-1}
TI=1.55%, Ru=25, Clip = 10^{12}
Locations: "Velocity Measurement" (N=636)

Degree of Freedom	Ux	Uy	Uz	P	KE	E	Total
Number of points with Convergence that was:							
Monotonic (26%)	117	115	281	171	158	157	999
Oscillatory (61%)	444	415	242	387	426	425	2339
Divergent (13%)	75	106	113	78	52	54	478
Percentage of Points with Convergence that was:							
		117	115	281	171	158	157
Monotonic	444	415	242	387	426	425	2339
Oscillatory	75	106	113	78	52	54	478
Divergent	117	115	281	171	158	157	999
Points with Monotonic Convergence with order of accuracy 1<p<2 :		444	415	242	387	426	425
		75	106	113	78	52	54
Number	117	115	281	171	158	157	999
Percentage, Overall	444	415	242	387	426	425	2339
Percentage of Monotonic	75	106	113	78	52	54	478

Table E.10
Convergence Behavior: M#keDC series, GSE=10^{-4}
U_o= 0.3 m s^{-1}, U_m = 1.07 m s^{-1}
TI=1.55%, Ru=25, Clip = 10^{12}
Locations: "Velocity Measurement" (N=636)

Degree of Freedom	Ux	Uy	Uz	P	KE	E	Total
Number of points with Convergence that was:							
Monotonic (17%)	102	100	98	136	105	103	644
Oscillatory (73%)	483	441	489	428	478	484	2803
Divergent (10%)	51	95	49	72	53	49	369
Percentage of Points with Convergence that was:							
Monotonic	16.0%	15.7%	15.4%	21.4%	16.5%	16.2%	
Oscillatory	75.9%	69.3%	76.9%	67.3%	75.2%	76.1%	
Divergent	8.0%	14.9%	7.7%	11.3%	8.3%	7.7%	
Points with Monotonic Convergence with order of accuracy 1<p<2 :							
Number	10	12	10	10	8	11	61
Percentage, Overall	1.6%	1.9%	1.6%	1.6%	1.3%	1.7%	1.6%
Percentage of Monotonic	9.8%	12.0%	10.2%	7.4%	7.6%	10.7%	9.5%

Table E.11
Convergence Behavior: M#keDC series, GSE=10^{-3}
U_o= 0.3 m s^{-1}, U_m = 1.07 m s^{-1}
TI=1.55%, Ru=25, Clip = 10^{12}
Locations: "Velocity Measurement" (N=636)

Degree of Freedom	Ux	Uy	Uz	P	KE	E	Total
Number of points with Convergence that was:							
Monotonic (9%)	15	131	1	61	58	79	345
Oscillatory (75%)	549	393	621	504	394	368	2829
Divergent (17%)	72	112	14	71	184	189	642
Percentage of Points with Convergence that was:							
Monotonic	2.4%	20.6%	0.2%	9.6%	9.1%	12.4%	
Oscillatory	86.3%	61.8%	97.6%	79.2%	61.9%	57.9%	
Divergent	11.3%	17.6%	2.2%	11.2%	28.9%	29.7%	
Points with Monotonic Convergence with order of accuracy 1<p<2 :							
Number	2	14	0	9	11	15	51
Percentage, Overall	0.3%	2.2%	0.0%	1.4%	1.7%	2.4%	1.3%
Percentage of Monotonic	13.3%	10.7%	0.0%	14.8%	19.0%	19.0%	14.8%

Table E.12
Convergence Behavior: M#keDC series, GSE=10^{-5}
U_o= 0.3 m s^{-1}, U_m = 1.07 m s^{-1}
TI=1.55%, Ru=25, Clip = 10^{12}
Locations: "Nozzle" (N= 2533)

Degree of Freedom	Ux	Uy	Uz	P	KE	E	Total
Number of points with Convergence that was:							
Monotonic (68%)	2462	1708	1792	34	2245	2088	10329
Oscillatory (17%)	37	273	146	1929	77	135	2597
Divergent (15%)	34	552	595	570	211	310	2272
Percentage of Points with Convergence that was:							
Monotonic	97.2%	67.4%	70.7%	1.3%	88.6%	82.4%	
Oscillatory	1.5%	10.8%	5.8%	76.2%	3.0%	5.3%	
Divergent	1.3%	21.8%	23.5%	22.5%	8.3%	12.2%	
Points with Monotonic Convergence with order of accuracy 1<p<2 :							15,198
Number	0	0	0	0	0	0	0
Percentage, Overall	0.0%	0.0%	0.0%	0.0%	0.0%	0.0%	0.0%
Percentage of Monotonic	0.0%	0.0%	0.0%	0.0%	0.0%	0.0%	0.0%

Table E.13
Convergence Behavior: M#keDC series, GSE=10^{-4}
U_o= 0.3 m s^{-1}, U_m = 1.07 m s^{-1}
TI=1.55%, Ru=25, Clip = 10^{12}
Locations: "Nozzle" (N=2533)

Degree of Freedom	Ux	Uy	Uz	P	KE	E	Total
Number of points with Convergence that was:							
Monotonic (28%)	1151	719	395	1080	404	455	4204
Oscillatory (54%)	1374	1125	781	950	2065	1948	8243
Divergent (18%)	8	689	1357	503	64	130	2751
Percentage of Points with Convergence that was:							
Monotonic	45.4%	28.4%	15.6%	42.6%	15.9%	18.0%	
Oscillatory	54.2%	44.4%	30.8%	37.5%	81.5%	76.9%	
Divergent	0.3%	27.2%	53.6%	19.9%	2.5%	5.1%	
Points with Monotonic Convergence with order of accuracy 1<p<2 :							15,198
Number	0	0	0	0	0	0	0
Percentage, Overall	0.0%	0.0%	0.0%	0.0%	0.0%	0.0%	0.0%
Percentage of Monotonic	0.0%	0.0%	0.0%	0.0%	0.0%	0.0%	0.0%

Table E.14
Convergence Behavior: M#keDC series, GSE=10^{-3}
U_o= 0.3 m s^{-1}, U_m = 1.07 m s^{-1}
TI=1.55%, Ru=25, Clip = 10^{12}
Locations: "Nozzle" (N=2533)

Degree of Freedom	Ux	Uy	Uz	P	KE	E	Total
Number of points with Convergence that was:							
Monotonic (11%)	672	141	602	1	142	112	1670
Oscillatory (67%)	1836	2237	1130	649	2191	2183	10226
Divergent (22%)	25	155	801	1883	200	238	3302
Percentage of Points with Convergence that was:							
Monotonic	26.5%	5.6%	23.8%	0.0%	5.6%	4.4%	
Oscillatory	72.5%	88.3%	44.6%	25.6%	86.5%	86.2%	
Divergent	1.0%	6.1%	31.6%	74.3%	7.9%	9.4%	
Points with Monotonic Convergence with order of accuracy 1<p<2 :							15,198
Number	196	14	92	0	14	10	326
Percentage, Overall	7.7%	0.6%	3.6%	0.0%	0.6%	0.4%	2.1%
Percentage of Monotonic	29.2%	9.9%	15.3%	0.0%	9.9%	8.9%	19.5%

Table E.15 Prediction agreements between mesh densities for GSE=10^{-5}, velocity measurement region.

Degree of Freedom	Meshes Compared	slope	intercept	R^2
U				
	coarse-mid	1.0205	-0.0038	0.9954
	mid-fine	0.9971	0.0008	0.9954
V				
	coarse-mid	0.9866	0.0008	0.9934
	mid-fine	0.9953	-0.0005	0.9995
W				
	coarse-mid	1.0246	-0.0014	0.9861
	mid-fine	0.989	-0.0006	0.9934
KE				
	coarse-mid	1.1425	-5.00E-05	0.8942
	mid-fine	0.968	9.00E-06	0.9857

Table E.16 Adjustments to standard deviation due to low sample replicates: n = number of replicates. Adjusted standard deviation = (computed standard deviation) (adjustment)

n	$[(n-1)/2]^{0.5}$	(n-1)/2	n/2	Γ [(n-1)/2]	Γ [n/2]	Adjustment
2	0.7071	**0.5**	1.0	1.772454	1	1.253314
3	1.0000	1.0	**1.5**	1	0.886227	1.128379
4	1.2247	**1.5**	2.0	0.886227	1	1.085402
5	1.4142	2.0	**2.5**	1	1.32934	1.063846
6	1.5811	**2.5**	3.0	1.32934	2	1.050936

Table E.17 Least-squares regression of simulated streamwise velocity (U) to experimental velocity, considering 0.5 mm positioning adjustments

adjustment to position (mm)			reference	U		
X	Y	Z		**Slope**	**Intercept**	**R^2**
0	0	0	vmeas	0.7775	0.0294	0.902
-0.5	-0.5	-0.5	-1-1-1	0.7845	0.0280	0.891
0.5	-0.5	-0.5	1-1-1	0.7407	0.0387	0.888
-0.5	0.5	-0.5	-11-1	0.8221	0.0184	0.899
0.5	0.5	-0.5	11-1	0.7669	0.0317	0.899
-0.5	-0.5	0.5	-1-11	0.7705	0.0316	0.892
0.5	-0.5	0.5	1-11	0.7250	0.0426	0.887
-0.5	0.5	0.5	-111	0.8048	0.0228	0.899
0.5	0.5	0.5	111	0.7475	0.0364	0.898
-0.5	-0.5	0	-1-10	0.7778	0.0297	0.892
0.5	-0.5	0	1-10	0.7326	0.0407	0.888
-0.5	0.5	0	-110	0.8132	0.0206	0.901
0.5	0.5	0	110	0.7589	0.0337	0.900
-0.5	0	-0.5	-10-1	0.8135	0.0207	0.900
0.5	0	-0.5	10-1	0.7574	0.0341	0.899
-0.5	0	0.5	-101	0.7980	0.0246	0.900
0.5	0	0.5	101	0.7388	0.0387	0.898
-0.5	0	0	-100	0.8054	0.0227	0.902
0.5	0	0	100	0.7478	0.0364	0.899
0	-0.5	-0.5	0-1-1	0.7639	0.0331	0.890
0	0.5	-0.5	01-1	0.7955	0.0248	0.901
0	-0.5	0.5	0-11	0.7477	0.0371	0.891
0	0.5	0.5	011	0.7782	0.0292	0.900
0	-0.5	0	0-10	0.7559	0.0350	0.891
0	0.5	0	010	0.7871	0.0269	0.902
0	0	-0.5	00-1	0.7856	0.0273	0.901
0	0	0.5	001	0.7700	0.0313	0.901

Table E.18 Least-squares regression of simulated lateral velocity (V) to experimental velocity, considering 0.5 mm positioning adjustments

adjustment to position (mm)			reference	V		
X	Y	Z		**Slope**	**Intercept**	**R^2**
0	0	0	vmeas	0.7878	0.0001	0.900
-0.5	-0.5	-0.5	-1-1-1	0.7627	0.0034	0.917
0.5	-0.5	-0.5	1-1-1	0.7206	0.0040	0.914
-0.5	0.5	-0.5	-11-1	0.8100	-0.0008	0.897
0.5	0.5	-0.5	11-1	0.7688	-0.0002	0.891
-0.5	-0.5	0.5	-1-11	0.7511	0.0035	0.911
0.5	-0.5	0.5	1-11	0.7087	0.0042	0.906
-0.5	0.5	0.5	-111	0.7985	-0.0006	0.892
0.5	0.5	0.5	111	0.7560	0.0000	0.885
-0.5	-0.5	0	-1-10	0.7566	0.0035	0.915
0.5	-0.5	0	1-10	0.7145	0.0041	0.910
-0.5	0.5	0	-110	0.8035	-0.0007	0.895
0.5	0.5	0	110	0.7619	-0.0001	0.887
-0.5	0	-0.5	-10-1	0.8157	-0.0002	0.904
0.5	0	-0.5	10-1	0.7733	0.0003	0.899
-0.5	0	0.5	-101	0.8044	-0.0001	0.900
0.5	0	0.5	101	0.7619	0.0005	0.893
-0.5	0	0	-100	0.8093	-0.0001	0.902
0.5	0	0	100	0.7665	0.0004	0.895
0	-0.5	-0.5	0-1-1	0.7425	0.0037	0.916
0	0.5	-0.5	01-1	0.7893	-0.0005	0.894
0	-0.5	0.5	0-11	0.7298	0.0039	0.910
0	0.5	0.5	011	0.7773	-0.0003	0.889
0	-0.5	0	0-10	0.7361	0.0038	0.913
0	0.5	0	010	0.7826	-0.0004	0.891
0	0	-0.5	00-1	0.7943	0.0000	0.902
0	0	0.5	001	0.7833	0.0002	0.897

Table E.19 Least-squares regression of simulated vertical velocity (W) to experimental velocity, considering 0.5 mm positioning adjustments

adjustment to position (mm)			reference	W		
X	Y	Z		**Slope**	**Intercept**	R^2
0	0	0	vmeas	0.7515	0.0269	0.837
-0.5	-0.5	-0.5	-1-1-1	0.6911	0.0282	0.765
0.5	-0.5	-0.5	1-1-1	0.6382	0.0299	0.795
-0.5	0.5	-0.5	-11-1	0.7908	0.0256	0.812
0.5	0.5	-0.5	11-1	0.7175	0.0278	0.838
-0.5	-0.5	0.5	-1-11	0.6993	0.0282	0.767
0.5	-0.5	0.5	1-11	0.6431	0.0299	0.796
-0.5	0.5	0.5	-111	0.7988	0.0256	0.816
0.5	0.5	0.5	111	0.7309	0.0276	0.846
-0.5	-0.5	0	-1-10	0.6992	0.0281	0.770
0.5	-0.5	0	1-10	0.6438	0.0298	0.800
-0.5	0.5	0	-110	0.7970	0.0255	0.820
0.5	0.5	0	110	0.7243	0.0277	0.849
-0.5	0	-0.5	-10-1	0.7792	0.0259	0.816
0.5	0	-0.5	10-1	0.7060	0.0281	0.842
-0.5	0	0.5	-101	0.7878	0.0259	0.818
0.5	0	0.5	101	0.7196	0.0279	0.846
-0.5	0	0	-100	0.7881	0.0258	0.822
0.5	0	0	100	0.7156	0.0280	0.851
0	-0.5	-0.5	0-1-1	0.6659	0.0290	0.781
0	0.5	-0.5	01-1	0.7548	0.0267	0.827
0	-0.5	0.5	0-11	0.6735	0.0290	0.781
0	0.5	0.5	011	0.7644	0.0266	0.831
0	-0.5	0	0-10	0.6721	0.0289	0.785
0	0.5	0	010	0.7612	0.0266	0.835
0	0	-0.5	00-1	0.7445	0.0270	0.830
0	0	0.5	001	0.7551	0.0269	0.834

Table E.20 Slope and confidence interval for $\mu_{Yi|Xi}$, the estimated value of "Numerical Velocity" given a value of "Measured Velocity" *(Data file: E6)*

Regression Equation: Numerical = b (Measured) + intercept, $\alpha = 0.05$					
Computed Terms	Velocity Considered				Explanation of terms
	U	V	W	Combined	
n	637	637	637	1911	Sample size
Xbar	0.199	0.023	0.046	0.089	Average of measured velocity
Ybar	0.219	0.029	0.025	0.091	Average of numerically predicted velocity
$b_{Y.X}$	1.162	1.138	1.115	1.149	Slope of regression ($\Sigma xy / \Sigma x^2$)
intercept	-0.0130	0.0029	-0.0259	-0.0117	Y-intercept
Σx^2	26.060	0.681	1.536	28.278	Sum of squared measures
$\Sigma \hat{y}^2$	31.452	1.201	0.6202	1.0751	Explained sum of squares
$\Sigma d^2_{Y.X}$	0.1114	0.0529	0.0962	0.6036	Unexplained sum of squares, $\Sigma y^2 - \Sigma \hat{y}^2$
$S^2_{Y.X}$	0.00018	0.00008	0.00015	0.00032	Unexplained mean square error, $\Sigma d^2_{Y.X} / (n-2)$
s_b	0.0026	0.0111	0.0099	0.0033	Standard error of the regression coefficient, $(S^2_{YX} / \Sigma x^2)^{0.5}$
ts	447.75	102.87	112.28	343.60	t-value to test significance of regression coefficient ($p<<0.001$)
Lower 95%CI	1.1569	1.1163	1.0954	1.1424	L-95% CI for slope ($t_{0.05,n-2}$) = 1.960
Upper 95% CI	1.1670	1.1596	1.1344	1.1555	U-95% CI for slope ($t_{0.05,n-2}$) = 1.960
S_{Ybar}	0.00052	0.00036	0.00049	0.00041	Standard error for the sampled mean, Ybar (at Xbar)

Table E.21 Size-specific capture efficiencies for anatomical mannequin in Baity Air Laboratory wind tunnel, $U_o = 0.3$ m s^{-1}, $U_m = 1.07$ m s^{-1}.

Particle Size (µm)	Experimental			Nozzle generation			Capture Efficiency
	Count/ min	Count /mL Average	Count /mL Std	Count/5sec	Count/mL Average	Count/mL Stdev	
48.5	42.5	73.9	112.4	n/a	n/a	n/a	n/a
51.5	79	137.5	106.2	51557	1374840	439459	0.00010
54.5	105.8	184.0	178.5	31570	841873	416566	0.00022
57.5	170.2	296.0	127.7	22532	600860	347982	0.00049
60.5	208.8	363.3	191.0	11903	317400	104060	0.00114
63.5	160.9	280.0	198.0	7702	205373	98606	0.00136
66.5	137.4	239.1	177.1	3946	105233	92845	0.00227
69.5	82	142.6	137.4	5665	151067	160993	0.00094

Figure E.1 Predicted streamwise velocities for fine and middle mesh, GSE = 10^{-5}, at velocity measurement locations.

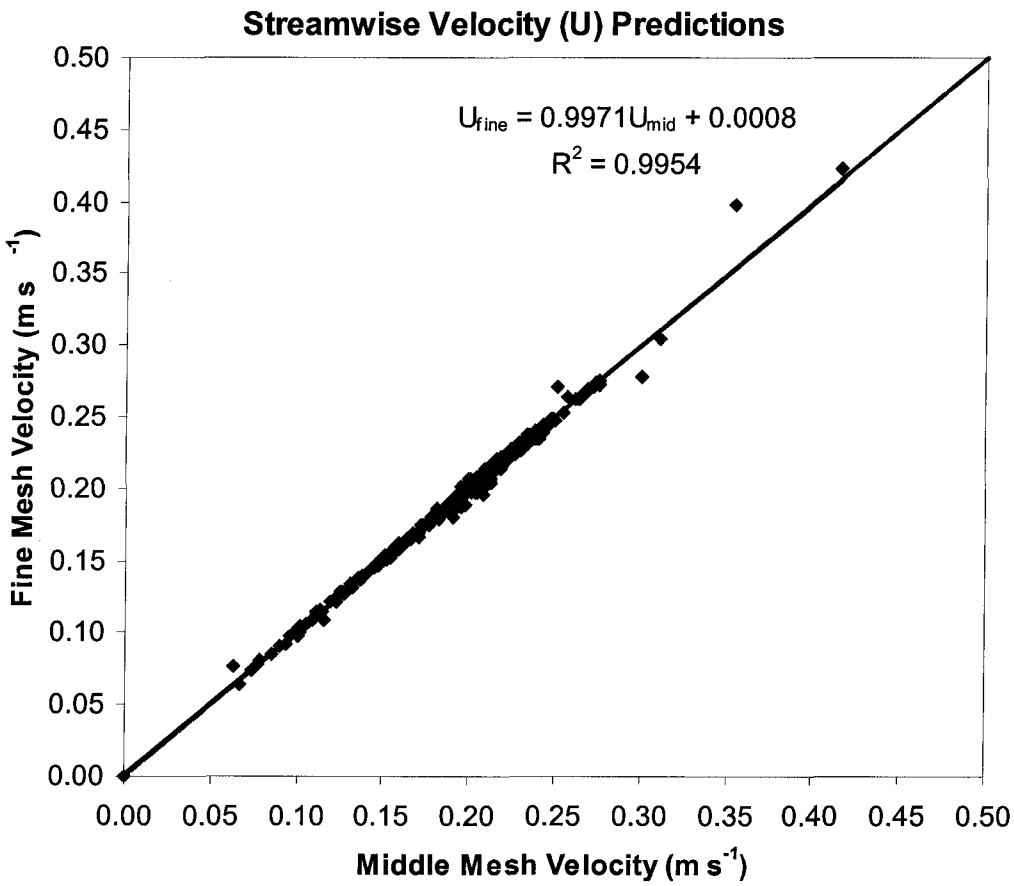

Figure E.2 Velocity comparison with confidence interval from equation E.18 *(Data file: E6)*

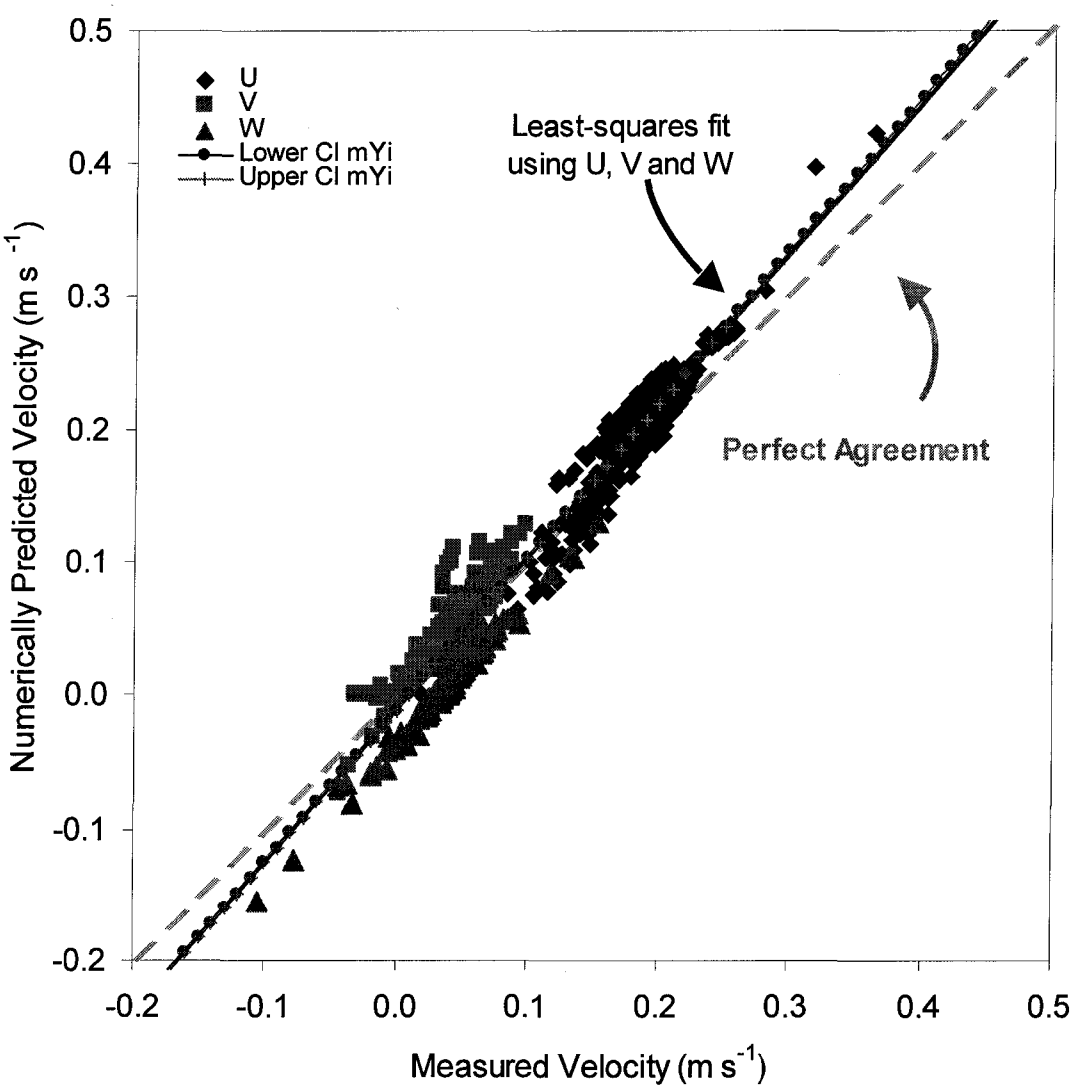

Figure E.3 Simulated capture efficiencies for 51.5 μm particle simulations

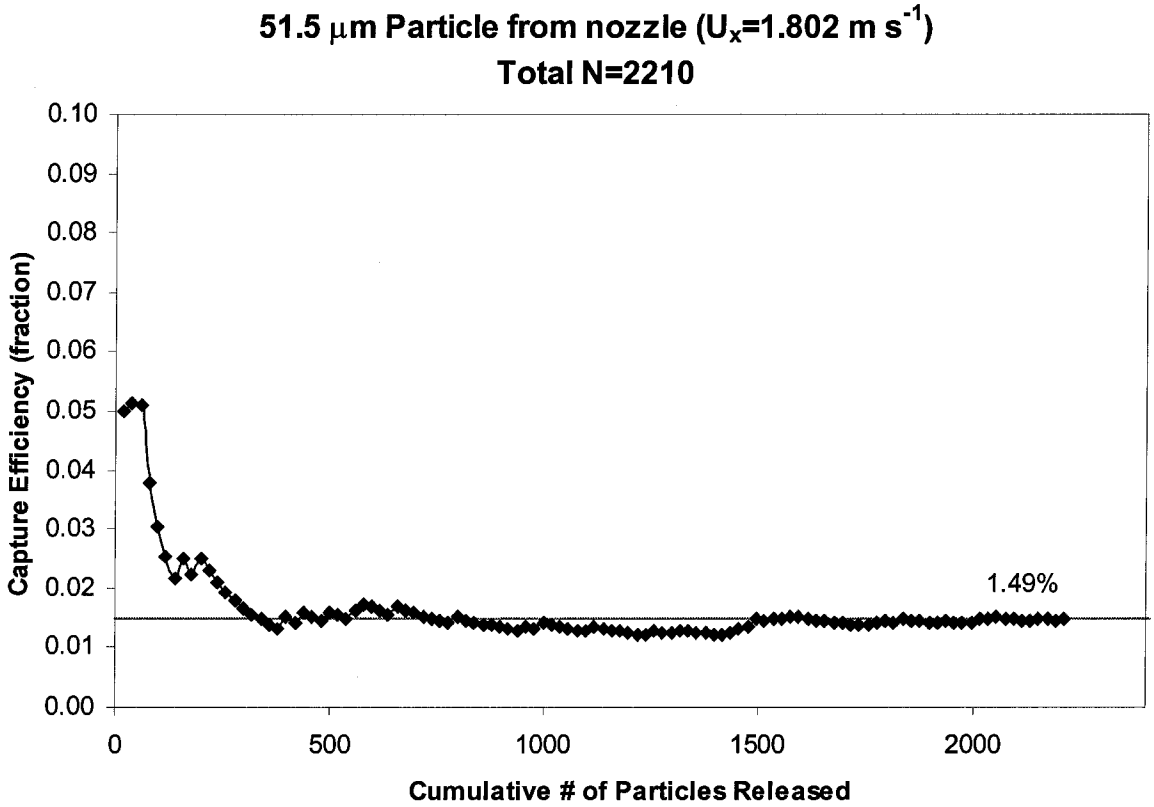

Figure E.4 Simulated capture efficiencies for 54.5 μm particle simulations

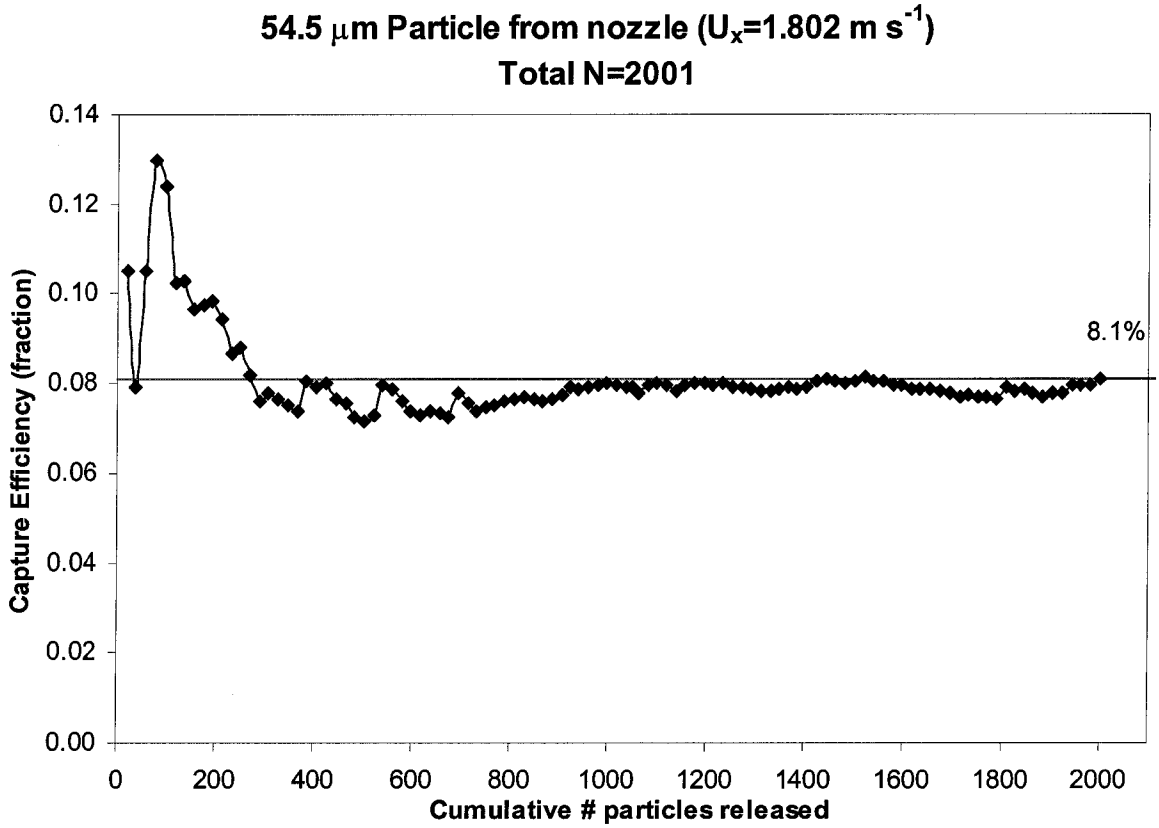

Figure E.5 Simulated capture efficiencies for 57.5 μm particle simulations

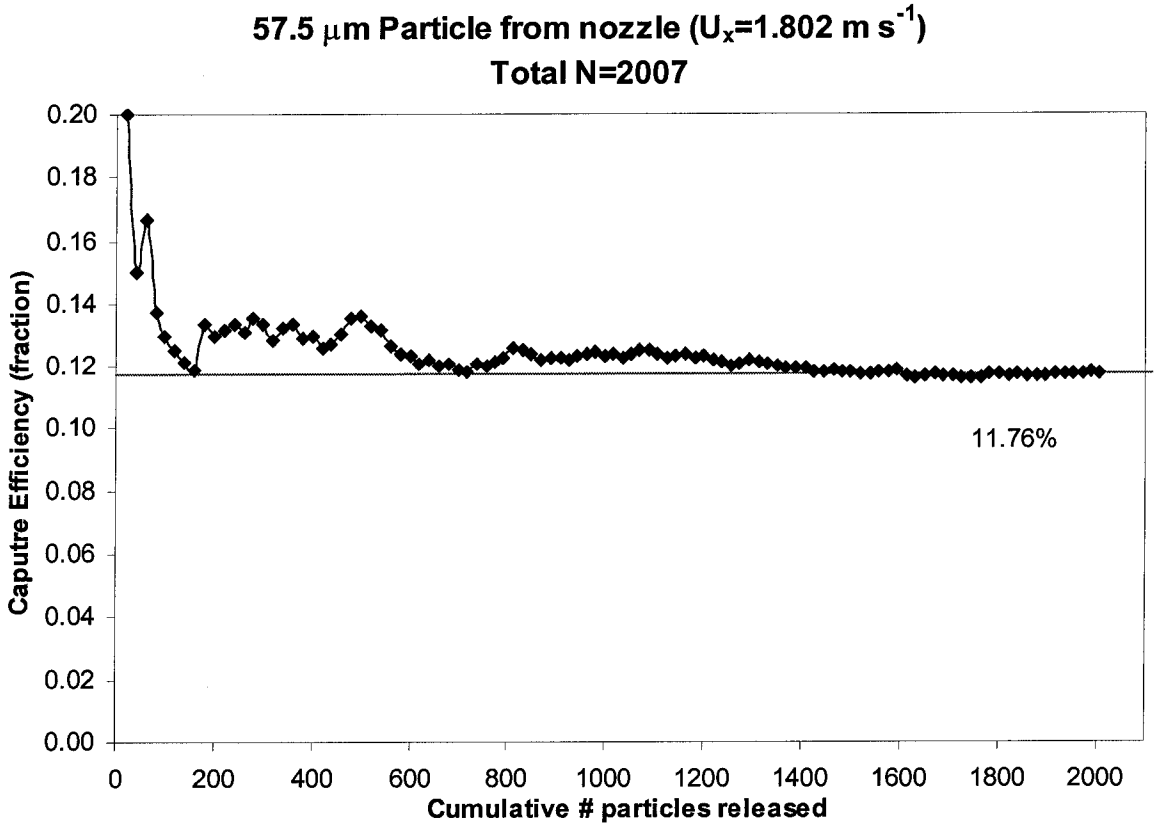

Figure E.6 Simulated capture efficiencies for 60.5 μm particle simulations

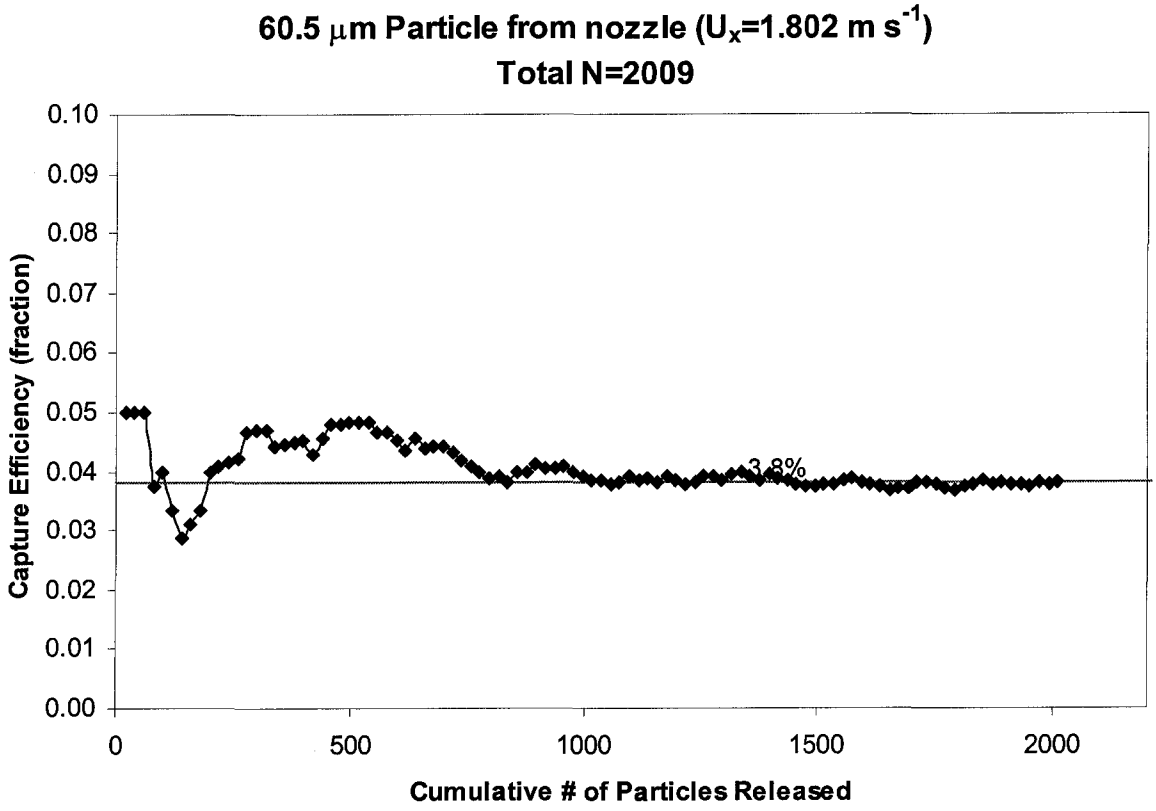

Figure E.7 Simulated capture efficiencies for 63.5 μm particle simulations

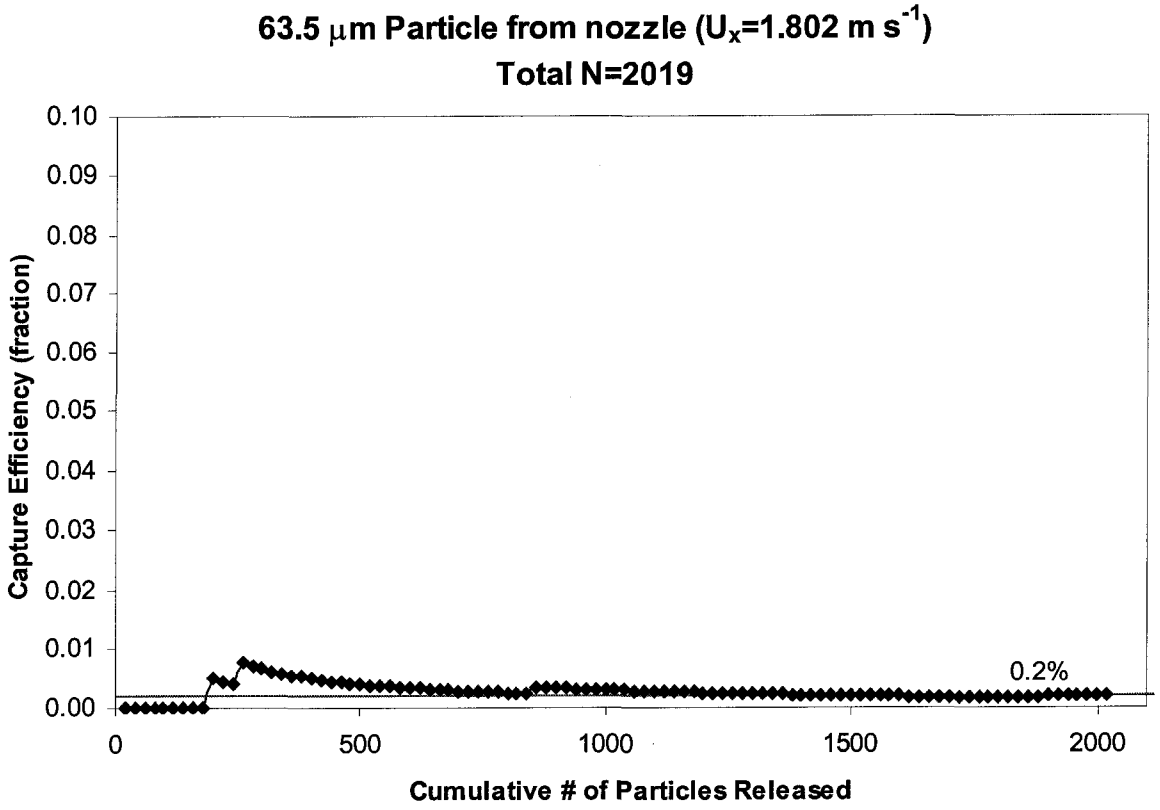

Figure E.8 Simulated capture efficiencies for 66.5 μm particle simulations

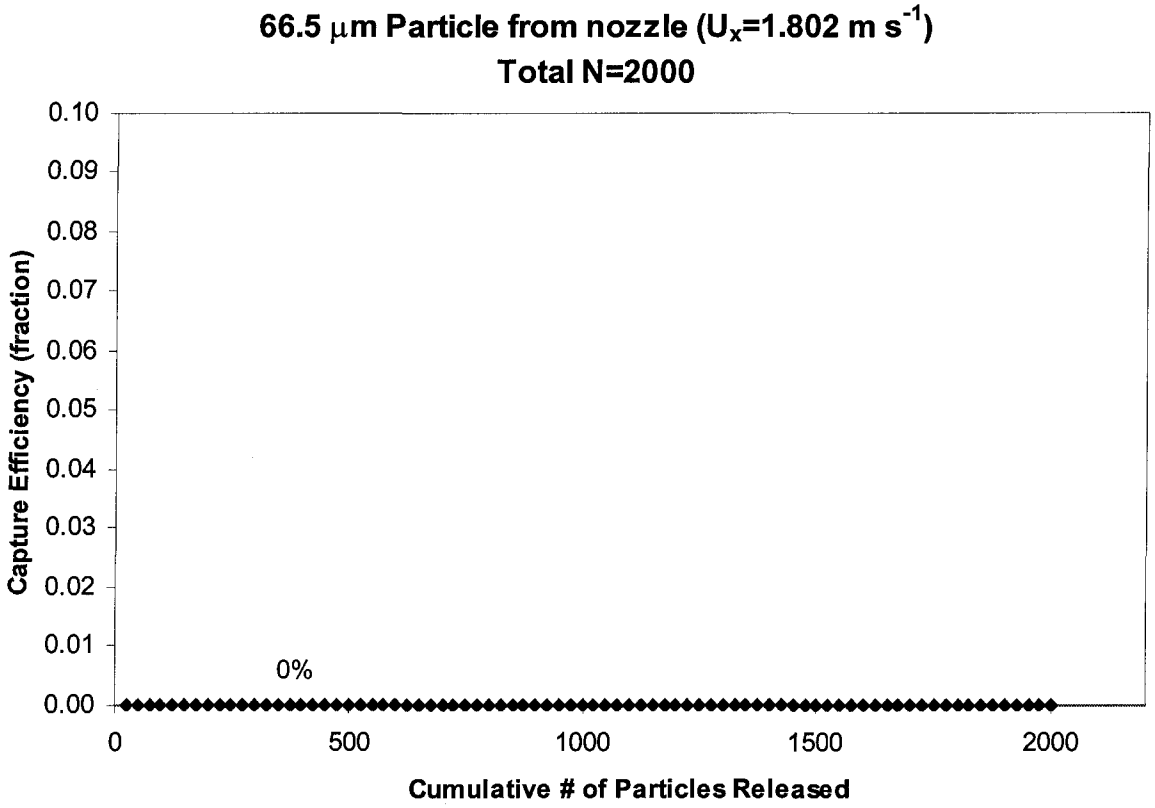

Figure E.9 Simulated capture efficiencies for 51.5 μm particle simulations with no initial particle velocity

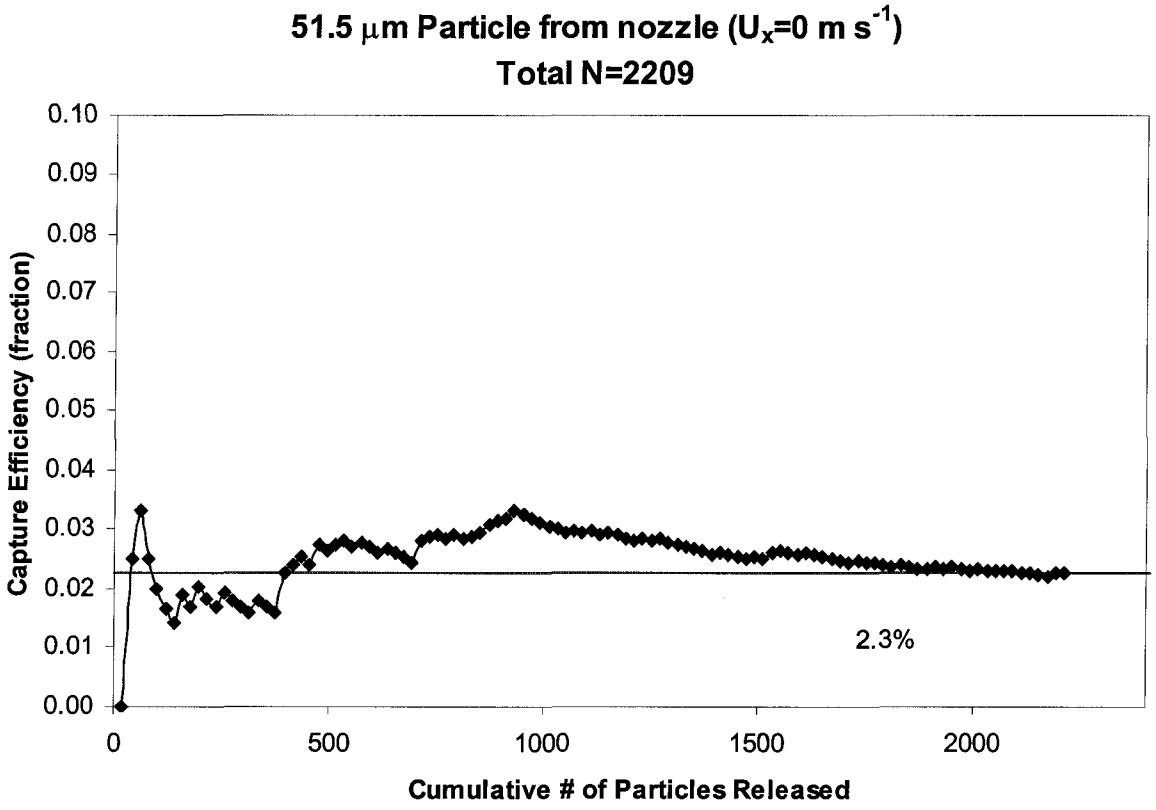

Figure E.10 Simulated capture efficiencies for 51.5 μm particle simulations with no initial particle velocity

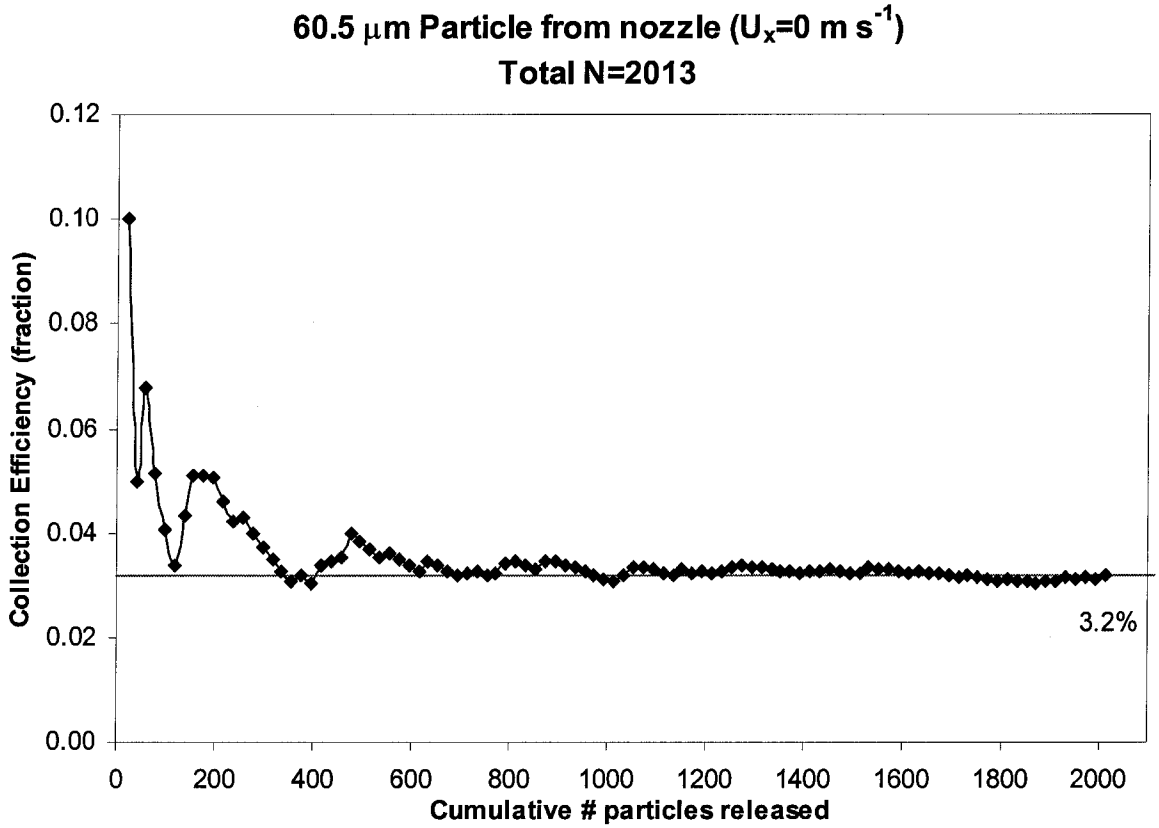

Figure E.11 Simulated capture efficiencies for 57.5 μm particle simulations with releases higher than nozzle centerline location (Z = +5 mm)

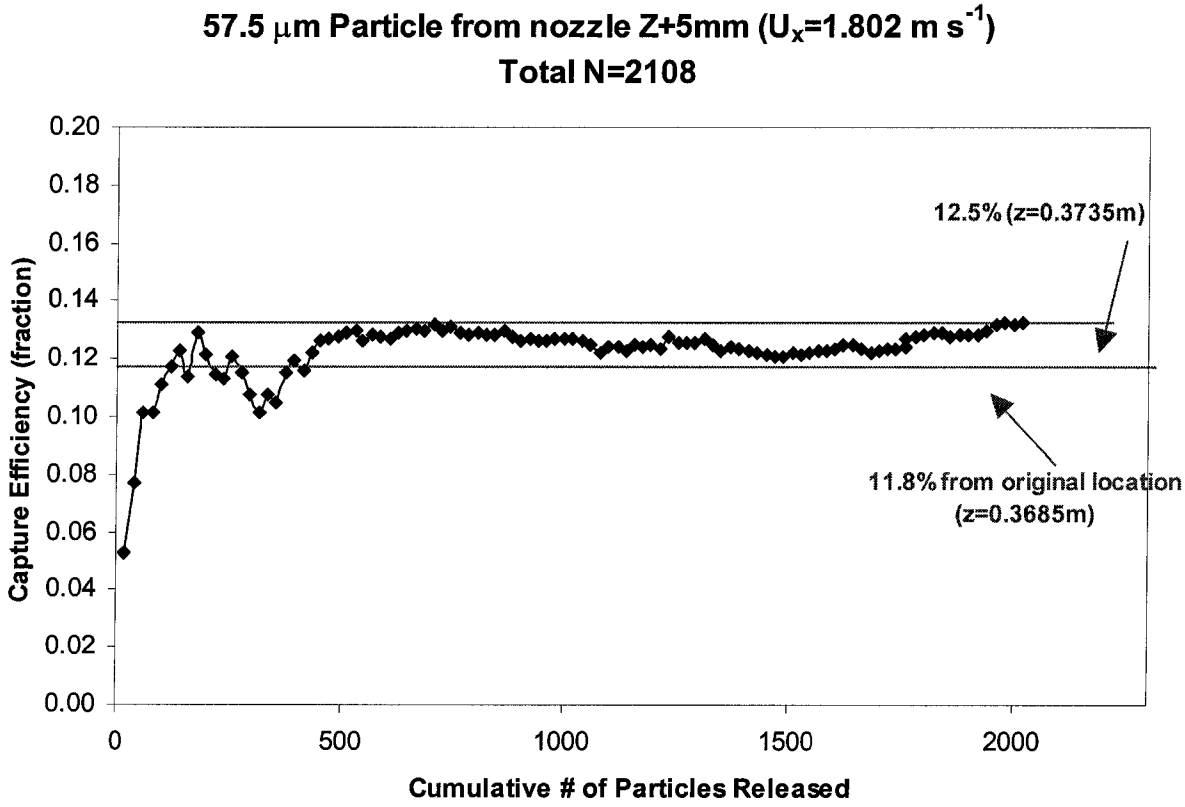

Figure E.12 Simulated capture efficiencies for 60.5 μm particle simulations with releases higher than nozzle centerline location (Z = +5 mm)

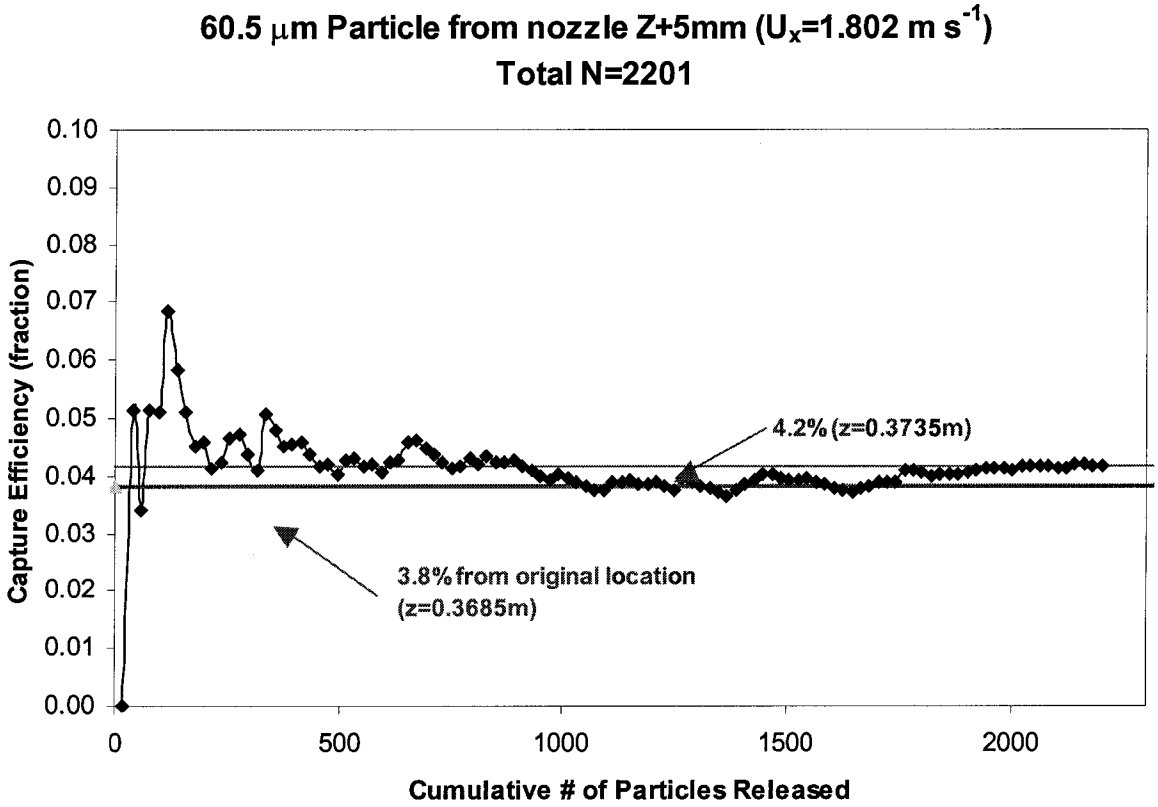

Figure E.13 Comparison of simulated and experimental capture efficiencies

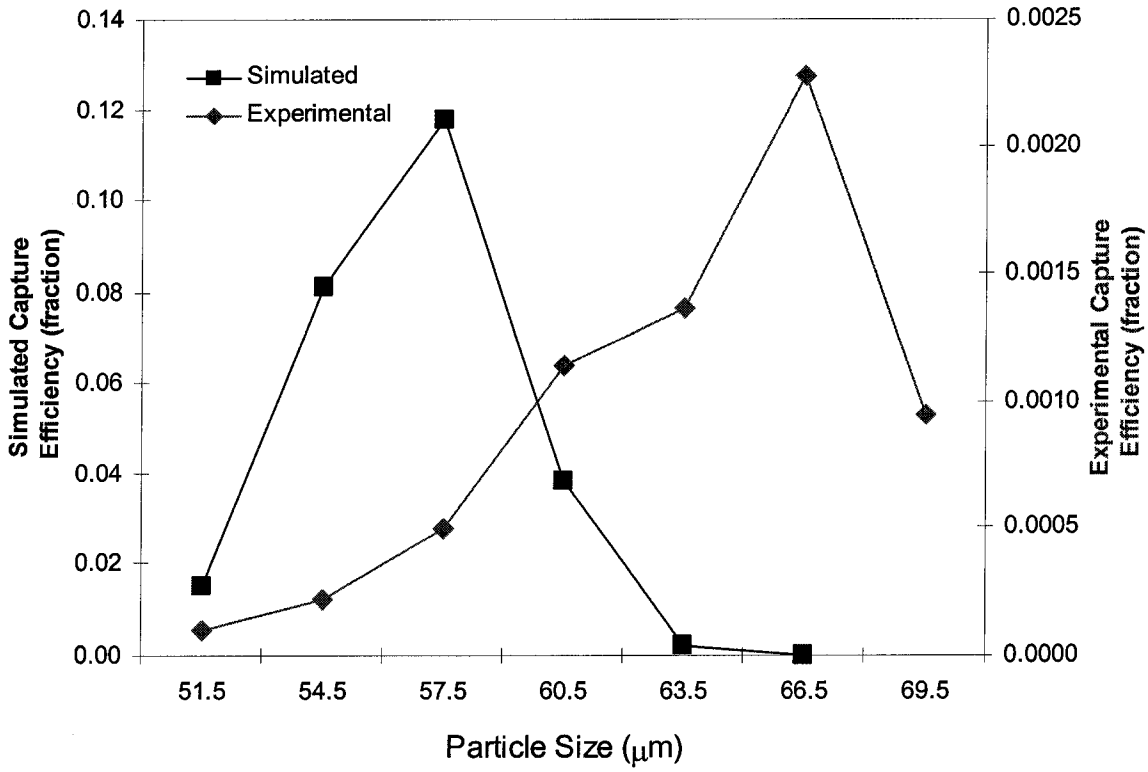

APPENDIX F: DATA AND CALCULATIONS FOR CHAPTER 4

This appendix documents the data and calculations from full-scale simulations of particle inhalability. A brief comparison of the selection of study conditions is provided, followed by a summary of velocity field and particle simulation verification. The method to determine the critical area for particle aspiration is detailed. Calculations of the critical areas and aspiration efficiencies are finally discussed. The supporting data files accompanying this work are summarized in Table F.1.

Table F.1 Data files supporting Appendix F

File Name	Description	Discussion Section
F1-verif 24vhm#D.xls	Verification calculations for $U_o = 0.2$ m s^{-1}, $U_m =$ 4.33 m s^{-1} velocity solutions	F.2
F2-verif v2hm#D.xls	Verification calculations for $U_o = 0.2$ m s^{-1}, $U_m =$ 1.81 m s^{-1} velocity solutions	F.2
F3-verif v4hm#D.xls	Verification calculations for $U_o = 0.4$ m s^{-1}, $U_m =$ 4.33 m s^{-1} velocity solutions	F.2
F4-Crit Area 24HM4D.xls	Critical area simulation data for $U_o = 0.2$ m s^{-1}, U_m = 4.33 m s^{-1}, using solution from middle mesh density (24HM4D)	F.4-F.6
F5-Crit Area V2HM4D.xls	Critical area simulation data for $U_o = 0.2$ m s^{-1}, U_m = 1.81 m s^{-1}, using solution from middle mesh density (V2HM4D)	F.4-F.6
F6-Crit Area V4HM4D.xls	Critical area simulation data for $U_o = 0.4$ m s^{-1}, U_m = 4.33 m s^{-1}, using solution from middle mesh density (V4HM4D)	F.4-F.6
F7-Summary Info.xls	Summary critical area and aspiration efficiency data from three velocity conditions	F.6
F8-Area In Locations.xls	Compiled list of locations where all particles are inhaled, over all test conditions	F.4

F.1 Scaled Meshes

This work was conducted on the human-scaled meshes described in Appendix D. The experimental-scale geometry and node spacing investigated in Chapter 3 were resized to human-scale by multiplying all dimensions by 1.5. To assess mesh convergence for this newly scaled system, three meshes were necessary and are summarized in Table F.2.

The velocity conditions of Chapter 2 (freestream velocity = 0.3 m s^{-1}, inhalation velocity = 1.07 m s^{-1}) were scaled to the new system by matching the Reynolds numbers and velocity ratios of the two systems:

$$Re_{head} = D_{head}U_o/\nu = 1920 \quad (F.2)$$

$$U_o/U_m = 0.11 \quad (F.3)$$

where ν is the kinematic viscosity of the fluid (1.51 x 10^{-5} m^2 s^{-1}).
This resulted in a freestream velocity of 0.2 m s^{-1} and inhalation velocity of 1.81 m s^{-1} in the human-scale system. Data files referencing this work are designated by "V2."

The conditions of Kennedy and Hinds (2002) were also simulated. Because their breathing was cyclical and the mouth opening was a different size than the simulated form, simulations were matched to their average inhalation velocity of 4.33 m s^{-1}. The freestream velocity of 0.4 m s^{-1} was matched in this velocity condition. Files referencing these simulations are designated by "V4."

A final velocity condition was investigated, using the low freestream velocity (0.2 m s^{-1}) and the higher inhalation velocity (4.33 m s^{-1}) in the other two simulations. Files referencing these simulations are designated by "24."

The values assigned to kinetic energy and dissipation were calculated using equations F.4 and F.5: :

$$KE = 1.5\,(TI\,U_x)^2 \quad (F.4)$$

$$E = \rho\, c_\mu\, KE^2 / (R_u\, \mu) \quad (F.5)$$

Where TI = 0.08 (turbulence intensity = 8%), R_u = 10, U_x = mean freestream velocity, ρ = air density = 1.205, c_μ = 1.09 (standard), μ = air viscosity =1.81 x 10^{-5} N s m^{-2}.

F.2 Velocity Convergence Calculations

Convergence was assessed using the same methods detailed in Appendix D. For each velocity condition investigated, convergence was assessed "close" (636 locations, $-0.15 \leq X < 0$ m) and "far" (2533 locations, $-2.4 \leq X < 0$ m), relative to the inhaling mouth. *(Data files: F1 through F3)*

F.2.a Oscillatory Behaviors

Tables F.3 through F.5 provide information on the convergence behavior of individual locations studied in the "close" locations, while Tables F.6 through F.8 provide the same assessment over locations further upstream. *Data files F1* through *F3* contain the supporting analyses. These assessments were based on the following error norm, as determined by:

$$R_1 = (f_{mid} - f_{fine})/(f_{coarse} - f_{mid}) \quad \text{(F.6)}$$

where f designates the degree of freedom and the subscript references the mesh density. A location with a negative value indicated oscillatory behavior, values greater than unity indicated divergence, and values between zero and one indicated monotonic behavior.

Order of accuracy (p) determinations were based on equation F.5:

$$p = \ln [(f_{coarse}-f_{mid})/(f_{mid}-f_{fine})] / \ln(r) \quad \text{(F.7)}$$

where r is the mesh refinement ratio, determined from equation F.6:

$$r = \exp(N_{fine}/N_{mid})^{1/3} = \exp (N_{mid}/N_{coarse})^{1/3} \quad \text{(F.8)}$$

where N is the number of elements in the mesh designated by its subscript. Because paved meshing was required for this complex geometry, the mesh refinement ratio was not constant: $(N_{fine}/N_{mid})^{1/3} = 1.259$ and $(N_{mid}/N_{coarse})^{1/3} = 1.278$. The average of the two was used for order of accuracy calculations.

Because this method is nearly second order accurate, locations with both monotonic convergence and with orders of accuracy between 1 and 2 were identified in Tables F.3 through F.8 as in the asymptotic range. The values of the order of accuracy are incorporated into uncertainty assessments, where the Grid Convergence Index, defined by Roache (1999):

$$GCI = F\,|(f_{mid}-f_{fine})/(r^p - 1)\,| \quad \text{(F.9)}$$

where f is the degree of freedom, r is the mesh refinement ratio, p is the determined order of accuracy. The value of F is an uncertainty factor: Roache recommends a value of 1.25 for well-behaved, converging meshes that have been assessed using the three-grid method used here. For less well-behaved meshes, a value of "3" is recommended. For this work, values of 1.25 were used at locations that were monotonically converging and had correct orders of accuracy ($1 < p < 2$); values of 3 were assigned to monotonically converging locations that had orders of accuracy outside of this range.

F.2.b Convergence Assessments

The main criteria for assessing convergence is the three-mesh L_2 error norm, defined by R_2 in equation E.3. These values are less than unity for all degrees of freedom in the locations close to the human form, indicating satisfactory convergence. Further away from the mannequin, convergence is less well demonstrated, indicating further mesh refinement is ideal. Examination of the two-mesh error norms provides information on the relative performance between simulations on sequentially denser grids. The magnitude of the error norm decreases when comparing more refined meshes: the maximum L_2 error norm for the fine-middle meshes is 0.096 (for U_y in the high freestream velocity study), indicating that the magnitude of velocity errors between these meshes was less than 10%. These values are provided in Tables F.7 through F.14 for the three simulations performed in human-scale.

F.3 Particle convergence

The two critical settings for particle transport simulations were the timestep and the number of iterations per timestep. For 7 and 116 μm particles, replicate particle releases were simulated at different timesteps and iterations to investigate any effects of these settings. Timesteps ranged from 0.05 seconds to 10^{-5} seconds, and allowable iterations within a timestep ranged from 10 to 100. No difference in the terminal particle location or the time to travel to these locations was identified for timesteps smaller than 10^{-4}. The computational time to calculate particle trajectories was insignificant for timesteps as small as 5×10^{-5}, but significantly more time was required for the same simulation using 10^{-6} seconds as the timestep. No difference in terminal particle location was identified for any of the maximum iterations per timestep. Particle aspiration experiments were conducted at 5×10^{-5} seconds per step and 10 iterations were allowed per timestep. The total time of tracking was 6.5 seconds, sufficient for particles to travel from the release point to the mannequin head where inhalation could be determined.

F.4 Particle Release Simulations

Particles were released upstream of the mouth. Chung and Dunn-Rankin (1997) found that the presence of the inhaling cylindrical form affected the flow only within 4

diameters upstream. The simulated head represented half of a 0.143 m head diameter These simulations released particles 0.75 m upstream of the mannequin, more than 4 head diameters upstream, sufficient to ensure minimal influences of the mannequin in the fluid flow field. Releases of 116 μm particles in 0.2 m s^{-1} freestream condition required releases closer to the mannequin (0.4 m) because of the dominance of gravitational settling, but these release locations were well above the head of the mannequin, thereby ensuring release in relatively freestream conditions. *(Data files: F4 through F6)*

Initial velocity was assigned to the particle to address the uniform particle concentration assumption. Particles were released with initial streamwise velocity equal to the freestream velocity at that release location: the actual velocities across the release areas were obtained from the solution to the velocity field, using Fidap's FIPOST. The vertical component of velocity combined the FIPOST vertical velocity and the terminal settling velocity (V_{ts}), as determined from equation (F.15).

$$V_{ts} = \rho_p d^2 g/(18\eta) \qquad \text{(F.15)}$$

where

V_{ts} = terminal settling velocity, m s^{-1}

ρ_p = particle density, 1000 kg m^{-3}

d = particle diameter (m)

g = 9.8 m s^{-2}

η = fluid (air) viscosity, 1.81 x 10^{-5} N s m^{-2}

Table F.15 is provided to illustrate the data from 82 μm particle simulations with 0.2 m s^{-1} freestream, 1.81 m s^{-1} inhalation velocities. These particles were released with an initial streamwise velocity of 0.2096 m s^{-1}, matching the freestream, and 0.20218 m s^{-1} downward vertical velocity to account for the large terminal settling velocity for these particles. The first column in table F.15 indicates the lateral (Y) release location. Twenty particles were released along the line at Y=0 extending from a height of 0.67 to 0.66 m (columns 4 and 5), with the spacing between these particles designated by the value of Δ in column 6. Particle transport was simulated, using laminar particle motion, and the bottom 11 particles were identified as passing into the mouth. The initial release location for this particle was calculated from equation F.16:

$$Z_{max} \text{ into mouth} = (Z_{min} \text{ of release}) + (\#\text{ that get in} - 1)\,\Delta \qquad \text{(F.16)}$$

Results from these calculations are provided in column 3.

At the same Y = 0 location, twenty more particles were released between heights between 0.6425 and 0.6325 m (columns 9 and 10) to determine the lowest release location where a particle would be aspirated. Here, only the top 3 particles were aspirated, and the initial release location for this particle was calculated from equation F.17:

$$Z_{min} \text{ into mouth} = (Z_{min} \text{ of release}) + (20 - \#\text{ that gets in})\,\Delta \qquad \text{(F.16)}$$

Results from these calculations are provided in column 8 of Table F.16.

These computed Z coordinates were used to determine the critical aspiration area, to be discussed in section F.5. This process was repeated at increments of $\Delta Y = 0.00025$ m. Near the most lateral locations where particles were aspirated, smaller ΔY increments were investigated to accurately determine the width of the critical area. For the simulations given in Table F.15, particles were inhaled at Y = 0.006 m but no particles were found at Y = 0.00625 m, so locations between these values were investigated. For this simulation, no particle was inhaled at Y = 0.0061 m, which was used for the calculation of the width of the most lateral critical area band.

Once the (Y, Z) coordinates defining the critical area were determined, the data quality was checked graphically, as shown in Figure F.1. Where these curves looked irregular, additional simulations were performed, often with smaller ΔZ release intervals to resolve the shape of the critical area.

In addition to recording the locations of aspirated particles, information was recorded on which particles deposited within the lips but did not reach the orifice at the back of the mouth and which particles moved toward the mouth but deposited on the outside of the lips and were not inhaled. Release coordinates for these particles were calculated also using equations F.15 and F.16. A complete summary of the critical aspiration locations for all velocity conditions and for all proposed critical area definitions has been compiled into the *data file F8*.

F.5 Critical Areas

Once particle simulations were completed, critical area calculations were performed. For the data presented in Table F.15, critical area calculations are provided in Table F.16.

The same Y locations are provided in column 1, with the corresponding height of the critical area band at that Y location provided in column 2 (Δz). The width of that section of the critical area is determined as half the distance between the given Y and the two corresponding lateral locations investigated:

$$\Delta Y_i = (Y_{i+1} - Y_{i-1}) / 2 \qquad \text{(F.17)}$$

For example, the width of the contribution to the critical area at Y = 0.0005 m is (0.00075 -0.00025)/2 = 0.00025. For the most lateral locations (*e.g.*, Y = 0), the ΔY is one-half the distance between that lateral location and the adjacent one.

The widths (ΔY) and heights (ΔZ) were multiplied to calculate a series of individual critical area contributions, as shown in column 4 of Table F.15. The critical area associated with inhalation was the summation of these smaller areas over all lateral locations.

Using the last particle inhaled introduces a bias toward underestimation of the critical area. To avoid this, the same critical area calculations were made using the initial release location of the adjacent particles that were not inhaled. Columns (5) – (7) in Table F.16 provide this calculation. The value of $\Delta z+$ in column (5) was the sum of the Δz in column (2) plus the particle release interval indicated in both columns (6) and (11) of Table F.15. Areas are again computed, and the sum of these slightly large critical area bands is given in column (7) of Table F.16. The true inhaled critical area is somewhere between these two calculated areas. Data presented for Paper 3 were the averages of these two "Inhaled" and "Just missed" areas, with the uncertainty being the difference between the average calculated and these two bounds. Similar calculations were performed for the other two critical areas ("between the lips" and "directed towards the mouth"). All particle aspiration data and analyses are included on the data disc accompanying this dissertation (*data files: F4 through F6*).

F.6 Aspiration Efficiency Calculations

The equation used to calculate aspiration efficiency was derived in Chapter 4, given as equation (4.7):

$$A = [\, A_c \; U_c \,] / [A_m \; U_m \,]. \qquad \text{(4.7)}$$

For each particle simulation, the critical areas (A_c) were determined as discussed in section F.5. Because the mesh densities were identical for each of the velocity conditions in this study, the mouth area (A_m) was constant for all particle experiments, 6.9341 x 10^{-5} m^2. The mouth velocity (U_m) changed for each velocity condition, and the mean velocity over the orifice was confirmed using output from Fidap's FIPOST. The critical velocity (U_c) was the average streamwise velocity within the determined critical area. Because U_c was also needed to assign the initial velocity to particles to determine the critical area, an iterative process was used to assign the initial particle velocities. Once the exact coordinates were known for the critical area, the streamwise velocities associated with these coordinates were reevaluated. Differences between the velocities assigned to particle simulations and the velocities from the coordinates contained within critical areas differed by less than 0.1% and were determined to be insignificant to the critical area simulations. The streamwise velocities within the upstream critical areas were averaged over the critical area and used as U_c for the corresponding aspiration efficiency calculations.

Aspiration efficiency calculations are included in the summary tab of the *data files F4* through *F6*, and a tabulated summary is provided in the *data file F7*.

Table F.2 Mesh density information for human-scale system

Mesh	# Nodes	# Elements
HM3D (coarse)	160,044	908,905
HM4D (middle)	333,772	1,916,038
HM5D (fine)	665,314	3,846,262

Table F.3 Convergence Information: 24HM#D series, close
U_o= 0.2 m s^{-1}, U_m = 4.33 m s^{-1}
TI=8%, Ru=10, Clip = 10^{12}
Locations: "Close" (N=636)

Degree of Freedom	**Ux**	**Uy**	**Uz**	**P**	**KE**	**E**	Total
Number of points with Convergence that was:							
Monotonic (38%)	194	201	245	349	238	204	1431
Oscillatory (42%)	266	317	240	177	278	310	1588
Divergent (21%)	176	118	151	110	120	122	797
Percentage of Points with Convergence that was:							
Monotonic	30.5%	31.6%	38.5%	54.9%	37.4%	32.1%	
Oscillatory	41.8%	49.8%	37.7%	27.8%	43.7%	48.7%	
Divergent	27.7%	18.6%	23.7%	17.3%	18.9%	19.2%	
Points with Monotonic Convergence with order of accuracy 1<p<2 :							3816
Number	32	22	45	64	30	43	236
Percentage, Overall	5.0%	3.5%	7.1%	10.1%	4.7%	6.8%	6.2%
Percentage of Monotonic	16.5%	10.9%	18.4%	18.3%	12.6%	21.1%	16.5%

Table F.4 Convergence Information: V2HM#D series, close
U_o= 0.2 m s^{-1}, U_m = 1.81 m s^{-1}
TI=8%, Ru=10, Clip = 10^{12}
Locations: "Close" (N=636)

Degree of Freedom	**Ux**	**Uy**	**Uz**	**P**	**KE**	**E**	Total
Number of points with Convergence that was:							
Monotonic (37%)	170	202	230	369	212	228	1411
Oscillatory (46%)	360	346	262	172	297	303	1740
Divergent (17%)	106	88	144	95	127	105	665
Percentage of Points with Convergence that was:							
Monotonic	26.7%	31.8%	36.2%	58.0%	33.3%	35.8%	26.7%
Oscillatory	56.6%	54.4%	41.2%	27.0%	46.7%	47.6%	56.6%
Divergent	16.7%	13.8%	22.6%	14.9%	20.0%	16.5%	16.7%
Points with Monotonic Convergence with order of accuracy 1<p<2 :							3816
Number	24	23	40	58	31	32	208
Percentage, Overall	3.8%	3.6%	6.3%	9.1%	4.9%	5.0%	5.5%
Percentage of Monotonic	14.1%	11.4%	17.4%	15.7%	14.6%	14.0%	14.7%

Table F.5 Convergence Information: V4HM#D series, close
U_o= 0.4 m s^{-1}, U_m = 4.33 m s^{-1}
TI=8%, Ru=10, Clip = 10^{12}
Locations: "Close" (N=636)

Degree of Freedom	**Ux**	**Uy**	**Uz**	**P**	**KE**	**E**	Total
Number of points with Convergence that was:							
Monotonic (39%)	241	188	210	399	217	239	1494
Oscillatory (42%)	293	342	322	93	267	282	1599
Divergent (19%)	102	106	104	144	152	115	723
Percentage of Points with Convergence that was:							
Monotonic	37.9%	29.6%	33.0%	62.7%	34.1%	37.6%	
Oscillatory	46.1%	53.8%	50.6%	14.6%	42.0%	44.3%	
Divergent	16.0%	16.7%	16.4%	22.6%	23.9%	18.1%	
Points with Monotonic Convergence with order of accuracy 1<p<2 :							3816
Number	33	22	23	64	33	38	213
Percentage, Overall	5.2%	3.5%	3.6%	10.1%	5.2%	6.0%	5.6%
Percentage of Monotonic	13.7%	11.7%	11.0%	16.0%	15.2%	15.9%	14.3%

Table F.6 Convergence Information: 24HM#D series, far
U_o= 0.2 m s^{-1}, U_m = 4.33 m s^{-1}
TI=8%, Ru=10, Clip = 10^{12}
Locations: "Far" (N=2533)

Degree of Freedom	**Ux**	**Uy**	**Uz**	**P**	**KE**	**E**	Total
Number of points with Convergence that was:							
Monotonic (53%)	2482	1139	1198	178	1407	1623	8027
Oscillatory (11 %)	35	591	121	166	463	263	1639
Divergent (36%)	16	803	1214	2189	663	647	5532
Percentage of Points with Convergence that was:							
Monotonic	98.0%	45.0%	47.3%	7.0%	55.5%	64.1%	
Oscillatory	1.4%	23.3%	4.8%	6.6%	18.3%	10.4%	
Divergent	0.6%	31.7%	47.9%	86.4%	26.2%	25.5%	
Points with Monotonic Convergence with order of accuracy 1<p<2 :							15,198
Number	1293	198	281	38	226	351	2387
Percentage, Overall	51.0%	7.8%	11.1%	1.5%	8.9%	13.9%	15.7%
Percentage of Monotonic	52.1%	17.4%	23.5%	21.3%	16.1%	21.6%	29.7%

Table F.7 Convergence Information: V2HM#D series, far
U_o= 0.2 m s^{-1}, U_m = 1.81 m s^{-1}
TI=8%, Ru=10, Clip = 10^{12}
Locations: "Far" (N=2533)

Degree of Freedom	**Ux**	**Uy**	**Uz**	**P**	**KE**	**E**	Total
Number of points with Convergence that was:							
Monotonic (54%)	2480	1087	1161	367	1408	1630	8133
Oscillatory (11 %)	37	595	118	180	464	263	1657
Divergent (36%)	16	851	1254	1986	661	640	5408
Percentage of Points with Convergence that was:							
Monotonic	97.9%	42.9%	45.8%	14.5%	55.6%	64.4%	
Oscillatory	1.5%	23.5%	4.7%	7.1%	18.3%	10.4%	
Divergent	0.6%	33.6%	49.5%	78.4%	26.1%	25.3%	
Points with Monotonic Convergence with order of accuracy 1<p<2 :							15,198
Number	1263	198	303	69	231	359	2423
Percentage, Overall	49.9%	7.8%	12.0%	2.7%	9.1%	14.2%	15.9%
Percentage of Monotonic	50.9%	18.2%	26.1%	18.8%	16.4%	22.0%	29.8%

Table F.8 Convergence Information: V4HM#D series, far
U_o= 0.4 m s^{-1}, U_m = 4.33 m s^{-1}
TI=8%, Ru=10, Clip = 10^{12}
Locations: "Far" (N=2533)

Degree of Freedom	**Ux**	**Uy**	**Uz**	**P**	**KE**	**E**	Total
Number of points with Convergence that was:							
Monotonic (59%)	2476	1415	1273	1206	941	1617	8928
Oscillatory (14 %)	29	465	181	254	1037	222	2188
Divergent (27%)	28	653	1079	1073	555	694	4082
Percentage of Points with Convergence that was:							
Monotonic	97.7%	55.9%	50.3%	47.6%	37.1%	63.8%	
Oscillatory	1.1%	18.4%	7.1%	10.0%	40.9%	8.8%	
Divergent	1.1%	25.8%	42.6%	42.4%	21.9%	27.4%	
Points with Monotonic Convergence with order of accuracy 1<p<2 :							15,198
Number	2228	200	317	307	126	338	3516
Percentage, Overall	88.0%	7.9%	12.5%	12.1%	5.0%	13.3%	23.1%
Percentage of Monotonic	90.0%	14.1%	24.9%	25.5%	13.4%	20.9%	39.4%

Table F.9 Error Norm Convergence Tests: 24HM#D series, close
U_o= 0.2 m s^{-1}, U_m = 4.33 m s^{-1}
TI=8%, Ru=10, Clip = 10^{12}
Locations: "Close" (N=636)

		Degree of Freedom					
		Ux	**Uy**	**Uz**	**P**	**KE**	**E**
Relative L2 Norm							
	Mesh 3 - 4	0.026	0.164	0.097	0.084	0.385	0.374
	Mesh 4 - 5	0.018	0.096	0.047	0.042	0.257	0.292
Relative L1 Norm							
	Mesh 3 - 4	-0.00314	0.02463	0.04733	0.02997	-0.16919	-0.22857
	Mesh 4 - 5	-0.00412	-0.00836	0.02006	0.01122	-0.18299	-0.15237
Absolute L2 Norm							
	Mesh 3 - 4	0.10900	0.09924	0.08831	0.03161	0.02130	0.19769
	Mesh 4 - 5	0.07324	0.05694	0.04268	0.01603	0.01676	0.16719
Absolute L1 Norm							
	Mesh 3 - 4	-0.31868	0.18122	0.50416	0.19405	-0.07389	-0.35528
	Mesh 4 - 5	-0.42028	-0.06200	0.20948	0.07187	-0.09792	-0.28245
3-Mesh Error Norms							
R_2		0.6720	0.5737	0.4833	0.5071	0.7866	0.8457
R_1		1.3188	-0.3422	0.4155	0.3704	1.3251	0.7950

Table F.10 Error Norm Convergence Tests: V2HM#D series, close
U_o= 0.2 m s^{-1}, U_m = 1.81 m s^{-1}
TI=8%, Ru=10, Clip = 10^{12}
Locations: "Close" (N=636)

	Degree of Freedom					
	Ux	**Uy**	**Uz**	**P**	**KE**	**E**
Relative L2 Norm						
Mesh 3 - 4	0.016	0.073	0.079	0.033	0.299	0.457
Mesh 4 - 5	0.011	0.047	0.047	0.016	0.137	0.228
Relative L1 Norm						
Mesh 3 - 4	-0.00392	0.01153	0.02514	0.01954	-0.06100	-0.15582
Mesh 4 - 5	-0.00246	0.00946	0.01720	0.00576	0.05978	0.06345
Absolute L2 Norm						
Mesh 3 - 4	0.06169	0.05056	0.04455	0.01157	0.00654	0.02782
Mesh 4 - 5	0.04245	0.03216	0.02599	0.00558	0.00289	0.01243
Absolute L1 Norm						
Mesh 3 - 4	-0.36337	0.14558	0.27228	0.16561	-0.02049	-0.04973
Mesh 4 - 5	-0.22852	0.11833	0.18314	0.04853	0.01896	0.01966
3-Mesh Error Norms						
R_2	0.6881	0.6361	0.5833	0.4818	0.4419	0.4467
R_1	0.6289	0.8128	0.6726	0.2930	-0.9254	-0.3954

Table F.11 Error Norm Convergence Tests: V4HM#D series, close
U_o= 0.4 m s^{-1}, U_m = 4.33 m s^{-1}
TI=8%, Ru=10, Clip = 10^{12}
Locations: "Close" (N=636)

	Degree of Freedom					
	Ux	**Uy**	**Uz**	**P**	**KE**	**E**
Relative L2 Norm						
Mesh 3 - 4	0.016	0.085	0.078	0.035	0.256	0.414
Mesh 4 - 5	0.012	0.058	0.043	0.019	0.153	0.291
Relative L1 Norm						
Mesh 3 - 4	-0.00348	0.02097	0.02828	0.02157	-0.05468	-0.10490
Mesh 4 - 5	-0.00328	0.00591	0.00326	0.01148	0.00527	0.03950
Absolute L2 Norm						
Mesh 3 - 4	0.12452	0.11326	0.09224	0.04671	0.01657	0.19479
Mesh 4 - 5	0.09062	0.07639	0.05029	0.02448	0.00978	0.11917
Absolute L1 Norm						
Mesh 3 - 4	-0.65866	0.49125	0.59489	0.68767	-0.04061	-0.19633
Mesh 4 - 5	-0.62244	0.13766	0.06834	0.36166	0.00390	0.07343
3-Mesh Error Norms						
R_2	0.7277	0.6744	0.5453	0.5241	0.5902	0.6118
R_1	0.9450	0.2802	0.1149	0.5259	-0.0960	-0.3740

Table F.12 Error Norm Convergence Tests: 24HM#D series, far
U_o= 0.2 m s^{-1}, U_m = 4.33 m s^{-1}
TI=8%, Ru=10, Clip = 10^{12}
Locations: "Far" (N=2533)

		Degree of Freedom					
		Ux	**Uy**	**Uz**	**P**	**KE**	**E**
Relative L2 Norm							
	Mesh 3 - 4	0.009	0.040	0.107	0.039	0.160	0.323
	Mesh 4 - 5	0.003	0.048	0.068	0.043	0.151	0.196
Relative L1 Norm							
	Mesh 3 - 4	0.00383	0.02356	0.03218	0.00594	-0.00029	-0.00004
	Mesh 4 - 5	0.00246	0.03105	0.02771	0.01343	0.00112	-0.00003
Absolute L2 Norm							
	Mesh 3 - 4	0.04520	0.00953	0.02939	0.00311	0.00092	0.00372
	Mesh 4 - 5	0.02842	0.01147	0.01889	0.00345	0.00083	0.00279
Absolute L1 Norm							
	Mesh 3 - 4	2.00109	0.08721	0.14581	-0.05725	-0.00033	-0.00407
	Mesh 4 - 5	1.27905	0.11146	0.12211	-0.11953	0.00138	-0.00254
3-Mesh Error Norms							
R_2		0.6288	1.2033	0.6426	1.1101	0.9058	0.7513
R_1		0.6392	1.2781	0.8375	2.0879	-4.1327	0.6248

Table F.13 Error Norm Convergence Tests: V2HM#D series, far
U_o= 0.2 m s^{-1}, U_m = 1.81 m s^{-1}
TI=8%, Ru=10, Clip = 10^{12}
Locations: "Far" (N=2533)

		Degree of Freedom					
		Ux	**Uy**	**Uz**	**P**	**KE**	**E**
Relative L2 Norm							
	Mesh 3 - 4	0.009	0.037	0.106	0.040	0.157	0.319
	Mesh 4 - 5	0.003	0.042	0.066	0.038	0.133	0.196
Relative L1 Norm							
	Mesh 3 - 4	0.00385	0.02378	0.03255	-0.00829	-0.00154	-0.00056
	Mesh 4 - 5	0.00245	0.03159	0.02810	-0.01814	0.00383	-0.00037
Absolute L2 Norm							
	Mesh 3 - 4	0.04529	0.00938	0.02978	0.00323	0.00092	0.00372
	Mesh 4 - 5	0.02834	0.01059	0.01882	0.00310	0.00075	0.00283
Absolute L1 Norm							
	Mesh 3 - 4	1.99782	0.09196	0.14999	-0.03255	-0.00085	-0.00422
	Mesh 4 - 5	1.26781	0.11844	0.12582	-0.07423	0.00211	-0.00239
3-Mesh Error Norms							
R_2		0.6257	1.1287	0.6319	0.9616	0.8100	0.7594
R_1		0.6346	1.2879	0.8389	2.2808	-2.4833	0.5666

Table F.14 Error Norm Convergence Tests: V4HM#D series, far
U_0= 0.4 m s^{-1}, U_m = 4.33 m s^{-1}
TI=8%, Ru=10, Clip = 10^{12}
Locations: "Far" (N=2533)

		Degree of Freedom					
		Ux	**Uy**	**Uz**	**P**	**KE**	**E**
Relative L2 Norm							
	Mesh 3 - 4	0.009	0.042	0.115	0.042	0.167	0.375
	Mesh 4 - 5	0.003	0.050	0.082	0.036	0.212	0.196
Relative L1 Norm							
	Mesh 3 - 4	0.00393	0.02090	0.02315	-0.01022	0.00023	-0.00029
	Mesh 4 - 5	0.00285	0.02361	0.01870	-0.01335	0.00425	-0.00017
Absolute L2 Norm							
	Mesh 3 - 4	0.09441	0.02082	0.06374	0.01208	0.00267	0.02691
	Mesh 4 - 5	0.06636	0.02483	0.04645	0.01034	0.00315	0.01743
Absolute L1 Norm							
	Mesh 3 - 4	4.09227	0.16293	0.21674	-0.06670	0.00041	-0.02588
	Mesh 4 - 5	2.95491	0.17981	0.17179	-0.09787	0.00756	-0.01326
3-Mesh Error Norms							
R_2		0.7029	1.1928	0.7288	0.8561	1.1793	0.6480
R_1		0.7221	1.1036	0.7926	1.4673	18.6133	0.5126

Table F.15: Particle release simulations (from data file: F5-Crit Area V2HM4D.xls: 82 μm particle in $U_o = 0.2$ m s^{-1}, $U_m = 1.81$ m s^{-1})

(1)	(2)	(3)	(4)	(5)	(6)	(7)	(8)	(9)	(10)	(11)
Y (m)	How many from bottom get in	**Zmax into mouth**	release 18+2 particles between: zmax	zmin	Δ	How many from top get in	**Zmin into mouth**	release 18+2 particles between: zmax	zmin	Δ
0	11	0.66526	0.67	0.66	0.000526	3	0.64145	0.6425	0.6325	0.000526
0.00025	12	0.66829	0.6725	0.6625	0.000526	3	0.64145	0.6425	0.6325	0.000526
0.0005	9	0.66671	0.6725	0.6625	0.000526	1	0.64250	0.6425	0.6325	0.000526
0.00075	10	0.66724	0.6725	0.6625	0.000526	3	0.64395	0.645	0.635	0.000526
0.001	6	0.66763	0.675	0.665	0.000526	4	0.64342	0.645	0.635	0.000526
0.00125	6	0.66763	0.675	0.665	0.000526	7	0.64184	0.645	0.635	0.000526
0.0015	1	0.66750	0.6775	0.6675	0.000526	10	0.64026	0.645	0.635	0.000526
0.00175	4	0.66908	0.6775	0.6675	0.000526	11	0.63974	0.645	0.635	0.000526
0.002	5	0.66961	0.6775	0.6675	0.000526	8	0.63882	0.6425	0.6325	0.000526
0.00225	9	0.67171	0.6775	0.6675	0.000526	4	0.63842	0.64	0.63	0.000526
0.0025	16	0.67539	0.6775	0.6675	0.000526	4	0.63842	0.64	0.63	0.000526
0.00275	2	0.68053	0.69	0.68	0.000526	3	0.63895	0.64	0.63	0.000526
0.003	1	0.68750	0.6975	0.6875	0.000526	2	0.64197	0.6425	0.6325	0.000526
0.00325	3	0.68105	0.69	0.68	0.000526	5	0.64289	0.645	0.635	0.000526
0.0035	4	0.67658	0.685	0.675	0.000526	4	0.64342	0.645	0.635	0.000526
0.00375	5	0.67211	0.68	0.67	0.000526	3	0.64395	0.645	0.635	0.000526
0.004	9	0.66921	0.675	0.665	0.000526	9	0.64329	0.6475	0.6375	0.000526
0.00425	5	0.66711	0.675	0.665	0.000526	10	0.64276	0.6475	0.6375	0.000526
0.0045	11	0.66776	0.6725	0.6625	0.000526	6	0.64237	0.645	0.635	0.000526
0.00475	3	0.66355	0.6725	0.6625	0.000526	7	0.64184	0.645	0.635	0.000526
0.005	3	0.66105	0.67	0.66	0.000526	6	0.64237	0.645	0.635	0.000526
0.00525	5	0.65961	0.6675	0.6575	0.000526	1	0.64750	0.6475	0.6375	0.000526
0.0055	1	0.65750	0.6675	0.6575	0.000526	7	0.64684	0.65	0.64	0.000526
0.00575	3	0.65355	0.6625	0.6525	0.000526	10	0.64526	0.65	0.64	0.000526
0.006	6	0.65013	0.6575	0.6475	0.000526	8	0.64632	0.65	0.64	0.000526
0.0061	none in	-	0.6565	0.6465	0.000526	none in	-	0.65	0.64	0.000526

Table F.16: Critical area determinations from particle release results in Table F.15.

(1)	(2)	(3)	(4)	(5)	(6)	(7)
Area Going into Mouth				**Area for particles Just Missing the Mouth**		
Y (m)	Δz (m)	ΔY (m)	(ΔY) (Δz)	Δz+ (m)	ΔY (m)	(ΔY) (Δz+)
0	0.02382	0.000125	2.97697E-06	0.02487	0.000125	3.1086E-06
0.00025	0.02684	0.00025	6.71053E-06	0.02789	0.00025	6.9737E-06
0.0005	0.02421	0.00025	6.05263E-06	0.02526	0.00025	6.3158E-06
0.00075	0.02329	0.00025	5.82237E-06	0.02434	0.00025	6.0855E-06
0.001	0.02421	0.00025	6.05263E-06	0.02526	0.00025	6.3158E-06
0.00125	0.02579	0.00025	6.44737E-06	0.02684	0.00025	6.7105E-06
0.0015	0.02724	0.00025	6.80921E-06	0.02829	0.00025	7.0724E-06
0.00175	0.02934	0.00025	7.33553E-06	0.03039	0.00025	7.5987E-06
0.002	0.03079	0.00025	7.69737E-06	0.03184	0.00025	7.9605E-06
0.00225	0.03329	0.00025	8.32237E-06	0.03434	0.00025	8.5855E-06
0.0025	0.03697	0.00025	9.24342E-06	0.03803	0.00025	9.5066E-06
0.00275	0.04158	0.00025	1.03947E-05	0.04263	0.00025	1.0658E-05
0.003	0.04553	0.00025	1.13816E-05	0.04658	0.00025	1.1645E-05
0.00325	0.03816	0.00025	9.53947E-06	0.03921	0.00025	9.8026E-06
0.0035	0.03316	0.00025	8.28947E-06	0.03421	0.00025	8.5526E-06
0.00375	0.02816	0.00025	7.03947E-06	0.02921	0.00025	7.3026E-06
0.004	0.02592	0.00025	6.48026E-06	0.02697	0.00025	6.7434E-06
0.00425	0.02434	0.00025	6.08553E-06	0.02539	0.00025	6.3487E-06
0.0045	0.02539	0.00025	6.34868E-06	0.02645	0.00025	6.6118E-06
0.00475	0.02171	0.00025	5.42763E-06	0.02276	0.00025	5.6908E-06
0.005	0.01868	0.00025	4.67105E-06	0.01974	0.00025	4.9342E-06
0.00525	0.01211	0.00025	3.02632E-06	0.01316	0.00025	3.2895E-06
0.0055	0.01066	0.00025	2.66447E-06	0.01171	0.00025	2.9276E-06
0.00575	0.00829	0.00025	2.07237E-06	0.00934	0.00025	2.3355E-06
0.006	0.00382	5E-05	1.90789E-07	0.00487	5E-05	2.4342E-07
0.0061						
Inhaled Area (m^2):			**0.000157082**	**Area Just Outside Inhaled (m^2):**		**0.00016332**

Figure F.1 Particle release location for inhaled particles (from data file: F5-Crit Area V2HM4D.xls: 82 μm particle in $U_o = 0.2$ m s^{-1}, $U_m = 1.81$ m s^{-1})

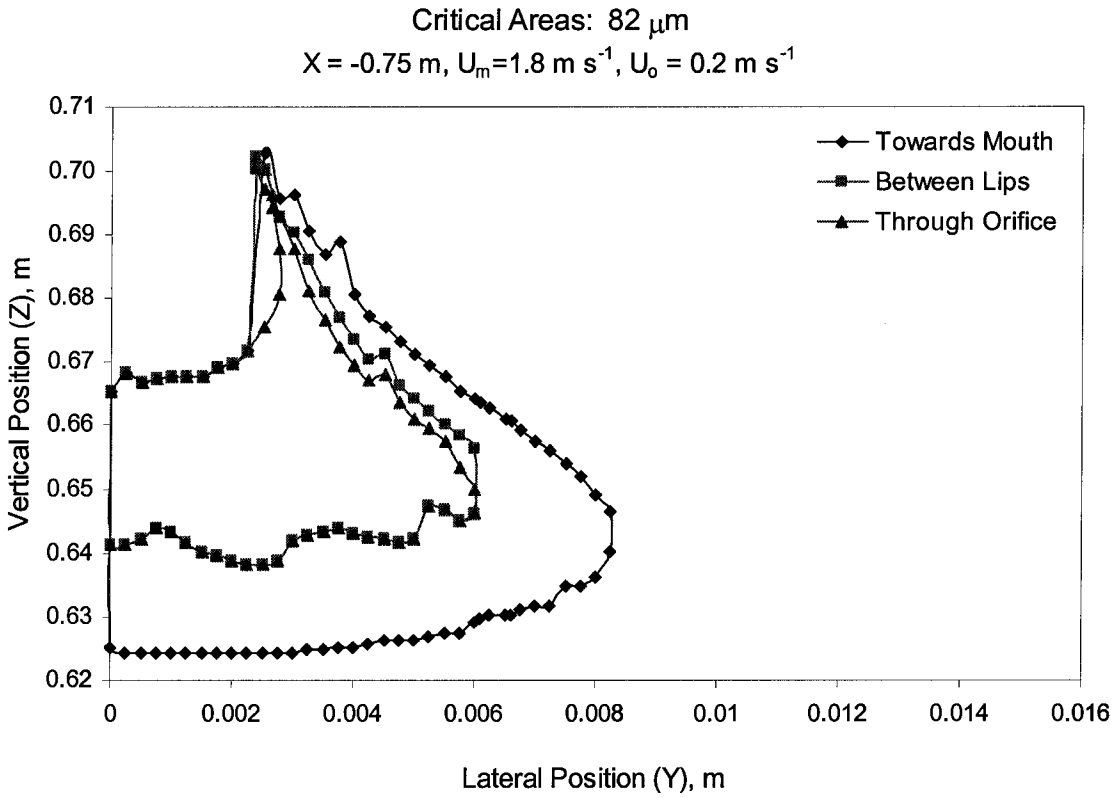

BIBLIOGRAPHY

Aitken,. R.J., P.E.J. Baldwin, G.C. Beaumont, L.C. Kenny, and A.D. Maynard (1999) Aerosol inhalability in low air movement environments. *J. Aerosol Sci.* 30(5): 613-626.

American Conference of Governmental Industrial Hygienists, 2004 TLVs and BEIs Based on the Documentation of the Threshold Limit Values for Chemical Substances and Physical Agents and Biological Exposure Indices. ACGIH Worlkwide, Cincinnati, OH, 2004.

Anthony, TR, M.R. Flynn, A.Eisner (2005) Evaluation of facial features on particle inhalation. *Ann. Occup. Hyg.* 49(2): 179-193.

Anthony, T.R., and M.R. Flynn CFD Model for a 3-D Inhaling Mannequin: Verification and Validation. Submitted to *Ann. Occup. Hyg.*

Armbruster, L. and H.Breuer (1982) Investigations into defining inhalable dust. *Ann. Occup Hyg* 26: 21-32.

Baldwin, P.E.J. and A.D. Maynard (1998) A survey of wind speeds in indoor workplaces. *Ann. Occup. Hyg.* 42(5): 303-313.

Brohus, H. and P.V. Nielsen (1996) CFD models of persons evaluated by full-scale wind channel experiments" *Proceedings of Roomvent '96, 5th International Conference on Air Distribution in Rooms,* Yokohama, Japan, July 17-19, 2:137-144 (1996)

Brohus, H. (1997) CFD simulation of personal exposure to contaminant sources in ventilated rooms. Proceedings of Ventilation '97, The 5th International Symposium on Ventilation for Contaminant Control, Global Developments in Industrial Ventilation, Ottawa, Canada, Vol. 1, pp. 215-226, September 14-17, 1997.

Brohus, H. (1997a) Personal Exposure to Contaminant Sources in Ventilated Rooms, Ph.D. Thesis, Aalborg University, Denmark, Department of Building Technology and Structural Engineering, December 1997.

Carlton, G.N. and M.R. Flynn (1997) Influence of spray painting parameters on breathing zone particle size distributions. *Appl. Occup. Environ. Hyg.* 12(11): 743-750.

Chung, I.P. and D. Dunn-Rankin (1992) Numerical simulation of two-dimensional blunt body sampling in viscous flow. *J. Aerosol Sci.* 23(3): 217-232.

Chung, I.P. and D. Dunn-Rankin (1997) Experimental investigation of a two-dimensional cylindrical sampler. *J. Aerosol Sci.* 25: 935-955.

Chung, I.P., T. Trinh and D. Dunn-Rankin (1994) Experimental investigation of a two-dimensional cylindrical sampler. *J. Aerosol Sci.* 25(5): 935-955.

Dunnett, S.J. (1997) A numerical study of the flow field in the vicinity of a bluff body with aspiration oriented to the flow. *Atmospheric Environment* 31(22): 3745-3752.

Dunnett, S.J. (1999) An analytical investigation into the nature of the airflow near a spherical bluff body with suction. *J. Aerosol Sci.* 30(2): 163-171.

Dunnett, S.J. and D.B. Ingham (1986) A mathematical theory to two-dimensional blunt body sampling. *J. Aerosol Sci.* 17(5): 839-853.

Dunnett, S.J. and D.B. Ingham (1987) The effects of finite Reynolds number on the aspiration of particles into a bulky sampling head. *J. Aerosol Sci.* 18(5): 553-561.

Dunnett, S.J. and D.B. Ingham (1988) The human head as a blunt aerosol sampler. *J. Aerosol Sci.* 19(3): 365-380.

Dunnett, S.J. and J.H. Vincent (2000) A mathematical study of aerosol sampling by an idealised blunt sampler oriented at an angle to the wind: the role of gravity. *J. Aerosol Sci.* 31(10): 1187-1203.

Erdal, S. and N.A. Esmen (1995) Human head model as an aerosol sampler: calculation of aspiration efficiencies for coarse particles using an idealized human head model facing the wind. *J. Aerosol Sci.* 26: 253-272.

Flynn, M.R. and A.D. Eisner (2004) Verification and validation studies of the time-averaged velocity field in the very near-wake of a finite elliptical cylinder. *Fluid Dynamics Research* 34:273-288.

Flynn, MR, K.W. Pickett, T.R. Anthony (2005) Numerical simulation of aerosol concentration in the near-wake of a finite elliptical cylinder-Application to exposure modeling. Submitted to F*luid Dynamics Research.*

Hayashi, T., I. Yoshiaki, K.S. Kato, and S. Murkami (2002) CFD analysis of characteristics of contaminated indoor air ventilation and its application in the evaluation of the effects of contaminant inhalation by a human occupant. *Building and Env.* 37: 219-230.

Heist, D.K., A.D. Eisner, W. Mitchel, and R. Wiener (2003a): Airflow around a child-size manikin in a low-speed wind environment. *Aerosol Sci. and Tech.* 37(4): 303-314.

Heist, D.K., J. Richmond-Bryant, A. Eisner, and T. Conner (2003b) Development of a versatile aerosol generation system for use in a large wind tunnel. *Aerosol Sci and Tech*; 37: 293-301.

Hsu, D.J, and D.L. Swift (1999) The measurement of human inhalability of ultralarge aerosols in calm air using manikins. *J. Aerosol Sci.* 30(10): 1331-1343.

Hyun, S. and C. Kleinstreuer (2001) Numerical simulation of mixed convection heat and mass transfer in a human inhalation test chamber. *Int. J. Heat Mass Transfer* 44: 2247-2260.

Ingham, D.B and M.L. Hildyard (1991) The fluid-flow into a blunt aerosol sampler oriented at an angle to the oncoming flow. *J. Aerosol Sci.* 22:235-252.

Kennedy, N.J. and W.C. Hinds (2002) Inhalability of large solid particles. *J. Aerosol Sci.* 33: 237-255.

Lasher, W.C. (2001) Computation of two-dimensional blocked flow normal to a flat plate. *J. Wind Engin.*; 89: 493-513.

Leith, D. and M.W. First (1976) Uncertainty in particle counting and sizing procedures, *Am. Ind. Hyg. Assoc. J*, 37(2): 103-176.

Murakami, S., J. Zeng, T. Hayashi (1999) CFD analysis of wind environment around a human body. *J. Wind Engin.*; 83: 393-408.

Nobach, H. E. Müller, C. Tropea (1998) Efficient estimation of power spectral density from laser Doppler anemometry data *Experiments in Fluids* 24: 499-509.

Ogden, T.L. and J.L. Birkett (1977) The human head as a dust sampler. In Halton, W.H. editor. Inhaled particles IV: proceedings of an international symposium organized by the British Occupational Hygiene Society. Oxford: Pergamon Press. p. 93-105. ISBN 0080205607.

Ogden, T.L. and J.L.Birkett (1978) An inhalable-dust sampler for measuring the hazard from total airborne particulate. *Ann. Occup. Hyg.* 21: 41-50.

Prabhu, P. Determination of Particle Size Distribution for Aerosol Generated by Lechler's Ultrasonic Atomizer. Masters Thesis, The University of North Carolina, Chapel Hill, NC, May 2003.

Roache, P.J. 1998. Validation in Computational Science and Engineering. Hermosa Publishers, Albuquerque, NM.

Sokal, RR, and Rohlf, F.J. 1981. Biometry, 2nd Edition. W.H. Freeman and Co., San Francisco, CA

Stern, F., Wilson, R.V., Coleman, H.W., Patterson, E.G. (2001) Comprehensive approach to verification and validation of CFD simulations – part 1: methodology and procedures. *J. Fluids Engin.*, 123:793-802.

Tilley, A.R. *The Measure of Man and Woman: Human Factors in Design*. John Wiley and Son, NY, 1993.

Tsai, P.-J., J.H. Vincent, D. Mark and G. Maldanodo "Impaction Model for the Aspiration Efficiencies of Aerosol Samplers in Moving Air under Orientation-Averaged Conditions" *Aerosol Sci. and Tech.* 22:271-286 (1995)

U.S. EPA. (1997) EPA/600/P-95/002Fa. Exposure Factors Handbook. Washington, D.C.: U.S. Environmental Protection Agency, Office of Research and Development, National Center for Environmental Assessment

Vincent, J.H. and D. Mark (1982) Applications of blunt sampler theory to the definition and measurement of inhalable dust. *Ann. Occup. Hyg.* 26(1): 3-19.

Vincent, J.H. and L. Armbruster (1981) On the quantitative definition of the inhalability of airborne dust. *Ann. Occup. Hyg.* 24: 245-248.

Vincent, J.H., D. Mark, B.G. Miller *et al* (1990) Aerosol inhalability at higher windspeeds. *J. Aerosol Sci.* 21(4): 577-586.